THE UNIVERSITY *of* EDINBURGH

Turbulence in Real-Sea Conditions and its Impacts on Tidal Energy Devices.

Alyona Naberezhnykh

Doctor of Philosophy

THE UNIVERSITY OF EDINBURGH

2023

Abstract

Tidal energy is unique among renewable technologies due to its high predictability, making it an essential part of the renewable energy mix. However, extracting energy from turbulent and energetic tidal sites poses durability and design challenges for developers. Existing standards and guides lack specific guidance on accounting for turbulence-induced fatigue loads so wind-based turbulence models are commonly used. Uncertainties arising from this approach lead to higher safety factors and increased device costs. This work investigates the suitability of current methodologies and wind-based turbulence models for tidal applications. It aims to identify the most important considerations for fatigue loading, helping to reduce uncertainty in device design.

Comparisons of semi-empirical models to turbulence measurements from four Acoustic Doppler Current Profilers deployed across two tidal sites, show that in many cases the models are not representative. Both sites show significant deviations from the theoretical length-scales, isotropy ratios and shear profile, and the agreement with spectral models is shown to be component and depth-dependent. The application of Fourier methods for analysing non-stationary phenomena such as turbulence is also examined. By novel application of wavelet analysis, it is shown that intermittent bursts of coherent turbulence are obscured by the averaging associated with Fourier analysis. The energy bursts have instantaneous turbulence intensities up to 80% higher than the average.

The consequences of using wind-based turbulence models in design are explored by testing the sensitivity of turbulence parameters to simulated loads, using the turbine design tool - Tidal Bladed. Varying the turbulence parameters profoundly impacts the loads with turbulence intensity, resulting in a 90% change in fatigue loads (for intensities $2-24\%$). Length-scales show a 49% difference in loads across the range tested ($5-70$m) and the load difference between shear profiles is over 20%. Additionally, load measurements from a full-scale, operational turbine demonstrate a load response to a broad range of turbulence scales, including scales much larger than the rotor, with blade pitching modulating this response. It is also shown that even when structure shadow loads are significant due to the downstream position of the rotor, stochastic turbulence is still the bigger driver of fatigue loads.

The findings highlight the need for clearer industry guidance for the treatment of turbulence in design and testing. Caution is raised against using wind-based models in tidal applications and the importance of accurate measurement and derivation of turbulence parameters, in particular turbulence intensity, is highlighted. If excessive conservatism in design is to be reduced, high-quality turbulence measurements for each site and location are required and appropriate measurement and analysis techniques must be employed.

Lay Summary

Tidal stream energy is a promising renewable technology known for its predictability, making it a valuable addition to the renewable energy mix. It works by extracting energy from tidal channels by placing turbines into the tidal flow. Turbulence refers to the irregular, fluctuating motion of the water, characterised by swirling eddies, and presents durability and design challenges for turbine developers. The fluctuating flow results in fluctuating loads on the turbine. These repetitive loading cycles result in the wearing out of the material, known as fatigue, and can lead to the eventual failure of components.

To design reliable tidal turbines, developers refer to standards and guidelines, but for the tidal industry, these lack specific information on how to account for the effects of turbulence on device fatigue. The developers often resort to using models and recommendations, originally developed for wind turbines. The uncertainty of their application to tidal conditions leads to higher safety margins and increased costs.

To address this issue, I tested the suitability of wind-based turbulence models for tidal energy applications by comparing them to real-sea turbulence measured at two tidal test sites. I found that in many cases, the models were not accurate representations of real-sea turbulence. To better understand the consequence of using misrepresentative parameters in load calculations, I investigated how the simulated loads change for varying turbulence inputs. Results showed that loads are highly sensitive to small changes in turbulence parameters, meaning that if wind-based models are used, the load calculations are likely to be misleading.

Measurements from full-scale operational tidal turbines are scarce. In this study, I analysed the load measurements from such a device to identify the most important drivers of fatigue loading. Results show that turbulence-induced loads are higher than the leg shadow loads - recurring loads arising from the turbine blades passing the turbine leg which are known to be significant contributors to fatigue.

This study emphasizes the need for clearer industry guidance on how to address turbulence in tidal turbine design and testing. It warns against using wind-based models for tidal applications and stresses the importance of accurate turbulence measurements and analysis techniques. By better understanding turbulence-induced loads, tidal energy devices can be made more robust and cost-efficient as we continue to embrace renewable energy technologies.

Acknowledgements

Having taken a somewhat unconventional route to doing an EngD, I was quite unsure of what to expect from the endeavor that lay ahead. However, as I now find myself at the end, I can genuinely say I have enjoyed every moment of it. Undoubtedly, one of the main reasons for this is the exceptional supervision team that has supported me throughout.

I would like to express my gratitude to the academic supervisors Prof. David Ingram and Dr. Ian Ashton. Your invaluable expertise, commitment and support have really guided me through the intellectual and personal challenges, and have made this journey enjoyable and dare I say it smooth!

I have also been fortunate to be involved with two amazing industrial partners. Being based at EMEC and learning about the exciting and meaningful work there has been inspirational and has served as a constant reminder of why I have taken this path. Thank you David Darbinyan for being my supervisor at the early stages of the project, your cheerfulness, knowledge and support have really helped me find my feet with this project. A special thanks to Calum Miller from Orbital Marine. The expertise and the steer you have offered throughout the project have really made it what it is. Your participation has made my research work feel very relevant and I am very grateful for your time and input. Also a big thank you to Mark Byers from Orbital Marine for your endless patience and for getting me up to speed with using Tidal Bladed. Additionally, I am grateful to Joel Culina from FORCE for an engaging collaboration, I have thoroughly enjoyed our discussions and rambles about turbulence.

Of course, thank you to my amazing family and friends for always being supportive of my endeavors, especially my parents. Thank you to Luke for sharing this experience and the adventures of moving from Edinburgh to Cornwall and then to Orkney during the pandemic. I will never forget what two lives packed into a hatchback looks like! Starting our projects during lockdown could've been a very difficult time, but instead, it is filled with countless fun memories. A special thanks to my dear friend and dedicated surf buddy Mark for ensuring I spend all my available time in the ocean, this has kept me sane through the most difficult times.

I would also like to acknowledge the IDCORE program, for providing the opportunity to carry out fascinating research in a subject I am passionate about. This work would not have been possible without the EPSRC and NERC funding, Grant number EP/S023933/1.

Declaration

I declare that this thesis was composed by myself, that the work contained herein is my own except where explicitly stated otherwise in the text, and that this work has not been submitted for any other degree or professional qualification except as specified.

Alyona Naberezhnykh

Contents

Figures and Tables

Figures

Tables

Nomenclature

α	Isotropy ratio
β	Power law shear model exponent
Γ	Spatial coherence
$\hat{s}(f)$	Discrete Fourier transform
λ	Tip speed ratio
μ_P	Mean power
μ_T	Mean thrust
μ_{M_y}	Mean flapwise bending moment
Ω	Rotational speed
$\overline{u}, \overline{v}, \overline{w}$	Mean streamwise, transverse and vertical velocity
$\overline{u'^2}, \overline{v'^2}, \overline{w'^2}$	Velocity variance in streamwise, transverse and vertical directions
$\overline{b_i'^2}$	Beam velocity variance where i is the beam number, $1-5$
$\overline{U}$	Mean current magnitude
ϕ	ADCP misalignment angle
ψ	Analysing Wavelet
σ	Standard deviation
σ_T	Thrust standard deviation
σ_{M_y}	Flapwise root bending moment standard deviation
θ	Beam inclination angle
θ_{leg}	Turbine leg angle
θ_{norm}	Normalising angle for blade angular position
b_i	Beam velocity where i is the beam number, $1-5$
C_p	Power coefficient
C_Q	Torque coefficient
C_t	Thrust coefficient
C_{M_y}	Root bending moment coefficient
D	Rotor diameter
DEL_i	Damage equivalent load calculated from thrust or root bending moment, $i = T, M_y$
H	Water depth
H_s	Significant wave height
I_i	Turbulence Intensity, where $i = u, v, w, total$
l	Chord length
L_i	Integral length-scale where $i = u, v, w$
L_{d_i}	Load range
M_y	Blade root bending moment in flap-wise direction

P	Power
Q	Torque force
$q^2/2$	Turbulent kinetic energy
R	Correlation coefficient
r	Separation distance between velocity measurements
$R(\tau)$	Auto-correlation function
r_r	Rotor radius
RS	Reynolds stress tensor
$S_{ii}(f)$	Turbulence spectrum where $i = u, v, w, b$
T	Thrust force
TKE	Turbulent kinetic energy
u', v', w'	Instantaneous velocity perturbation in streamwise, transverse and vertical directions
u, v, w	Velocity vectors in the streamwise, transverse and vertical directions
$W(s,n)$	Continuous wavelet transform
z	Elevation from seabed

Chapter 1

Introduction

1.1 Topic Background

As the world moves to a greater reliance on renewable energy, predictability and dependability of the energy source will become critical, giving tidal energy a key place in our energy system (Frost, 2022). Unlike tidal barrages, which use the rise and fall of the tides to generate electricity, tidal stream turbines make use of the kinetic energy of the ebb and flow. They typically have a horizontal or vertical axis rotor connected to a generator, which is driven by the current in tidal channels. While tidal barrages require blocking off of large sections of water, tidal stream turbines are individual devices placed in the tidal stream, resulting in a lesser impact on the environment.

Studies have estimated that 11.5 GW of tidal stream energy could be deployed in the waters of the UK and Channel Islands, equating to 11% of the current electricity demand (Coles et al., 2021). In the shorter term, it can provide a viable, competitive solution for remote islands and other locations where access to energy is difficult and prices are higher. Incorporating tidal energy into the energy mix can help reduce the overall cost of the energy system. Predictability of the resource means it can reduce curtailment - deliberate reduction in power output in order to balance the energy supply. It can also help to maintain a reserve capacity - a backup generation used by the grid. The cyclical power generation profile of tidal energy generators also has synergies with battery storage (Frost, 2022).

In the UK, 18MW of tidal stream capacity has been installed since 2008 (Coles et al., 2021). Having completed the testing programmes 7.7MW of this has been decommissioned, leaving 10.4MW still operating. Having access to government funding has been essential for the development of tidal stream projects, however the availability of this has been inconsistent. The Contracts for Difference (CfD) scheme offers a set fee for electricity output to a renewable power generator, known as the strike price, in order to protect generators from fluctuating wholesale electricity costs (Coles et al., 2021). The inclusion of tidal energy projects in the July 2022 CfD Round 4 is providing secure, long-term funding support for the delivery of ≈ 40 MW of tidal energy capacity across three developers in the UK. This should help accelerate progress in the sector.

There have been a number of successful full-scale deployments of floating tidal energy converters (TECs), which are demonstrating the potential of the technology. Figure 1.1 summarises the recent deployments by key tidal energy developers. It is evident that there are a variety of designs and concepts with floating technology gaining prominence.

HydroQuest: *OceanQuest*
- Paimpol-Bréhat, Brittany
- Seabed, 4 x VA rotors
- 1 MW
- No pitch or yaw

Tested between 2019 and 2021

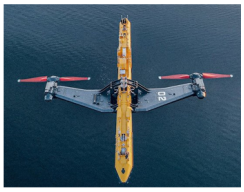

Orbital Marine Power: *O2*
- Fall of Warness, EMEC
- Floating , 2 x 20m rotor
- 2MW @ 2.5m/s
- Blade pitch system

Currently generating to grid at EMEC

Magallanes: *Atir*
- Fall of Warness, EMEC
- Floating , 2 x 19m rotors
- Rated 1.5 MW @ 2.9m/s
- Blade pitch system

Currently testing at EMEC

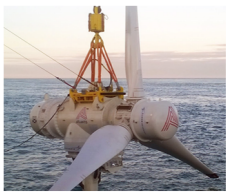

Andritz Hammerfest: *MK1/* **Simec Atlantis:** *AR1500*
- Pentland Firth, Scotland
- Sea-bed, 18m rotor
- 1.5MW
- Blade pitch system/ yawing system

Currently generating to the grid at Meygen

Sustainable Marine: *PLAT-I 6.40*
- Grand Passage, Canada
- Floating, 6 x 4m rotors
- Rated 420kW @ 2.7m/s
- Passively aligned by swivel joint mooring

Tested and exported to grid in 2022

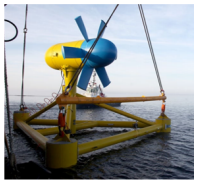

Sabella : *D10*
- Ushant Island, France
- Sea-bed , 10m rotor
- Rated 1MW @ 4.0m/s
- Fixed blades/no yaw

Long term testing in Ushant Island in France

Nova Innovation: *M100-D*
- Shetland, Scotland
- Sea-bed , 8.5m rotor
- Rated 100 kW @ 2.0m/s
- Blade pitch system

Currently 4 devices exporting to grid at Shetland Tidal Array

Minesto: DG100/DG500
- Vestmannasund, Faroe
- Kite, 4-5m wing span
- Rated 100kW
- n/a

Tested and exported to grid in Dec 2022.

Figure 1.1: Summary of key tidal stream energy developers and their status as at July 2023. HydroQuest (2021), Orbital (2022b), Magallanes (2021), SimecAtlantis (2022), SME (2022), Sabella (2022), Nova (2020), Minesto (2021).

Despite the steps forward in the tidal stream energy industry, the risks associated with the survivability of the relatively young technologies are not yet fully understood. Devices have been historically conservatively engineered to demonstrate proof of concept and ensure operability. Optimising devices to reduce costs will help tidal energy become more attractive to investment as the sector enters commercialisation. To do this it is increasingly important to develop a robust understanding of the complex interaction between energetic tidal flows and the TECs.

1.2 Why Focus on Turbulence

Prospective tidal energy sites are highly energetic, providing significant opportunities but they are also characterised by high levels of turbulence and often waves. Such conditions can considerably impact the structural and electrical performance of devices.

To be commercially viable, devices must endure up to 25 years in the water without requiring major overhaul or repair (Scarlett and Viola, 2020). A number of studies (McCann et al., 2008; Blackmore et al., 2015; Milne et al., 2015; Clark et al., 2015b; Milne et al., 2016; Scarlett and Viola, 2020), have concluded that turbulence, as well as other sources of unsteady loading such as waves, significantly affect fatigue loading and energy yield, affecting the device's commercial viability. As a rotor blade rotates through unsteady flow, large differences in the loads can occur compared to those experienced under steady conditions. This can create a number of issues for the TEC design, for example rotor blades can experience stall delay, load hysteresis and dynamic stall (explained in Section 2.3), but the range of flow conditions which cause these effects for full-scale devices are unclear (Scarlett and Viola, 2020). Energy yield is affected by turbulence because a dynamic controller may sacrifice energy yield for power quality during turbulent flow (McCann et al., 2008).

While unsteady loading is also an issue for the more mature wind turbine technology, the effects on tidal devices is likely to be more severe. For a given power output, the torque and thrust on a tidal turbine are much higher than for a wind turbine. Hence, for the same percentage velocity fluctuation, the generated unstable forces will be higher. Water has a higher density than air, so the turbine rotor itself has less inertia than the fluid surrounding it, which makes it more responsive to changes in velocity (Smyth, 2019).

An accurate characterisation of the turbulence quantities and their impact on devices is essential to reduce the risk associated with unsteady flow conditions. Despite the large body of research on this subject, many questions still remain and tidal energy device manufacturers do not yet have robust means to understand, predict or model unsteady interactions between their devices and tidal turbulence (Clark et al., 2015a).

Standards and Guidelines

Standards, design guides and models used for tidal device design are often adapted from other industries such as wind energy. There are two main sources for tidal turbine design guidelines, IEC 62600 suite of technical specifications (IEC, 2019b) and DNV-ST-0.164: Tidal turbines design standard (DNV, 2015) (see Figure 1.2). While both sources acknowledge the importance of turbulence, they provide limited information on how turbulence-induced loads are to be accounted for, so wind standards are often used as reference. Where direct measurements of turbulence are not available, it is recommended to use semi-analytical models which were developed for the wind industry and are based on atmospheric flows.

These recommendations are implemented in commercial and open-source models such as Tidal Bladed and OpenFAST / TurbSim. These models were originally developed for wind energy and hence many of the recommendations are aligned with the wind standard BSI Standards Publication, Wind energy generation systems IEC 61400 (IEC, 2019a).

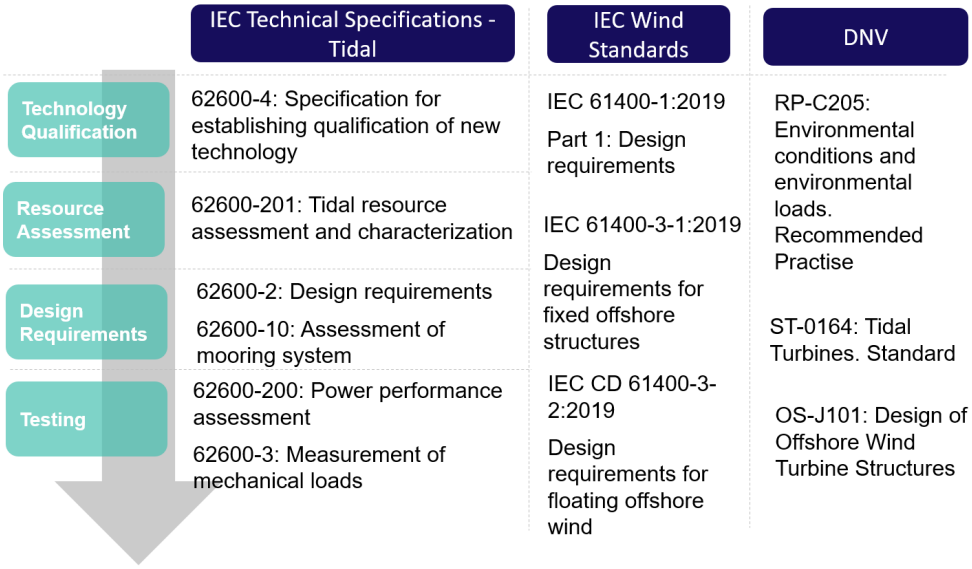

Figure 1.2: Summary of the IEC and DNV standards and technical specifications for the design of tidal energy devices, as well as the wind standards they are based on.

1.3 Research Questions and Aims

The question of turbulence-induced impacts on devices remains partially unanswered because turbulence field measurements and modelling come with many complexities and limitations. This research work aims to address two areas of this multi-faceted problem, through an industry-focused approach.

1. Are turbulence models and analysis methods typically used in the tidal energy industry appropriate for real-sea turbulence?
2. How does turbulence affect TEC loads and which turbulence characteristics are the most critical when considering fatigue loads on devices?

The aim of answering these two questions is to help advance the current industry practices for measuring and modelling turbulence and its effects on devices.

1.4 Project Overview

This EngD project is supervised by three universities - University of Edinburgh, Strathclyde and Exeter as well as two industrial partners European Marine Energy Centre (EMEC) and Orbital Marine Power.

The European Marine Energy Centre (EMEC) Ltd. was founded in 2003 and is the first facility in the world for demonstrating wave and tidal energy converters. EMEC is also involved in the creation of smart energy systems and a green hydrogen economy. EMEC operates two accredited open-sea, grid-connected test sites, the Fall of Warness tidal site and the Billia Croo wave test site. There are also two scale test sites where smaller size devices at an earlier stage in their development can obtain real sea experience in less demanding conditions (EMEC, 2023).

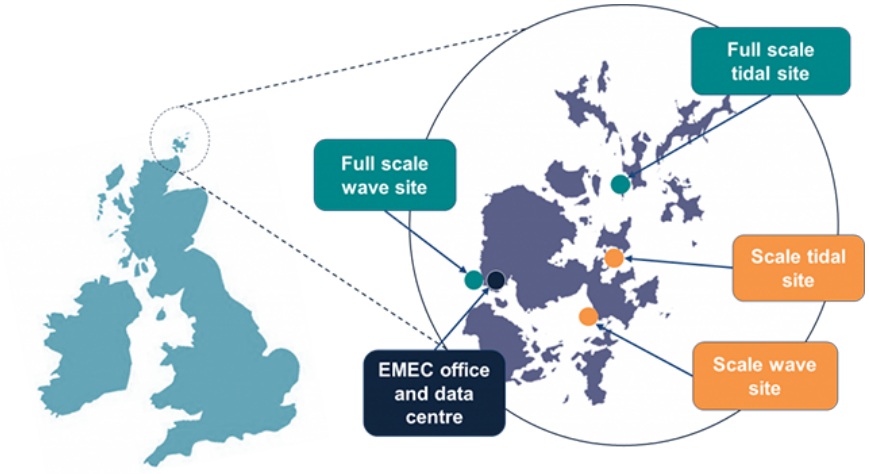

Figure 1.3: Locations of the EMEC test sites on the Orkney Islands, Scotland.

Orbital Marine Power is a Scottish engineering company focused on the development of tidal energy turbine technology. By using floating technology Orbital are able to provide a lower-cost solution by enabling easier installation, access and maintenance. Orbital's device - the O2 - is a 2 MW turbine which has been undergoing testing at EMEC's full-scale tidal site (Figure 1.3) since April 2021. The device has a unique design where the rotors can be brought up above the water line for onsite access and maintenance (Orbital, 2022a).

The industry partnership enables access to expertise and data to study full-scale, operational devices and real sea environments, both through model simulations and field data. The main aim of this research is to provide practical answers to the research questions to help accelerate progress in the industry.

1.5 Synopsis

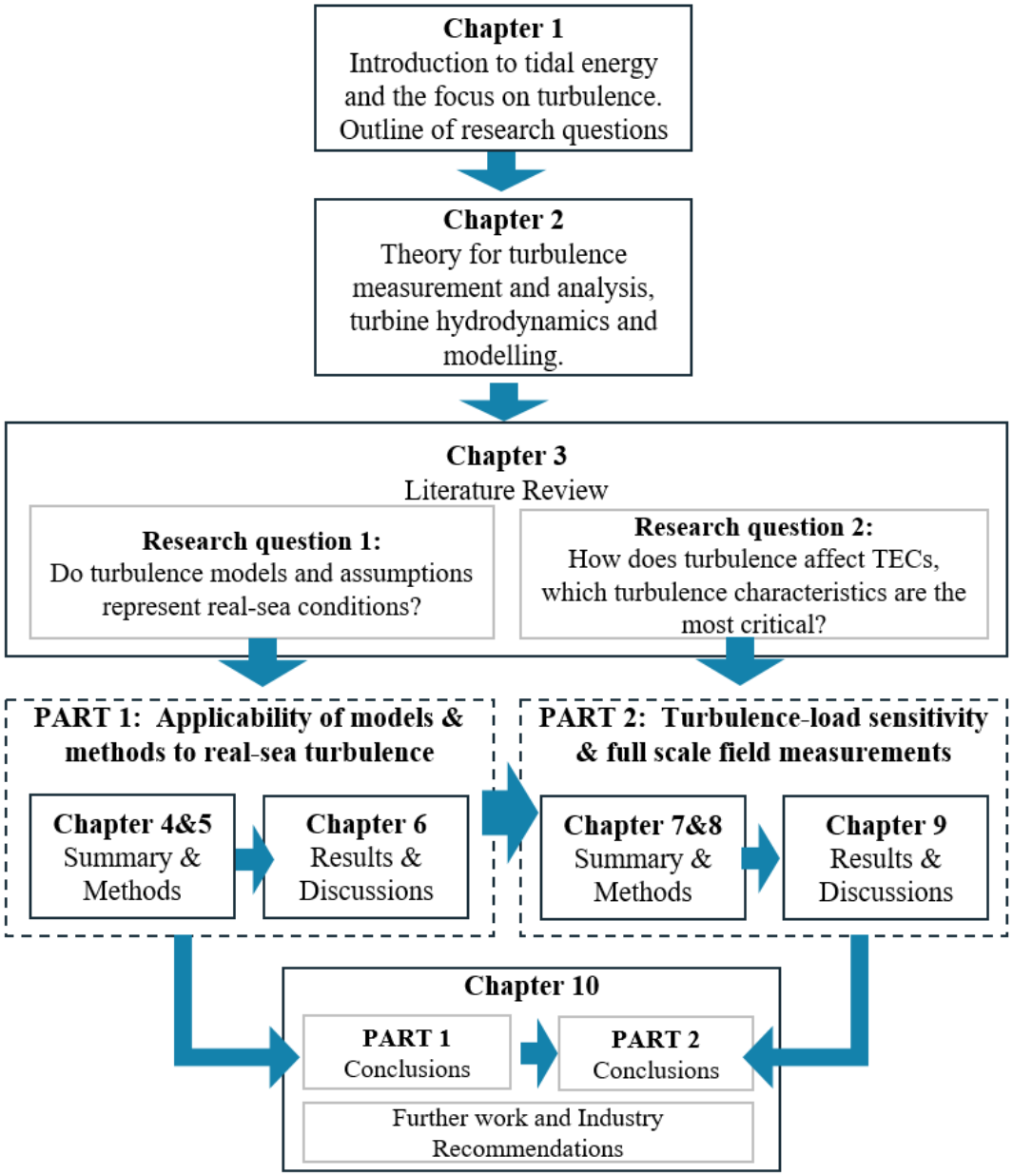

Figure 1.4: Overview of the thesis structure.

Chapter 2

Theory

This chapter introduces all the relevant theory for the upcoming sections of the thesis. Sections 2.1 and 2.2 define the turbulence phenomenon and the key parameters used to characterise it. Section 2.3 provides an explanation of the hydrodynamic responses to unsteady flows and defines the parameters typically used to describe turbine loads. Finally, Section 2.4 summarises different modelling approaches and outlines the key operating principles of the models used in this study.

2.1 What is Turbulence

Turbulence comprises of a field of vortices which are stretched and twisted by the velocity field, which itself is dictated by the instantaneous vorticity distribution (Davidson, 2015). Turbulent flows are characterised by a high Reynolds number, which is the ratio of inertial and viscous forces acting within a fluid. Turbulence is a chaotic process occurring at a large range of scales, constantly evolving in space and time, presenting many challenges for measuring, modelling and analysing turbulent flows.

Much of the knowledge about turbulence is based on atmospheric flows because the amount of experimental research conducted in the aerodynamic industry, particularly for wind turbines, is much larger. However, there are key differences between atmospheric and tidal channel flows which will impact hydrodynamic effects on devices:

- **Density**: Under standard atmospheric conditions, water is over 800 times denser than air, which makes the moving fluid significantly more energetic. This means tidal devices can be smaller than wind turbines, but will also experience higher loads (Winter, 2011).
- **Velocity**: Wind flow velocities tend to be much higher than tidal flows. The average offshore wind turbine has a rated velocity (the wind speed at which the turbine produces its maximum, or rated power) of around 15m/s and tidal turbines tend to be rated at 2-2.5m/s (Winter, 2011).
- **Waves**: Tidal turbines may be subjected to induced orbital velocities from waves travelling past them, a cause of unsteadiness not experienced in atmospheric flows.

- **Turbulence**: The turbulence intensity at tidal sites is likely to be lower than for wind. For example, the turbulence intensity measured at the EMEC test site was found to be around 10%, whereas the normal turbulence intensity seen by a land-based wind turbine would be close to 20% for rated flow speeds (Winter, 2011).
- **Boundary layer**: Much of the tidal flow field of interest will be exposed to boundary layer effects e.g., seabed, sea surface, coastline. This may affect the structure of turbulence and energy distribution amongst scales. Turbulence length-scales in atmospheric flows are typically far larger than the wind turbine, which means they have less of an impact on the blade fatigue stresses. The length-scales in a tidal channel are likely to be of the order of the channel depth as they will be physically restricted by the bottom and surface. Since tidal turbine rotors will occupy a significant portion of the depth, the length-scales will be in the order of the rotor size and hence are likely to impact fatigue loads (Milne et al., 2010).
- **Tidal cycles**: Change in the direction of flow tends to give two distinct profiles. Tidal flows past obstructions (e.g., headlands, islands, and in-stream structures) can result in flow separation, vortex (eddy) formation and shedding that may significantly alter inflow characteristics to devices positioned leeward of these bathymetric features (IEC, 2015).
- **Stratification**: Stratification refers to a density gradient between a surface mixed layer and the underlying water, typically arising from variations in temperature and salinity within these layers. This phenomenon is frequently observed in estuaries, areas influenced by freshwater, or seasonally in regions where tidal mixing is insufficient. Turbulence is inherently linked with stratification and hence the differences between atmospheric and tidal stratification will result in differences in the boundary layer and turbulence properties.

2.2 Turbulence Characterisation

Site characterisation involves the deployment of measurement instruments to understand the metocean conditions at a site. Typically, such measurements would be used in resource assessments, power performance assessments, and by design engineers. One of the more challenging aspects is the characterisation of turbulence. While the IEC Technical Specifications for Marine Energy (IEC, 2013) advise on the importance of considering turbulence, no methods are specified to characterise it. This Chapter discusses the methods of obtaining measurements and their limitations, as well as the recommended techniques to calculate turbulence parameters, based on research studies in this area.

2.2.1 Site Measurements

Measuring turbulence in energetic tidal channels presents a number of challenges. Strong flows cause significant drag on instrument support structures, and the range of spatial and temporal scales that sensors can accurately resolve limits their ability to measure turbulence. Potential tidal sites are surveyed using almost exclusively Acoustic Doppler Current Profiler (ADCP) instruments (Clark et al., 2015b). ADCPs measure the speed and direction of currents using the principle of Doppler shift. The instrument does this by emitting high frequency pings of sound, which scatter off moving particles in the water. Depending on whether the particles are moving toward or away from the sound source, the frequency of the return signal bounced back to the ADCP is either higher or lower. Typically, ADCPs will have 4 slanted acoustic beams measuring along-beam velocities with a 5th vertical beam, although other configurations exist. Each opposite pair of beam measurements are used to resolve one horizontal and one vertical velocity component. The two perpendicular pairs of beams then allow for the resolution of the 3-D velocity vector, by assuming the flow is homogeneous across the beam spread at a given depth (Figure 2.1) (Nortek, 2018).

Other instruments such as Acoustic Doppler Velocimetry (ADV) devices, or shear probes can also be used for measuring turbulence. These are less common due to the difficulty of having to deploy them at the point of measurement. ADVs can resolve the turbulence spectrum up to higher frequencies due to their 3D point measurements of velocity and greater sampling rates (Milne et al., 2016). However, since the ADV only measures at one point, its placement in the water column is crucial. ADCPs are easier to deploy and provide measurements along the water column rather than a single point however they do have limitations in terms of spatial resolution, instrument stability, noise floor magnitude and acoustic reflections (Guion and Young, 2015). Although ADVs are considered to be more accurate (Pearson and Hernon, 2015), Milne et al. (2016) compared ADCP data to estimate of the Reynolds stresses and turbulence intensities measured by an ADV and found good agreement between the two measurements at the Sound of Islay, with differences of 5% or less, demonstrating the ADCP's can provide quality turbulence data.

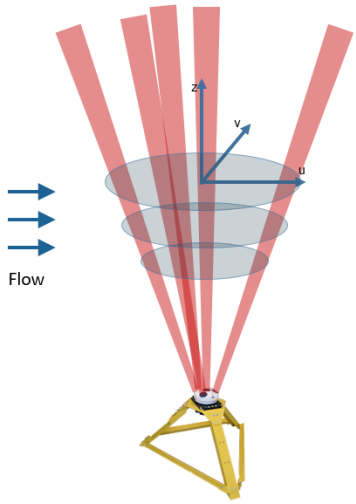

Figure 2.1: Illustration of a 5-beam ADCP in a tripod mounting frame. The shaded region shows the acoustic beam spread area across which the flow must be assumed homogenous.

Limitations of ADCP instruments

Due to the wide range of turbulence scales, it is difficult to measure the whole energy spectrum with a single instrument. Figure 2.2 shows approximate ranges of the scales that can be measured with different instruments, as well as the scales known to be important for TEC loading. In order to correctly interpret ADCP measurements, it is important to understand the limitations of these instruments.

Beam Separation

One of the main limitations of ADCPs is that the 3-D velocity vector is determined from acoustic beam measurements, requiring the assumption that the flow across the beams is homogeneous. As the beams are diverging (see Figure 2.1), the space across which this assumption has to be made increases with the distance from the sensor. In other words, the beam spread may be interpreted as the minimum length scale of turbulence that is measured accurately by the ADCP. Guion and Young (2015) showed that for a 40m deep channel, scales below 3-4 m are attenuated by 90% or more due to filtering effects of spatial averaging across the beam spread (inter-beam). By truncating the observed spectrum, this low-pass filtering may change some global statistics and might create issues when data is required for specific frequencies. Moreover, there is filtering due to averaging within a single beam cone (intra-beam). The same study found that ADCPs can capture up to about 92 % of the spectrum at the top of the tidal channel and up to 98% at the bottom (Guion and Young, 2015) if only the intra-beam effects are considered. The study also found that anisotropy and any phase difference between horizontal and vertical components have significant filtering effects which can cause amplification or attenuation.

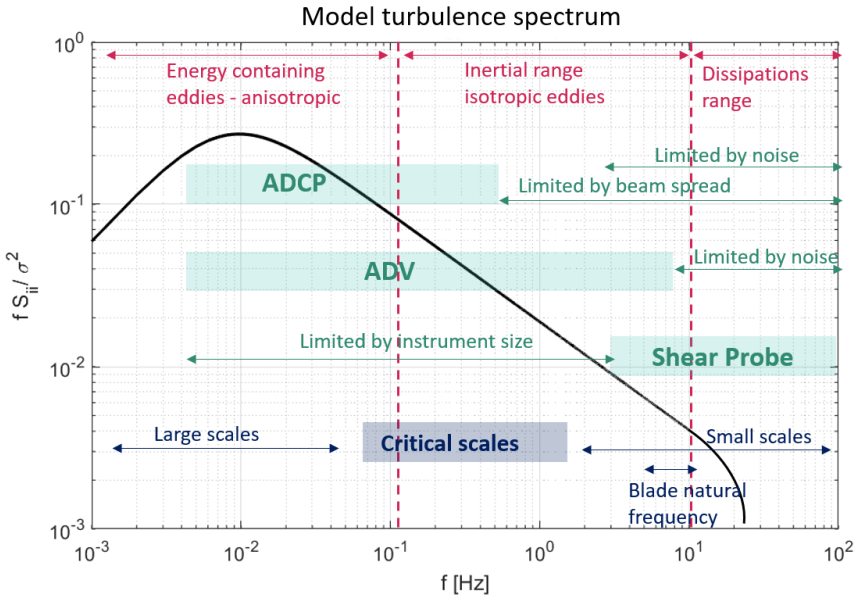

Figure 2.2: Illustrative turbulence spectrum showing approximate frequencies that can be measured by different instruments as well as the turbulence scales considered to have the most significant impact on loads. Frequencies were estimated based on 20m rotor diameter, 1m chord length, 1.5m/s flow. ADCP limits were calculated based on beam spread at 20m from the seabed.

Due to the filtering effects, instantaneous estimates of velocity components from different beams should not be combined directly. Instead, to obtain turbulence statistics, the variance method (explained in Section 2.2.2) should be applied. Rather than assuming that the instantaneous flow is homogeneous across the beams, this method requires the assumption that the statistical properties are homogeneous. While this helps to compute some statistical properties of turbulence, other parameters such as the turbulent length-scale, spectrum and coherence require instantaneous velocity values. Greenwood et al. (2019) carried out a direct comparison of the length scales derived from the streamwise velocity component (making a homogeneity assumption) and the along-beam velocities. They found that the largest length-scales for both methods were similar, however, the component velocity method missed most of the peaks shown by the along-beam velocities.

Frequency

Increasing the sampling rates of ADCP instruments improves accuracy in the measurement of smaller-scale (faster) fluctuations. Due to the fundamental limitation of the instrument geometry, raising the sampling frequency of the instrument above the limiting beam separation frequency (Figure 2.2) would have limited advantages. High-resolution data increases the amount of random noise and reduces the profiling range as well as increasing power consumption (Pearson and Hernon, 2015), and so this trade-off must be considered when

choosing sampling rates. For observations of the smallest length scales, ADV measurements are usually required (Thomson et al., 2012). Observations of the very large turbulence scales require longer averaging windows and hence longer continuous sampling, which can also affect battery life.

Noise

Doppler noise results from errors in measuring the phase shift of the reflected pulse. Factors that contribute to Doppler noise include the processing scheme, operational mode, bin size, and pulse design coding, length and strength. Flow conditions such as shear and turbulence also affect the noise level of ADCPs (Pearson and Hernon, 2015). Incomplete removal of Doppler noise will cause the resultant fluctuating velocities to be biased slightly high, and thus be conservative for the purpose of tidal design loading specification. For example, Sellar et al. (2018) calculated rotor averaged turbulence intensity for flood tides to be 11.7% for operating velocity range, which reduces to 10.9% (6.8% relative reduction) following the implementation of noise correction techniques. There are various ways to reduce the Doppler noise in post-processing. A commonly used method (Sellar et al., 2018; Thomson et al., 2012; Durgesh et al., 2014) is based on the spectral analysis of the measured signal with respect to turbulence theory (inertial range), under the hypothesis of a white Doppler noise contamination. The noise-induced variance is assumed to be distributed as an additional flat PSD layer over the whole frequency domain and hence can be removed.

Waves

Although not a limitation of the instrument, surface waves pose a significant problem for ADCP measurements. The presence of long surface gravity waves means velocity fluctuations are not only driven by turbulence but also by wave orbital motion, which can bias turbulence measurements. Waves can also affect mean flow measurements and distort the shear profile in the upper part of the water column. Wave orbital motions generate coherent structures that appear in the variance of the along-beam velocity time series. Moreover, the wave and turbulence spectral signatures often occupy the same frequency band, complicating any attempt of wave-turbulence separation (Thiébaut et al., 2020b; Perez et al., 2020). In order to improve the accuracy of turbulence measurements, wave orbital motion and turbulent fluctuations must be decomposed and for this, knowledge about the wave conditions is required. Literature presents a number of methods for filtering the effects of waves from ADCP data (Perez et al., 2020; Togneri et al., 2021; Bian et al., 2018). None of the methods offer a perfect solution and can add uncertainty to turbulence measurements.

Instrument Orientation

Methods for obtaining turbulence statistics e.g. the variance method (explained in Section 2.2.2), are based on the assumption that the beam pairs are aligned to the flow direction. This way, one beam pair resolves the streamwise and vertical components and the perpendicular beam pair resolves the transverse and vertical. If the instrument is misaligned, these quantities will be incorrect. The geometric rotation of the Reynold's stress tensor (see Section 2.2.2) is also not possible because to carry out a full rotation, all six unique terms must be known. A typical 5-beam ADCP only provides five of the terms. Vermeulen et al. (2011) have attempted to overcome this issue by using two coupled 4-beam ADCPs, essentially creating an 8 beam instrument. With eight beams, all six terms can be calculated allowing for rotation of the tensor into the right co-ordinate system (Vermeulen et al., 2011). Most instruments deployed for characterisation are likely to be 5-beam ADCPs and therefore unless they're well aligned to the flow direction, the turbulence statistics will not be in the right co-ordinate system.

In summary, an ADCP can provide reliable statistical turbulence metrics, providing correct methods are used and the inherent limitations are understood. Mainly this means limiting the beam spread, sufficient resolution on vertical sampling cells, adequate sampling frequency, alignment of the instrument and appropriate post-processing methods.

2.2.2 Turbulence Parameters

Turbulence characterisation is defined by Clark et al. (2015a) as a representation of the properties of a complex, three-dimensional turbulent flow, using a reduced parameter set. The measured parameters are typically used as model inputs, used to generate synthetic turbulent flow fields in order to estimate loads on devices.

Reynold's Stress Tensor

Reynolds stresses represent the momentum flux due to turbulent fluctuations and relate to the auto- and cross- spectra (S_{ij}). The Reynold's stress tensor is defined as (Clark et al., 2015a):

$$RS_{ij} = -\rho\overline{u_i u_j} = -\rho \begin{pmatrix} \overline{u'^2} & \overline{u'v'} & \overline{u'w'} \\ \overline{u'v'} & \overline{v'^2} & \overline{v'w'} \\ \overline{u'w'} & \overline{v'w'} & \overline{w'^2} \end{pmatrix} \tag{2.1}$$

where ρ is the fluid density and u', v', w' are instantaneous streamwise, transverse and vertical velocity perturbations respectively. The overbar indicates the temporal mean. Due to symmetry, the tensor contains six unique terms. The normal stresses, on the diagonal, are used to calculate turbulence intensity, I, defined in equation 2.3 or turbulent kinetic energy , TKE , defined as:

$$TKE = \frac{1}{2}(\overline{u'^2} + \overline{v'^2} + \overline{w'^2}) \tag{2.2}$$

The off-diagonal terms are the shear stresses, also known as Reynolds stresses. For example, the stress term $u'w'$ represents a vertical exchange of axial momentum; where turbulent mixing between a faster (top of water column) and a slower (bottom) region of flow results in momentum transfer between the regions.

Turbulent intensity, I is a term adopted from the wind industry and is a measure of the magnitude of fluctuations as a percentage of the mean flow velocity $\overline{U}$ (Sellar and Sutherland, 2016). The total intensity I_{total} and streamwise intensity I_u are given by the following equations respectively:

$$I_{total} = \frac{\sqrt{\frac{1}{3}(\overline{u'^2} + \overline{v'^2} + \overline{w'^2})}}{\overline{U}} \times 100 \tag{2.3}$$

$$I_u = \frac{\sqrt{\overline{u'^2}}}{\overline{U}} \times 100 = \frac{\sigma_u}{\overline{U}} \times 100 \tag{2.4}$$

A 5-beam ADCP allows for a true measurement of vertical velocities and the estimation of five Reynolds stress terms (all but $u'v'$), TKE, I and anisotropy directly from the along-beam velocities (Guerra and Thomson, 2017). As already mentioned in Section 2.2.1, the orientation of the beams to the flow is vital. If the beams are not aligned with the flow direction, only the total I_{total} or TKE quantities can be reliably calculated (Greenwood et al., 2019). In other words, unless the beam pairs are aligned to the flow, the Reynolds stress components will not be resolved in the right co-ordinate system, and rotation of the tensor is not possible, as all six Reynolds stress terms are not known.

To calculate Reynolds stresses, the variance method is used. The variances in velocity components are first determined in along-beam coordinates, then combined by assuming statistical characteristics (variances) are homogeneous over the beam spread, for further explanation of the method see (Dewey and Stringer, 2007; Thiébaut et al., 2020b). The benefit of the variance method is that the turbulent velocities need not be homogenous across the beam separation distance, but the statistical characteristics do (Dewey and Stringer, 2007). Variance method calculations, however, are highly sensitive to both the pitch and roll of the ADCP, and the physical orientation of the beams relative to the channel.

Turbulence Spectrum

A property of turbulence in the tidal channel environment is the wide range of scales that are associated with motions in the fluid flow. The largest scales of turbulence consist of anisotropic eddies, arising from and driven by the mean fluid flow. Large eddies are dynamically unstable and enter a complex cascade (Richardson's energy cascade), evolving into successively finer structures. According to Kolmogorov's law, in the Fourier space representation, the energy

spectrum must approach an asymptotic limit proportional to $f^{-5/3}$ at high frequency (where f denotes the frequency, in Hz) (Pope, 2000) . Ultimately, the eddies become so small that the fluid viscosity becomes significant and the kinetic energy progressing down the cascade is dissipated to heat.

The distribution of energy amongst the turbulence scales is described by the turbulence spectrum. This is normally obtained using Fourier transform. Discrete Fourier Transform (DFT) of a detrended, statistically stationary velocity sample is defined as:

$$\hat{s}(f_k) = \sum_{n=0}^{N-1} x(n) e^{-i f_k n} \tag{2.5}$$

where $x(n)$ is a time series for example of flow velocities, f_k is the discrete frequency (0,1...N-1), n is the time index and $\hat{s}(f_k)$ is the spectrum. The power spectral density (PSD) defines the spectrum in terms of variance per unit frequency:

$$S(f_k) = \frac{2}{N\Delta t} |\hat{s}(f_k)|^2 \tag{2.6}$$

where N is the number of points in $\hat{s}(f)$ (Emery and Thomson, 2001).

Coherency

Spatial coherence, Γ is usually estimated from two independent measurements of the same component of velocity, u_1, u_2 that are separated in space by a distance, $r = (\Delta x^2 + \Delta y^2 + \Delta z^2)^{1/2}$. Using fast Fourier transform, $\mathscr{F}$ and $S_u = |\mathscr{F}_{u'}|^2$, coherency is defined as (Thomson et al., 2014):

$$\Gamma(u) = \frac{|\overline{\mathscr{F}_{u_1'} \mathscr{F}_{u_2'}}|^2}{\overline{S_{u_1} S_{u_2}}} \tag{2.7}$$

Non-stationarity and Time-Frequency Analysis

Analysis of turbulence data requires the assumption that the flow is statistically stationary over some period of time, for example, the mean is expected to converge to a value as stationarity time is approached. Typically, the stationarity period for tidal channel data is assumed to be 5-10 minutes (Clark et al., 2015a). Short-term variations in turbulent fluctuations are referred to as intermittency i.e., the motion sporadically varies between more and less turbulent, in both space and time (McMillan, 2017). Intermittency can result in non-stationarity of the data.

When the spectrum is analysed using the Fourier transform, the turbulent signal is decomposed into a sum of infinite sine and cosine functions with different frequencies and hence generates record-averaged values of amplitude and phase for each frequency component. It is assumed that vortices at each scale occupy the entire timeline, so when applied to a non-

stationary time series, information on the changing processes will be smeared out (Emery and Thomson, 2001; Chen et al., 2019). In other words, if a non-stationary time-series is dissected, the statistical properties of the parts will not be similar to those of the whole series, and the usual Gaussian statistics based on the record will be deceptive (Flinchem and Jay, 2000).

In such cases, short-time Fourier transform (STFT), a sequence of Fourier transforms performed over a sliding window across the entire time series, may be used (Akansu and Haddad, 2001). This approach attempts to address a signal's non-stationarity by analysing parts of the signal and providing the time-localized frequency information. However, the window size is predetermined and fixed, so some inaccuracies arise from the aliasing of high and low frequency components that do not fall within the frequency range of the window (Indrusiak, 2004; Torrence and Compo, 1997).

Wavelet Theory

Wavelet analysis can be thought of as stretching and compressing the window of the short-time Fourier transform, according to the frequency to be localized. This allows the definition of scales in both time and frequency domain, helping to identify intermittent features of the flow such as the passing of coherent structures. While the Fourier transform uses trigonometric functions as the basis, the wavelet transform bases are a broad range of functions named wavelets (Chen et al., 2019).

The continuous wavelet transform (CWT) of a discrete sequence, $x_{n'}$ is defined as the convolution of $x_{n'}$ with the analyzing wavelets ψ. The transform gives the wavelet coefficients:

$$W(s,n) = \sum_{n'=0}^{N-1} x_{n'} \psi * \left[\frac{(n'-n)\delta t}{s} \right] \tag{2.8}$$

where the $(*)$ indicates the complex conjugate and δt is the time step of the time series. By varying the wavelet scale, s and translating along the localized time index, n, a picture of amplitude versus the scale and how this amplitude varies with time can be constructed (Torrence and Compo, 1997).

The relationship between the equivalent Fourier frequency and the wavelet scale can be derived analytically for a particular wavelet function as described in (Torrence and Compo, 1997), to yield $W(f,t)$. The wavelet function, ψ is in general complex, so the wavelet transform is also complex. The transform can then be divided into real and imaginary parts, amplitude and phase respectively, and the wavelet power spectrum is then $|W(f,t)|^2$.

The global wavelet spectrum, $\tilde{W}(f)$ is the time-averaged wavelet spectrum over a defined period, it must be normalised according to the measured variance, u'^2 :

$$\tilde{W}(f) = \frac{1}{C}\int_0^\infty |W(f,t)|^2 dt \tag{2.9}$$

where the constant C makes:

$$\int_0^\infty \tilde{W}(f) df = u'^2 \tag{2.10}$$

Without normalisation, the scale of the wavelet spectrum would be arbitrary and not comparable to the Fourier spectrum. Once normalised, the mean wavelet spectrum, $\tilde{W}(f)$ should be a smoothed version of the Fourier energy spectrum $S(f)$.

Wavelet analysis depends both on the signal and on the analyzing wavelet. The basic analysing wavelet is referred to as the mother wavelet. It should exhibit a fast decay for t tending to infinity, must be oscillating and its Fourier transform $\hat{\psi}(f)$ must decay fast as wave numbers tend to infinity. For analysis of turbulent signals, (Farge and Schneider, 2004) recommend to use the continuous wavelet transform with complex valued wavelet such as the Morlet.

The Morlet wavelet scale is closely related to Fourier period, thus keeping the wavelet analysis close to the classical Fourier. It is common to set the frequency parameter of Morlet wavelet equal to 6. The frequency parameter relates the wavelet scale to the Fourier period. In this way, besides satisfying the necessary wavelet admissibility condition (where the function must have zero mean), good time-frequency localization is achieved. This makes the Morlet wavelet especially useful for detecting localized, sporadic periodicities in time series, as well as the time evolution of these periodicities (Mihanović et al., 2009). The Morlet wavelet has been used in open channel studies and been shown to have a good balance between time and frequency localization (Chen et al., 2019).

Length-scales

Length-scales are determined by the longest correlation distance between two points in the flow that are separated either by distance or time. Time correlations are typically used (Equation 2.12), which requires the application of the Taylor's Frozen Field hypothesis - a method to convert between frequency content of a time-domain signal to scale. The hypothesis can be applied under the assumption that turbulence advects faster than it evolves, for further explanation see Schlipf et al. (2010). Time correlation is defined as follows:

$$R(\tau) = \frac{\langle (u_t - \overline{u})(u_{t+\tau} - \overline{u}) \rangle}{\sigma_u^2} \tag{2.11}$$

$$L_u = \overline{u} \sum_{\tau=0}^{R(\tau)=0} R(\tau) d\tau \tag{2.12}$$

where $R(\tau)$ is the time-based auto-correlation function. Alternatively, the spectral slope method (Sellar and Sutherland, 2016; Parkinson and Collier, 2016) can be used but requires the fitting of the measured spectrum to a model and hence depends on whether the models properly represent the flow. Clark et al. (2015b) defines the turbulent scales ranges as follows:

Large scale eddies have a characteristic length scale, $L_{large} > D_{rotor}$, where D_{rotor} is the rotor diameter. These would be felt as uniform gusts across the rotor area, they describe intermittency and fluctuations on a larger scale (e.g. over the propagation length of a turbine wake or on the scale of turbine separations within an array).

Mid-scale eddies have a characteristic length-scale $l_{chord} \leq L_{mid} \leq D_{rotor}$. The turbine disc diameter is taken as the upper limit for this range and the chord length, l_{chord} is taken as the minimum. The rotational velocity field around an eddy produces a rapid shift in the angle of attack and inflow speed into the blade section as it moves through the turbulent flow. As a result, the blades experience stochastic load distributions and bending mode forms, affecting fatigue life. Local extreme variations in inflow angle and speed, brought on by mid-scale turbulence can lead directly to dynamic stall or cavitation effects.

Small scale eddies have a characteristic length-scale less than a typical blade chord length (the distance between the leading edge and the trailing edge of the blade) $L_{small} < l_{chord}$. The size of the eddies is much smaller than that of the equipment itself and the exerted loading averages out over the surface of components. Turbulence in this range typically impacts the detailed hydrodynamic performance of a device without imposing direct loading. Very small eddies can be predicted from standard turbulence theory, as they are unaffected by local bathymetry.

Clearly, not all scales of turbulence will affect loads on tidal devices in the same way. Partitioning of length-scales is useful in considering the portion of the total turbulence that may be relevant to tidal turbines and hence enables simplification by limiting analysis to the range in interest. For example, the large scales dominate the velocity variance but may not be the critical scales for tidal turbines. Additionally, as can be seen in Figure 2.2, measurement instruments can only measure limited ranges of scales, so its important to use an instrument that captures the critical range.

When measurements are not available, the length scale is often estimated according to open channel flow theory. This theory suggests that the length-scales across the lower half of the water column can be approximated as $L_u \approx \sqrt{zH}$, where z is the relative elevation from the sea bottom (Nezu and Nakagawa, 1993).

Flow Shear

The shear profile of the velocity normal to the seabed in a tidal race constitutes a high Reynolds Number turbulent boundary layer. The shape of the shear profile is dominated by two effects (Clark et al., 2015a):

1. Turbulence in the flow resulting in vertical mixing.
2. Channel expansion and contraction, which does not necessarily accelerate or decelerate uniformly throughout the water column.

The power law (Equation 2.13) is traditionally assumed (Gunn and Stock-Williams, 2013) to represent the shear profile in channels:

$$u = u_r(\frac{z}{z_r})^{\beta}, \tag{2.13}$$

where u_r is the velocity at reference height z_r, β is the shear exponent normally taken as $1/7$. The seabed roughness, bathymetric effects and the free surface mean that measured tidal flow shear profiles can deviate from such analytical cases. It has been reported that the maximum velocity in an open channel flow is frequently not near the surface, even in a uniform channel with a developed flow. Additionally, secondary flow caused by drag will cause veer at some points across the channel (Gunn and Stock-Williams, 2013). Moreover, the shear models recommended by the IEC wind turbine design standards (IEC, 2019a) are originally intended for neutral stratification. Stratification in the water column may violate the shear profile assumptions (Zhu et al., 2016).

Isotropy

Isotropy describes the degree to which turbulence is statistically invariant under rotations. The biggest scales of turbulence in the marine boundary layer are often anisotropic because they are constrained by the seabed and the free-surface boundaries, and are deformed by the mean shear through the water column. This implies that isotropy would only apply to length-scales smaller than the water depth (McCaffrey et al., 2015).

Anisotropy ratio, α is a measure of turbulence anisotropy, given by Equation 2.14. This ranges from zero for extremely anisotropic turbulence to 0.5 for isotropic turbulence (Lu and Lueck, 1999):

$$\alpha = \frac{\sigma_w}{\sigma_u + \sigma_v}, \tag{2.14}$$

where σ_i is the standard deviation for velocity components $i = u, v, w$. This parameter can only be obtained with a 5-beam ADCP or an ADV. Kolmogorov's theory of locally isotropic turbulence predicts that amplitude of the spectral components S_{uu}, S_{vv} and S_{ww} will be equal in the inertial sub-range (Kolmogorov, 1961).

2.3 Turbine Hydrodynamics

This section introduces the relevant hydrodynamics theory, in particular relating to the turbine response in unsteady flows. This is followed by the description of key parameters used to analyse rotor loading.

2.3.1 Wind vs Tidal Turbine Dynamics

Given that the shape and function of tidal turbines are similar to wind turbines, much of the design and analysis principles are based on methods inherited from the wind industry. However, while the hydrodynamic mechanisms remain the same (e.g. actuator disc, blade element momentum theory), the differences in fluid behaviour (Section 2.1) mean that marine turbine blades are not simply scaled wind turbine blades and will encounter different operating conditions. These are related to the range of Reynolds number, stall characteristics, cavitation, the ratio of the turbine height to the boundary layer thickness and free-surface effects.

A number of factors mean that unsteady loading is a more significant problem for tidal devices than for wind turbines. Tidal turbines' torque and thrust are significantly higher than wind turbines for the same power output since the flow velocity and blade rotational speeds are lower. As a result, tidal turbines generate unstable forces that are substantially greater than those produced by wind turbines from the same percentage velocity fluctuations. Since water has a higher density than air, the turbine rotor itself has less inertia than the fluid surrounding it, which makes it more responsive to changes in velocity (Smyth, 2019). Moreover, the close proximity of the water surface has a significant effect on the structure of the flow field (Chamorro et al., 2013), restricting and distorting large-scale motions. It also means that devices will be subject to wave loading.

2.3.2 Unsteady Loading

There are four main aspects that contribute to unsteady loadings on tidal turbine blades (Finnegan et al., 2020):

1. Variation in the vertical velocity profile of the tidal flow
2. Shadow effects from the support structure
3. Forces generated from surface waves
4. Turbulence in the approaching flow

While the main focus of this study is primarily on the turbulence effects, in practice it is difficult to decouple the above effects when analysing turbine response. For example, structure shadow effects occur when the rotor blades pass the supporting structure e.g. tower or leg. The shear layer, structure wake and turbulent coherent eddies mean the turbine blades rotate through a flow field that varies in space, resulting in significant energy contributions at multiples of the rotational frequency. This means that the load contributions from rotational sampling i.e. blades passing through varying flow, will depend on all four contributors above.

These structure shadow effects occur whether the rotor is up or downstream of the support structure but will be much more significant when the rotor is downstream due to the wake effects of the support structure. In wind, these are undesirable due to increased fatigue loading but also due to "thumping" noise at high-operational wind speeds (Noyes et al., 2020). In tidal application, due to the bidirectionally of the flows, it is likely that some rotors will operate upstream during one tide and downstream during another, meaning such effects will be important to understand.

Unsteady (fluctuating) loads can result in high-cycle fatigue or extreme loading events exceeding the ultimate tensile strength of components, potentially causing damage to devices. Unsteady velocity fluctuations are associated with rapid angle of attack changes, which may lead to phenomena such as dynamic stall and stall delay.

Stall is related to the flow separation that occurs on the suction side of the blade. In static stall conditions, a vortex forms at the leading edge of the blade and separates. Viscosity causes the vortex to completely disappear by the time it reaches the trailing edge and the stall is fully established, resulting in a decrease in lift force. Rapid changes in angle-of-attack - which strengthen the leading edge vortex and induce dynamic stall - occur in unsteady flow conditions (Perez et al., 2022b). The strong leading edge separation vortex convects along the aerofoil suction surface, increasing lift to a level significantly exceeding the stall limit of the aerofoil under steady conditions (Smyth, 2019).

Dynamic stall can be categorized as weak or fully developed. In the first case, the rapidly changing angle-of-attack moderately exceeds static stall values causing increased lift forces. In the second case, the angle of attack exceeds static conditions even further, inducing the formation of a leading-edge vortex (Perez et al., 2020). Past studies show that in unsteady flow conditions, the flow around the blade is dominated by dynamic stall, which means this phenomenon is a key cause of large load peaks and lower energy efficiency (Scarlett and Viola, 2020).

Stall delay is a phenomenon that occurs as a result of the blade rotation, and refers to the differences between the measured performances and predictions based on 2D hydrofoil characteristics. As the fluid approaches the trailing edge of the blade, it is slowed by the pressure gradients, causing lift coefficients to greatly exceed those of static hydrofoil testing. This effect is most noticeable near the blade root (Galloway, 2013).

2.3.3 Quantifying Loads

TEC design usually considers two load contributions - ultimate and fatigue loads. Ultimate loads are loads that can cause damage due to the stresses exceeding the yield strength for the materials. Fatigue loads relate to the failures due to the cumulative damage effect of cyclic loading (Hammerum et al., 2007).

To measure the loads acting on a tidal energy device, strain gauges and load cells can be incorporated into the blades, blade root and the supporting structure of the TEC (Lake et al., 2021). Since they have historically been linked to failures, the blades are frequently the main focus of load studies. The basic output of a load measurement campaign, or modelling output, is the loading time series data. The time series are post-processed to provide summary statistics, damage equivalent loads, and cumulative rain-flow spectra (IEC, 2020).

Performance Coefficients

The hydrodynamic loads experienced by the blades can result in blade deformations in the flap-wise (thrust), edge-wise (torque), and twist directions based on the structural properties of the blade. Summary statistics of the rotor thrust T, the rotor torque Q, and the blade root bending moment M_y (in the flap-wise direction) are usually taken as the key performance parameters. Torque is the sum of the forces acting on the blades in the rotor plane and thrust is the sum of forces acting on the blades perpendicular to the rotor plane and parallel to the rotor axis (Lake et al., 2021). Although both torque and thrust are important for calculating fatigue life, rotor thrust tends to be the dominant load on the device. The blade roots are subject to the highest loads so the blade root bending moment is of greater interest. The flap-wise bending moments are considered the most critical as their values have been found to be 3-4 times higher than those from edge-wise bending moments (Ouro and Stoesser, 2019). Negligible deformation is expected in the edgewise direction as blades tend to have high structural stiffness in this direction. The mechanical power P can be derived from the torque using the angular frequency of the rotor.

The performance parameters can be expressed as non-dimensional performance coefficients that are used to characterize tidal turbines: C_P, C_T, C_Q and C_{M_y}, given by the following equations (Old et al., 2018a).

The rotor power coefficient, C_p is the ratio of the mechanical power developed by the rotor, to the power available in a body of water flowing through a disk of equivalent swept area.

$$C_P = \frac{P}{\frac{1}{2}\rho\pi r^2 U_0^3} \tag{2.15}$$

The rotor thrust coefficient, C_T normalises the axial loading on the rotor, T .

$$C_T = \frac{T}{\frac{1}{2}\rho\pi r^2 U_0^2} \tag{2.16}$$

where T is the axial loading on the rotor.

$$C_{M_y} = \frac{T}{\frac{1}{n}\rho\pi r^3 U_0^2} \tag{2.17}$$

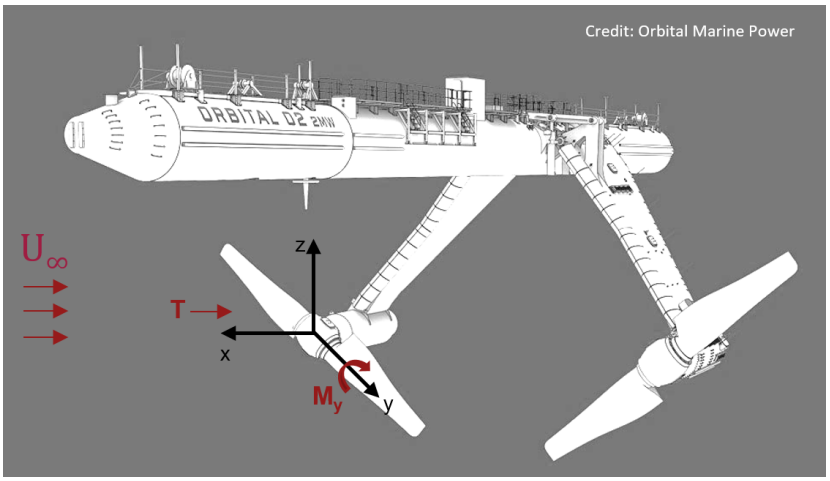

Figure 2.3: The direction of thrust, T and flap-wise root bending moment, M_y with respect to the Orbital O2 floating tidal turbine.

The turbine thrust and power coefficients are functions of tip-speed ratio and depend on the turbine operating strategy. The tip speed ratio, λ is the rotor tip speed relative to the undisturbed upstream flow velocity, U_∞

$$\lambda = \frac{\Omega r_r}{U_\infty} \tag{2.18}$$

where Ω and r_r are the rotational speed and radius of the rotor respectively.

At high flow velocities, the developed power and mechanical loading are often controlled to avoid overloading the turbine. This is commonly accomplished by active pitch control in wind turbines. Alternatively, stall control or an overspeed control method can accomplish the same goal in the absence of an active pitch mechanism. Overspeed control strategy is where the turbine is allowed to accelerate to high λ to reduce power and axial loading. Stall control is

where the rotor is slowed to a lower λ, requiring an increase in generator torque to slow the rotor hence reducing electrical efficiency (Harrold and Ouro, 2019). Most large modern wind and tidal turbines use variable rotational speed and variable blade pitch systems, which tend to be hydrodynamically more efficient but add to the mechanical complexity.

Fatigue Load

To determine damage equivalent loads, the load time series are rainflow counted. Rainflow counting is used to simplify a complex stress spectrum into a number of simpler constant amplitude cycles. Miners rule allows to account for the cumulative damage caused by each of these constant amplitude stress ranges. The rainflow counting method assumes that the bending moment cycles can be considered independently of each other and that the order they are applied does not matter, for further details the reader is referred to IEC (2020).

The damage equivalent load is given by the following formula:

$$DEL = \sqrt[m]{\frac{\Sigma {L_d}_i{}^m n_i}{fT}} \tag{2.19}$$

where L_{di} is the load range of bin i, T is the length of the simulations, f is the repetition frequency, n_i is the number of rain flow cycles at stress range bin i and m is a material property given by the slope of the S-N curve for the material (Mullings and Stallard, 2019). An S-N curve is a plot of the number of cycles to failure at a given cyclic load range, based on measured data from cyclic loading tests.

The curve takes the form of a straight line with slope equal to $1/m$, where m is the negative inverse slope of the S-N curve. The same slope m can be applied to load cycles (forces or moments) to compare the fatigue loading from a set of load histories. For composite materials (with m in the order of 10), high load-range events dominate the fatigue damage despite the fact that they are rare events (Milne et al., 2010).

Load Spectrum

It is important to consider the transfer of rotor load from low frequencies to those associated with the rotational speed and its harmonics as these can be a significant source of fatigue loading (McCann et al., 2008). Studies by (McNae, 2013), (Milne et al., 2010) and (Milne et al., 2016) used simulations to demonstrate that both the induced velocity and the dynamic inflow effect are significantly influenced by the ratio between the velocity perturbation and rotational frequency.

The dominant frequencies of interest for quantifying the blade loads are expected to range from those corresponding to the integral (most energetic) turbulent scales, up to those which are equivalent to the rotor frequency. The blade frequency is given by:

$$f_{blade} = n\frac{RPM}{60} \tag{2.20}$$

where n is the number of blades. Unsteady tidal turbine loads consist of both periodic (deterministic) and stochastic components. The periodic fluctuations can occur due to the blade passing the support structure, slicing through the shear layer or passing near flow boundaries or neighboring turbines. The stochastic components result from the random nature of turbulence. These include the full spectra of eddies due to blade-generated turbulence (high-frequency), approach-flow turbulence (low to mid frequencies) and waves (low frequencies) (Ahmed et al., 2015; Adcock et al., 2021).

2.4 Models

This section describes the types of models available to simulate turbulence loading on tidal energy devices. Their advantages and limitations are compared and the rationale for model selection is provided. This is followed by a more detailed description of the theory and working principles of TurbSim and Tidal Bladed - the models used in this work.

2.4.1 Model Types and Model Selection

The modelling approaches for analysing the hydrodynamic effects of turbulent flows on a tidal turbine broadly fall into three categories. Blade Element Momentum Theory Models (BEM), Computational Fluid Dynamics (CFD) models, or a hybrid of the two CFD-BEM, as summarised in Figure 2.4. BEM is a one-way method, where a turbulent flow field is generated separately, then used in a later calculation of device performance. Two-way methods model the turbulent field and device performance simultaneously. The turbulent inflow for BEM is generated by computed methods such as Spectral or Synthetic Eddy (SEM) methods. These are simplified models which generate a turbulent field from a limited number of turbulence parameters. CFD models simulate fluid flow by solving the Navier-Stokes equations, in a domain representing the environment, for example by including bathymetric features (Clark et al., 2015b).

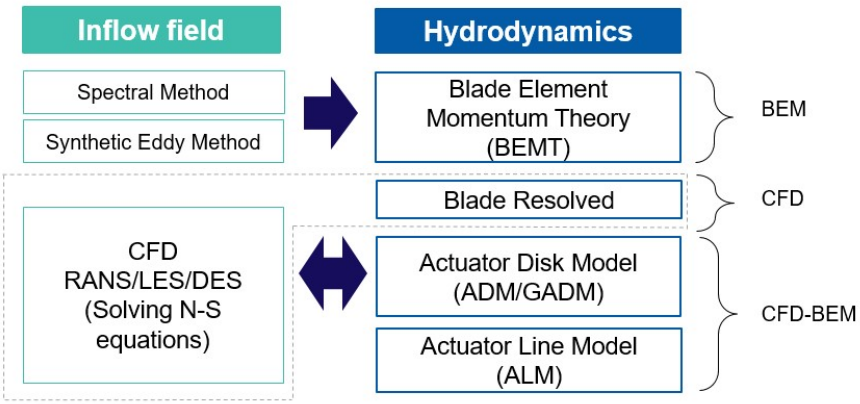

Figure 2.4: High-level summary of modeling approaches for flow generation and hydrodynamic analysis. The model types are explained further in the text.

BEM

BEM models use well-established theory for analysis of conventional horizontal-axis rotors in wind and tidal applications. The blade element approach analyses the forces generated by the airfoil lift and drag at various sections along the blade, and momentum theory evaluates the rate of change of the axial and angular momentum of the fluid that passes through the swept area. BEM models break the blade down into 2-D sections (elements), iterating for the flow induction factors for each blade element and then integrating over the entire blade to determine forces and moments (Murray et al., 2018).

Due to the simplifications made in BEM theory, correction factors have been developed to improve its accuracy. These correction models include tip and root losses, high induction factor, dynamic inflow and dynamic stall. These are discussed in more detail in Section 2.4.3.

Some examples of BEM model are OpenFast and Tidal Bladed. OpenFAST is an open-source code developed by the National Renewable Energy Laboratory. It is an unsteady aero-structural code forced by the TurbSim model (a turbulent simulator initialized with measured inputs). Tidal Bladed is a commercial software and works on the same principles as OpenFast but rather than using TurbSim, it has an internal module which can generate a flow field. TurbSim can also be used to generate flows which are compatible with Tidal Bladed. The flow field consists of 2-D grids at specific intervals along the streamwise axis, essentially forming a 3-D vector field. These grids are advanced along the streamwise axis through the turbine, hence providing the velocity input along each blade section. This kind of approach invokes the 'Frozen Turbulence' hypothesis i.e. within each time interval the structure of turbulence advects past the turbine without changing in time. The execution time for BEM analysis is low since the computations are based on simplified theories.

Blade-Resolved CFD

Blade-Resolved CFD is the most detailed numerical model available to simulate the operation of tidal turbines in realistic conditions. Large Eddy Simulation (LES) involves high-resolution meshing of a large domain, encompassing bathymetric features. Thus, compared to more straightforward techniques like BEM, CFD is much better able to incorporate turbulent content originating from complex bathymetry. The approach for LES is to split the turbulent content by scale where mid-large eddies are directly simulated, whilst smaller eddies are modelled (Clark et al., 2015b).

To take into account the blade geometry, a mesh is used to discretise the associated 3D CAD model of the turbine and implemented in the numerical model. This enables the turbine rotation to be resolved accurately providing a good capture of the hydrodynamics. By accounting for the blade geometry, the Blade-Resolved CFD model allows comprehensive estimations of the pressure loads on the blades and wake development behind the turbine. The small time step required to run such simulations as well as the model complexity significantly increase the required computation time (Old et al., 2018b).

Reynolds Averaged Navier Stokes (RANS) models are more efficient than LES, however do not properly represent the turbulent structures. In an attempt to retain some benefits of the LES approach whilst accessing the computational efficiency of RANS models, a hybrid approach called Detached Eddy Simulation (DES) uses an LES formulation on sub-grids within a wider RANS computation. The objective is to capture details of turbulent behaviour in important regions, whilst using the more efficient computation approach elsewhere (Clark et al., 2015b).

The CFD models for turbines can be separated into those that represent the actual geometry of the turbine rotor and those that replace the real geometry by the set of reaction forces that it produces, known as "actuator models". This is analogous to how laboratory studies may utilize physically exact models or porous disks of comparable cross-section and resistance. While this simplification does improve CFD computation time, such models are unable to fully describe near-wake flow structure or resolve the fluctuations associated with blade-generated turbulence (Ahmed et al., 2017).

Model comparison

In a comparison of the three simulation approaches, Ortega et al. (2020) found that all methods over-predicted loads compared to experiments of scale models of the Edinburgh university turbine and under-predicted for the Sabella D12 turbine. The simulated spectral response was not well represented by any of the models (Ortega et al., 2020).

Tidal Bladed has been validated against the field performance of a full-scale turbine in Parkinson and Collier (2016). The simulation results showed that the numerical model was slightly conservative, with the flood simulation results comparing better than the ebb. The highest error between the simulated and measured damage equivalent load was 30% for the ebb flow dropping to less than 10% for above-rated speeds and 20% for flood again dropping to under 10% for above-rated speeds. Evidence of rotational sampling of turbulent eddies was visible in the observed stochastic spectrum with large amplitudes at multiples of the blade passing frequency. Some spectral peaks weren't represented by the simulated loads, the authors suggest that this is due to turbulence being incorrectly defined.

While CFD is considered the most accurate approach for modelling turbulence, Ortega et al. (2020) found that Blade-Resolved CFD models can face difficulties with the scale models of turbines due to the transition between laminar and turbulent flow. This is a known issue from research on propellers where lowering the Reynolds number for scaling results in different viscous behavior (Ortega et al., 2020). In the same study it was found that the Blade-Resolved CFD blade frequency response appeared very low due to the lack of large scale turbulent structures in these simulations.The majority of numerical solvers for the Navier-Stokes equations of fluid motion will contain a model for sub-grid size turbulence closure, but large-scale turbulent structures won't develop in the absence of boundary friction or flow separation points inside the domain.

CFD models provide greater fidelity however require significantly more computational effort. To compute an output of 30 seconds for the same model turbine considering flow and wave conditions, Ortega et al. (2020) reported simulation time for the BEM model of 25 minutes, whereas CFD took 4 days (on a 224-core Linux Cluster). This clearly shows that CFD is not a practical tool for carrying out studies which require many simulations, such as parameter sensitivity studies. While BEM models are not entirely representative of the flow physics that occurs during the flow of water around the rotating blades of a turbine, they have been successfully applied to predict the performance of TECs (El-Shahat et al., 2020; Parkinson and Collier, 2016; Perez et al., 2020). BEM modelling is also the dominant approach used in industry.

2.4.2 TurbSim Theory

TurbSim and Tidal Bladed use the spectral method to generate the flow field. This method was first described by Veers (1988), in which separate velocity time series are computed at each point across the rotor plane grid by inverse Fourier transform of a chosen turbulence spectral model and its associated coherence model. Each single point has predefined spectral characteristics and each pair of points has predefined coherence characteristics. The turbulent flow field is then scaled according to the specified shear profile and the turbulence intensity level (Milne et al., 2010).

TurbSim allows two routes for generating turbulence, IEC and non IEC. The IEC method is based on models defined in the IEC 61400-1 and DNV-0164 Standards (IEC, 2019a; DNV, 2015), and includes options such as Kaimal or von Kármán spectrum models (Equations 2.21 - 2.22) and their associated coherence functions. The non-IEC route allows user input velocity, standard deviation, and length-scale profiles as well as user specification of the spectral model. Tidal Bladed provides an additional option to use the Mann spectral model. This is based on a model of the spectral tensor for atmospheric surface-layer turbulence at high flow speeds and allows for simulation of two- and three-dimensional fields of one, two or three components of the wind velocity fluctuations (DNV, 2015). The Mann method is considered

more advanced, using a spectral tensor to provide a more efficient algorithm, together with a more natural representation of the second-order structure of the flow. Despite offering a more natural representation than the Veers (1988) method, the Mann method presents challenges with specifying an artificial field that is consistent with a measured environment (due to the large number of parameters involved) (Clark et al., 2015b).

To simulate the level of variability found in natural flows, TurbSim randomizes the occurrence and scaling of coherent event structures. Such simulations have up to 10 degrees of stochastic freedom and hence using 30 or more different random seeds for a specific set of boundary conditions is recommended (Kelley and Jonkman, 2009).

The set of measured or assumed input parameters required to define a turbulent flow field is illustrated in Figure 2.5.

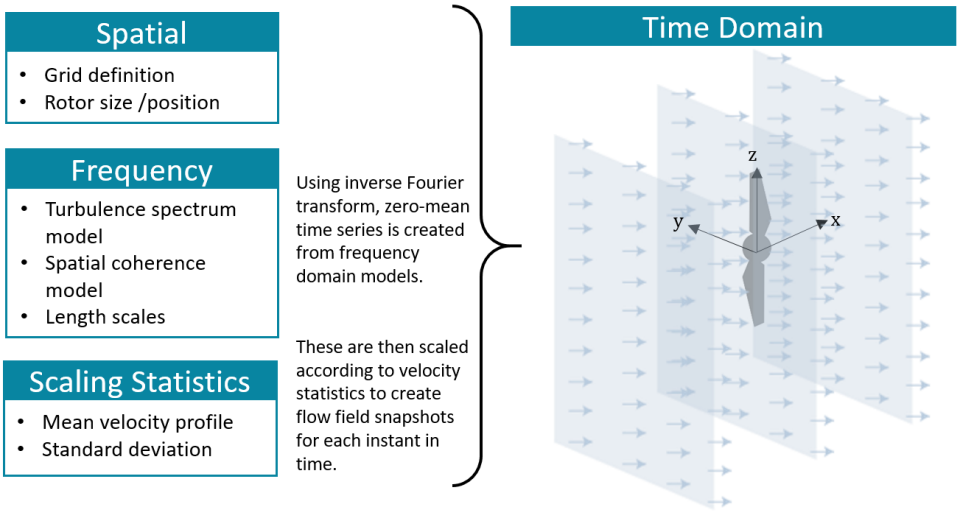

Figure 2.5: Simplified illustration of the input parameters required to construct the flow fields in Tidal Bladed and TurbSim, adapted from TurbSim user's guide (Kelley and Jonkman, 2009).

Frequency Parameters

The turbulence spectrum expresses how the turbulence energy is distributed across a range of frequencies. Typically, this would be represented by a model spectrum, which is a function of the current magnitude U, variance σ_u^2 and length scales, L. The Kaimal and von Kármán spectra are the most commonly used models in commercial codes and guides. These semi-empirical forms use coefficients applicable to atmospheric boundary-layer flows. Length scales can be specified by the user or theoretical values may be applied. The models are defined in the variance-preserving format as follows:

$$\text{Kaimal: } \frac{fS_u(f)}{\sigma_u^2} = \frac{4fL_{u_K}/\overline{U}}{(1+6fL_{u_K}/\overline{U})^{5/3}}, \tag{2.21}$$

$$\text{von Kármán: } \frac{fS_u(f)}{\sigma_u^2} = \frac{4fL_{u_{VK}}/\overline{U}}{(1+70.8(fL_{u_{VK}}/\overline{U})^2)^{5/6}}. \tag{2.22}$$

The Kaimal spectrum has the same form for v and w components as in Equation (2.21), but with different length scales. The von Kármán form for components $i = v, w$ is:

$$\frac{fS_i(f)}{\sigma_i^2} = \frac{4fL_{i_{VK}}/\overline{U}(1+755.2(fL_{i_{VK}}/\overline{U})^2)}{(1+283.2(fL_{i_{VK}}/\overline{U})^2)^{11/6}}. \tag{2.23}$$

The anisotropy ratio, α is given by Equation (2.14) and ranges from 0 for extremely anisotropic turbulence to 0.5 for isotropic turbulence (Lu and Lueck, 1999).

Isotropy is implied when using the von Kármán model (Burton, 2001); the Kaimal model assumes an anisotropy ratio, $\sigma_u : \sigma_v : \sigma_w = 1 : 0.8 : 0.5$.

Spatial coherence describes the correlation of the streamwise fluctuations across a separation distance, r, at each distinct frequency. The IEC 61400-1 wind standard provides an empirical model of streamwise coherence (IEC, 2019a), which can be used with the Kaimal or von Kármán model spectra. This IEC coherence model is used in TurbSim. The model is a function of the average current magnitude $\overline{U}$, length scales L_u, and separation distance Δr, and is defined as:

$$C_u(\Delta r, f) = exp\left(-8.8\Delta r\sqrt{\left(\frac{0.12}{L_u}\right)^2 + \left(\frac{f}{\overline{U}}\right)^2}\right). \tag{2.24}$$

Length-scale values are required as input into the spectral and coherence models. Tidal Bladed and TurbSim give the option to use the default values or user input length scales (Jonkman and Kilcher, 2012). The default values for the IEC models define the streamwise length scale, $L_u = 8.10\ \Lambda_U$, where $\Lambda_U = 0.7\times$ min (30 m, hub height), in line with the IEC 61400-1 wind standard (Kelley and Jonkman, 2009; IEC, 2019a). The default length scale values are based on atmospheric flows and tend to ignore the upper limit on eddy size imposed by the air-water interface (McMillan, 2017).

Scaling Parameters

The shear profile of the velocity normal to the seabed in a tidal race constitutes a high Reynolds number turbulent boundary layer. The DNV-ST-0.164: Tidal turbines standard (DNV, 2015) states that, when detailed field measurements are not available, the variation in sub-surface current velocity with depth may be modeled as a simple power law (see Equation 2.13), where the exponent β is typically taken as $1/7$. This is the default profile in TurbSim however there is functionality to change the exponent value or to implement a user-defined profile.

Tidal Bladed and TurbSim apply the standard deviation (or turbulence intensity, defined in Equation 2.3) for each velocity component to scale the velocity fluctuations. They typically allow input of only the hub height value, neglecting any variation across the rotor. TurbSim has the functionality to input a user-defined standard deviation profile.

2.4.3 Tidal Bladed Theory

Tidal Bladed is a commercial software, which implements BEM theory with modifications ad improvements. The blades are divided into different segments known as blade elements. The two key assumptions in this model are that there are no aerodynamic interactions between the blade elements and that the forces on the blade elements are solely determined by the lift and drag components. By integrating the forces acting on each component the total force on the blade is calculated. The dynamic force on each blade element can be computed based on the local flow conditions.

The fluid's rate of change in its axial and angular momentum as it moves through the swept area is assessed using the momentum theory. The rotor is represented by an actuator disc, which slows down the incoming flow velocity far upstream of the rotor. Thrust can be determined by the application of linear momentum conservation to the control volume. Momentum theory is extended for the case where the rotor generates angular momentum, which can be related to rotor torque (El-Shahat et al., 2020). Full explanation and BEM equations used in Tidal Bladed are provided in the Tidal Bladed Theory Manual (Khairuzzaman, 2016).

BEM is a 'one-way' method, so the turbulent inflow is usually generated using a separate model or module. The flow modification by the rotating turbine is modelled in terms of induction factors. The axial induction factor represents the change in the axial velocity magnitude as flow passes through the turbine (Old et al., 2018a).

The performance of the tidal turbine depends on its geometrical parameters such as the blade shape, and thickness. The type of blade section at each blade element, provided by the user, would determine its lift and drag coefficients and subsequently the force generated at the blade element.

Modifications

Tip vortex shedding occurs in fast-moving rotors such as turbine blades or propellers. Tidal Bladed accounts for the tip losses by means of Prandtl correction factor, which simplifies the wake of a turbine by modeling the helical vortex wake pattern as vortex sheets that are convected by the mean flow and have no direct effect on the wake itself (Khairuzzaman, 2016).

Conventional BEM models assume that the changes in the pitching moment and hence the rotor load, result in an instantaneous response in the wake and the induced velocities. However, changes in the rotor load have an effect on the vorticity that is followed into the rotor wake and, as a result, have a delayed effect on the induced flow field. The hydrodynamics associated with this phenomenon is referred to as dynamic wake or dynamic inflow. Pitt and Peters or Oye's dynamic wake models can be implemented in Tidal Bladed to account for this effect (Khairuzzaman, 2016).

Dynamic stall refers to the stalling of a hydrofoil during unsteady flow conditions. The variation of fluid velocity over the rotor disk creates unsteady angles of attack at the blade sections, resulting in a significant delay in the stall of the hydrofoil when compared to the static case, this can result in larger values of lift. These events can be accounted for by a dynamic stall model. The dynamic stall implemented in Tidal Bladed follows the Beddoes-Leishman model (Old et al., 2018a).

Structure Shadow

Tidal Bladed provides 3 different models to account for the distortion of the steady-state mean flow field by the structure shadow. A potential flow model for upstream rotors, an empirical tower wake model for downstream rotors, and a combined model for yawing rotors.

The potential model modifies the longitudinal flow velocity component upstream of the tower using the assumption of incompressible laminar flow around a cylinder of a given diameter.

The empirical model for downstream rotors is based on the work of Powles, which uses a cosine bell-shaped tower wake. The user inputs for this model include the maximum velocity deficit at the centre of the wake as a fraction of the local flow speed, the width of the tower shadow as a fraction of the local tower diameter, and the reference position.

The combined model uses Potential Flow Theory for a majority of the flow-field, but uses a combination of Powle's and Potential Flow in the region where Powle's is active (i.e. within the wake according to whichever downstream variation that the Powle's model is using) (Khairuzzaman, 2016).

Chapter 3

Literature Review

3.1 The Nature of Real Turbulence; Are Models and Assumptions Valid?

When specific site measurements are not available, semi-empirical models and assumptions are used to represent turbulence. Many of these are based on atmospheric flows and their applicability to tidal flows is still not well understood. This section summarises past investigations into the nature of turbulence in energetic tidal channels and how well it is represented by commonly used models and assumptions.

3.1.1 Turbulence Intensity

The most common parameter used in characterisation is turbulence intensity, I (see Equation 2.3). However, studies have found that it is not a simple function of the local flow conditions. Turbulence not only varies across different sites, but also at the same site where complex bathymetry and channel shape is likely to result in strong spatial variation (Thiébaut et al., 2020c). There is often a significant ebb/flood asymmetry in turbulence and boundary layer properties arising from differences in the bathymetry upstream. Table 3.1 shows that turbulence intensity can vary between 5-45% depending on the tidal site.

Typically, streamwise turbulence intensity I_u is the most significant and is normally expressed relative to the mean flow U. McCaffrey et al. (2015) argue that due to the large spread of I_u for each U, the local velocity values are not a good predictor of I_u . Hence, further investigation is needed into what causes the turbulence intensity to peak. Moreover, ADCP measurements of I can be biased high by noise or the presence of waves (discussed in Section 2.2.1), so analytical tools to correct this must be used to ensure accurate characterisation (Sellar et al., 2018).

Location	Peak flow	I_u	z/H	Ref.
Alderney Race	4.5m/s	17.5%	0.2	(Thiébaut et al., 2020b)
East River	2m/s	13-18%	0.5	(Milne et al., 2016)
Puget Sound	0.8-2.0m/s	8-11%	0.2	(Thiébaut et al., 2020c)
Sea Scheldt	0.8-1.4m/s	4-5%	0.9	(Thiébaut et al., 2020c)
Sound of Islay	2.0-2.5m/s	11-13%	0.1	(Thiébaut et al., 2020c)
Strangford Loch	2.5-3.5m/s	4-9%	0.5	(Thiébaut et al., 2020c)
Fall of Warness	3.7m/s	5-7%	0.5	(Sellar et al., 2015)
Minas Basin	5.0m/s	5-8%	0.5	(McMillan and Hay, 2017)
Fall of Lora	1.7m/s	45%	0.9	(Lake et al., 2021)
Bank Straits	2.0m/s	12-17%	0.2	(Perez et al., 2022b)

Table 3.1: Reported turbulence intensities (I_u) for various tidal sites. z/H is the relative position in the water column where turbulence was measured.

Flow Shear

Although not strictly a turbulence parameter, the shear profile is an important characteristic of flow, and is a key parameter in specifying turbulent flow fields (Kelley and Jonkman, 2009). The shape of the shear profile is dominated by turbulence in the flow and channel expansion and contraction (Clark et al., 2015b). Shear profiles require measurements of mean velocity magnitude throughout the water column which are more straightforward to obtain from ADCPs than other parameters.

Section 2.4 highlights that when measurements are not available, a 1/7th power law profile (Equation 2.13) is assumed in models. Due to the seabed roughness, bathymetric effects and the free surface, the real shear profiles can deviate from such analytical cases. A number of studies (Parkinson and Collier, 2016; Gunn and Stock-Williams, 2013; Greenwood et al., 2019; McNaughton et al., 2013), found the shear profiles at EMEC's Fall of Warness tidal site had large velocity variations with complex profiles that do not follow the analytical models. Furthermore, the flood and ebb tides had two distinct profile shapes, one logarithmic and one roughly polynomial. The shear profiles were also found to vary by velocity and acceleration/deceleration (Sellar et al., 2018). Togneri and Masters (2016) found the velocity profile at Ramsey Sound (Wales, UK) during ebb tides followed a power law distribution over the entire water column, while during flood tides the logarithmic distribution of velocities was observed over the bottom half of the water column only, with the remainder being almost uniform up the to the free-surface.

3.1.2 Turbulence Structure

Although turbulence intensity is commonly used by engineers to quantify the level of ambient turbulence, it does not alone capture the changes in the turbulent regime during the tidal flow (Sentchev et al., 2020), nor does it give any information about turbulence structure (McCaffrey et al., 2015). To understand turbulence structure, calculations of the integral length-scales, isotropy, turbulence spectrum and coherence are required.

The integral length-scale, L is defined qualitatively as the average size of the largest eddies in a turbulent flow (Pope, 2000), it is calculated from the instantaneous velocity data using Equation 2.12. A large variation in measured length-scales across different sites, but also between calculation methods, has been reported (Thiébaut et al., 2020a). Thiébaut et al. (2020c) and Thiébaut et al. (2020a) found that the dynamics of the large scale turbulent eddies at Alderney Race are anisotropic with predominantly horizontal motions, at scales 2-3 times the local water depth. The largest integral scales observed in Elkhorn Slough estuary by Walter et al. (2011) were several orders of magnitude greater than the channel depth. In a study from the Sound of Islay, Milne et al. (2013) reported integral length scales of approximately 1/3 of the channel depth. Kilcher et al. (2014) also reported length-scales approximately a third of the channel depth at Admiralty Inlet, while Greenwood et al. (2019) measured length-scales similar to the channel depth at the Fall of Warness. Thomson et al. (2012) reported that the broad distribution of length scales contrasts to most wind energy studies, which typically show a maxima of turbulent energy at mesoscales and a decrease at very large scales. The authors suggest that the absence of a preferential turbulence scale at tidal sites is consistent with wind studies in regions with strong topography, which are more comparable to tidal channels, where the dominant length scales relate to the lengths and widths of the headlands. Studies also found that the length-scales are dependent on the tidal cycle and flow speed (Thiébaut et al., 2020c), as well as flow acceleration (Sellar and Sutherland, 2016).

Chapter 2.4 described the principles of stochastic models which require length-scale values as input into the spectral and coherence models. The available design standards and commercial models (see Section 1.2) provide theoretical length scale values based on depth, which are sometimes used in the absence of measurements. However, these are based on atmospheric flows and tend to ignore the upper limit on eddy size imposed by the air-water interface (McMillan, 2017). Although studies looking at length-scale model applicability are scarce, Milne et al. (2016) found scales at Puget Sound were within 7% of the open channel flow model $L_u = \sqrt{zh}$ proposed by Nezu and Nakagawa (1993), in-spite of its inherent assumptions associated with an idealised steady flow and a relatively smooth bed. However, Milne et al. (2016) also emphasized that given the large degree of length-scale variability in tidal channels, such a model may not always be applicable.

While the integral length-scale describes the most energetic scales, the turbulence spectrum shows the distribution of turbulent kinetic energy across all the length-scales. In other words, the integral length-scale represents the frequency at which the turbulence spectrum peaks. Turbulence consists of vortex motions with a broad range of scales - from the order of the channel geometry down to molecular scale - so obtaining accurate measurements across the full range of scales is non-trivial. Using ADCP measurements, Richmond and Durgesh (2011); Guerra and Thomson (2017); McMillan (2017); Perez et al. (2020) have observed the TKE energy cascade and the $-5/3$ slope in the spectral estimates. Guerra and Thomson (2017) compared the spectra from vertical beam of an ADCP and an ADV at two different sites and found the ADCP measurement in good agreement with the spectra from ADV measurements.

Typically, the observed spectrum shows that at low frequencies $f < 0.1$ Hz, the horizontal motions are far more energetic than vertical motions, consistent with large-scale anisotropic 2-D eddies (Thomson et al., 2012). The vertical motions are likely to be suppressed at these frequencies by the available water depth. Moreover, evidence for a linear region starting at $f \approx 0.1$ Hz has been found in a number of studies from tidal energy sites across the world (Thiébaut et al., 2020c; Thomson et al., 2012; Guerra and Thomson, 2017). These observations suggest that the approximate frequency at which the inertial sub-range starts could be a universal property for fast-flowing shallow tidal streams.

Kaimal and von Kármán models were introduced in Section 2.4, these are typically used to represent the turbulence spectra when simulating device performance in unsteady flows. Comparisons of the Kaimal and von Kármán spectrum models to measurements generally show an agreement with the shape of the curve, however, the peak of the spectrum is often not aligned (McMillan, 2017; Milne et al., 2017; Walter et al., 2011). Moreover, there is no agreement on which of the two models is more appropriate for tidal flows. Comparing these models to ADCP data from the Grand Passage in Nova Scotia, McMillan (2017) found that the streamwise variance at large scales is better predicted by the Kaimal model, provided that the degree of anisotropy is permitted to vary throughout the water column. Conversely, a study from the Sound of Islay (Milne et al., 2017), found that the Kaimal model over-predicted the energy content at the lowest frequencies of the streamwise spectrum while the von Kármán provided a better fit. Comparison of ADV measurements from a shallow tidal flow ($<$10m depth) to non dimensionalised Kaimal spectrum, showed agreement with the general shape of the spectrum although the variance in the measured curves was shifted toward higher frequencies (Walter et al., 2011). Previous studies mostly focused on measurements near the seabed (Milne et al., 2017; Walter et al., 2011) so little is known about the applicability of models higher up in the water column, which is critical for floating devices. Both Walter et al. (2011) and McMillan (2017) concluded that the models are only applicable when the

measurement height is much less than the depth of the flow because the anisotropy and length scales will vary with height above bottom. The extent of the discrepancies higher up in the water column or the variation across different sites is not well understood, neither is it known to what degree the discrepancy would make a difference (if any) to device simulations.

The von Kármán spectral model requires the assumption of isotropic turbulence, while the Kaimal model applies theoretical anisotropy ratios. Comparisons by Milne et al. (2017) of observed tidal and atmospheric anisotropic ratios showed that the anisotropy is more pronounced in a tidal channel than in the atmospheric boundary layer. This is consistent with the notion that energy in a tidal channel is restricted by the presence of a free surface, particularly in the vertical direction. In an LES simulation, Ouro and Stoesser (2019) found the anisotropy ratio $\sigma_u : \sigma_v : \sigma_w$ to be 1:0.64:0.88 which was quite different to the 1:0.75:0.56 found at the Sound of Islay (Scotland) tidal site or to two-dimensional channel flows in which the ratio is 1:0.71:0.55 (Nezu and Nakagawa, 1993). Tidal flows are anisotropic so assumptions of isotropy can yield high inaccuracies, e.g. Vermeulen et al. (2011) found that the difference between fully anisotropic and fully isotropic turbulence results in a six-fold difference in the value of TKE for an ADCP with a beam separation of 20 degrees.

Coherence describes the correlation of turbulent fluctuations across a spatial separation, see Section 2.2.2. Without taking into account spatial coherency, at least over the turbine disc area, the interactions between fluid flow and TECs cannot be effectively resolved by simulation, even if the length-scales and their energy distribution are known (Clark et al., 2015a). Coherence measured in tidal channels has been shown to be highly dependent on scale, with high coherence for mid-large scale eddies, and low coherence for the smaller scales, however it also depends on the measurement separation distance, r (Kilcher et al., 2014). Thomson et al. (2014) found that coherent motion is found to be largely isotropic, such that coherence is high only at scales less than the advective length scale or the water depth, whichever is less. Stochastic models (see Section 2.4) define a coherence model alongside the spectrum model. As with the spectral models, the coherence model contains semi-empirical coefficients which have been obtained from atmospheric studies, and the applicability of such models to tidal flows is not well understood.

3.1.3 Intermittency

Spectral and coherence characteristics are typically determined using Fourier analysis e.g. Thomson et al. (2014). This is a widely used method for identifying periodic components in oceanographic time series however requires the assumptions of stationarity (Emery and Thomson, 2001). Turbulent signals may contain transient, energetic bursts, which result in

non-stationarity and can be seen in the wide tails of the signal's probability density function (PDF). Second-order statistics such as the energy spectrum are relatively insensitive to these rare events because their duration is small compared to the sampling period and consequently they do not dominate the integral (Farge and Schneider, 2004).

McCaffrey et al. (2015) found that there were small coherent features ($L = 10$ m) in comparison to the local depth (approximately 30 m) at Puget Sound, with occasional extreme events $L = 80$ m, which contribute to the turbulent energy spectrum. McCaffrey et al. (2015) concluded that these turbulent features are not well-represented in coarse-resolution statistical models. Such organised inflow structures and the accompanying rotor responses typically have timescales of only a few seconds and therefore do not lend themselves to analysis by conventional Fourier spectral techniques.

Wavelets (see Section 2.2.2 for theory) are a powerful tool for studying time–frequency behaviour of finite energy signals. The advantages of the wavelet decomposition over Fourier transforms present themselves when transforming a signal that has time-varying characteristics. The wavelet representation shows the dynamics in both space and scale, retaining only those degrees of freedom which are essential to compute the flow evolution (Farge and Schneider, 2004). Wavelet analysis can also enable the spectral decomposition of short-period events such as the interaction of coherent turbulence with a moving rotor blade (Kelley et al., 2000).

Wavelet analysis has been widely used across different disciplines, including for processing ADCP data in oceanography. Mihanović et al. (2009) applied a multiple cross-wavelet spectral analysis to study the relationship between the wind and tidal forcing mechanisms on the temperature variability in Lastovo, Croatia. Phanikumar et al. (2007) used multi-resolution wavelet analysis of the 2-D mean velocity fields obtained from ADCP surveys to separate the flow into regions of slow and fast-moving zones and to estimate the relative sizes of the main channel and the storage zones. Petrusevich et al. (2020) analysed ADCP-measured current velocities and used wavelet transformation to derive the time-dependent behaviour of horizontal and vertical current velocities at the semi-diurnal tidal frequency band that dominates the backscatter spectrum. Wavelets have also been used in tidal applications for de-tiding (Chiao and Wang, 2004) and harmonic analysis to differentiate tidal species (Garel and Cai, 2018). In previous studies the investigation focused on variability with the scales of interest in the order of hours, days and above. ADCPs in these cases have predominantly been used to obtain mean current velocities, showing long-term variations. Turbulence characterisation is concerned with scales on a shorter time scale, in the region of seconds to minutes.

Since Farge and Schneider (2004) introduced wavelets into turbulence, they have become more frequent in turbulent signal analysis. There are examples of wavelet methods being applied to study the turbulent boundary layer (Chen et al., 2019; Nan, 2016; Hu and Du, 2020) in experimental tanks and flume settings, and turbulence-rotor interactions for wind turbines (Kelley et al., 2000, 2005). Some studies have applied wavelet analysis to field

measurements for turbulence study however only for single point measurements (Camussi et al., 2008). ADCPs profile the water column and therefore offer more potential to understand the spatial structure of turbulence, however to the author's best knowledge wavelet analysis is not generally used as a tool to characterise turbulence for tidal energy applications. Moreover, while the theoretical limitations of stationary techniques such as Fourier analysis for non-stationary phenomena such as turbulence are understood, the implications of doing so in performing turbulence characterisation have not been quantified.

3.2 How Does Turbulence Affect Tidal Energy Devices?

The tidal sites suitable for energy extraction are by their nature energetic and turbulent. Such unsteady flows create variations in power and device loading (Clark et al., 2015b; Milne et al., 2016; Scarlett and Viola, 2020), affecting the device's performance. This section presents the key findings of investigations into tidal energy device-turbulence interaction both from real deployments and from simulations.

3.2.1 Lessons from Full-Scale Deployments

Despite numerous experimental and numerical studies on the mechanical loading of tidal turbines, very little is known about full-scale devices operating in real sea conditions. Where full-scale devices have been deployed, there is added complexity in parameterising marine environments, sensor synchronisation, obtaining sufficiently long data records and commercial confidentiality restrictions. A review of the available literature on TEC deployments is presented in this section, giving special attention to any findings relating to turbulence-induced loads in real-sea environments.

Harrold and Ouro (2019) reported the rotor loads measured on a 400 kW tidal turbine, deployed at Ramsey Sound in 2015. They found that instantaneous variations of the loadings at low and high frequencies were observed signifying that the approach flow was characterised by a wide spectrum of scales. Spectral analysis of the loadings confirmed the relevance of the largest flow scales, in addition to those induced from the structure shadow effects (Harrold and Ouro, 2019).

Performance of the Alstom Ocean Energy's 1MW tidal turbine, deployed at EMEC has been analysed in some detail, predominantly for model validation. For example, Ahmed et al. (2015) compared the results of a geometry-resolved CFD simulation to field data and Parkinson and Collier (2016) used field data to validate simulations using Tidal Bladed. Parkinson and Collier (2016) found that the biggest contributor to fatigue loads is the stochastic load due to turbulence although the magnitude of the blade flapwise bending 1P spectrum spikes were higher in magnitude. The authors also reported that the numerical model results were conservative compared to measurements.

MacEnri et al. (2013) performed a comprehensive analysis of the SeaGen TEC performance deployed at Strangford Lough, Northern Ireland. They demonstrated that velocity fluctuations (measured by the standard deviation), are likely to be one of the significant factors that contributes to voltage flicker. In an experiment involving a vertical axis turbine by Water2EnergyB.V. deployed at Sea Scheldt, in a tidal stream estuary, Sentchev et al. (2020) also found a large increase in magnitude of power fluctuations caused by turbulent fluctuations.

Jeffcoate et al. (2015) analysed the performance of the full-scale SCHOTTEL tidal turbine, tested at Queen's University Belfast's tidal site at Strangford Lough, however this didn't include turbulence analysis. Lake et al. (2021) investigated the blade strain of the PLAT-I (Figure 1.1) floating tidal energy converter. There were a number of challenges reported such as limited testing period, clock synchronisation issues between instruments and potential frequency limitations of strain gauges.

Most of the published studies on full-scale deployments do not provide any firm analysis of turbulence-device interactions and so the full-scale device loads induced by real-sea turbulence are still not well understood.

3.2.2 Turbulence-Device Interaction

Numerical modelling and tank test investigations have provided some insight into the TEC load response to unsteady flow conditions.

In a simulation study, Scarlett and Viola (2020) found that turbulence and waves can lead to load peaks that are twice the median load. Using planar oscillatory forcing experiments in a still water towing tank, Milne et al. (2015, 2016) have studied the relative contribution of hydrodynamic unsteadiness on the blade-root bending moments. They showed that the blade bending moments can increase by 15% in a uniform unsteady flow when compared to the steady state condition, demonstrating the significance of dynamic flows on turbine performance.

A CFD study by Ouro and Stoesser (2019) showed that the instantaneous flow contained energetic mid-large scale turbulence structures that are generated by the bathymetry, mainly in the form of roller and hairpin vortices and that these have a profound impact on the tidal turbine. The authors reported that these induce sudden drops in the turbine's instantaneous performance as well as large fluctuations in the hydrodynamic loading on the blades.

As explained in Section 2.3, unsteady flow conditions can lead to a number of issues for the TEC design, for example rotor blades can experience stall delay, load hysteresis and dynamic stall. However, the understanding of the range of flow conditions that cause these effects for full-scale devices still remains unclear (Scarlett and Viola, 2020).

3.2.3 Which Characteristics of Turbulence are the Most Important?

To determine which turbulence parameters are the most critical, turbine response must be linked with measurable properties of turbulence. Although there is a general agreement that streamwise turbulence intensity increases unsteady loading, there has been less consistency in findings on the contribution of turbulent length-scales and other parameters to turbine loads.

Turbulence Intensity

Experimental investigations by Mycek et al. (2014) and Blackmore et al. (2016) demonstrated a sensitivity of the load fluctuations and mean loads respectively to the turbulence intensity in the flow. Using real site data as input to BEM models, Perez et al. (2022a) and (Mullings and Stallard, 2021) also have found strong correlations of I to load fluctuations. Turbulence intensity is a measure of the overall fluctuations in the flow so it is unsurprising that it affects load fluctuations, what does remain unclear is the relative effect of the other key parameters.

Shear Profiles

It is expected that shear profiles will have implications for turbine loading because the non-uniform inflow velocity gradient across a turbine's rotor will cause eccentric bending moments (Nevalainen et al., 2016). CFD studies by McNaughton et al. (2013) and Nevalainen et al. (2016) observed large fluctuations in the loading coefficients for varying velocity profiles. Clark et al. (2015b) also reported a large difference in fatigue loads between the various shear profiles and Perez et al. (2022a) found increased load standard deviations when the rotor was located closer to the seabed (associated with the pronounced shear). However, none of these studies give the context for how big the shear load impact is compared to other turbulence parameters. Results from a sensitivity study of TurbSim parameters (for wind applications) suggest that the sensitivity to wind shear can be equal to or even higher than the turbulence standard deviation (Robertson et al., 2018).

Length-scales

An important question is what range of scales in the approach turbulent flow are able to dynamically interact with the device and interfere with its ability to produce power. Using tank experiments, Blackmore et al. (2015) found a larger increase in load fluctuations from increasing integral length scales than from increasing turbulence intensity (for $L = 0.95\times$rotor diameter). Conversely, Milne et al. (2010) and Perez et al. (2022a) both conducted BEM studies using different models and found load standard deviations were substantially more sensitive to turbulence intensities than integral length-scales. In analysing power fluctuations of a turbine in real-sea conditions, Sentchev et al. (2020) found a correlation with length-scales, the strongest impact of turbulence on power generation was detected when the integral length-scale attains and exceeds the turbine size. There is also evidence from wind energy literature that the most damaging wind gusts are those manifesting at a scale at which they engulf the entire structure or have length-scales of similar scale to the structure (Hu et al., 2018).

Turbulence Spectrum

Studies have shown that the design of hydro-kinetic turbines needs to take into account the spectral content of the approach flow. Results from a simulation study by Chamorro et al. (2013) showed that for sufficiently low frequencies the instantaneous power generated by the turbine is modulated by the turbulent structure of the approach flow. Two distinctive regions were observed in the frequency domain: a low-frequency region within which the turbine power appears to be conditioned by and strongly coupled with the energy cascade in the flow; and a high-frequency region where the turbine power fluctuations appear to be non-responsive to the dynamics of turbulence in the flow.

Findings from simulations by McNae (2013), Milne et al. (2010) and Milne et al. (2016) suggest that the ratio between the velocity perturbation and the rotational frequency has a critical role on both the induced velocity and therefore the dynamic inflow effect. These studies show that the 1-P (1 times the blade passing frequency) velocity fluctuations are a significant source of loading. Conversely, a study of a grid-connected full-scale tidal turbine in Ramsey Sound, observed an energy peak in the blade load spectrum at the turbine rotational frequency however this energy peak had a similar magnitude to peaks found at lower frequencies. This goes against previous data from laboratory tests showing that the maximum energy may be attained at the turbine rotational frequency (Harrold and Ouro, 2019).

It is uncertain to what extent different spectrum models can affect the simulated load outcomes. For example, in analysing the loads in a simulation using a BEM model, Milne et al. (2010) found no pronounced difference in the loads between simulations using the von Kármán and Kaimal turbulence models.

Standard Deviation Profile

Stochastic models such as TurbSim or Tidal Bladed reconstruct the velocity time series field based on spectral and statistical flow characteristics and make a number of simplifications. One such simplification is to assume a constant standard deviation throughout the water column. In real flows, the standard deviation will follow a profile (Sellar et al., 2018). While it is known that standard deviation (or turbulence intensity) will impact load fluctuations, the effects of different profiles are not known.

Coherence

Wind turbine installations have shown that significant stress events on the rotor blades are frequently accompanied by brief bursts of coherent turbulent energy in the turbine intake. The greatest structural fatigue damage in field experiments tends to occur during the night-time hours due to coherent motions associated with Kelvin–Helmholtz instability (KHI). The KHI billows develop when temperature and wind speed vertical gradients induce atmospheric wave motions. As wind turbine rotor blades pass through coherent turbulence zones, intermittent loading events occur, impacting different subsystem components (Kelley et al., 2005). Coherent turbulent structures can contain large velocity shears over small distances as well as significant local vorticity. Analogous to the KHI, large local features in bathymetry or the shape of the channel can add coherent structural content to an already turbulent inflow (Clark et al., 2015a).

Stochastic flow models incorporate coherency by explicitly defining the coherence function. In a sensitivity study of TurbSim parameters (for wind applications) Robertson et al. (2018) found that coherency and veer both impacted load estimates, although secondary to parameters such as shear or turbulence intensity. To the author's knowledge, no studies have been carried out to assess the suitability of coherence models for tidal channel turbulence or the effect of varying coherency on load outcomes.

Isotropy

No explicit sensitivity studies of anisotropy were found in the literature, this is likely to be because most models do not generate anisotropic turbulence. However, it is understood that the mid-large length-scale motions have a significant impact on loads and since anisotropy is more pronounced at larger scales it is also likely to correlate with loads.

3.3 Chapter Summary: Identification of Knowledge Gaps and Research Focus

Despite the considerable body of research, there remains a lot of uncertainty regarding both the characterisation of real environmental conditions and the turbulence-induced impacts on tidal turbines. The literature review outlines the state of the art of knowledge with regards to the research questions stated in Chapter 1.1. This Section summarises the important knowledge gaps, identified through the literature review process, which will be addressed in two parts.

Part 1: Are models and methods typically used in the industry valid for tidal flows?

Turbulence is known to influence fatigue loads and power production, so developers use turbulence models to generate unsteady flows in order to simulate device performance. To construct a synthetic flow field a combination of measured parameters and semi-empirical models are used. The majority in use today are based on atmospheric flow conditions and may have limited applicability in tidal environments. The degree of non-conformity to models and assumptions still remains unclear. The available research is inconclusive about whether atmospheric spectral models can adequately represent tidal turbulence and investigations into other turbulence parameters are lacking. Given the physical differences between marine and atmospheric boundary layers, there is no compelling reason to believe that atmospheric models will be adequate. The investigation into model suitability is the first aim of Part 1.

Much of the turbulence theory has been developed in the context of atmospheric flows and theories of turbulence have mostly focused on the theoretical case of statistically stationary, homogeneous and isotropic turbulence. While a number of tidal site turbulence characterisations have been carried out, they're often limited to high-level turbulence statistics. Where a more detailed analysis of the turbulence spectra and coherency are carried out, Fourier transform is used. This method can only yield parameters that are averaged over the signal length or the analysing window, requiring the assumptions of a stationary signal. Flows with coherent turbulent structures are often non-stationary and hence this method may not fully represent real flow turbulence, smearing out information on intermittency. Alternative spectral analysis methods such as Wavelet analysis could offer a more appropriate way to study coherency in tidal turbulence characterisation, however, have not been used in this application. The second aim of this Part of the thesis is to investigate the suitability and benefits of wavelets in analysing ADCP turbulence data.

Part 2: Turbulence - device load interactions

Simplified BEM models such as Tidal Bladed are used in industry to simulate loads and fatigue life, however, there is uncertainty among users of how well these models represent real turbulence or turbulence-induced loads. Tidal Bladed has been found to yield conservative values and some have reported this is due to misrepresentation of the approach flow turbulence. It is also uncertain from all the parameters used to characterise turbulence, which ones are the most important for accurate load modelling. It is understood that turbulence intensity and shear profile are highly correlated with loads, however, the effects of parameters describing the more complex nature of turbulence such as length-scales, spectrum, anisotropy and coherence are less understood.

Previous efforts to understand the sensitivity of parameters focused on replicating specific flow conditions (a combined set of parameters), rather than varying each parameter at a time. This means it is difficult to decouple the effects of the individual parameters. Moreover, experimental studies such as those using static grids in tanks can be limited by the range of conditions that can be generated. This Part of the thesis aims to investigate the sensitivities of turbulence characteristics to device loading in Tidal Bladed. Together with the first part, this will help to determine where the most precision is required when measuring and characterising turbulence for load studies.

To date, there are very few studies on measurements of mechanical loads on full-scale operational tidal turbines. Much of our understanding is based on simulations and scale tests but so far very few have been fully validated by full-scale case studies. Real-sea deployments provide an invaluable opportunity for learning about device performance, however, are also very challenging due to the complex dynamic environments that are being measured. The final part of this work investigates the rotor loads from the full-scale operational O2 device currently deployed at EMEC. The aim of this is to identify the key contributors to fatigue loading, in particular those related to turbulence.

PART I

Turbulence in Real-Sea Conditions: Are Models and Methods Typically Used in the Industry Valid for Tidal Flows?

Chapter 4

Part I Summary

This Part of the thesis presents the work carried out to test the applicability of semi-empirical turbulence models to measured turbulence in tidal channels. The turbulence parameters are computed from site measurements from 4 ADCPs at two key tidal sites and compared to the theoretical values which would be used in the absence of measurements.

The question of non-stationarity of turbulent flows is also addressed by novel application of wavelet analysis to ADCP turbulence data. Results from the wavelet analysis are compared to the traditional Fourier analysis (which requires assumptions of stationarity) and the implications of using stationary methods are discussed.

Highlights

- Turbulence measurements at the two tidal sites show different levels of conformity to theoretical models, with significant variability even within nearby locations.
- The agreement with spectral models is shown to be component and depth-dependent. The vertical component spectrum is better represented by the Kaimal model, while the streamwise spectrum is better represented by the von Kármán model.
- Length-scales based on atmospheric flows (which are used as default values in commercial software) are not representative of real tidal flows at the two sites considered. Neither are length-scales approximated by open channel flow theory.
- Results indicate that the coherence models which complement the spectral models are not representative of the flows at the sites studied.
- In the 3 of 4 measurement locations, the shear profiles adhere to a power law, although not a 1/7th power law as is commonly assumed.
- Instantaneous spectra and coherence by wavelet analysis show that at this site, high energy bursts occur at frequencies known to be significant for TEC loading and have turbulence intensities up to 80% higher than the average.
- Comparisons to conventional Fourier analysis demonstrate that these intermittent, coherent bursts are obscured by the averages associated with Fourier analysis, highlighting the need for methods such as wavelets to understand interactions between fluid flow and TEC.

Chapter 5

Methodology

This chapter describes the data and the methods employed in the analysis for Part I. Section 5.1 introduces the measurement campaigns where the ADCP data was collected. Section 5.2 explains the data processing techniques, methods for turbulence characterisation and intermittency analysis - which was carried out on a smaller sub-sample of data.

5.1 ADCP Measurements

The ADCP velocity measurements were gathered at two tidal sites, the European Marine Energy Centre (EMEC) and the Fundy Ocean Research Centre for Energy (FORCE).

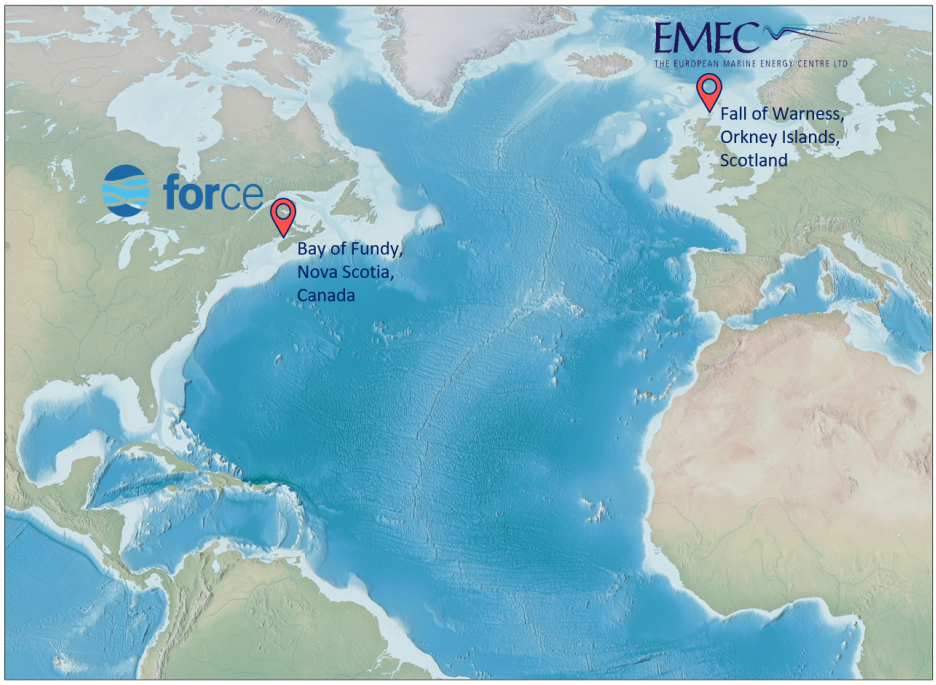

Figure 5.1: Locations of the case study tidal sites. Fundy Ocean Research Center for Energy (FORCE) is located in Nova Scotia, Canada and The European Marine Energy Centre (EMEC) is located in the Orkney Islands, UK.

The EMEC tidal test site is located in the Fall of Warness tidal channel, south of the Eday Island in Orkney, UK. The FORCE tidal test site is located in the Minas Basin - an inlet of the Bay of Fundy located in Nova Scotia, Canada. Both sites are unique as they are the leading research facilities for tidal stream technology in their respective geographies, offering some of the fastest tidal flows globally.

Instruments were deployed at two nearby locations at each site at different periods in time, as shown in Figure 5.2. EMEC-1 and EMEC-2 instruments were approximately 400 m apart and FORCE-1 and FORCE-2 instruments were located approximately 300 m apart. The instrument configurations, water depths and peak flows recorded by the instruments are summarised in Table 5.1.

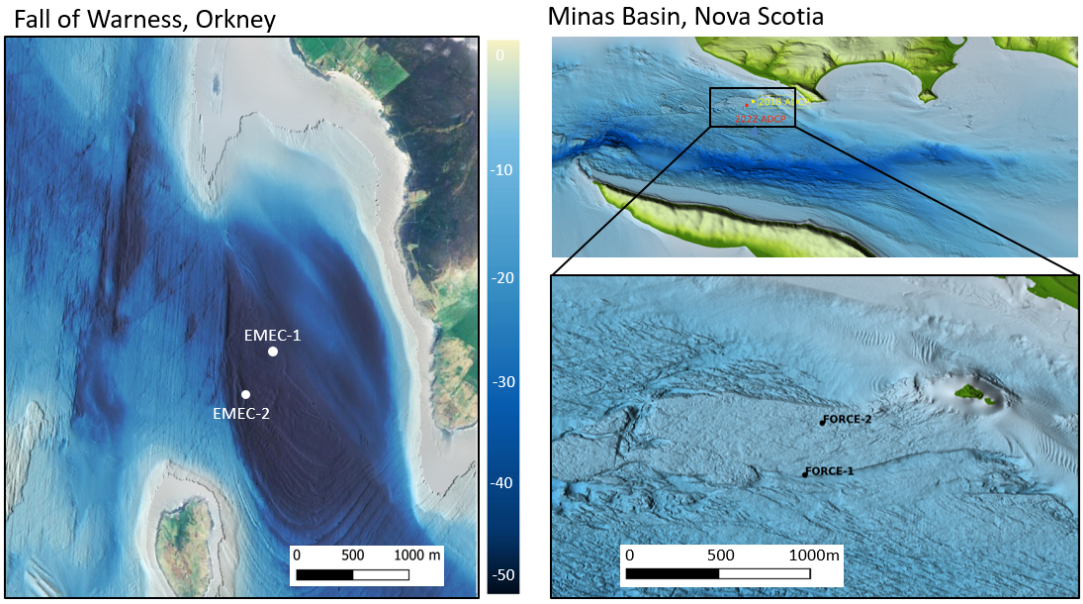

Figure 5.2: Channel bathymetry and the location of the ADCP instruments at EMEC and FORCE tidal energy test sites.

Table 5.1: ADCP instrument summary. The parameter f_{bs} indicates the limiting frequency (based on eddies of the vertical cell size advecting at 2.5m/s, Equation 5.1).

Reference	Instrument	Sample Rate	Cell Size	Measurement Period	Peak Flow	Depth	f_{bs}
EMEC-1	Nortek Signature 500	4Hz	1m	10 Apr 2020 - 22 Apr 2020	3.8m/s	48m	2.5Hz
EMEC-2	Sentinel V50	1Hz	1m	08 Nov 2019 - 19 Dec 2019	3.7m/s	48m	2.5Hz
FORCE-1	Nortek Signature 500	2Hz	1m	27 Jan 2022 - 02 Apr 2022	4.6m/s	38m	2.5Hz
FORCE-2	Sentinel V100	1Hz	0.5m	29 Jun 2018 - 29 Aug 2018	4.7m/s	34m	5.0Hz

The average heading on both of the EMEC ADCP's was such that one beam pair was oriented approximately in the streamwise direction of the tidal current; however, the FORCE ADCPs were not aligned with the flow (see Figure 5.3). This has important implications for the turbulence parameters which can be derived using the data, as explained in more detail in the following section.

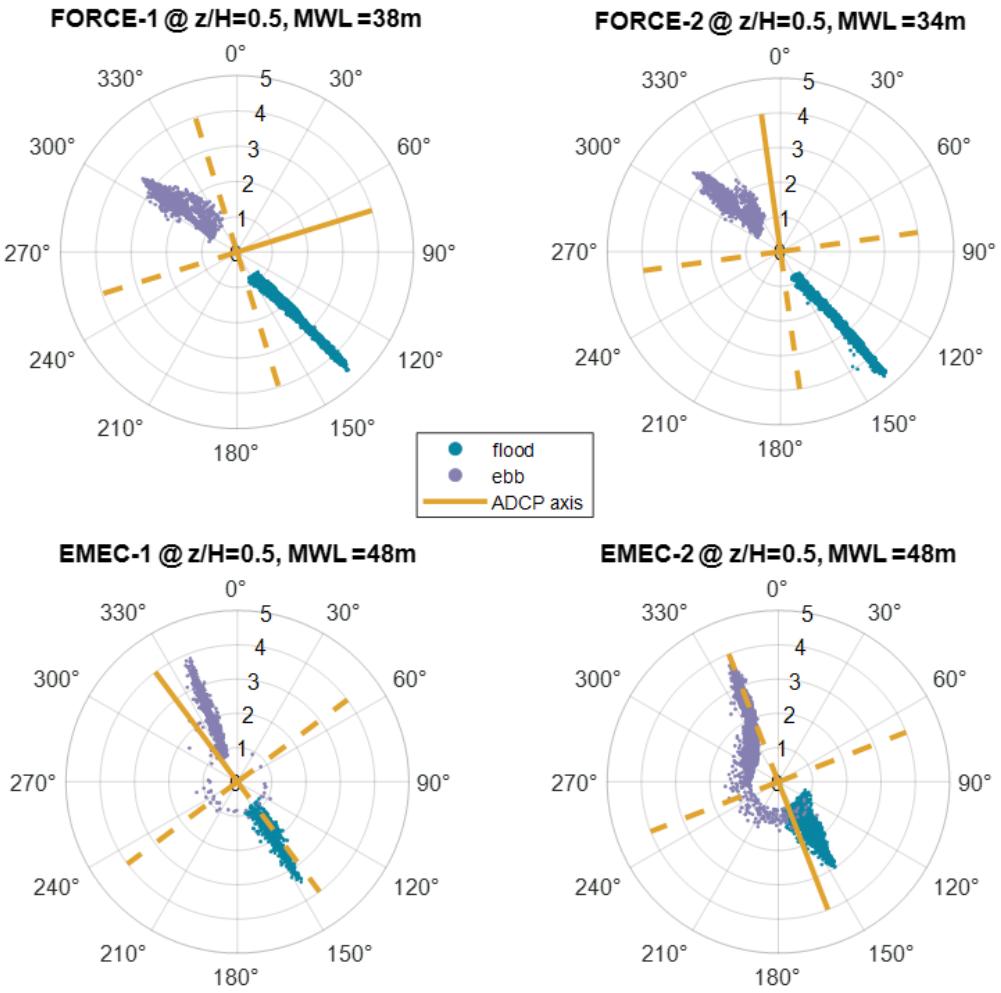

Figure 5.3: Tidal rose plots showing flow direction as well as ADCP orientation. Solid yellow line corresponds to the instrument heading.

5.2 ADCP Data Processing

5.2.1 Quality Control

The raw data were processed and quality-controlled (QC) using EMEC's proprietary QC tool, IMPAQCT. This tool follows the Quality Assurance and Quality Control of Real Time Oceanographic data (QARTOD) standard (IOOS, 2019), alongside the Nortek instrument manual (Nortek, 2018) and flags any data which do not meet the QC thresholds.

5.2.2 Data Selection

Instantaneous along-beam data was retained for turbulence analysis to avoid making the assumptions of homogeneity in resolving velocity vectors and averaging out important fluctuations. However, for some parameters such as length-scales, instantaneous velocities in the channel co-ordinates (u, v, w) are required so for these, the instantaneous velocity vector was resolved. The consequences of doing this and checks which were put in place are discussed in Section 5.2.4.

To ensure parameters are comparable across the sites, all data have been split into 10-minute intervals and binned by tidal cycle, mean flow velocity and relative depth, z/H. Turbulence statistics were calculated for each 10-minute interval and averaged for each tidal cycle and flow velocity band for all datasets. The tidal cycles are identified by tracking zero-crossing points of flow acceleration e.g. see Figure 5.4.

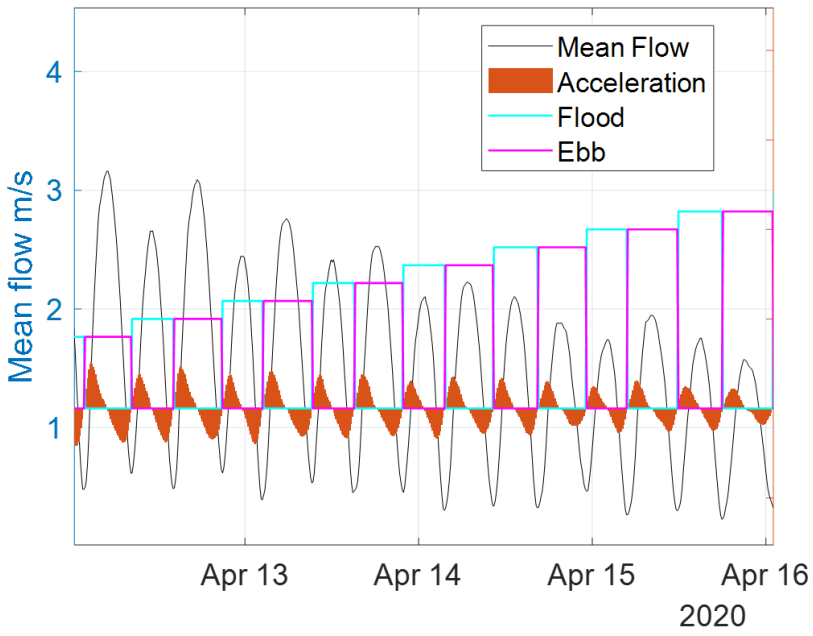

Figure 5.4: A subset of EMEC-1 data demonstrating the method for identifying tidal cycles. The crossing points in acceleration determine where the tide reverses.

Due to the ADCP sampling rates (Table 5.1), only EMEC-1 and FORCE-1 datasets were used for the spectral and coherence analysis. In the higher frequency range, the turbulence is expected to be isotropic and the smallest turbulent eddies that can be captured will be limited by the vertical cell size Δz (as opposed to the beam spread). According to Taylor's Frozen Eddy Hypothesis, the frequency of these eddies can be approximated by (Pearson and Hernon, 2015):

$$f_{bs} = \frac{\overline{U}(z_{bin})}{\Delta z} \tag{5.1}$$

where $\overline{U}(z_{bin})$ is the mean current magnitude at the required depth and Δz is the vertical cell size. The spatial averaging inside each beam is an inevitable feature of ADCPs and fluctuations below these scales would be significantly attenuated.

Pearson and Hernon (2015) recommend that f_{bs} should be used as a guide to determine the appropriate sampling frequency to capture the full range of scales. To avoid aliasing, the sampling frequency should be $2 \times f_{bs}$, however, this may be limited by instrument capability. The f_{bs} frequency for 1m eddies for a typical rated velocity at the measurement locations is shown in table 5.1. It is evident that 1Hz sampling rate would not be high enough to capture the smaller scales. Moreover, as the advecting velocity increases so will the required sampling rates. EMEC-1 and FORCE-1 instruments were considered to capture enough of the high-frequency range to be able to fit model spectra.

For the intermittency analysis (described in Section 5.2.5), a small number of short data samples from EMEC-1 were selected. Figure 5.5 shows the suitable data samples after filtering by cycle, periods of low waves and peak flow velocities of 2.8-3.2m/s.

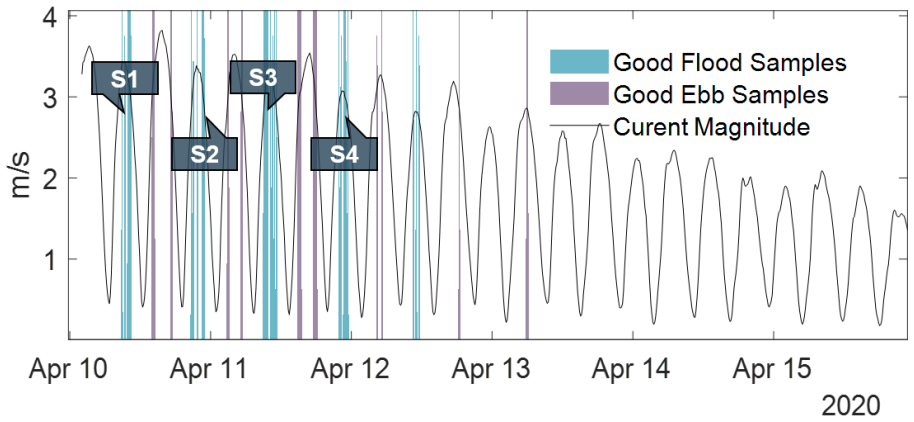

Figure 5.5: Subset of EMEC-1 data showing suitable 10-min samples based on velocity, waves and cycle criteria, which were used for detailed intermittency analysis.

Concurrent wave height data was not available for this period so wave presence was identified by detecting peaks in the turbulence spectrum in the frequencies (0.1-0.2Hz) known to be common to waves in this area (Osalusi, 2010). Figure 5.6 shows an example spectrum of two 10-min samples, with high and low wave presence. Figure 5.7 shows the identified wave peaks for the data set and the spectrum magnitude cut-off threshold, chosen as 0.1 in this case.

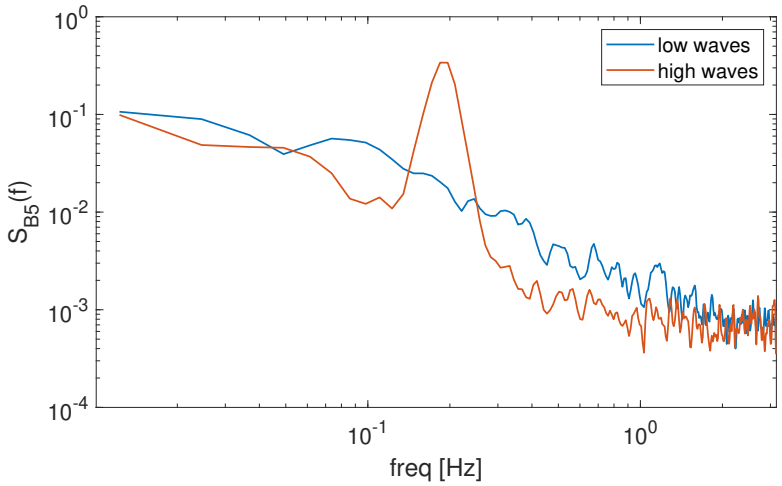

Figure 5.6: Vertical beam spectrum for time samples with low and high wave presence (identified by a sharp peak around 0.1 Hz).

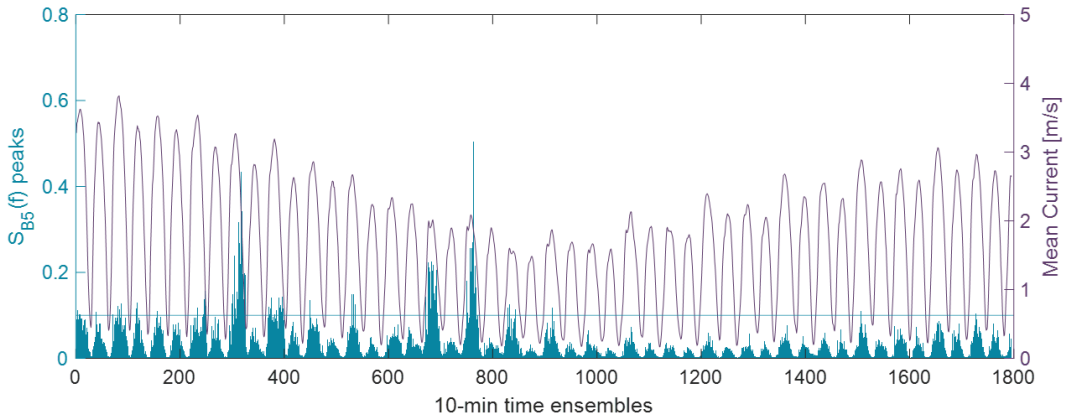

Figure 5.7: Method to identify waves by detecting peaks in the vertical beam spectrum (teal) within the wave frequency range above a threshold, as well as the mean velocity magnitude (purple) for the ADCP-1 dataset.

5.2.3 Doppler Noise

De-noising was carried out by identifying Doppler noise variance for each beam using the spectral-fitting method (Sellar et al., 2018; Durgesh et al., 2014) and subtracting this variance from the total beam variance. These studies have demonstrated that the spectra at higher frequencies tend to flatten out when there is instrument noise present. The spectral-fitting method, which works under the assumption that the noise is "white," includes fitting the power spectral density of velocity variations to both the $f^{-5/3}$ slope and a flat line that represents the noise (Sellar et al., 2018), as shown in Figure 5.8.

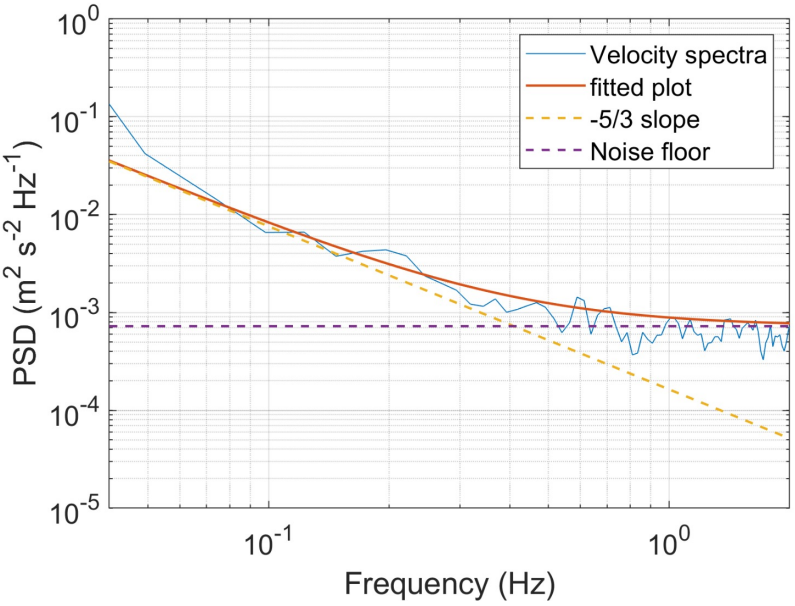

Figure 5.8: Example of the spectral Doppler noise technique shown for a single 10-minute sample of beam 1 velocities from the EMEC-1 dataset

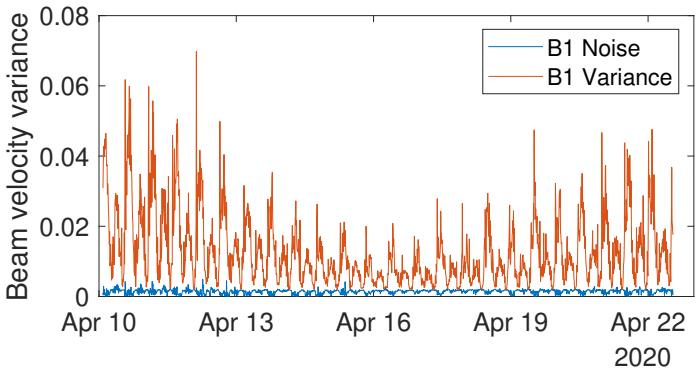

Figure 5.9: The total variance and noise variance (determined by the spectral method) for beam 1 for the EMEC-1 dataset.

Figures 5.8 and 5.9 show the applied spectral method for a single 10-minute sample and the results for the whole data set respectively, for a single beam. This technique was applied to each beam for all datasets, the noise variance was then subtracted from the total variance to give the de-noised values.

5.2.4 Calculating Turbulence Parameters

Codes such as Tidal Bladed or TurbSim construct a turbulent flow field from a set of measured or assumed input parameters, as illustrated in Figure 2.5. This section describes the methods for calculating these parameters from measured velocities. The measured parameters are then compared to the assumed parameters, calculated from semi-empirical models.

Turbulence Intensity

The 5-beam ADCP's allow for a true measurement of vertical velocities and hence the estimation of five Reynolds stress terms (all but $u'v'$), see Equation 2.1 (Guerra and Thomson, 2017). The channel-coordinate variances are determined using the variance method, Equations 5.2-5.6. The variances are first determined in along-beam coordinates, then combined by assuming statistical characteristics (variance) are homogeneous over the beam spread (for further explanation of the method and for equations including the tilt of the instrument, see Dewey and Stringer (2007) and Thiébaut et al. (2020b)). The resulting variances in channel co-ordinates $\overline{u'^2}, \overline{v'^2}, \overline{w'^2}$ are used to calculate I and TKE using Equations 2.2 - 2.4.

$$\overline{u'^2} = \frac{\overline{b'_1} + \overline{b'_2} - 2\overline{b'_5}cos^2(\theta)}{2sin^2(\theta)} \tag{5.2}$$

$$\overline{v'^2} = \frac{\overline{b'^2_3} + \overline{b'^2_4} - 2\overline{b'^2_5}cos^2(\theta)}{2sin^2(\theta)} \tag{5.3}$$

$$\overline{w'^2} = \overline{b'^2_5} \tag{5.4}$$

$$\overline{u'w'} = \frac{\overline{b'^2_2} - \overline{b'^2_1}}{2sin(2\theta)} \tag{5.5}$$

$$\overline{v'w'} = \frac{\overline{b'^2_4} - \overline{b'^2_3}}{2sin(2\theta)} \tag{5.6}$$

ADCP Alignment Error

The orientation of the ADCP beams to the flow is vital. If the beams are not aligned with the flow direction, only the total turbulence intensity I_T, or turbulent kinetic energy $\frac{q^2}{2}$, quantities can be reliably calculated (Greenwood et al., 2019). The FORCE site instruments used in this work were not aligned with the principal flow direction. Moreover, the EMEC instruments that were aligned would still have misalignment errors due to flow asymmetry between flood and ebb directions, as can be seen in Figure 5.3. To quantify the misalignment error, we can define the approximate variance $\overline{u'^2}_{appx}$, as calculated from the misaligned ADCP data, in terms of the actual variance $\overline{u'^2}$ and the misalignment angle ϕ. The derivations are included in Appendix A.0.1, and the resulting equations are:

$$\overline{u'^2}_{appx} = \overline{u'^2}\cos^2(\phi) + \overline{v'^2}\sin^2(\phi) - \overline{u'v'}\sin(2\phi) \tag{5.7}$$

$$\overline{v'^2}_{appx} = \overline{v'^2}\cos^2(\phi) + \overline{u'^2}\sin^2(\phi) + \overline{u'v'}\sin(2\phi) \tag{5.8}$$

$$\frac{q^2}{2}_{appx} = \frac{\overline{u'^2}_{appx} + \overline{v'}_{appx} + \overline{w'^2}}{2} = \frac{\overline{u'^2} + \overline{v'^2} + \overline{w'^2}}{2} \tag{5.9}$$

$$\alpha = \frac{\overline{w'^2}}{\overline{u'^2}_{appx} + \overline{v'}_{appx}} = \frac{\overline{w'^2}}{\overline{u'^2} + \overline{v'}} \tag{5.10}$$

The derived Equations 5.7-5.10 were applied to calculate the error in I_u. This was done by computing I_u using the actual $\overline{u'^2}$ and misaligned variances $\overline{u'^2_{appx}}$ in Equation 2.3. In the case of the FORCE-1 and FORCE-2 datasets, with an approximate misalignment of 30°, I_u could have errors between 20–60% depending on the relative values of the u and v components. In the case of slight misalignment due to asymmetry, as in the EMEC-1 case (approximately 10°), the error would range from 5–15%. The error will depend on the relative magnitudes of $\overline{u'^2}, \overline{v'^2}$ and $\overline{u'v'}$, as well as on the degree of misalignment ϕ. The curves in Figure 5.10 show the range of errors based on reported anisotropy ratios and relative $u'v'$ magnitudes. The ratio σ_v/σ_u was found to be 0.75 at the Sound of Islay tidal site (Milne et al., 2017); the ratio $\overline{u'v'}/\overline{u'^2}$ ranged between 0.3–0.75 at Mahakam River, East Kalimantan, Indonesia (Vermeulen et al., 2011).

These equations also demonstrate that the total quantities, such as total turbulence intensity I_T, total TKE and the total anisotropy ratio remain unaffected by the misalignment due to the cancelling out of the covariance term $\overline{u'v'}$.

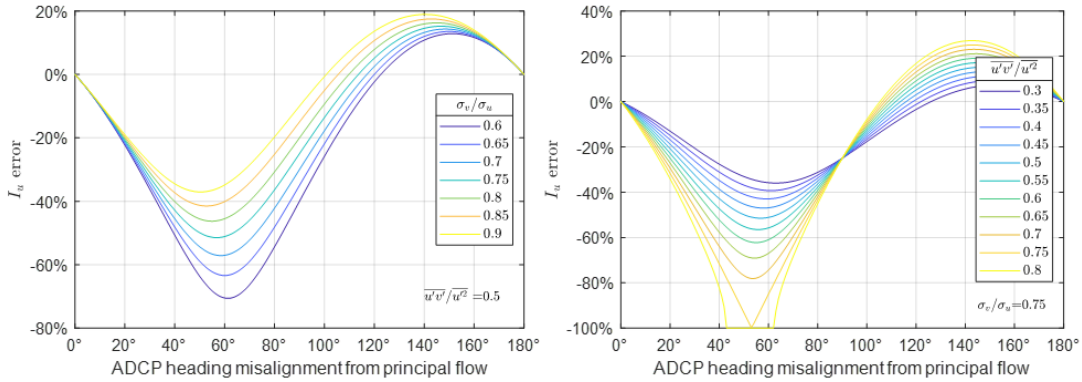

Figure 5.10: Error ranges for streamwise turbulence intensity I_u calculated from the misaligned ADCP data for various anisotropy ratios and relative $u'v'$ magnitudes.

Turbulence Spectrum

The MATLAB function `pwelch` was used to compute the discrete Fourier transform of each 10-minute time series. This function uses the fast Fourier transform (fft) algorithm. The time series is divided into segments and a 50% overlap is applied using a Hamming window. The resulting spectra are averaged to obtain the power spectral density (PSD) estimates (MathWorks, 2022c). In the PSD format, the area under the spectrum curve represents the variance for the data record.

In order to compare the measured spectra to the models, the measured spectra were denoised using methods described in Section 5.2.3 and normalised by the variance so that the area under the spectrum curve equals one. The vertical and streamwise model spectra were constructed from Equations 2.21-2.23, using measured values of $\overline{U}$ and L_i where $i = u, v, w$ component. The measured vertical spectrum was computed directly from the vertical beam velocities. To calculate the streamwise spectrum, the variance method is applied to the individual beam velocity spectra as in Milne et al. (2021):

$$S_{uu} = \frac{S_{b1b1} + S_{b2b2} - 2cos^2\theta S_{b5b5}}{2sin^2\theta}, \tag{5.11}$$

where S_{b1b1} and S_{b2b2} are the spectra of the two opposite beams aligned to the streamwise direction, S_{b5b5} is the vertical beam spectrum, and θ is the beam inclination angle.

In the case of the FORCE-1 dataset, due to the misalignment of the instrument, streamwise metrics could not be reliably calculated. In this case, the total energy spectrum was compared, as this is unaffected by the rotation of the instrument. Applying the expression for obtaining the total kinetic energy (Dewey and Stringer, 2007) from the individual beam variances, the

total measured spectrum was calculated as follows:

$$S_{total} = \frac{S_{b1b1} + S_{b2b2} + S_{b3b3} + S_{b4b4} - 2(2cos^2\theta - sin^2\theta)S_{b5b5}}{4sin^2\theta}. \tag{5.12}$$

The total model spectrum is constructed using equation:

$$S_{total} = \frac{S_{uu} + S_{vv} + S_{ww}}{2}, \tag{5.13}$$

where S_{uu}, S_{vv} and S_{ww} are calculated using Equations (2.21) to (2.23). The spectra were calculated for relative depths, $z/H = 0.2, 0.5, 0.7$.

Coherence

Spatial coherence describes the correlation of velocity fluctuations across a separation distance r as a function of frequency, returning a correlation coefficient between 0 and 1 (Torrence and Compo, 1997). In turbulence analysis, spatial coherence Γ is defined by Equation 2.24 and is usually estimated from two independent measurements of the same component of velocity, u_1, u_2 that are separated in space by a distance, $r = (\Delta x^2 + \Delta y^2 + \Delta z^2)^{1/2}$ (Kilcher et al., 2014).

To calculate coherence using Fast Fourier Transform (FFT), the MATLAB function `mscohere` is used. This function finds the magnitude-squared coherence estimate for two input signals (MathWorks, 2022a).

The IEC only provides a streamwise coherence model so streamwise velocity measurements are required. ADCP's do not provide a direct measurement of the instantaneous streamwise velocity component, so a rotation is applied to instantaneous beam velocities to convert them into channel co-ordinates (making the assumption of homogeneity across the beam spread). The converted velocities are used in the coherence calculation. Due to the uncertainty relating to the homogeneity assumption (explained in Section 2.2.1), coherence was also calculated from the instantaneous beam velocities for comparison.

The 95% confidence level of Γ measurements - above which Γ estimates can be considered valid with 95% confidence - is equal to $\sqrt{6/n_{DOF}}$, where n_{DOF} is the number of degrees of freedom in the coherence estimate (Kilcher et al., 2014). In discrete Fourier transform (DFT), the degrees of freedom are related to the number of distinct frequency components that can be independently varied. A method by Welch (1967), sections the record into windows, takes modified periodograms of the sections, and averages these to get a spectrum. The number of segments in Welch depends on the overlap and the length of segment specified. Welch (1967) defined degrees of freedom (DOF) as follows:

$$DOF = 2[(N - W)/O + 1], \tag{5.14}$$

where N=signal length, W=window length, O =offset .

Coherence was analysed at relative depths $z/H = 0.2, 0.5, 0.7$ for a 5 m separation distance above and below the analysing depth. The model coherence was constructed using Equation (2.24) using measured L, U and r.

Length-scales

Length-scales were calculated by the auto-correlation method (Equation (2.12)), again using the converted instantaneous velocities in stream co-ordinates. Such a calculation method becomes unreliable at depths where the beam spread becomes significant. At these depths the beam spread may be interpreted as the minimum length scale of turbulence that is measured accurately by the ADCP (Greenwood et al., 2019). For this reason, a check is carried out to ensure the computed length-scales are greater than the beam spread.

Shear Profile

Shear profiles were calculated by averaging velocity magnitudes at each depth bin for the flood and ebb cycles and for the velocity range 1–3m/s. A power-law model, as described in Equation (2.13), was fitted to the data, calculating the exponent, β.

5.2.5 Intermittency Analysis

Intermittency was assessed by analysing the instantaneous turbulence spectra and coherence, as well as stationarity of the measured signal.

The spectrum and coherence were calculated by two methods, Fourier and wavelets. Wavelets enable the instantaneous spectrum to be resolved, however as the application of wavelet analysis to turbulence characterisation is novel, the averaged wavelet spectra are also compared with the traditional Fourier methods.

The continuous wavelet transform (CWT) is defined by Equation 2.8. The MATLAB function `cwt` - part of the Wavelet Toolbox - was used to compute the continuous wavelet spectrum. This function uses the sampling frequency of the signal to determine the scale-to-frequency conversions and therefore returns the spectrum on a frequency scale. The `cwt` function uses L1 normalization which overcomes the issue of the peaks at higher frequencies being reduced more than the peaks at lower frequencies. With L1 normalization, if there are equal amplitude oscillatory components in the data at different scales, they will have equal magnitude in the CWT. Using L1 normalization shows a more accurate representation of the signal, for a more detailed explanation see the Wavelet Toolbox documentation (MathWorks, 2023). The Morlet wavelet was chosen as it has been shown to have a good balance between time and frequency localization (Chen et al., 2019), and the wavelet scale is closely related to Fourier period.

The wavelet spectrum was normalised according to Equations 2.9 and 2.10 in order to be comparable with the Fourier spectrum. For the wavelet coherence the `wcoherence` function is used. This function is also part of the Wavelet Toolbox, it determines the wavelet coherence and cross-spectrum for two input signals (MathWorks, 2023).

In the PSD format, the area under the spectrum curve represents the variance, u'^2 for the data record. This can be related to turbulence intensity by:

$$I_i = \frac{\sqrt{u_i'^2}}{\overline{U}} \tag{5.15}$$

where i is the velocity component and $\overline{U}$ is the mean current magnitude.

Figure 5.11 shows the measurement points used in analysis, as well as beam orientation in relation to hypothetical floating and bottom fixed TEC cases. Coherence was analysed along the vertical and inclined beams for half a rotor separation distance.

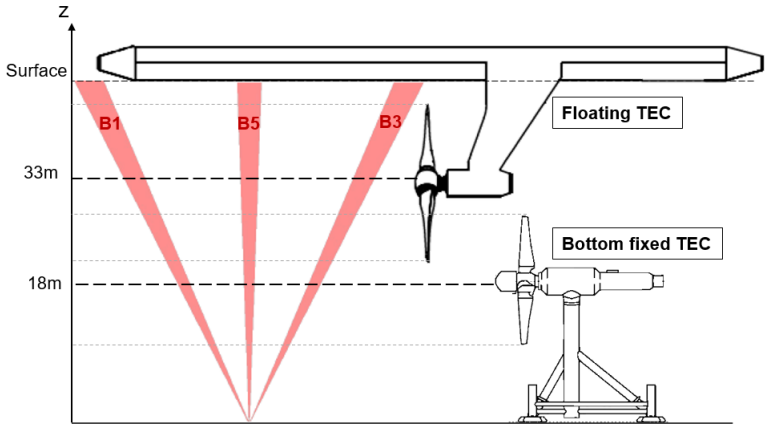

Figure 5.11: Floating and bottom fixed turbine concepts, relative to the water depth and the ADCP beams at EMEC tidal test site. The assumed hub heights are as shown and rotor diameters are assumed to be 20m.

Stationarity test

One of the ways to assess data for stationarity is to examine how statistics converge with increasing averaging time. This was done by selecting a 20 minute instantaneous velocity record and subdividing it into a range of periods from 20 seconds to 20 minutes in 20 second increments, with the mean, $\overline{u}$ and standard deviation, σ_u calculated for each period as in Sutherland et al. (2017). In stationary data, the mean is expected to converge to a value as stationarity time is approached. Typically stationarity period for tidal channel data is assumed to be 5-10 minutes (Clark et al., 2015a).

Important scales

It is important to understand which scales of turbulent motions are important for device fatigue loading. Previous studies found that the most important turbulent scales (size of large eddies) for load considerations range from 0.5 - 3 times the rotor diameter, D (Ouro et al., 2017; Milne et al., 2010; Sentchev et al., 2020; Blackmore et al., 2015). According to Taylor's Frozen Eddy Hypothesis, the frequency f_L at which an eddy with a length scale L is advected by the tidal flow $\overline{U}$ past a point can be defined as (Pearson and Hernon, 2015):

$$f_L = \frac{\overline{U}}{L} \tag{5.16}$$

Using the mean current velocity for the data sample, we can approximate the frequency limit below which the fluctuations might be less important for loads on a typical tidal rotor (e.g. 20m diameter). This is because length scales much larger than the rotor diameter are would exert a fairly uniform velocity increase over a turbine disc area and will be felt as a change in the mean flow, contributing less to turbine fatigue (fluctuating) load.

Another important frequency is the the blade passing frequency (BPF), which depends on the rotational speed of the turbine. Flow velocity fluctuations at this frequency are known to be a significant source of fatigue loading due to blade slicing through the spatially coherent eddies. This action can give rise to significant energy contributions at multiples of the rotational frequency of the rotor, and is a significant contributor to the fatigue of components (Milne et al., 2016; McCann et al., 2008).

Chapter 6

Results and Discussions

This Chapter presents the results and discussions for the research questions addressed in Part 1 - concerned with the nature of turbulence in real-sea conditions and the applicability of models and methods typically used by the industry.

In Section 6.1, the key turbulence parameters obtained from four ADCP instruments are presented. By comparing models and theories to measurements, their applicability to real-sea turbulence is assessed. Unlike previous studies, these comparisons are carried out across the full turbulence parameter set (as required for model inputs) and using data from two different tidal test sites.

Section 6.2 presents an analysis of the non-stationarity of flows in real tidal channels, using a sub-sample of the data. Here, the traditional Fourier transform methods are compared to novel applications of wavelet transform. The additional time-frequency analysis capabilities of wavelets are demonstrated and the limitations of traditional methods are discussed.

6.1 Real-Sea Turbulence: Applicability of Models & Assumptions

6.1.1 Length-scales

In order to define the spectrum and coherence models, length-scale values must be specified (see Equations 2.21-2.24). Measurements from EMEC-1 and FORCE-1 (Figure 6.1) show significantly larger streamwise length scales L_u than the other datasets, which may be due to their proximity to bathymetric features (Figure 5.2). Moreover, EMEC-1 has a notably larger lateral length-scale L_v, in particular on the ebb tides, relative to the streamwise component. The other datasets have a much smaller L_v compared to L_u. There is a significant variation in the profile shapes on the ebb tides across all instruments. The results demonstrate the degree of variability found in real-sea conditions, even at nearby locations at the same site.

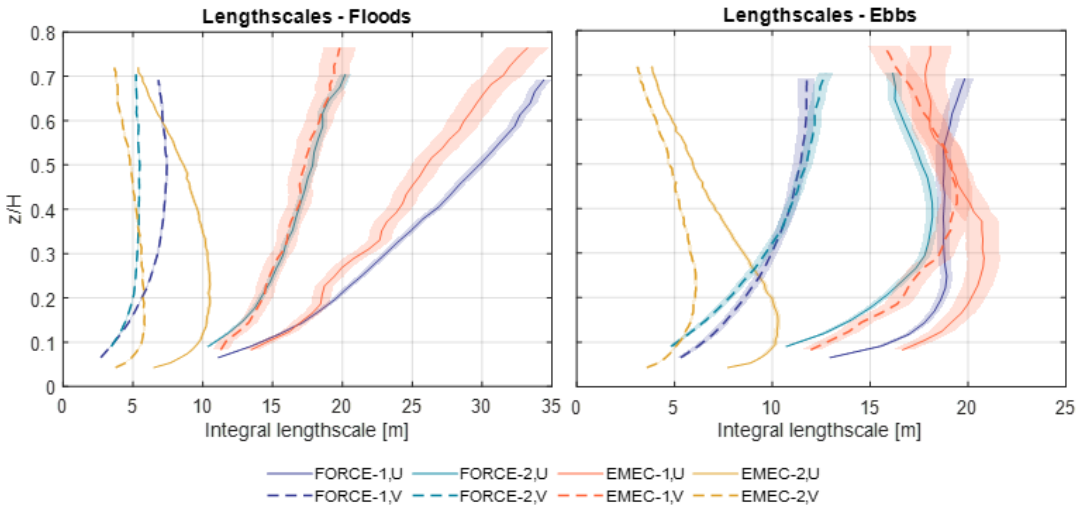

Figure 6.1: Length-scales calculated using time-correlation method on instantaneous velocity data. Shaded areas show standard error, which is larger for EMEC-1 due to a shorter dataset.

Length-scales are sometimes approximated according to open-channel flow theory, where the integral length-scale across the lower half of the water column is defined as $L_u \approx \sqrt{zH}$, (Nezu and Nakagawa, 1993). At the two sites considered, such theoretical values are not representative. Only one instrument, FORCE-2 showed agreement and only up to $z/H = 0.2$, with the rest deviating significantly (Figure 6.2). The FORCE-1 length-scale profile follows the theoretical shape on the floods, although skewed towards higher values. All other results show a significant deviation from the theoretical profile, especially on the ebb tides.

When measurements are not available, TurbSim and Tidal Bladed models define the stream-wise length-scale, $L_u = 8.10\ \Lambda_U$, where $\Lambda_U = 0.7$ min (30 m, hub height), in line with the IEC 61400-1 wind standard (IEC, 2019a). This would suggest a length scale, L_u = 113 m for the mid-water column for the present sites, which is almost four times higher than the highest measured length scale across all data-sets (Figure 6.1). The theoretical values are based on atmospheric turbulence and are clearly not applicable to the tidal channels analysed here.

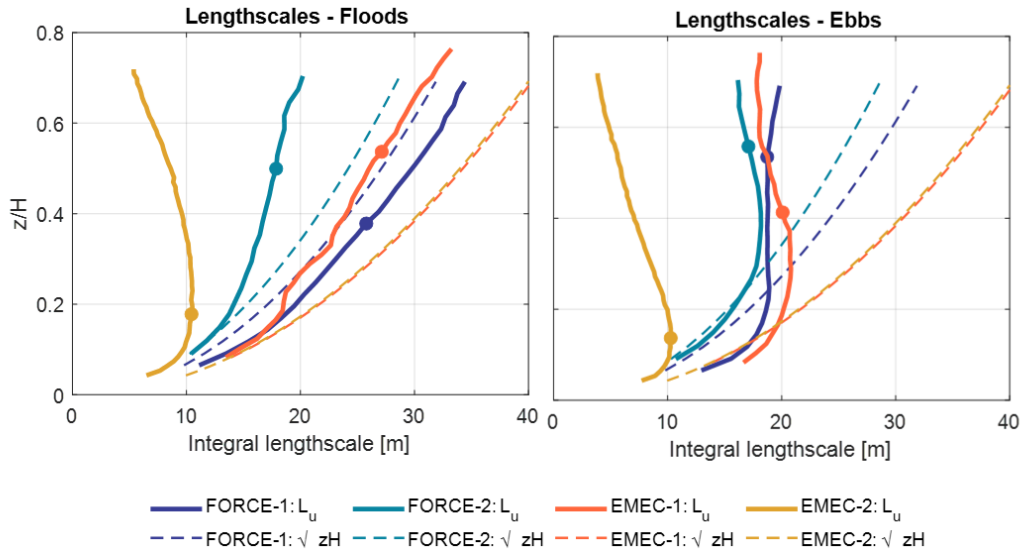

Figure 6.2: Streamwise length-scales calculated by the time-correlation method on instantaneous streamwise velocity data. The dashed lines indicate a theoretical length-scale based on open-channel theory, $L_u = \sqrt{zH}$. The bold dot indicates the point above which the beam spread is larger than the length scales.

6.1.2 Turbulence Spectrum

The spectral analysis was only carried out for the FORCE-1 and EMEC-1 data-sets due to the sampling rate limitations of the other instruments.

Vertical Spectrum

The direct measurement of the vertical velocity spectrum (S_w) is available from the vertical ADCP beam. The computed spectra were normalised by the velocity variance and are compared to the Kaimal and von Kármán models in Figures 6.3 and 6.4.

For both sites, the Kaimal model provides a good fit for the vertical spectrum, with better agreement near the seabed. The von Kármán model shows less agreement with the observed spectra, with the peak located at a higher amplitude and a shift towards lower frequencies. The FORCE-1 spectra show better agreement on the flood tides (Figure 6.3) than the ebb (Figure 6.4), whereas EMEC-1 spectra are similar for both.

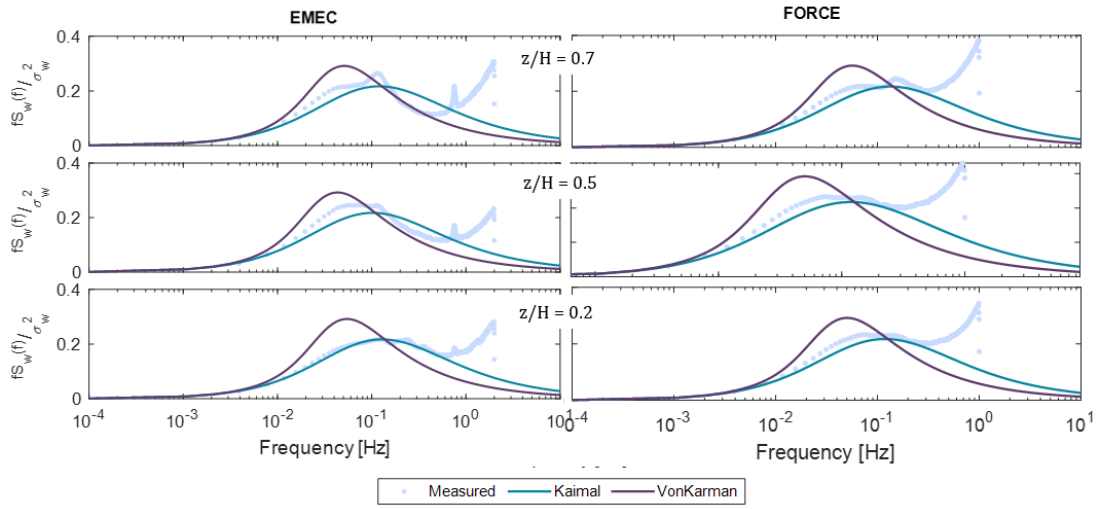

Figure 6.3: Comparison of the vertical Kaimal and von Kármán models (calculated using a measured length-scale) to measured spectra for flood cycles. The 10-minute spectra were normalised by variance and are averaged across all flood cycles for velocities 1-3 m/s.

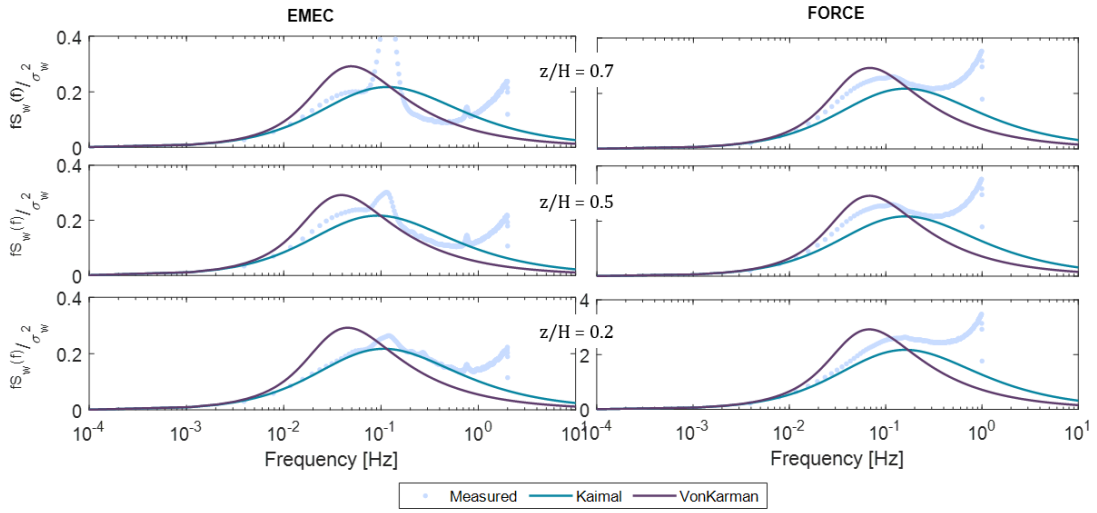

Figure 6.4: Comparison of the vertical Kaimal and von Kármán models (calculated using a measured length-scale) to measured spectra for ebb cycles. The 10-minute spectra were normalised by variance and are averaged across all ebb cycles for velocities 1-3 m/s.

Streamwise Spectrum

The streamwise spectrum (S_u) model is compared with the measurements for the EMEC-1 dataset only as this instrument was aligned to the flow. Section 5.2.4 demonstrated that total second-order quantities are unaffected by instrument orientation. Therefore, the FORCE-1 (misaligned instrument) spectra were analysed at a total energy level.

Interestingly, for the streamwise component (and for the total spectrum), the von Kármán model showed much better agreement (Figures 6.5, 6.6), although as before there is a peak shift, but towards lower frequencies this time. This is in contrast to findings from the Grand Passage, Nova Scotia (McMillan, 2017), where the Kaimal model was found to better predict the streamwise spectra.

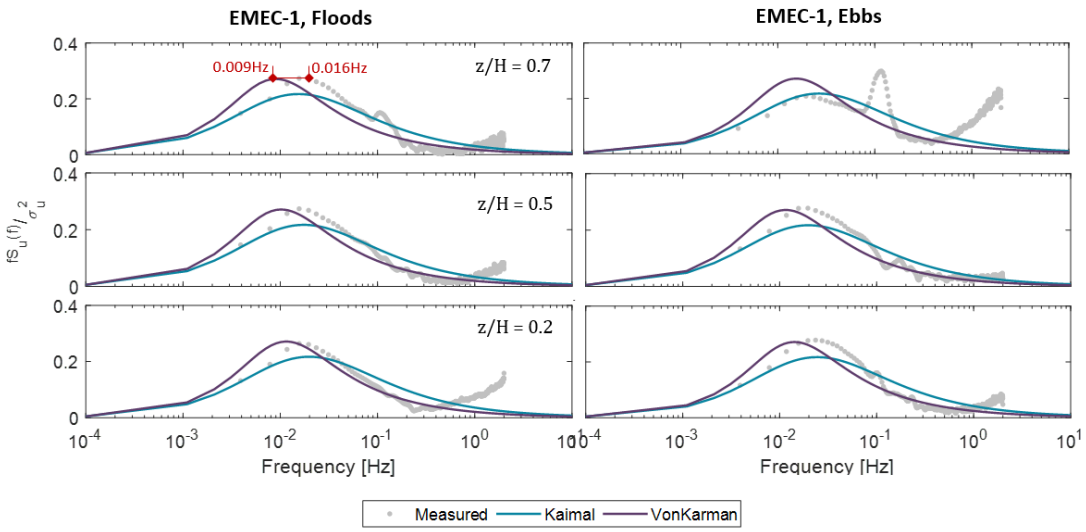

Figure 6.5: Comparison of the streamwise Kaimal and von Kármán models (calculated using a measured length-scale) to measured spectra. The 10-minute spectra were normalised by variance and are averaged across all flood and ebb cycles with velocities 1-3 m/s.

The peak shift in Figure 6.5 means that the measured energy is concentrated around a frequency almost twice as high as the model suggests. This shift occurs even though measured length-scales are used as input to the spectrum model, suggesting that the issue is with the coefficients used in this semi-empirical model. In other words, even though the correct length-scale is used in constructing the model, the effective length-scale (determined by the position of the peak) is incorrect. In previous studies (Milne et al., 2013, 2017; McMillan, 2017; Walter et al., 2011), regardless of which model provided a better fit, the streamwise spectrum peak was always shifted towards low frequencies, as in this study. In practice, using the 'shifted' spectrum would mean assuming fewer load cycles at the same magnitude than would be encountered at the site in question. This is likely to underestimate fatigue loads. So although the general shape of the spectra seem to agree with the measurements, care must be taken that the spectrum peak is not significantly shifted.

On the ebb tides, near the top of the water column (Figure 6.5), the measured spectrum deviates from the von Kármán model and aligns more to the Kaimal model. This may be due to wave interference, clearly visible as a spike at around 0.1 Hz, creating an energy deficit in the lower frequencies in the spectrum calculation.

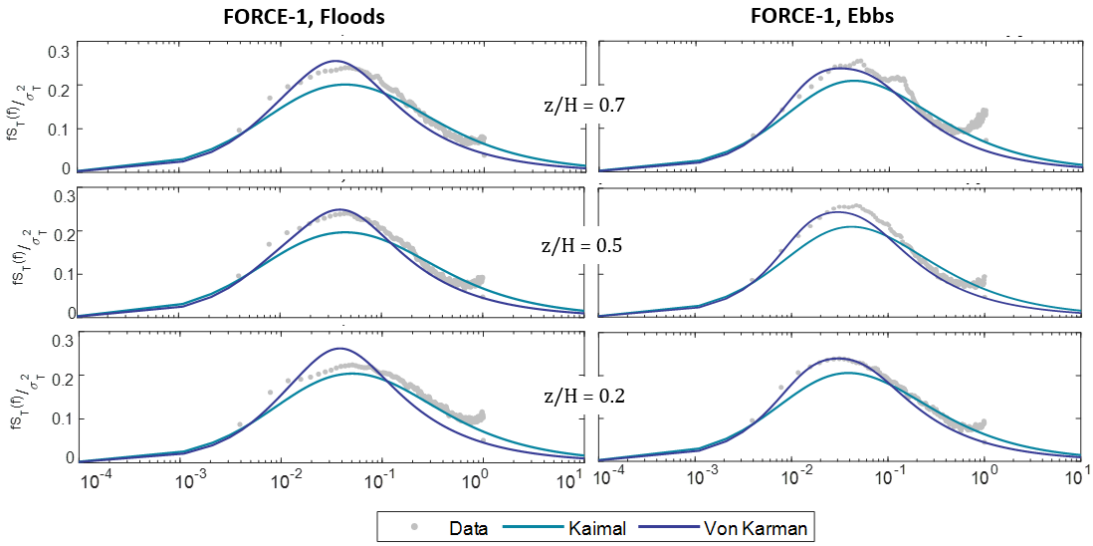

Figure 6.6: Comparison of the stream-wise Kaimal and von Kármán models (calculated using a measured length-scale) to measured spectra. The 10-minute spectra were normalised by variance and are averaged across all flood and ebb cycles with velocities 1-3 m/s.

Figure 6.6 shows comparisons of total measured spectra to the total model spectra (constructed using Equation 5.13). Given that the streamwise component is the largest contributor to the overall energy spectrum, the totals are considered to give an indication of applicability of the streamwise models. Similar to the streamwise comparison of the EMEC-1 data, the von Kármán total spectrum model agrees better with the measured spectrum than the Kaimal model, with a better peak alignment than seen in EMEC-1 data. This could be an artifact of using the total model (which includes vertical and transverse components) or different conditions e.g. length-scales at the FORCE site.

6.1.3 Coherence

As there is no definition of the general coherence model for the vertical component, the horizontal model defined by Equation (2.24) is compared to the coherence calculated from the instantaneous streamwise velocity component. Due to the uncertainty of using instantaneous data in such a way, the coherence from the inclined beams is included for comparison. The results presented in Figures 6.7 and 6.8 show that the EMEC-1 measurements agree well with the model at low frequencies in the upper water column, while the FORCE-1 measurements show less agreement. In both cases, the measured coherence curve is less steep, i.e., the coherence is higher in the high-frequency range than the model suggests. For both data-sets, coherence tends to be higher in the upper water column. The measured streamwise coherence is similar to the highest beam coherence, suggesting the method used is appropriate.

To the authors knowledge, there have been no studies on validating the IEC coherency models for tidal-energy applications. In this work, the coherence measurements did not show a good agreement with the models, in particular for the FORCE-1 location. It is known that complex interactions between turbulence and TECs cannot be adequately resolved by simulation without taking spatial coherency into consideration (Clark et al., 2015a).

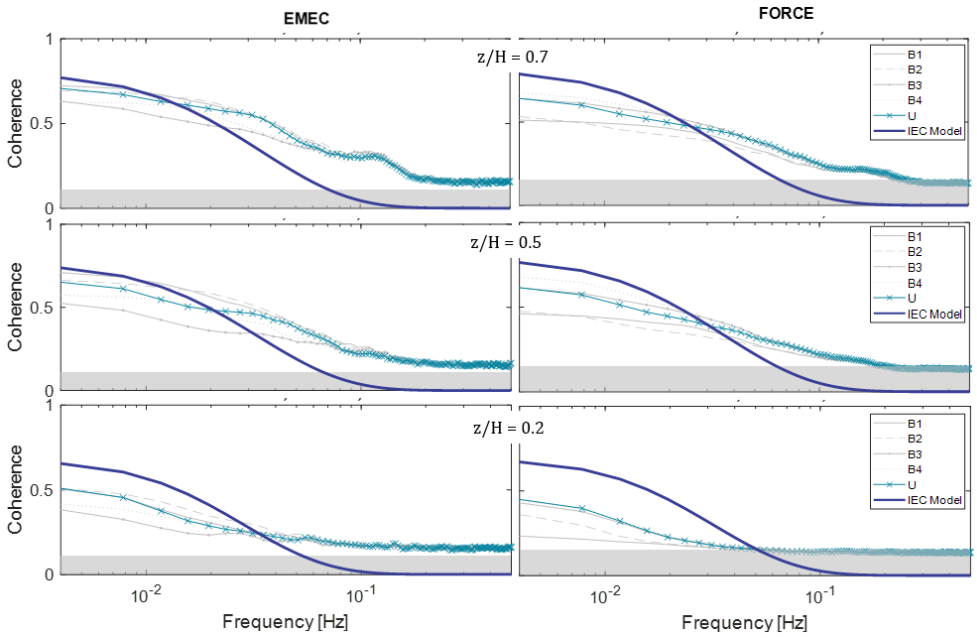

Figure 6.7: Measured coherence compared to the general IEC coherence model for flood cycles with velocities 1-3 m/s. Shaded areas show the 95% confidence level for the measurements.

6.1.4 Shear, Standard Deviation and Isotropy Profiles

Shear Profile

In turbulence simulators e.g. TurbSim, the shear (mean velocity) profile model and standard deviation parameters are used to scale the flow field in the time domain (see Figure 2.5) . The recommended shear profile is a 1/7th-power-law model. From the four datasets analysed, all the measured flood profiles conform to a 1/5th- or a 1/6th-power-law model relatively well on the flood cycles (Figure 6.9), with the FORCE-1 and FORCE-2 datasets showing the closest fit.

In line with previous studies (Parkinson and Collier, 2016; Gunn and Stock-Williams, 2013; Greenwood et al., 2019; McNaughton et al., 2013), the EMEC-1 ebb cycle profile clearly deviates from the power-law model, with a three-fold increase in the sum squared error compared to the flood cycle.

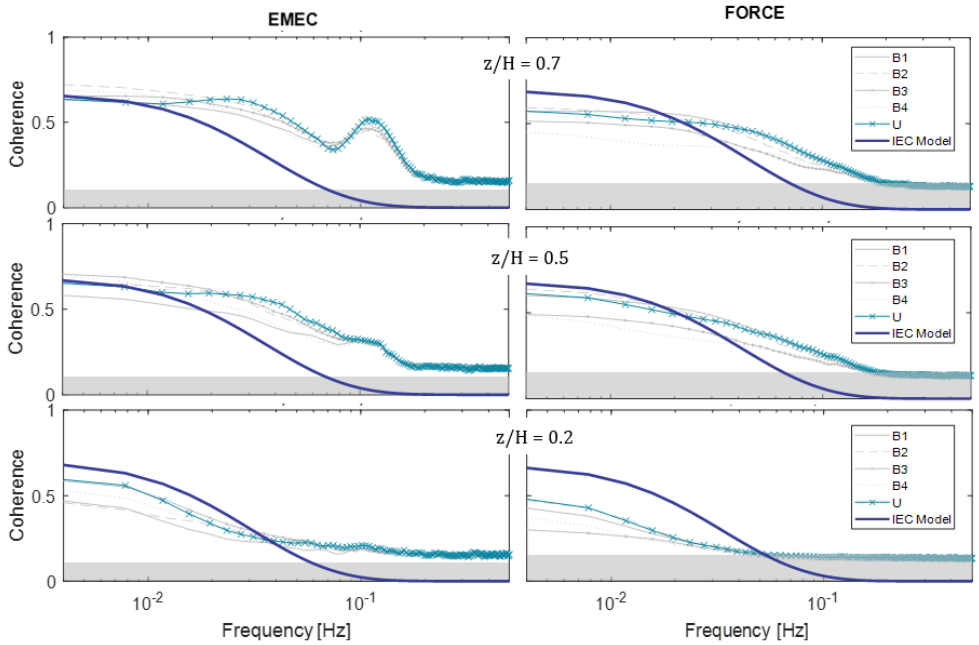

Figure 6.8: Measured coherence compared to the general IEC coherence model for ebb cycles, velocities 1-3 m/s. Shaded areas show the 95% confidence level for the measurements.

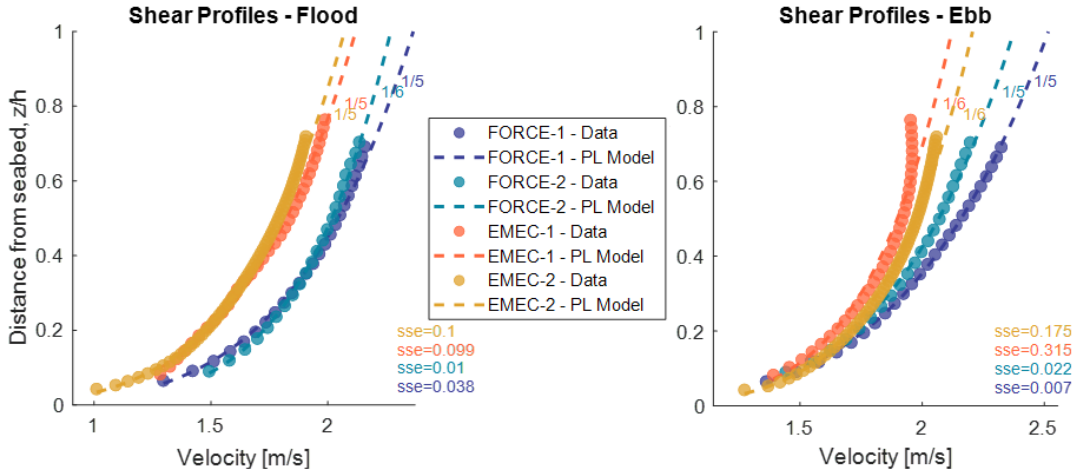

Figure 6.9: Measured shear profiles vs. Power Law model fit for velocities 1-3 m/s. The best-fit power-law exponents and sum squared errors (sse) are displayed for each case.

It is expected that shear profiles will have implications for turbine loading. A turbine's rotor will experience eccentric bending forces due to the non-uniform inflow velocity gradient. These forces may be transferred into the drive-train and may cause damage to components like bearings and seals (Nevalainen et al., 2016). It can also mean that the hub height velocity (typically taken as the reference velocity) is not representative of the average across the rotor disk.

Standard Deviation Profiles and Anisotropy

The turbulence intensity profiles across all locations are very similar on the flood tides, especially in the upper part of the water column (Figure 6.10). The EMEC-1 profile deviates from the rest below $z/H = 0.4$; this is likely due to bathymetry-driven turbulence, also seen in the TKE profiles. The EMEC-2 profiles deviate in the upper part of the water column across all parameters due to significant wave presence. The anisotropy ratios are also very similar for all sites, especially in the lower half of the water column, with the EMEC-2 location showing the most isotropic ratio.

The Tidal Bladed turbulence module represents the turbulent-flow field with a constant TKE profile, which clearly does not accord with these site measurements. The impacts on load modelling when using a realistic TKE profile rather than a constant value are not known but may result in different estimates of loads.

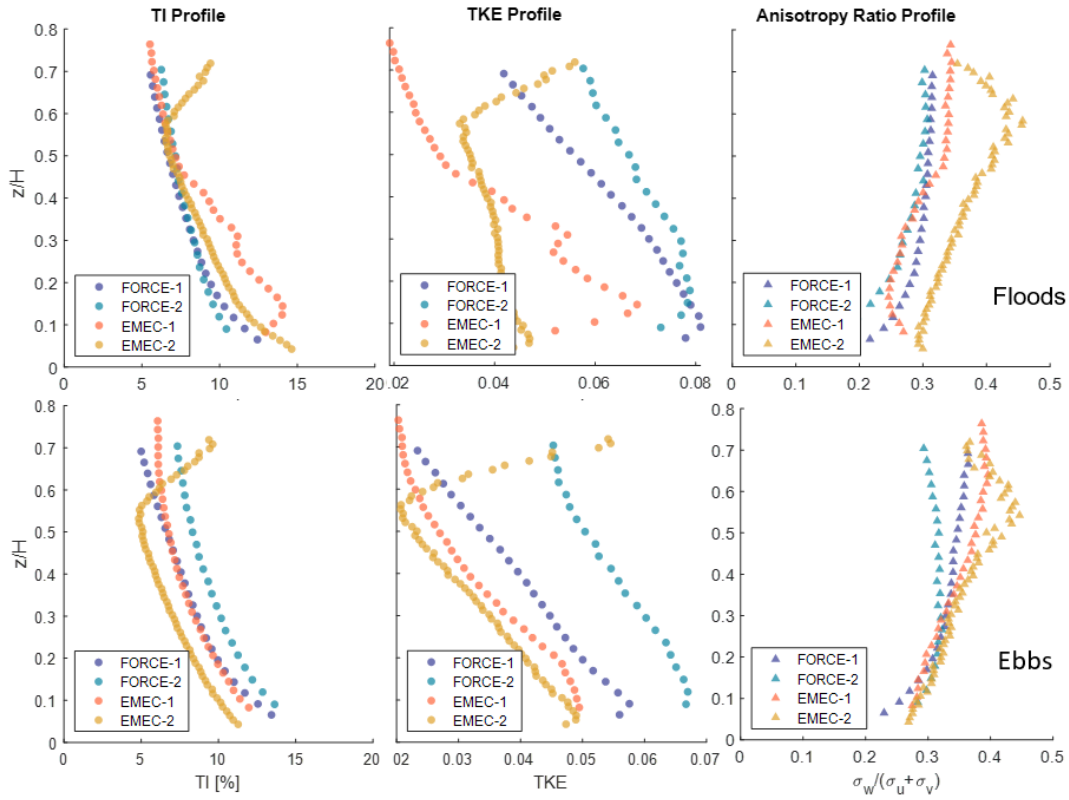

Figure 6.10: Total turbulence intensity, TKE and anisotropy ratios for all measurement sites for flood (top row) and ebb (bottom row) tides with flows 1–3 m/s.

The measured anisotropy ratio profiles (Figure 6.10) are similar to those reported in other studies, where α increases from 0.2 near the seabed to 0.4 near the surface (Vermeulen et al., 2011). The EMEC-1 site shows the highest ratios overall, suggesting the turbulence is more isotropic. When using the von Kármán model, the flow is assumed to be isotropic, i.e., the anisotropy ratio (Equation (2.14)) is equal to 0.5. This is clearly not the case for any of the site measurements in this study, in particular near the seabed.

Overall, the measurements from the two FORCE locations showed more uniformity between flood and ebb cycles, and between each other, in particular in terms of the shear profiles, turbulence intensity and TKE. They also showed a closer fit to the theoretical length-scale profile in the lower part of the water column. On the contrary, the coherence for large scale fluctuations was found to be much lower than the model predicts. The EMEC measurements showed a significant variation between floods and ebbs and also between the two nearby measurement locations. This is likely driven by the more complex bathymetry and a more confined channel with a number of headlands and islands closer to the measurements locations than the FORCE locations. These differences highlight the high variability in the turbulence conditions across different tidal channels but also within a particular site, and hence the importance of getting measurements from specific locations of interest.

6.2 Real-Sea Turbulence - Intermittency

This section presents the comparisons of Fourier and wavelet methods, followed by the time-frequency analysis using wavelets. The effects of non-stationarity in the flow due to intermittent, turbulence bursts and the suitability of the traditional Fourier method are discussed.

6.2.1 Stationarity

The stationarity of the data sample was assessed by evaluating the convergence of the variance of the along-beam velocities, for a range of averaging periods. Unlike data from tank experiments such as in (Sutherland et al., 2017), some samples do not exhibit stationarity, with the standard deviation continuing to change as the averaging time increases, see Figure 6.11.

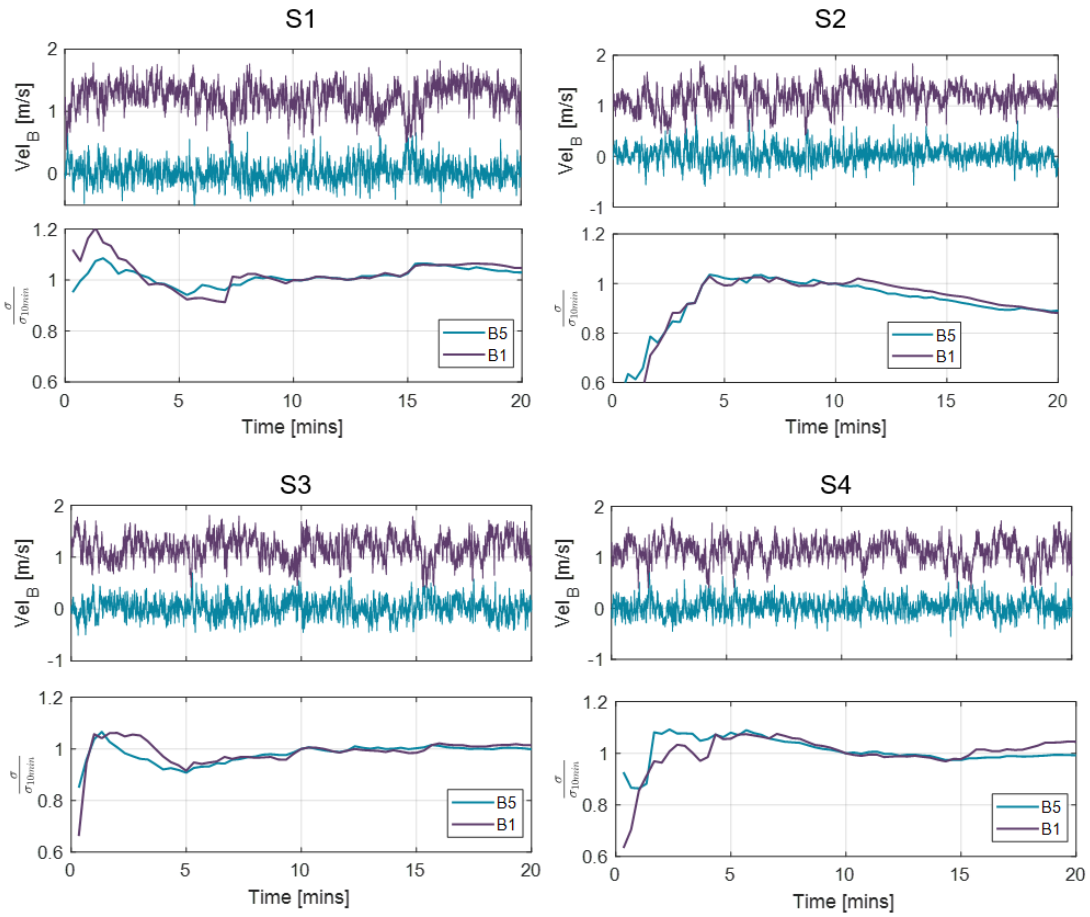

Figure 6.11: Time series (top) and convergence (bottom) of the standard deviations σ (normalised by the 10 min standard deviation σ_{10min}) of along-beam velocities for the inclined (B1) and vertical (B5) beams at an elevation from seabed, $z = 18m$ for four short samples $S1 - S4$. The convergence plot shows cumulative statistics for the increasing averaging time shown on the x-axis.

It is also clear that the stationarity time of 5 minutes, frequently assumed for turbulence analysis (Clark et al., 2015a), is not applicable in any of the samples analysed. In samples $S1$ and $S3$ stationarity is observed around 10 minutes however in other samples it is not. The non-stationarity of real turbulent flows suggests that methods such as Fourier analysis (which require stationary time series) may not be totally applicable.

6.2.2 Fourier and wavelet comparison

A comparison of the Fourier and wavelet analysis results are presented to test the application of wavelets.

For context, turbulence frequencies which are important for device fatigue loads are marked on all the spectral analysis results. The cut-off frequency representing turbulent length-scale equivalent to 3 rotor diameters (60m for the present case study) and a mean current velocity $\overline{U}$ = 3m/s is determined using Equation 5.16, giving a frequency $f_{60m} = 0.05$Hz. The BPF is based on an assumed rotational speed of 12 rpm, giving 0.2Hz.

The average energy spectrum was calculated for a 10-minute velocity sample (first 10 minutes of $S4$) using wavelet and Fourier analysis. A 10-minute interval is considered suitable to capture the relevant turbulent scales (IEC, 2013). To compare the two methods, instantaneous wavelet spectra were time-averaged to give a global spectrum. Figure 6.12 shows that the global wavelet spectrum has arbitrary scaling but once scaled using Equations 2.9 and 2.10, the wavelet and Fourier magnitudes are in close agreement, with the wavelet spectrum appearing as a smoothed version of the Fourier spectrum as described in (Dynamique et al., 1995).

The variances calculated from the time series data and from integrals of the PSDs are highlighted at the bottom of the plots in Figure 6.12. In all presented cases, the Fourier spectrum variances agree relatively well with the calculated variance for the vertical beam, but show significant deviation for the slanted beam. The inertial sub-range - a linear region with a -5/3 slope (Pope, 2000) is visible for both methods, albeit obscured by the instrument noise at higher frequencies.

Both the Fourier spectrum in Figure 6.12 and Fourier coherence in Figure 6.14 exhibit windowing effects for the inclined beam - the aliasing of low-frequency components that do not fall within the frequency range of the window, characterised by a sharp tail at the low frequencies. This effect is not seen in the wavelet spectra and coherence.

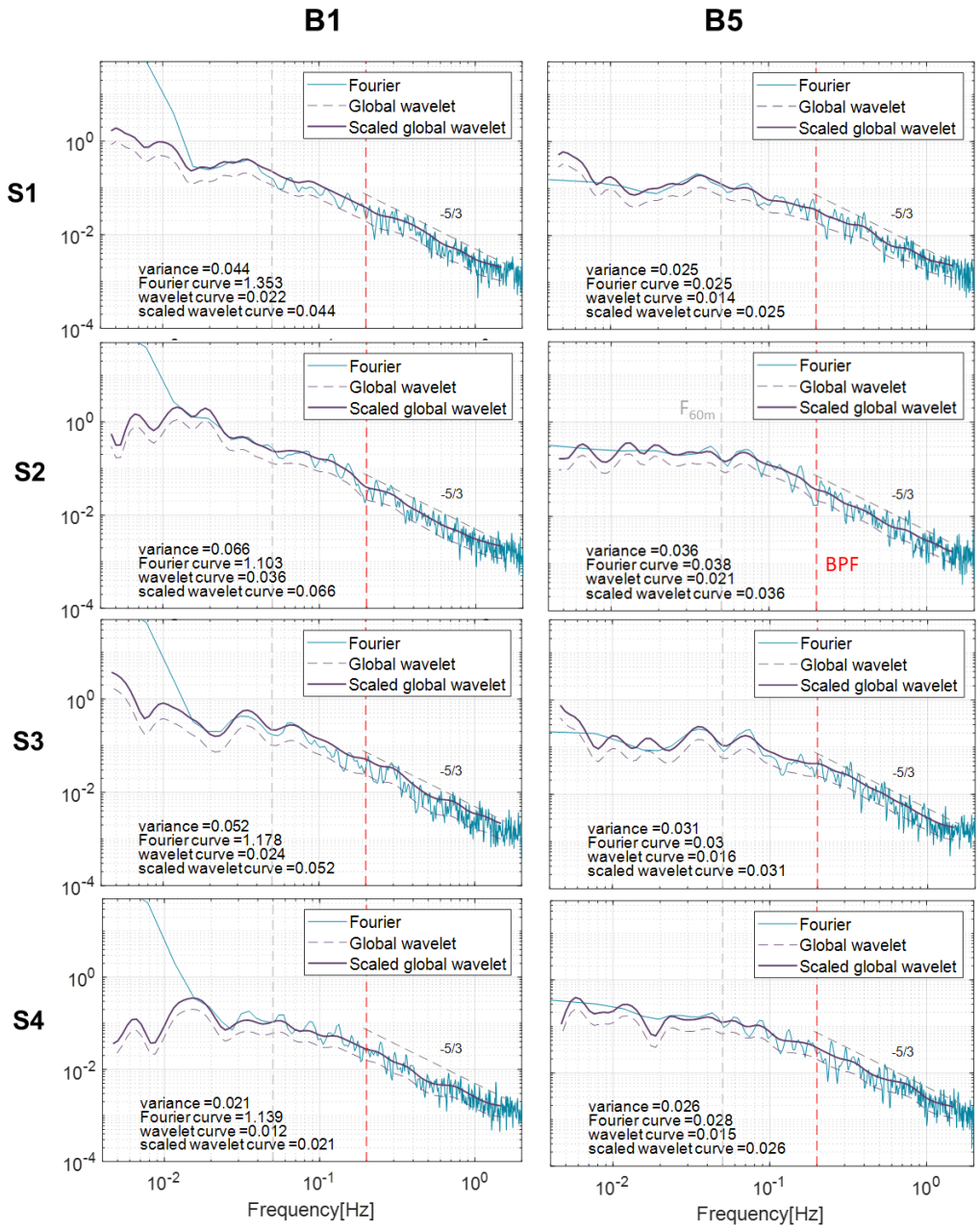

Figure 6.12: Power spectral density (PSD) obtained using Fourier and wavelet methods. B1 is the slanted beam and B5 is the vertical beam. Measurements were taken for bottom-fixed TEC hub height, z =18m. Variances were calculated from the time series and by integrating the PSD curves. BPF = Blade passing frequency, f_{60m} = frequency representing 60 m length-scale. The time samples $S1 - S4$ are shown in Figure 5.5

The advantage of using ADCP data, compared to point measurements as has been done in previous studies, is that turbulence spectral characteristics can be studied throughout the water column. Figure 6.13 shows the averaged spectra obtained by both methods throughout the water depth. The two methods show a similar result, with higher turbulence energy closer to the seabed. Similar to the results in Figure 6.12, the wavelet spectra appear as a smoothed version of the Fourier.

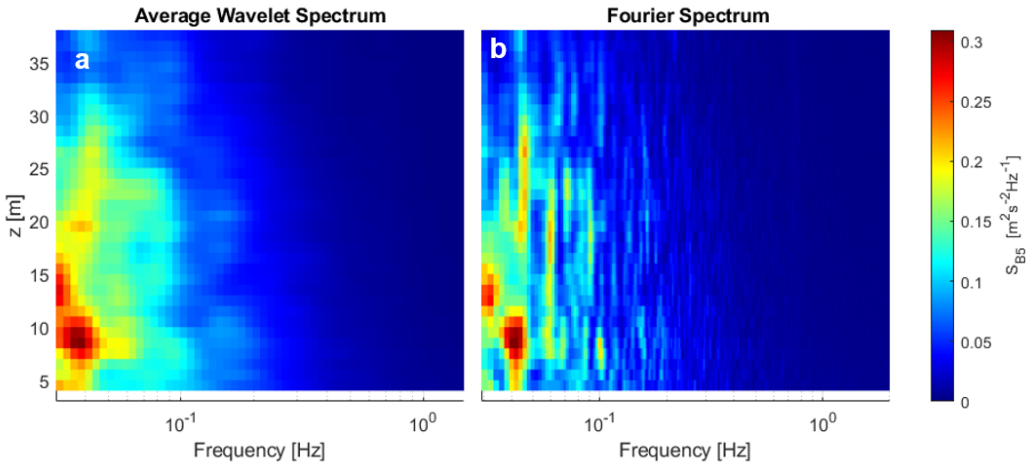

Figure 6.13: Isosurface of the time-averaged wavelet PSD (a) and Fourier PSD (b).

Coherence was calculated using both Fourier and wavelet analysis for the same 10-minute data extract, between two depths z=18m and z=28m, see Equation 2.24. This spatial separation represents the coherence across the top half of the rotor for a seabed-mounted device (Figure 5.11). To compare the two methods, instantaneous wavelet coherence was time-averaged to give a global coherence curve.

Results from both methods (Figure 6.14) show higher coherence at lower frequencies with the wavelet coherence appearing as a smoothed version of the Fourier coherence, where magnitudes agree. The wavelet coherence tends towards a higher confidence level (due to a different number of degrees of freedom in coherence calculation) resulting in a higher discrepancy between the methods at high frequencies. There is more variation between methods in coherence than in spectra. Some samples show a good agreement between the methods e.g. $S1 - B1$ or $S4 - B5$. There are significant differences at the lower frequencies, which again may be due to windowing effects in the Fourier coherence.

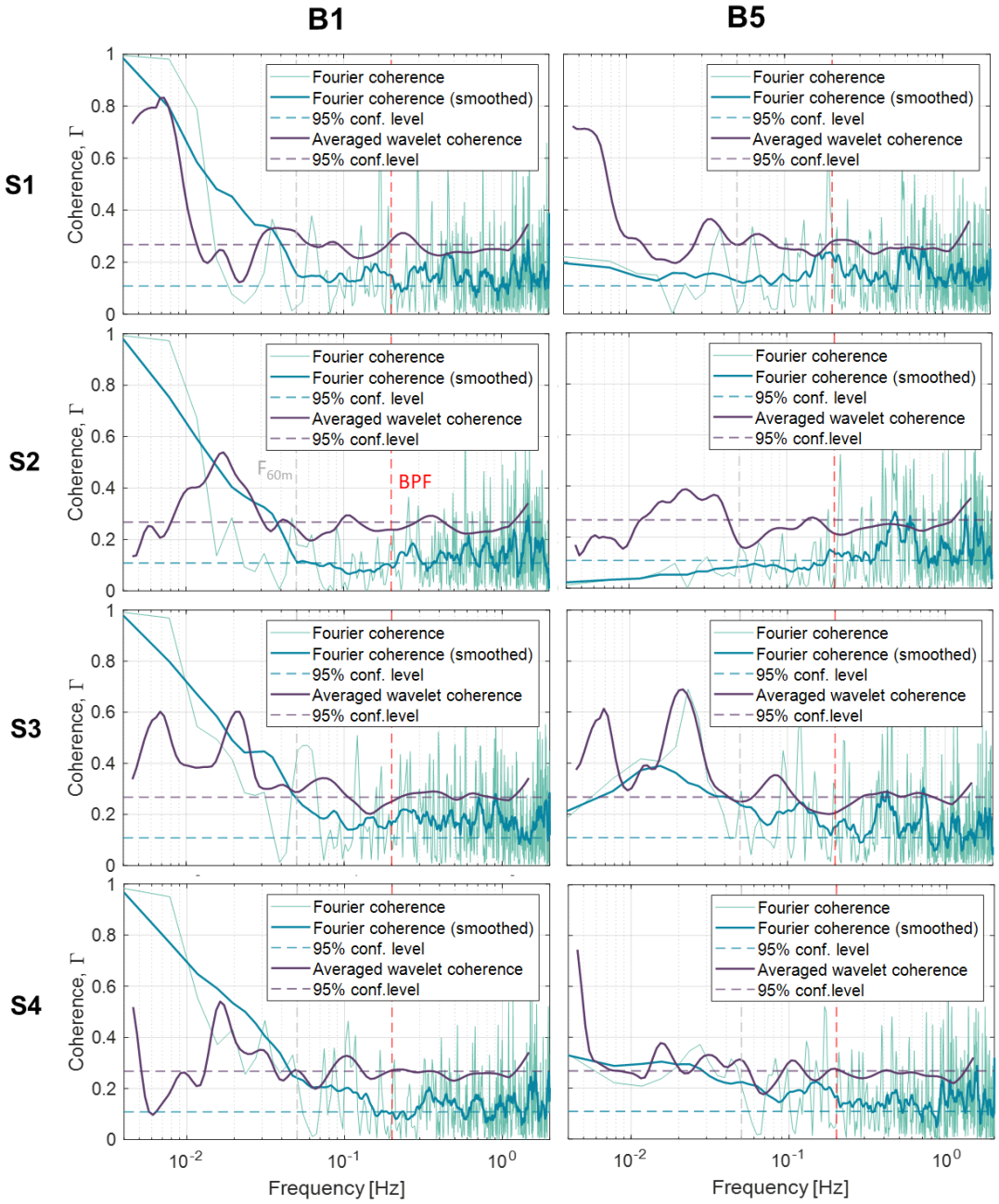

Figure 6.14: Comparison of the averaged wavelet coherence and Fourier coherence calculated for a 10minute velocity sample. B1 is the slanted beam facing into the flow, B5 is the vertical beam. The coherence is measured between two points at z = 18m and z = 28m, see Figure 5.11, representing the spatial correlation across half a rotor span of a seabed mounted turbine

Overall the averaged wavelet spectra agree well with the Fourier results, suggesting that this method is appropriate for analysing ADCP turbulence data. Coherence shows more discrepancy, however it unclear whether this is due the Fourier windowing effects or other factors. The main utility of wavelets is the time-frequency analysis, which is presented in the following section.

6.2.3 Time-frequency analysis

Wavelet time-frequency analysis can be used to study the instantaneous spectra and coherence, allowing to detect the presence of intermittent coherent bursts. A 20-minute data interval (sample $S4$) was used for instantaneous analysis to observe how the instantaneous turbulence spectra change over time.

Instantaneous turbulence spectrum

The instantaneous turbulence spectrum shown in Figure 6.15 (a) reveals intermittent, energetic fluctuations, which can persist for up to several minutes depending on the frequency.

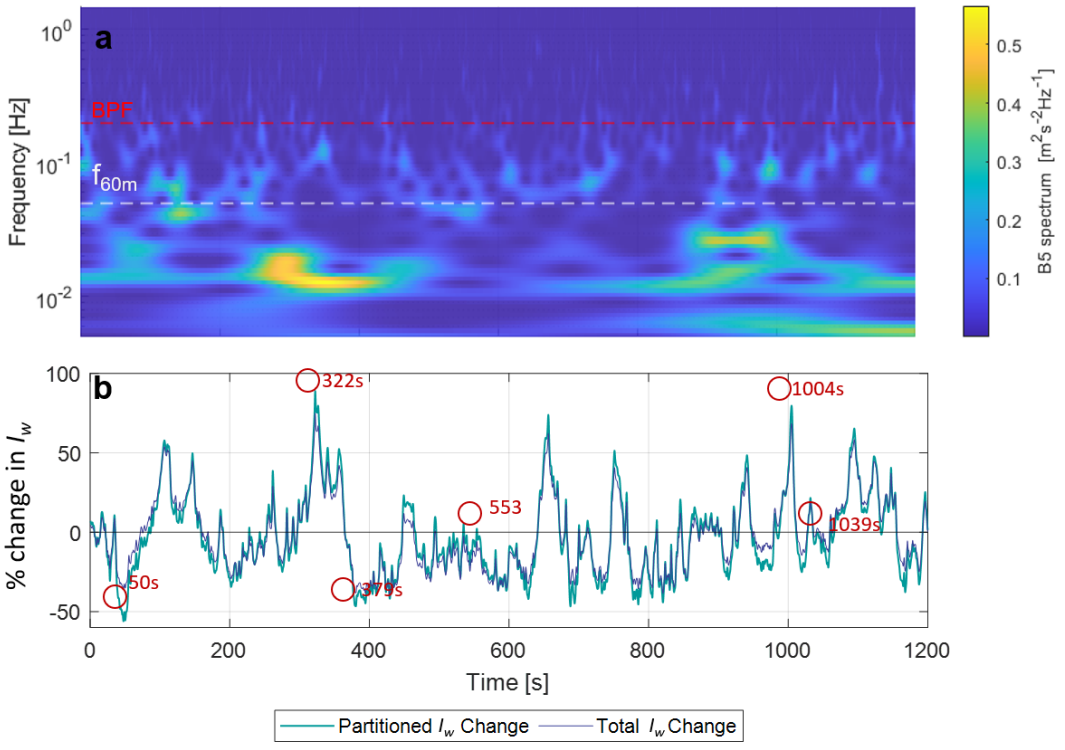

Figure 6.15: Top panel (a) - instantaneous wavelet spectra calculated for the 20-minute data sample ($S4$) for the vertical beam, B5 velocities at z =18m. Panel (b) - instantaneous turbulence intensity I_w as a % change of the average I_w. The time markers show the time instants presented in Figure 6.16.

To quantify these instantaneous bursts, the instantaneous vertical turbulence intensity I_w is calculated using the area under the PSD spectra and Equation 2.3. Figure 6.15 (b) shows the instantaneous I_w as a percentage of the 20-minute average. The total I_w is calculated using the whole spectrum and the partitioned I_w is based on a band of frequencies which are the most relevant to TEC fatigue loads (0.05Hz - 2Hz). Figure 6.15 (b) shows that the I_w peaks can be up to 80% higher than the average I_w. This is important because typically, device designers would use the average values for load calculations. These findings show that the instantaneous fluctuations can be much higher but are not represented well by averages due to their intermittency.

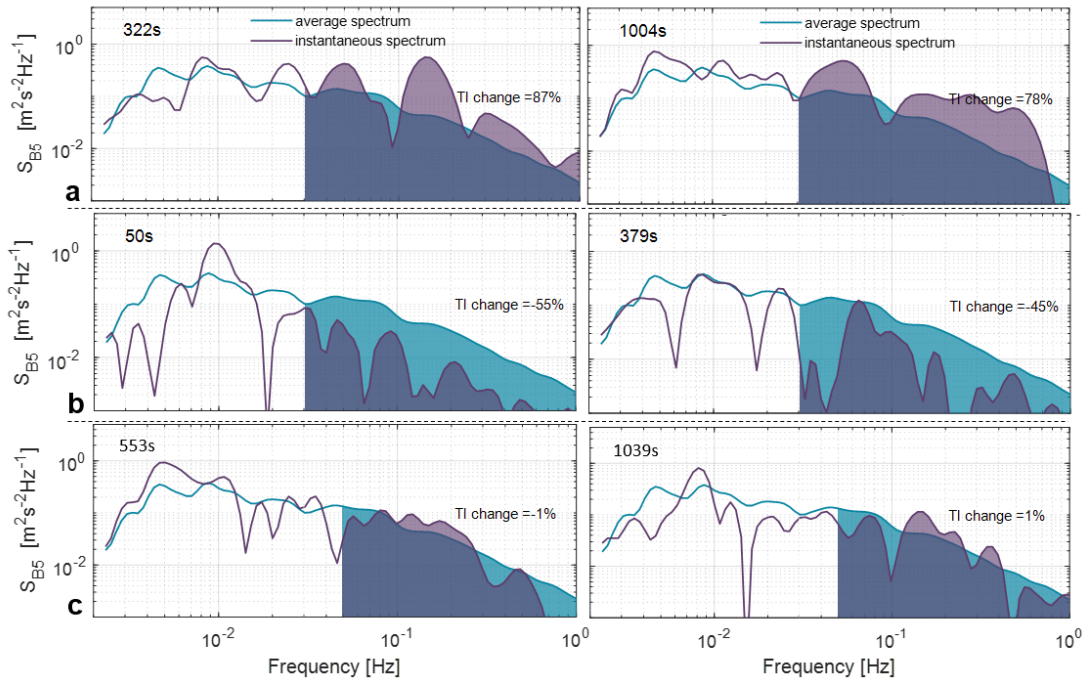

Figure 6.16: Average and instantaneous spectra at time intervals shown in Figure 6.15. The shaded parts show the area used in calculation of the partitioned variance and turbulence intensity changes. Row (a) shows examples where instantaneous I_w is significantly higher than average, (b) shows where instantaneous I_w is lower than average and (c) shows where there is no significant change.

The results presented in Figure 6.15 are for the vertical beam measurements and hence demonstrate variability in the vertical velocity components. Streamwise oriented, inclined beams (B1 and B3) were also analysed in the same way and the bursts were found to peak to similar levels 60-85%. Additionally, the partitioned turbulence intensity (which is based on the most damaging TEC frequencies) deviates slightly more from the average than the one based on all frequencies, Figure 6.15 (b).

Figure 6.16 shows how the instantaneous spectra compare to the average for the selected time instants. These demonstrate that the bursts occur across a range of frequencies, and in particular at the most damaging frequencies ($f_{60m} = 0.05Hz$) which contribute the most to fatigue loads.

Spatial coherence

Instantaneous wavelet coherence is compared to the Fourier coherence in Figure 6.17. The very large coherent structures (f <0.01Hz) persist for longer, occupying a large part of the timeline, whereas smaller structures tend to be more intermittent with durations ranging from several minutes to several seconds. Between the two marked frequencies, the average coherence line mostly sits below the 95% confidence level (region highlighted in red on Figure 6.17) , whereas the instantaneous view shows that there are frequent coherent bursts within these bands. This reflects the intermittent nature of real turbulent flows and highlights the limitations of using methods which yield average parameters, such as Fourier analysis, which tend to obscure the intermittent features.

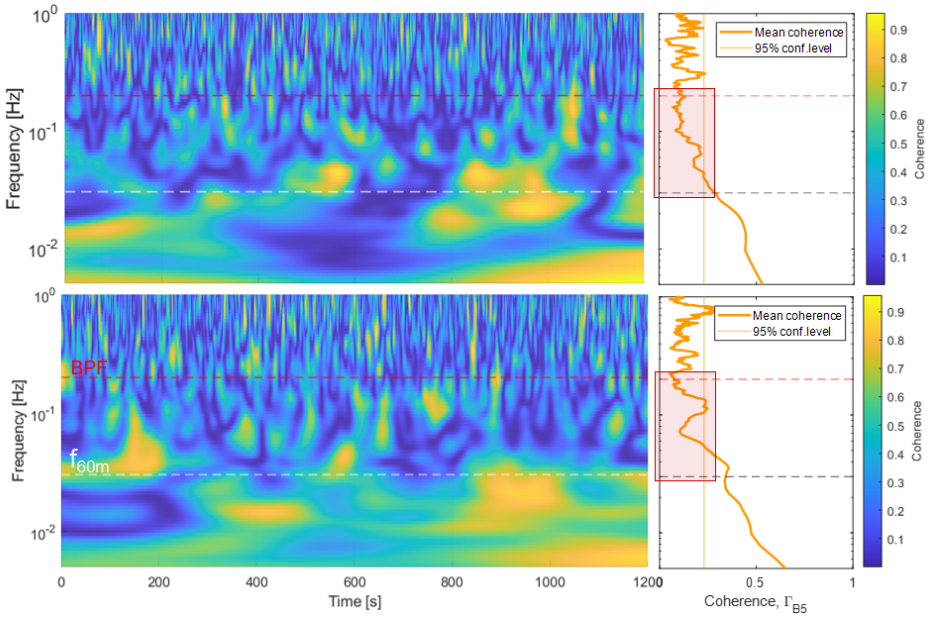

Figure 6.17: Instantaneous coherence for the vertical beam (B5) compared to the average coherence obtained by Fourier analysis. Coherence was calculated for a 10m separation distance for the bottom half of the rotor for the floating (a) and bottom mounted (b) cases as shown in Figure 5.11.

In addition to identifying the passing of coherent structures in time, spatial analysis can be used to understand the position and extent of such structures throughout the water column. Utilising the profiling capabilities of ADCPs, the spatial variation of coherence along the vertical beam is presented in Figure 6.18 for a single time instant at 1004 seconds.

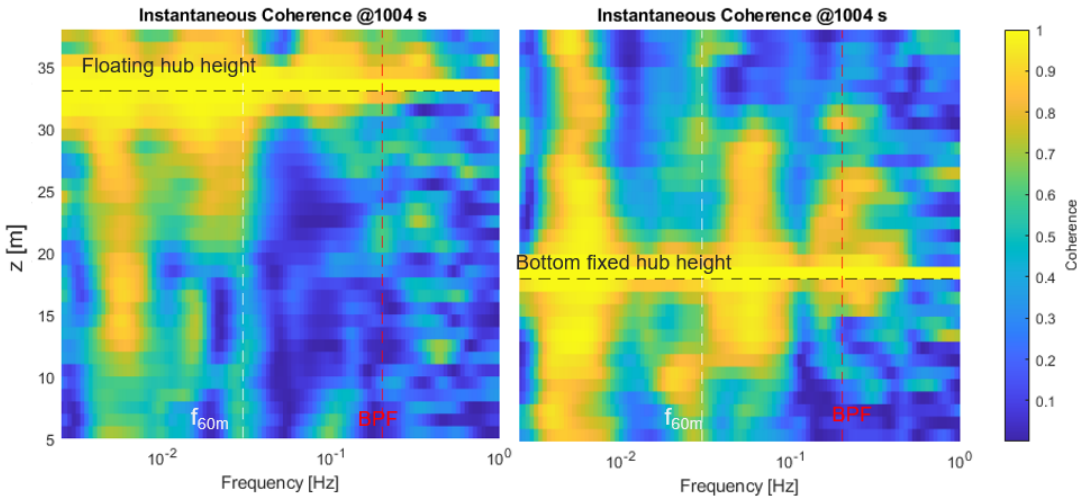

Figure 6.18: Instantaneous wavelet coherence at 1004 seconds showing spatial correlation along the vertical beam, B5. The hub heights refer to the two case studies presented in Figure 5.11

Figure 6.18 shows that coherent structures tend to reside in fairly discrete frequency bands as described by Kelley et al. (2005). Coherency depends on the frequency analysed as well as on the separation distance. This is clearly visible in Figure 6.18 , where larger scale structures ($f < 0.01$Hz) extend across most of the water column, whereas smallest scales show only a weak coherence across 2-3 meters.

The large scale structures are unlikely to have a fatigue load impact on the TEC rotor as they occupy the whole water column and last for several minutes. These bursts will likely be experienced as a change of mean flow, and are unlikely to contribute to high frequency fatigue loading.

In the bottom-fixed TEC case (Figure 6.18), the structures near the f_{60m} frequency occupy a spatial region similar to the rotor size i.e. approximately 20m. Energetic bursts at the rotational frequency are likely to be amplified and result in significant load peaks.

Application of wavelet analysis to carry out such spatial analysis over time, for example by counting the occurrence and durations of coherent structures in key positions, will help to better understand the turbulence loads that will be experienced by a TEC.

It must be noted that as the turbulent flow field approaches the rotor, the blockage will result in the distortion of the flow field. In a study by (Milne and Graham, 2019), the authors found that depending on the operating velocity and length scales, the blockage can result in an attenuation of the low-frequency spectral components or can lead to an amplification of these

components. Such distortion would change the position of coherent structures and affect the intermittency of the flow. This should be taken into account when carrying out predictions of unsteady loading of turbine blades using undisturbed turbulence as the input boundary condition (Milne and Graham, 2019).

PART II

Turbulence - Device Load Interactions.

Chapter 7

Part II Summary

In this part of the thesis, turbulence-device interactions are investigated using BEM modeling as well as field measurements of a full-scale TEC. The sensitivities of simulated loads to varying ranges of turbulence input parameters in a BEM model are explored. In Part 1, it was demonstrated that semi-empirical turbulence models do not always represent real-sea turbulence. Part 2 puts this into context by demonstrating the resulting variation in loads, when unrepresentative turbulence parameters are used in simulations. The field measurements of a full-scale, operational floating TEC offer a rare opportunity to study the load response to real-sea conditions. Effects of the leg shadow, waves and turbulence are explored to understand the most critical considerations for design.

Modelling Sensitivity Study Highlights

- From the five turbulence parameters tested, turbulence intensity was found to have the highest sensitivity to fatigue loads with up to 90% change in loads for the range tested(2-24%).
- Varying length-scales between 2-80m showed a 49% variation in fatigue loads and a coherent flow field increased loads by 45%.
- Shear profiles had a small impact on thrust but did significantly affect blade-bending (16%) and hub-bending (30%), with the 1/4th power law profile generally resulting in the highest loads.

Field Measurements Highlights

- During the measurement period at this site, wave presence was found to have only a modest impact with DELs increasing by up to 10% due to waves.
- Stochastic fluctuations contribute a larger portion to the total DELs than the periodic, even in the presence of significant leg shadow effects.
- The loads respond to a range of turbulence scales, including those much larger than the rotor.
- When the rated velocity is exceeded, the load response changes due to blade pitching, with evidence of de-coupling of load and turbulence spectra.

Chapter 8

Methodology

8.1 Modelling

Two models are used to simulate turbulence-induced loads: TurbSim, which is used to define the sea-state, and Tidal Bladed, which simulates the operation and performance of the tidal turbine. The detailed principles of operation and model theory are provided in Section 2.4. This section describes the configuration of the models as well as the user input parameters.

8.1.1 Tidal Bladed

Software Overview

The commercially available design code Tidal Bladed from DNV (DNV, 2022) is an integrated software package for tidal turbine performance and loading calculations. It is an adaptation of Bladed for wind turbines and has undergone its own experimental validation program (Milne et al., 2010). Tidal Bladed uses blade element momentum theory to model the hydrodynamic forces on the blades, requiring a data set giving the aerofoil shape and twist angle at a number of stations along the blade, and coefficients of lift and drag. These blade design parameters for the O2 TEC model were provided by and are proprietary to Orbital Marine Power Ltd. Corrections to the classical BEM model account for a finite number of blades, and describe the effect of the tip vortex on the induced velocities. Tidal Bladed accounts for the tip losses by means of Prandtl correction factor. The formulation also includes corrections for flow blockage, dynamic inflow/wake model and stall models (Khairuzzaman, 2016). These models are discussed in more detail in Section 2.4.

Turbine details

The TEC used in the investigation was based on Orbital's floating O2 tidal turbine, illustrated in Figure 8.1. A simplified geometry was used, with each leg of the device holding a 2-bladed 20m rotor. The turbine and simulation set-up are summarised in Table 8.1. Wave and platform motion aspects were intentionally excluded for simplicity. Although the tests were carried out for a floating device model, the simulation results are equally applicable to seabed turbines. All tests were run in power production mode, which means the power production control characteristics apply.

The developed power and mechanical loading in flows exceeding the rated velocity are usually regulated to prevent the turbine from becoming overloaded. In this case, the device aims to maintain a constant rotational speed by controlling its blade pitch angle to suit the changing incoming velocity. Up to rated velocity, torque control is implemented to follow the optimum torque-speed curve and maximise the power coefficient C_p. When the rated velocity is exceeded, the torque is shed by pitching the blades.

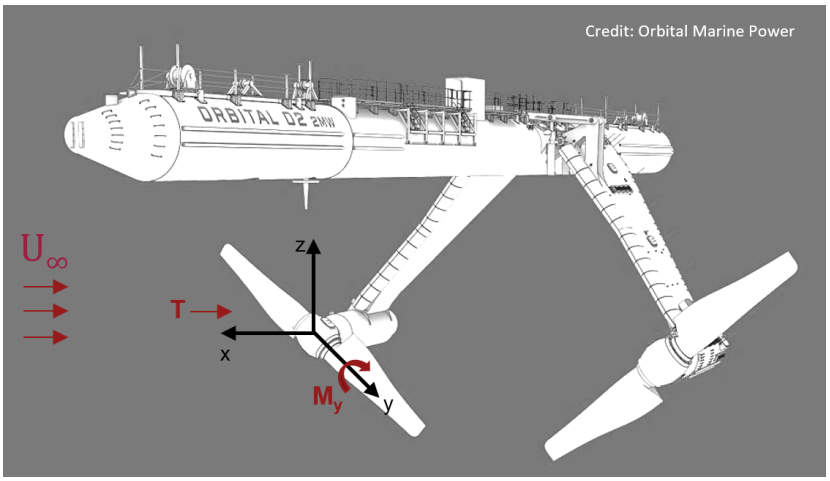

Figure 8.1: Visualisation of the floating tidal turbine used in Tidal Bladed simulations with representations of the flap-wise root bending moment, M_y and thrust T forces.

No. of rotors	2
Rotor size	20m
No. of blades	2
Control system	Pitch Control, Variable Speed
Simulation Mode	Power Production
Simulation time	600s
Time step	10Hz

Table 8.1: Tidal Bladed simulation parameters summary.

8.1.2 TurbSim

Although Tidal Bladed can be used to generate turbulent flow fields, here TurbSim (NREL, 2021) was preferred. TurbSim is an open-source turbulence simulator developed by NREL. The flow field generation functions by the same principles as Tidal Bladed but allows more flexibility to vary turbulence parameters. TurbSim enables the addition of user input length-scale, standard deviation and shear profiles as well as varying coherence. It can output the flow fields as *Bladed-Style Full-Field Files*, which are compatible with Tidal Bladed (Jonkman and Kilcher, 2012).

The principles of generating a 3-D turbulent flow field are based on the spectral method (Veers, 1988), in which separate velocity time series are computed for several points across the rotor plane. Each point has predefined single-point spectral characteristics and each pair of points has predefined coherence characteristics (Milne et al., 2010). The time series are scaled according to the mean velocity, which varies with depth according to the specified shear profile and turbulence intensity. This is illustrated in Figure 2.5. The detailed principles of operation are described in Section 2.4

The three-dimensional flow-field files contain instantaneous u, v, w velocities and were processed (as described in Section 8.2) to check that the desired turbulence parameters were achieved. The resulting flow field files were then used as inputs to Tidal Bladed simulations.

8.2 Flowfield Specification

Figure 2.5 summarises the inputs required for generating a turbulent flow field in TurbSim. The key parameters which define the flow characteristics, and which were used in the sensitivity study are listed below:

- turbulence intensity
- length-scales
- shear profile
- standard deviation profile
- coherence

The tests are designed so that only one parameter is varied at a time, keeping all other characteristics the same. Each of these parameters and the ranges applied during tests are described in this section.

Test 1: Turbulence Intensity

The streamwise turbulence intensity, I_u is defined in Equation 2.4. A range of $I_u = 2 - 24\%$ in increments of 2% was tested. This was sufficient to cover the range of intensities reported in the literature (and those found in Part 1 of this work), which vary from $5 - 20\%$ (Thiébaut et al., 2020a,c; Perez et al., 2020) across different tidal sites (Table 3.1). The other parameters were held constant with a length-scale $L = 10$m, $1/7$th power law shear profile and a uniform standard deviation profile. A user-defined von Kármán model was specified because in Part 1 it was found that the stream-wise spectra at two tidal sites were better represented by this model (Figure 6.5). A general coherence model was also applied to ensure the spatial correlation of parameters. For the tests where other parameters were varied, I_u was held constant at 10%.

Test 2: Length-scales

Length-scales (L) were computed by the auto-correlation method (Equation 2.12), which measures the duration for which the largest eddies remain correlated and assumes Taylor's Frozen Field hypothesis (Schlipf et al., 2010).

Length-scales will vary by site and bathymetry; Thiébaut et al. (2020a) found L to be 2-3 times the local water depth at Alderny Race, Walter et al. (2011) observed L several orders of magnitude greater than the depth at Elkhorn Slough estuary, and Milne et al. (2013) reported scales of approximately 1/3 of the channel depth at the Sound of Islay.

Length-scales and turbulence intensity are invariably linked. To ensure the test ranges represent realistic flows, they are checked against measurements reported in Part 1. Turbulence conditions from the two test sites, Fundy Ocean Research Center for Energy (FORCE) and European Marine Energy Centre (EMEC) were found to have a broad range of length-scales

and turbulence intensities (presented in Figure 8.2). Across the four different measurement locations at the two sites, the length-scales can vary between $1-100$m for I_u range of $\approx 2-20\%$, although most of the points were concentrated below $I_u = 15\%$. Based on these measurements, the input length-scales were varied between $2-100$m.

For all length-scales, the generated flow turbulence intensity was held constant at 10%, and the rest of the parameters were the same as in Test 1. Although the specified range of length-scales was $2-100$m, the resulting flows had a slightly smaller range of $2-72$m. This is likely because the simulation time of 15 minutes is too short to capture the largest scales at some velocities. For all other tests, where other parameters were varied, L_u was held constant at 10m.

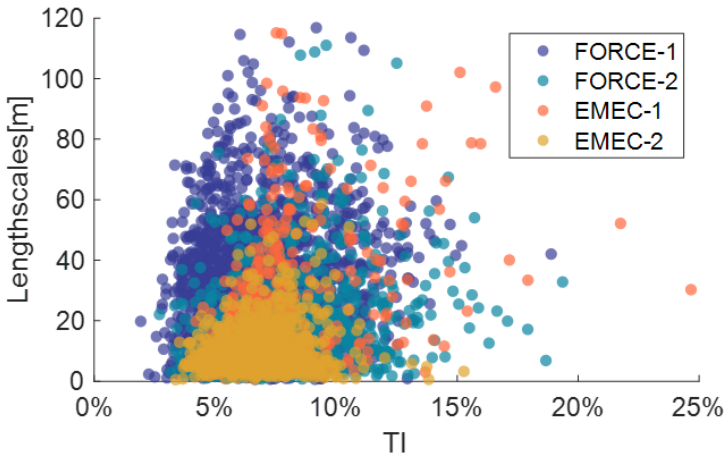

Figure 8.2: Stream-wise length-scales and total turbulence intensity measurements from Fundy Ocean Research Centre for Energy (FORCE) and European Marine Energy centre (EMEC) tidal test sites.

Test 3: Shear profiles

According to the DNV-ST-0.164: Tidal turbines standard (DNV, 2015), if site measurements are not available, the current velocity should be modeled according to power law in Equation 2.13, where the exponent β is taken as $1/7$.

Investigations from various tidal sites often report that the real shear profiles can deviate from this law. A number of studies (Parkinson and Collier, 2016; Gunn and Stock-Williams, 2013; Greenwood et al., 2019; McNaughton et al., 2013), found the shear profiles at EMEC's Fall of Warness tidal site had two distinct profile shapes, one logarithmic and one approximately polynomial. In Part 1, even when the profiles at the two sites were found to follow a power law, it often wasn't a 1/7th power law (see Figure 6.9). Togneri and Masters (2016) analysed the velocity profiles at Ramsey Sound (Wales, UK) and reported that during ebb tides they followed the power law throughout the water depth, however, during flood tides the bottom

half of the profile was logarithmic, with the upper half showing a uniform profile. Based on the findings from these studies, the test shear profiles were chosen as 1/4th, 1/7th and 1/9th power law, polynomial and uniform. For all other tests, where other parameters were varied, a 1/7th power law shear profile was applied.

Test 4: Standard deviation profile

Although standard deviation σ_u is expected to vary with depth, models such as Tidal Bladed assume a uniform σ_u profile throughout the water column, normally scaling the turbulence according to the hub height values only (Jonkman and Kilcher, 2012; Khairuzzaman, 2016). The measured σ_u profiles presented in Part 1 (Figure 6.10) appeared approximately linear. Closer analysis of the EMEC-1 dataset shows that for both ebb and flood cycles a linear fit has a lower error than the logarithmic fit, see Figure 8.3. During flood cycles, there is evidence of energetic eddies near the seabed, distorting the profile and resulting in a poor fit. Based on these measurements, two profiles were generated for testing - uniform and linear. The rotor average σ_u was held equal for both profiles to ensure only the effect of the profile shape is investigated. In all the other tests, the default uniform standard deviation profile was applied.

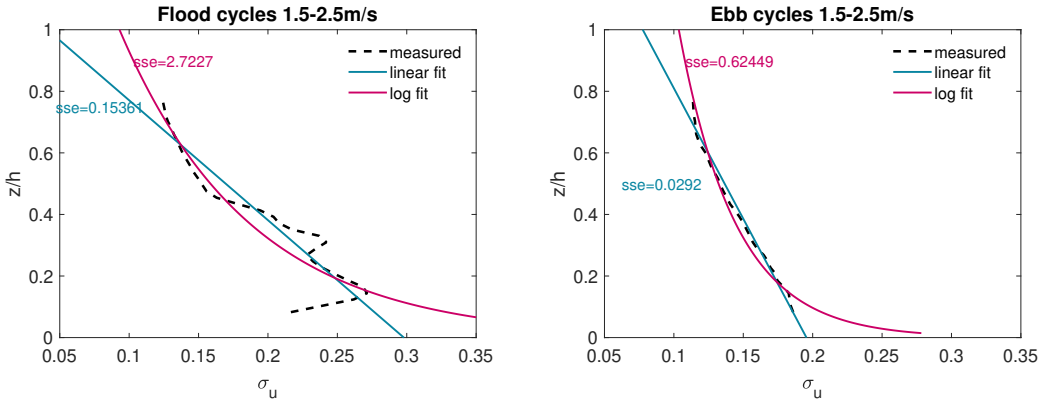

Figure 8.3: Standard deviation profiles for Fall of Warness, EMEC-1 data set with linear and logarithmic fits. Sum squared errors (sse) are also shown for each fit.

Test 5: Spatial coherence

Spatial coherence describes the correlation of the streamwise fluctuations across a separation distance, r, at each distinct frequency. The IEC 61400-1 (IEC, 2019a) wind standard describes an empirical model of stream-wise coherence, which can be used alongside the Kaimal or von Kármán model spectra. Tidal Bladed and TurbSim codes both use this IEC coherence model, it is a function of frequency f, velocity $\overline{U}$, length scales L_u and separation distance Δr and is defined by Equation 2.24.

Rather than varying the coherence model parameters, this test simply included flows with and without coherence to establish whether this has a notable impact on the loads. For all other tests, coherency was always switched on.

8.2.1 Test Matrix

Table 8.2 summarises the five tests described in this Section. Each test was conducted for different incoming velocities; cut-in, $0.75\times$rated velocity, rated-velocity (where the turbine starts to exceed rated) and $1.25\times$ rated velocity. All simulations were 10 minutes long (length-scale tests were extended to 15 minutes) with a time resolution of 10Hz. For each test case, 30 flow iterations were produced. TurbSim randomizes the occurrence and scaling of coherent events. Simulations that generate coherent turbulence time series have up to 10 degrees of stochastic freedom. The random phases associated with each frequency at each grid point and velocity component are designed to represent the expected variability in real flows. Because of the degree of variability, using 30 or more different random seeds for a specific set of conditions is recommended (Jonkman and Kilcher, 2012). In total, 3720 simulations were completed.

Mean flow	Length scales	TI	Shear Profile	SD Profile	Coherence
>rated (1.25 x rated)	2-100m	2-24%	1/4th 1/7th 1/10th polynomial uniform	uniform realistic	on off
rated	2-100m	2-24%	1/4th 1/7th 1/10th polynomial uniform	uniform realistic	on off
mid (0.75 x rated)	2-100m	2-24%	1/4th 1/7th 1/10th polynomial uniform	uniform realistic	on off
cut-in	2-100m	2-24%	1/4th 1/7th 1/10th polynomial uniform	uniform realistic	on off

Table 8.2: Summary of the input turbulence parameter ranges tested for four different incoming velocity scenarios.

8.3 Field Measurements

This section describes the measurement campaign for obtaining full-scale, operational TEC loads as well as flow and turbulence measurements. The subject of this study is Orbital's O2 device, which has been operating at EMEC's Fall of Warness test site since July 2021. The 2 MW turbine comprises of a 72 m long floating superstructure, supporting two 1 MW turbines on either side. The retractable legs hold the nacelles at a 14 m depth and the 20 m diameter rotors span an area of 600 sqm. The rotors can be brought up above the water line for onsite access and maintenance. A modular gravity-based anchoring system holds the mooring lines used to anchor the O2 (Orbital, 2022b).

8.3.1 Instrumentation

Strain Sensors

Strain measurements were carried out with a Fibre Bragg Grating (FBG) optical strain sensors, mounted within the turbine blade material. FBG is an optical sensor recorded within the core of a standard optical fibre. It reflects a narrow bandwidth of light, which responds to changes in temperature and strain. The sensors were bonded to the composite laminate, in line with the blade coordinate system, as recommended by IEC TS 62600-3:2020 (IEC, 2020). This allowed measurement of the flapwise M_y and edgewise M_x blade bending moments, 0.9m from the root connection. Optical sensors are scanned at a fixed rate by the interrogator, streaming values at 10Hz to the turbine control system.

The sensors were calibrated in air. The blades were mounted to the turbine with the rotor and pitch systems locked and lumped masses were used to apply known loading to the blade tip to complete a part load calibration. This was done at a low load level of approximately 10-15% of the operating load. To obtain values of flapwise M_y and edgewise M_x, calibration constants were calculated from the known bending moment and average strain response at the sensor during the hold period in each direction.

Flow Sensors

To capture the mean current flow, two downward-facing ADCPs (D-ADCP) are mounted on the TEC hull on the bow and stern. Both the D-ADCPs are 4-beam, Teledyne Workhorse 600, configured to sample at 1Hz with 0.5m vertical bin resolution (Figure 8.4).

In addition, a sideways-mounted Nortek Signature 500 ADCP (S-ADCP) is fixed to the back of one turbine leg. This has 5 beams and was set up to sample at 4Hz, with horizontal bins of 0.5m. With such configuration, the central (5th) beam (Figure 2.1) was aligned with the flow, directly measuring the streamwise velocity component, the other beams were affected by reflections from the surface or interference with the moorings and hence were not used.

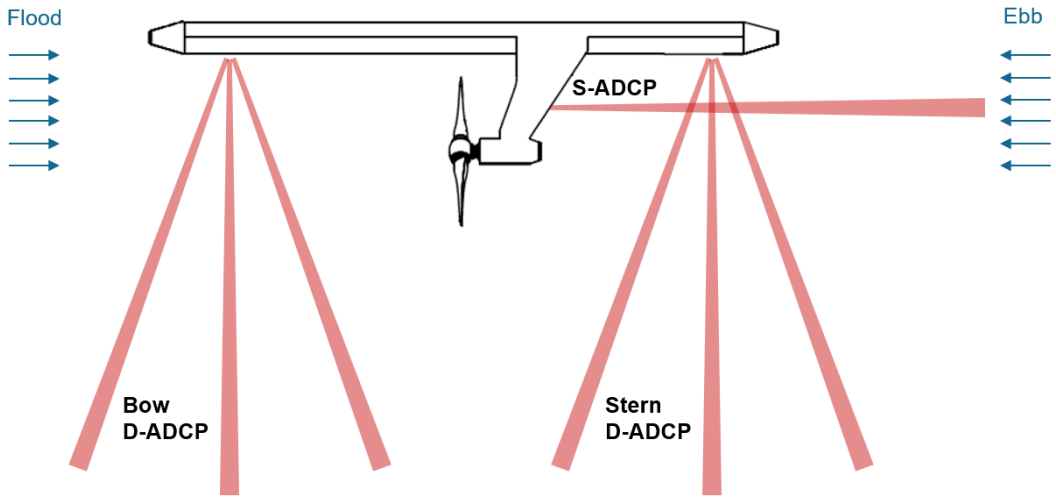

Figure 8.4: Position of instruments for capturing flow data. S-ADCP is a sideways-mounted ADCP and D-ADCPs are downward-facing ADCPs. Only the central (5th) beam on the S-ADCP is shown.

8.3.2 Data Capture and Processing

The data available for analysis covered the period between 1 August 2022 and 30 September 2022 as shown in Figure 8.5.

The D-ADCP beam velocities at rotor hub height were resolved to provide the current magnitude, with the bow and stern D-ADCPs providing the flood and ebb measurements respectively, to avoid interference and flow disturbance by the rotor. No QC was carried out on the data as only the high-level mean flow was required.

The high-resolution (4Hz) flow data from the S-ADCP was available for a 4-day period (12-15 August). Figure 8.4 shows that on the ebb tides, S-ADCP is measuring undisturbed flow, however, during the flood tides the would be affected by the rotor wake. This means only the ebb data is suitable for analysis. The raw S-ADCP data was QC'd following the steps outlined in the Quality Assurance and Quality Control of Real-Time Oceanographic data (QARTOD) standard (IOOS, 2019).

Inspection of the S-ADCP data revealed interference with the mooring lines at a certain distance away from the sensor, during times of generation. To determine a suitable horizontal bin for the S-ADCP data, a number of tidal cycles during turbine generation were compared to similar magnitude cycles when the turbine is not generating. and the distance at which the flow matched the undisturbed flow (i.e. not affected by blockage or interference) was identified. All further analysis was carried out for these bins only.

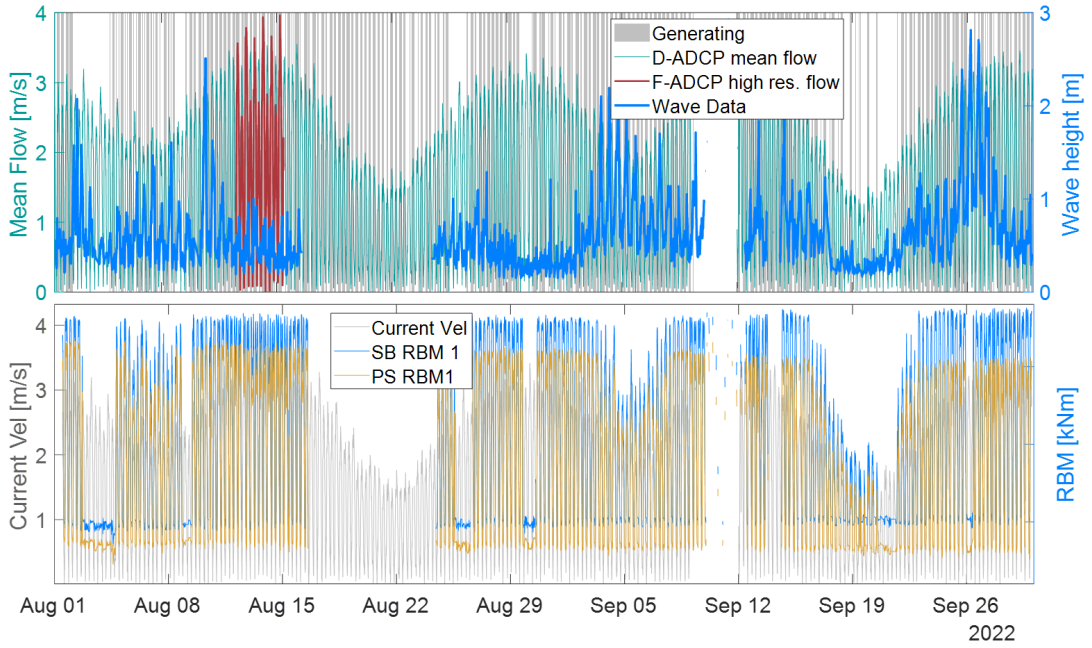

Figure 8.5: Overview of the available data set showing periods of generating and available flow, load and wave data.

The effects of interference were also evident in the velocity spectra, see Figure 8.6. Spectral analysis also revealed that during S-ADCP data collection period, there was frequent wave presence, identified by the spectral peaks around 0.1Hz (known to be the dominant wave frequency at this site).

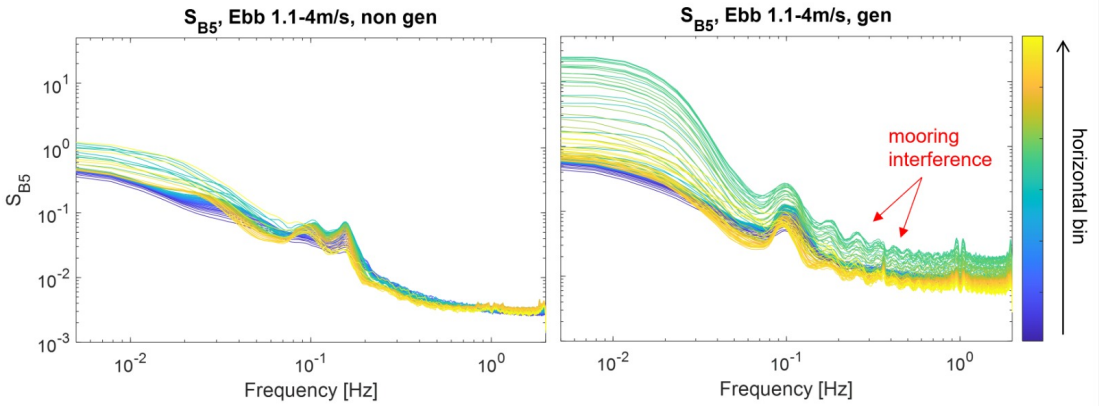

Figure 8.6: Velocity spectra of the S-ADCP measurements, averaged across all operational velocities for each horizontal bin. The spectra show spikes due to mooring interference and waves.

Figure 8.5 shows a consistent discrepancy between the portside (PS) and starboard (SB) load measurements, with PS root bending moment estimates shifted lower, and falling below the zero line. This is likely due to sensor calibrations and was adjusted by realigning the minimum to the zero line.

8.4 Load Analysis

The methods employed in calculating the load parameters from simulated and measured data are described in this section.

8.4.1 Simulated Loads

Tidal Bladed calculations of instantaneous power, thrust, torque and blade and hub bending moments were recorded at hub and blade points shown in Figure 8.7. The approaching velocity vector was also sampled at the flow check locations shown in Figure 8.7 to validate the flow fields against those generated in TurbSim and ensure the flow fields are compatible.

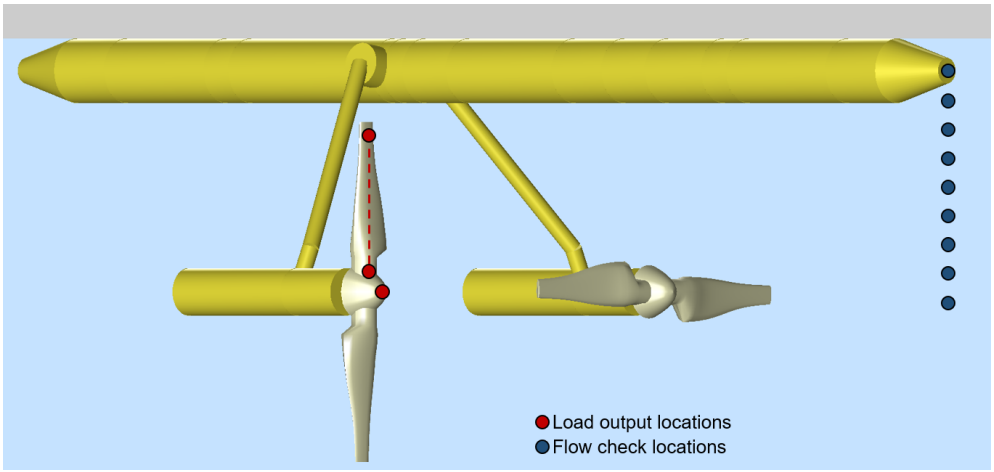

Figure 8.7: Rendered image of the simplified TEC geometry used in the Tidal Bladed model.

Simulations were 10 minutes long for all sensitivity studies apart from the length-scale tests, where the simulation time was extended to 15 minutes to capture the largest scales. Temporal resolution for all tests was set to 10Hz.

The device loads are described in terms of thrust (T) and flap-wise blade root bending moment (M_y) averages and standard deviations (see Figure 8.1), as well as damage equivalent loads (DEL). The flap-wise bending moment is the main contributor to the structural stresses at the blade root (Ouro and Stoesser, 2019) and hence the only bending moment considered. For the shear and standard deviation profile tests an additional hub-bending (HB) parameter was also considered. All the parameters (except DELs) were calculated within Tidal Bladed, details of the model algorithm are available in the Tidal Bladed Theory Manual (Khairuzzaman, 2016). Typically, loads would be described in terms of their coefficient C_T, C_{M_y}etc., which give the actual forces normalised by the total energy/force available in the flow. However, in this case, the relative effects of varying turbulence parameters are of interest so all the resulting forces are normalised by the maximum values in the test set, meaning that loads and load coefficients would yield the same result.

Fatigue Load

The damage equivalent load is calculated using Equation 2.19. Parameter m was based on the typical material properties of composites and assigned a value of 12. MATLAB function `rainflow`, which returns cycle counts for load time histories, according to the ASTME 1049 standard (MathWorks, 2022b), was used to perform rainflow counting.

Only short-term DELs are reported because of the limited data available for analyzing fatigue. As such, the results from the field test data may not be directly extrapolated to lifetime fatigue.

Load Spectrum

The most important frequencies for quantifying the blade loads are likely to range from those corresponding to the integral length-scales, up to those which are equivalent to the blade passing frequency (Milne et al., 2010). Turbulence slicing can be a substantial source of loading since it can contribute to the periodic loads, making them greater than those due to the support structure alone.

Load spectra are determined by applying the MATLAB function `pwelch` to each 10-minute load time series. This function uses the fast Fourier transform (fft) algorithm. The time series is divided into segments and a 50% overlap is applied using a Hamming window. The resulting spectra are averaged to obtain the power spectral density (PSD) estimate (MathWorks, 2022c). The turbulence spectra were determined the same way by applying the function to the instantaneous velocity time series.

8.4.2 Analysis of Measured Loads

Blade bending moment (M_y, M_x) measurements were obtained from the optical strain sensors integrated into the blades. The M_y values were used to estimate the rotor thrust (T) by:

$$T = \frac{M_y}{x_c} \tag{8.1}$$

where x_c is the theoretical distance along the blade that represents the hydrodynamic force's action center. The rotational speed, azimuth position of the blade and generated power (P) parameters were also available, all captured at 10Hz.

As the turbine response is expected to be dependent on flow velocity and the turbine controller, each 10-minute time sample was binned by tidal cycle, flow velocity, wave presence and power generation.

Similar to the simulations, the device loads are described in terms of thrust (T) and flap-wise blade root bending moment (M_y) averages, standard deviations maximums and minimums, as well as damage equivalent loads (DEL).

Phase Averaged Loads

In order to investigate the impact of the angular position of the blades on the loads, M_y and T are binned by the instantaneous azimuth angle (in 1° intervals). Load values in each bin are then averaged to yield phase-averaged M_y and T, as in Payne et al. (2018). The leg passing is recorded at 0° however the legs of the O2 are angled 52° from the water surface so the data is rotated to represent the actual position of the leg and blades. The rotors are counter-rotating with a static coordinate system i.e. clockwise being recorded as positive. The effects of the leg shadow are analysed by calculating the percentage change of M_y and T loads at each position compared to normal loads - defined as loads at $\theta_{norm} = 90^\circ$ and $\theta_{norm} = 270^\circ$ from the vertical for PS and SB rotors respectively (see Figure 8.8). This is based on the assumption that the leg shadow, surface effects, and rotor interaction would have the least impact on the flow, and hence the load response, at these positions.

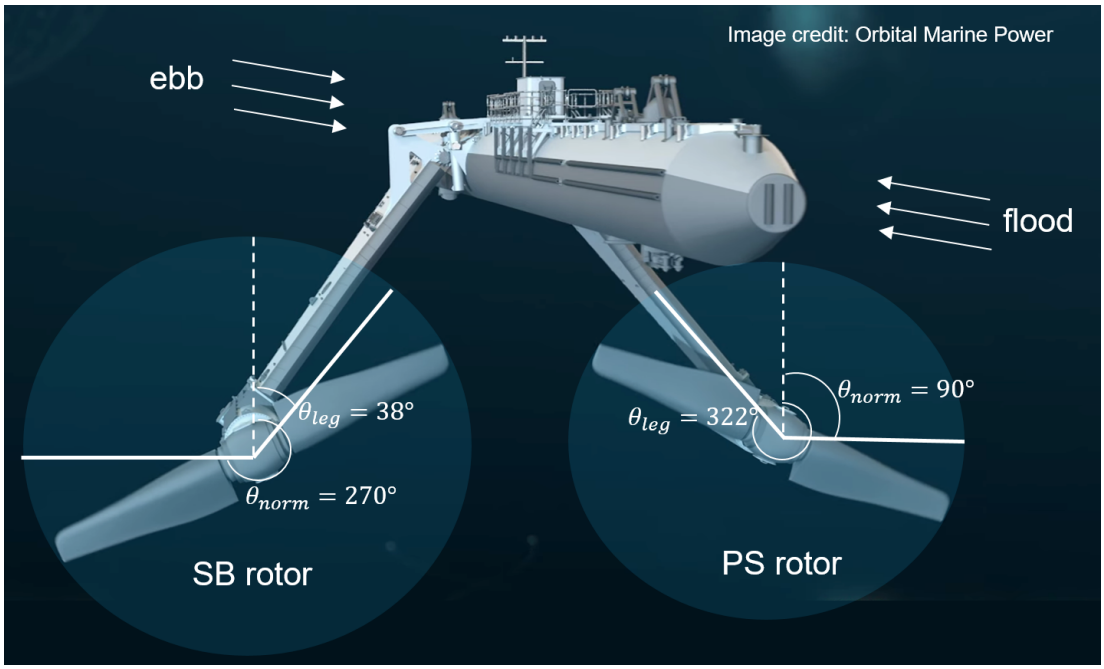

Figure 8.8: Diagram of the O2 TEC showing the angle of the leg, angular position of the blade for normalising loads (θ_{norm}) as well as tide directions.

Stochastic vs Periodic Loads

The load time series were separated into the cyclic (periodic) and the more random (stochastic) component, using the azimuth angle of the blade. The periodic component captures mean loadings that occur each revolution of the blade because of leg shadow, flow shear, and turbulence slicing. Stochastic loads are typically dependent on unsteady flow due to turbulence and waves. To identify the periodic loading, a method presented by Parkinson and Collier (2016) is applied. Load data from each 10-minute sample is binned by azimuth angle and

then averaged. This average is different for each azimuth angle, giving rise to a periodic load that depends on the blade position. The mean periodic load is subtracted from the original load time series, giving the stochastic component of loading. The separated time series are then used in further calculations to determine DEL and spectra as described below.

DEL and Spectra

For each 10-min sample, DEL was calculated using Equation 2.19 and load spectra were determined using methods described in Section 8.4.1. The spectra and DELs were then averaged according to the required velocity, wave and power generation ranges.

To determine instantaneous spectra using wavelets, the same steps were followed as described in Section 5.2.5. Time-averaged wavelet spectra had to be scaled in order to match the Fourier (Equations 2.9 and 2.10). To quantify the instantaneous bursts for both flow and load data, the areas under the instantaneous and mean spectral curves are computed. The area represents the total variance σ^2. To get the change in energy or turbulence intensity :

$$\left(\sqrt{\frac{\sigma^2_{inst}}{\sigma^2_{mean}}} - 1 \right) \times 100 \tag{8.2}$$

To compare the time series of the calculated turbulence and load burst time series, a correlation coefficient is computed using the MATLAB function `corrcoef` . This function returns the correlation coefficient of two random variables and is a measure of their linear dependence.

Chapter 9

Results & Discussion

9.1 Sensitivity Tests in Tidal Bladed

9.1.1 Sensitivity Test 1: Turbulence intensity

Input flow characteristics

Figure 9.1 shows the turbulence parameter profiles of the TurbSim generated flow fields for Test 1. As described in Section 8.2, all parameters other than turbulence intensity (and hence the standard deviation) were kept constant. Due to interactions between parameters within the model, some small variation in length-scales is present (hub height value varies between 9-10m), this is considered negligible compared to the variation in turbulence intensity.

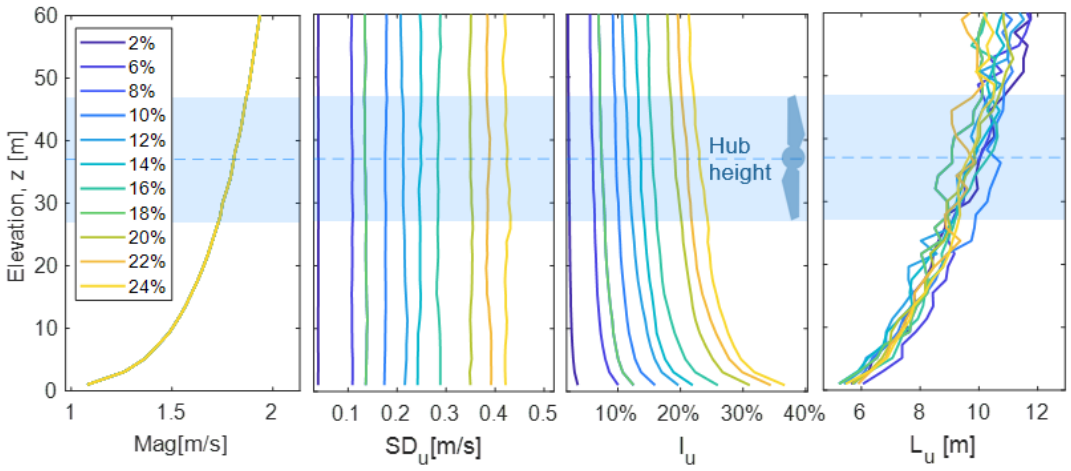

Figure 9.1: Left to right: shear, standard deviation σ_u, turbulence intensity I_u and length-scale L_u profiles of TurbSim flows for Test 1 - averaged over 30 flow iterations.

Load response

Turbulence intensity was the only test that demonstrated an impact on the mean load quantities. For operating velocities up to rated the most significant effect was seen on the mean electrical power (Figure 9.2), with approximately 17% difference between highest and lowest turbulence intensities. The changes in T and M_{yx} were less than 5%. For velocities exceeding rated, there was a pronounced change in μ_P, μ_T and $\mu_{M_{yx}}$, with significant drop off from $I_u = 10\%$ up to $I_u = 25\%$.

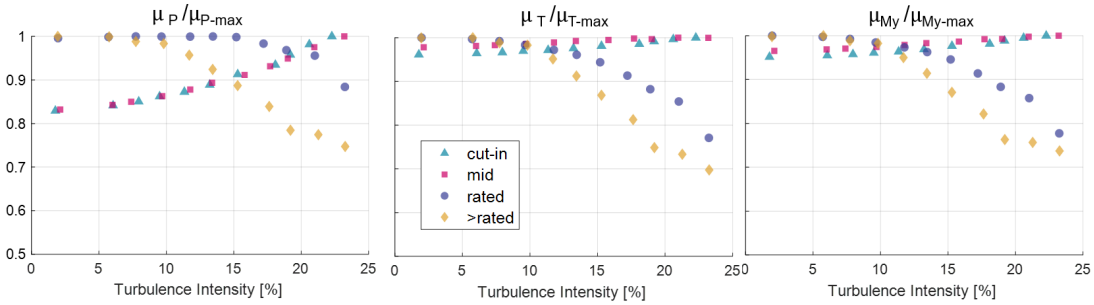

Figure 9.2: Turbine response results for Test 1 - turbulence intensity. Left to right, mean power μ_P, mean thrust μ_T and mean blade-root bending moment μ_{Myx}, all normalised by the highest value in the test set.

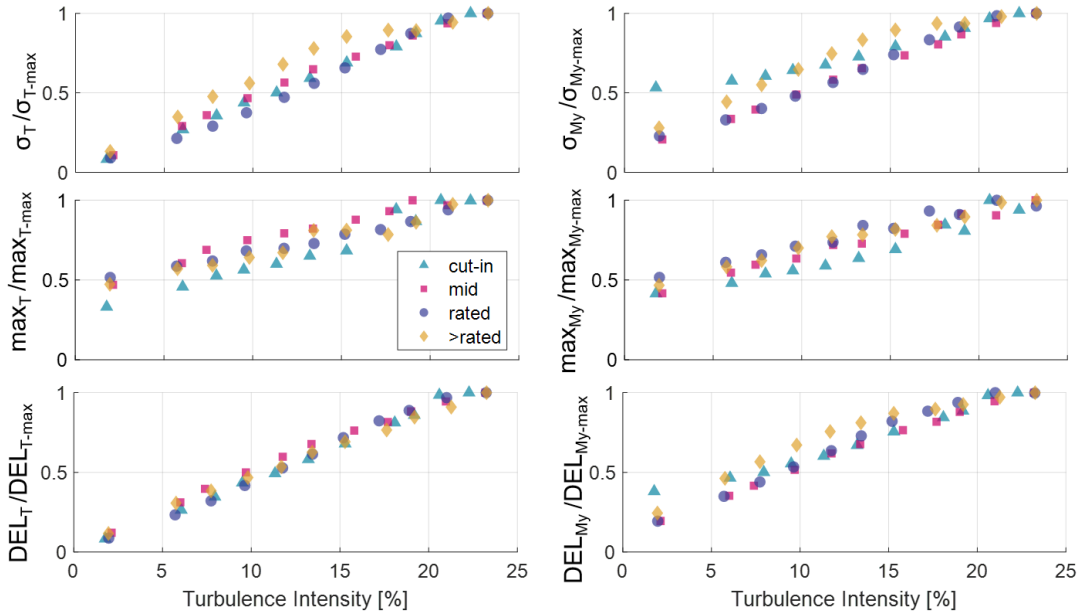

Figure 9.3: Turbine response results for Test 1 - turbulence intensity. Left column (top to bottom): thrust standard deviation σ_T, maximum max_T and DEL. Right column (top to bottom): blade root bending moment standard deviation σ_{M_y}, maximum max_{M_y} and DEL. All values are normalised by the highest value in the test set.

The σ_T, σ_{M_y} and DEL load parameters were all found to be highly sensitive to turbulence intensity (Figure 9.3). For most velocities, the relationship is approximately linear, showing $\approx 4\%$ increase for every additional 1% in I_u for σ_T,σ_{M_y} and DEL.

Spectral analysis of both the incoming flow field and loads presented in Figures (9.4a) & (9.4b) shows that there is a T peak at frequency equal to 2 $\times$ blade passing frequency ($2P$) for mid and rated velocities, with rated showing a more prominent peak as well as another peak at $4P$. Below rated velocities, the T spectrum follows the general shape of the turbulence spectrum in the lower frequencies. As rated velocity is exceeded, the blade pitch control system sheds forces and hence the load spectrum no longer reflects the flow spectrum.

Blade root bending moments in Figure (9.4c) & (9.4d) have acute peaks at $1P$ and $2P$. At higher turbulence intensities (e.g. $I_u = 18\%$), the peak at $2P$ is less pronounced. Similar to the T spectrum, M_y spectrum does not follow the turbulence curve above rated velocity.

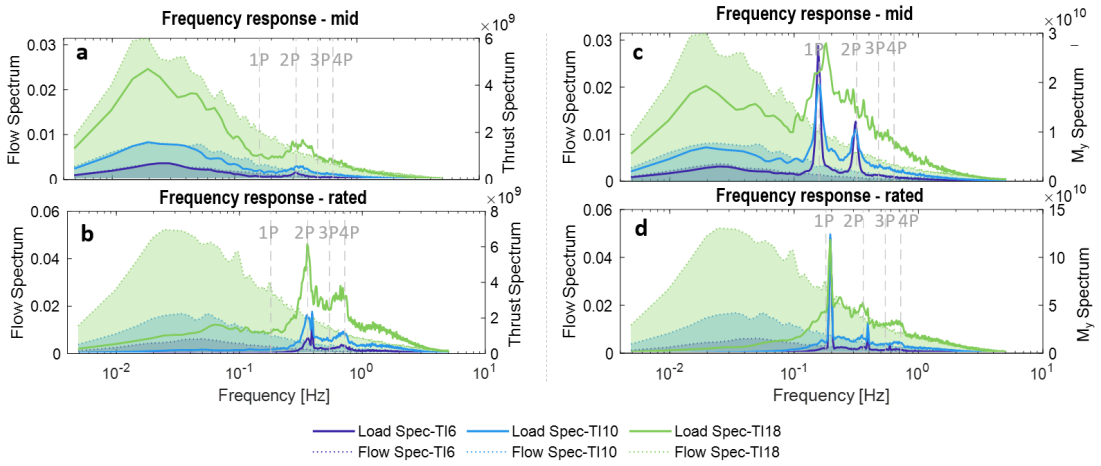

Figure 9.4: Spectral analysis of the thrust T response in panels (a) and (b) for mid and rated velocities respectively, and blade root bending moment M_y in panels (c) and (d) for Test 1. The shaded areas show the turbulence spectra (left axis), the bold lines show the corresponding load spectra (right axis).

Sellar and Sutherland (2016) showed that the presence of waves during turbulence measurements can more than double the I_u values, in particular near the top of the water column. In such a situation (with $I_u = 20\%$ rather than 10%), the $DELs$ could easily be overestimated by 40%, based on findings in this study. In Part 1 in Figure 5.10 it was shown that instrument misalignment to the flow direction of 20° could result in I_u errors up to 30% (i.e. $I_u = 13\%$ instead of 10%), in which case the DELs would be overestimated by around 12%. These examples highlight the significant errors that can result from the inaccurate classification of turbulence intensity in the flow due to inadequate measurement or processing techniques.

9.1.2 Sensitivity Test 2: Length-scales

Input flow characteristics

Figure 9.5 presents the properties of the flow-fields with specified length-scales ranging 2-100m. The largest length-scales are restricted by the simulation time, so where a 100m length-scale was specified the resulting $L = 72$m. This still gave a reasonable range of length scales to test. Although all other parameters were held constant as described in Test 1, there are some small variations due to the constraints of the model. The stream-wise standard deviation has a small variation of around $\approx$ 5% resulting in a range of TI values $\approx$ 10-11%.

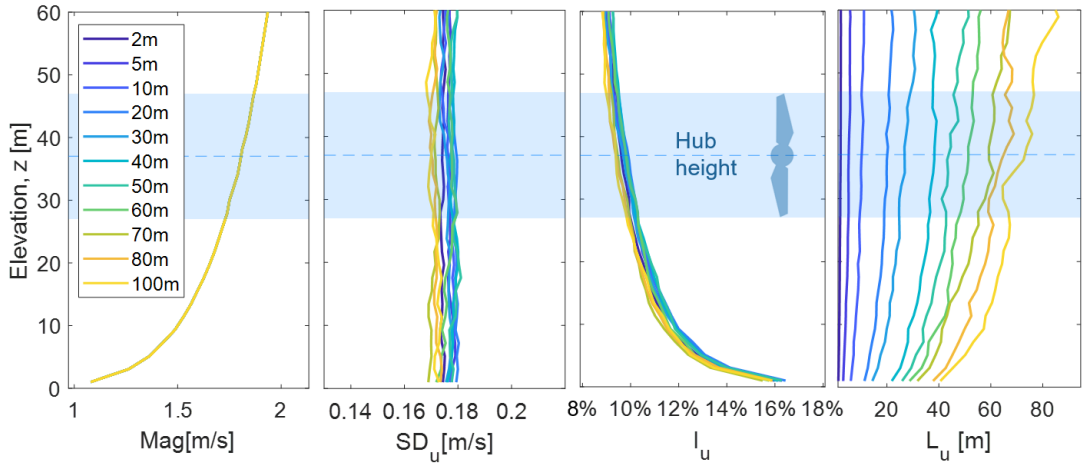

Figure 9.5: Left to right: shear, standard deviation σ_u, turbulence intensity I_u and length-scale L_u profiles of TurbSim flows for Test 2 - averaged over 30 flow iterations.

Load response

The resulting mean loads showed less than 1% change between the lowest and highest length-scale tested (not shown). Load standard deviations and DELs showed a significant response to varying length-scales (Figure 9.6). Both σ_T and σ_{M_y} show a maximum at $L \approx 20$m for below-rated velocities. Between the smallest length-scale tested (2m) and the rotor equivalent length-scale (20m), σ_T increases by $\approx 20\%$ for below-rated velocities. However, from rotor equivalent length-scale (20m) to the largest length-scale tested (70m) σ_T varies by less than 10%. The changes for below-rated velocities are less pronounced for σ_{M_y}. For above-rated velocities, both σ_T and σ_{M_y} show a non-linear downward trend with increasing length-scale, the same trend is seen in the $DELs$. The biggest change is seen in $DELs$ where they reduce by around 50% for above-rated velocities and 25% for above-rated between the smallest and largest length-scales.

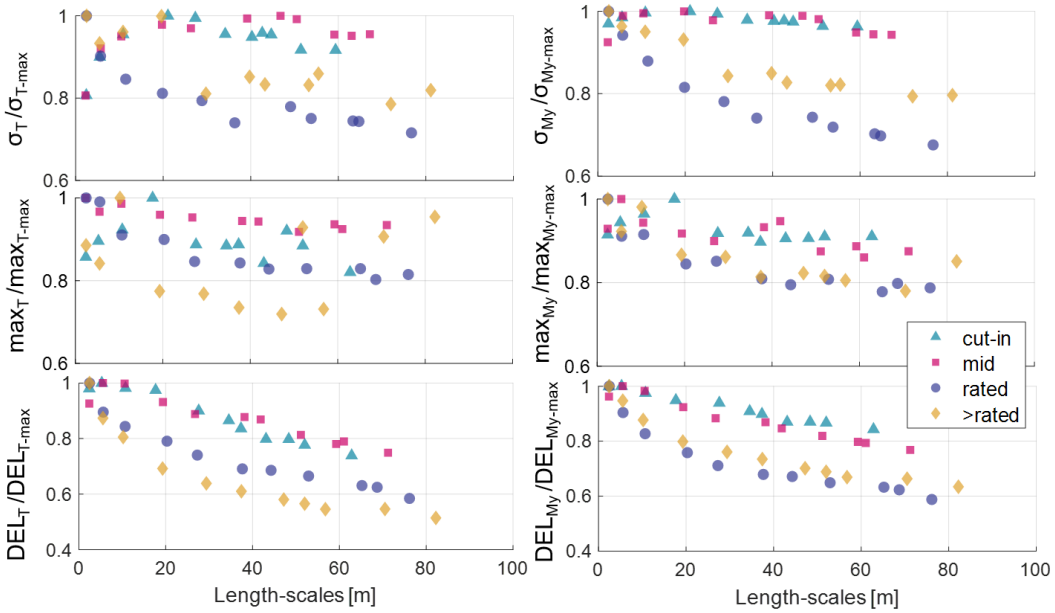

Figure 9.6: Turbine response results for Test 2 - length-scales. Left column (top to bottom): thrust standard deviation σ_T, maximum max_T and DEL. Right column (top to bottom): blade root bending moment standard deviation σ_{M_y}, maximum max_{M_y} and DEL. All values are normalised by the highest value in the test set.

Spectral analysis in Figure (9.7a) shows that at mid-velocity the load spectrum does not reflect the shape of the turbulence spectrum for the smallest (2m) length-scales, neither is there a peak at $2P$ frequency as seen for larger length-scales. The result is similar although to a lesser extent for the 5m length-scale test (not shown). A peak around $3P$ frequency is seen in 2m length-scale test for rated velocity, which is not seen in larger length-scales, see Figure (9.7b). The M_y spectra look similar for all length-scales at mid-velocities, Figure (9.7b), with rotational sampling peaks at $1P$ and $2P$ which are higher for smaller length-scales.

Although turbulence intensity showed the highest sensitivity, other parameters also had a pronounced effect on loads. The effect of varying length-scales was most evident in the DEL results. Results show that DELs were reduced by 25% between the smallest and largest length-scales tested for below-rated velocities and by 49% for above-rated. This is because smaller length-scales represent higher frequency loading. In other words, if the turbulent energy is concentrated at higher frequencies, there will be more loading cycles, leading to higher fatigue loads. A maximum value of σ_T occurred at the length-scale value similar to rotor size (Figure 9.6). This corresponded to a 20% increase when compared to length scales equivalent to 1/10th rotor size. The lack of response from the smallest length-scales is also evident in the spectral analysis (Figure (9.7a)), where for $L_u = 2$m, the load spectrum doesn't reflect the turbulence spectrum and the $1P$ frequency peak doesn't occur as it does for larger length-scales. This is in agreement with other investigations (Blackmore et al., 2015; Sentchev et al., 2020). In Part 1, it was shown that the IEC model length-scales were up to

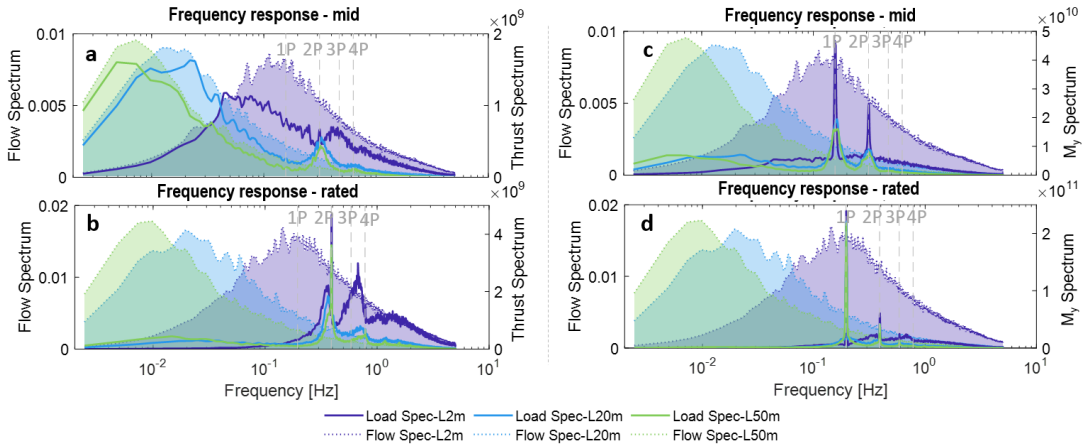

Figure 9.7: Spectral analysis of the thrust T response in panels (a) and (b) for mid and rated velocities respectively, and blade root bending moment M_y in panels (c) and (d) for Test 2. The shaded areas show the turbulence spectra (left axis), the bold lines show the corresponding load spectra (right axis).

4 times the average measured length-scale at two tidal sites ($L_{IEC} = 113$m vs. $L_{observed} = 30$m), Figure 6.2. In such cases, if a theoretical value is used in modelling, it is likely to result in a DEL underestimation of $\approx 30\%$. These results show, that similar to the turbulence intensity, inaccuracies in specified length-scales would result in significant load errors. This is particularly important given that IEC standards and models have been shown to deviate significantly from tidal site measurements.

9.1.3 Sensitivity Test 3: Shear profiles

Input flow characteristics

The properties of the five flow fields with varied shear profiles are shown in Figure 9.8. The mean velocity across the rotor area is consistent with the hub height value, see Table 9.1, so only the effects of the profile shape are considered. As with other tests, a small variation in σ_u and L_u is present.

Hub velocity	Rotor average velocity (m/s)				
(m/s)	PL4	PL7	PL10	Poly	Uni
1.10	1.10	1.10	1.10	1.09	1.10
1.80	1.81	1.80	1.80	1.78	1.80
2.50	2.51	2.50	2.50	2.47	2.50
3.00	3.01	3.01	3.00	2.96	3.00

Table 9.1: Rotor-averaged velocities for the shear profiles compared to the hub height velocity.

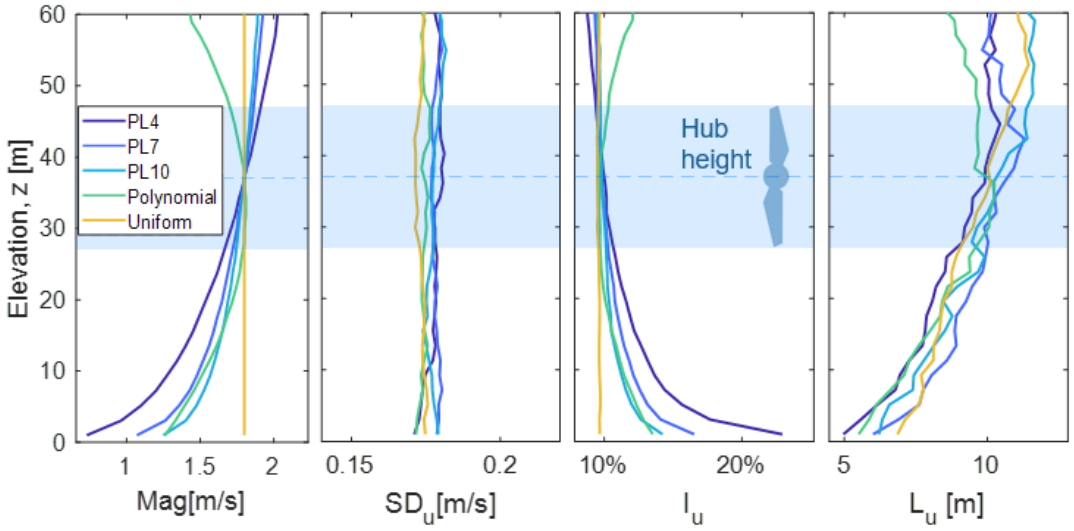

Figure 9.8: Left to right: shear, standard deviation SD_u, turbulence intensity I_u and length-scale L_u profiles of TurbSim flows for Test 3 - averaged over 30 flow iterations.

Load response

The thrust loads did not show a consistent response to varying shear profiles and generally did not vary by more than 10% across the tests (Figure 9.9). The exception is the result for above-rated velocities where σ_T varied by 15% between the 1/10th power-law and polynomial profiles. The blade bending σ_{M_y} and DEL_{M_y} showed a more consistent response with the 1/4th power law profile resulting in the highest loads. The biggest difference was seen at rated velocity - 16% change in σ_{M_y} between 1/4th power law and uniform profiles.

The thrust spectrum looks similar for all shear profiles tested, see Figure (9.10a) and (9.10b). The M_y spectrum (Figure (9.10c) and (9.10d)) has a significantly higher 1P peak for the 1/4th power law profile than for the others which is the cause for the higher M_y loads.

Figure 9.11 shows the additional parameters - hub-bending mean μ_{HB}, standard deviation σ_{HB}, maximum max_{HB} and DEL. These show significant variations between the different shear profiles, with the 1/4th power law resulting in the highest load response - 31% increase in μ_{HB} compared to the polynomial profile.

This result is in agreement with other studies that found a significant load sensitivity to shear profiles (McNaughton et al., 2013; Clark et al., 2015b). However, our results were not as extreme as those reported by Robertson et al. (2018), who found load sensitivities to varying shear in line with turbulence intensities.

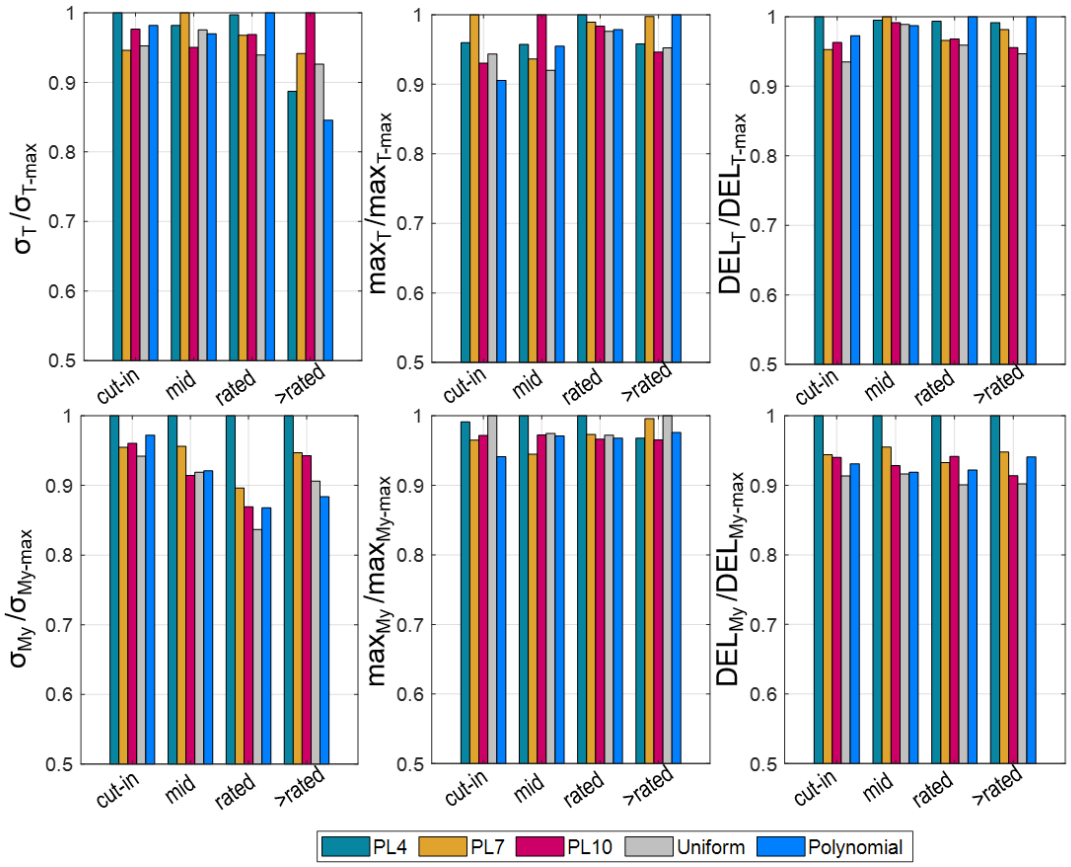

Figure 9.9: Turbine response results for Test 3. Top row (left to right): thrust standard deviation σ_T, maximum max_T and DEL. Bottom row (left to right): blade root bending moment standard deviation σ_{M_y}, maximum max_{M_y} and DEL. All values are normalised by the highest value in the test set.

Both the blade and hub bending parameters showed the highest response to the 1/4th power law profile (Figure 9.10). This is because for shear profiles, where the vertical velocity gradient within the swept area of the rotor is high (see Figure 9.8), the bending moment cycles through a larger change in amplitude every revolution of the rotor. This effect is evident in the significantly increased 1P spectral load peak for the 1/4th power law profile compared to others (Figure 9.10).

A 1/7th power law is typically assumed representative of open channel flows in modelling. However, measurements often show that even when the power law applies, the exponent can vary e.g. in Part 1, 1/5th power law was found to be more representative (Figure 6.9). Given that the difference in hub bending between 1/4th and 1/7th power law was found to be more than 20%, the 1/7th power law assumption is likely to result in significant inaccuracies for some sites. Assuming a 1/7th power law instead of a polynomial profile (as observed at the EMEC tidal site), could result in a 10% load overestimation, according to this study (Figure 9.11).

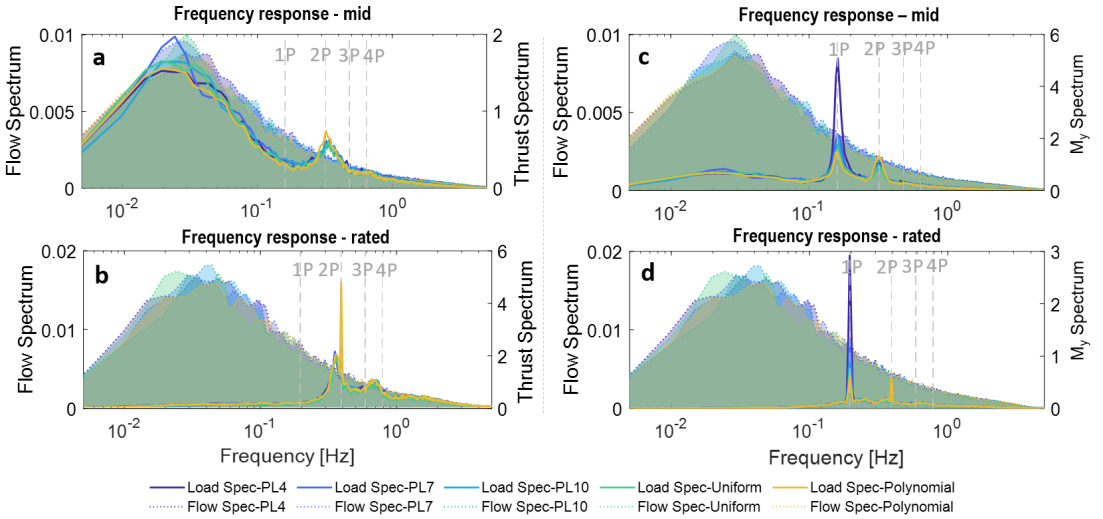

Figure 9.10: Spectral analysis of the thrust T response in panels (a) and (b) for mid and rated velocities respectively, and blade root bending moment M_y in panels (c) and (d) for Test 3. The shaded areas show the turbulence spectra (left axis), the bold lines show the corresponding load spectra (right axis).

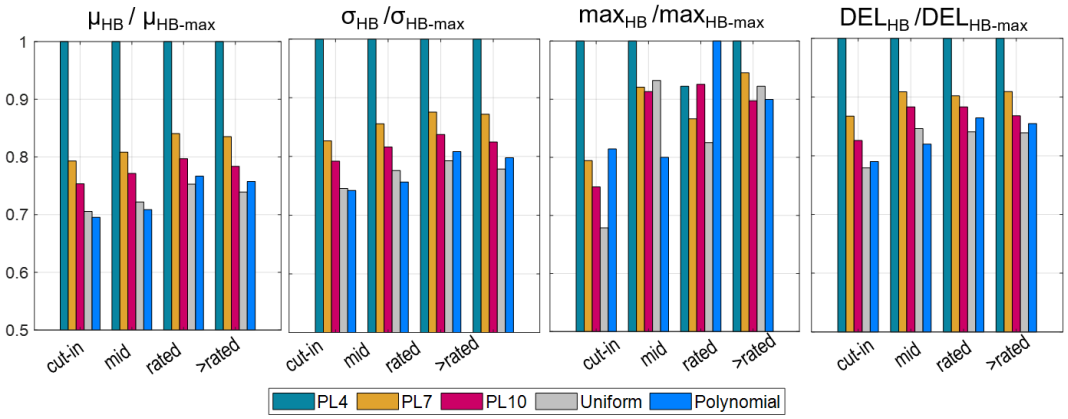

Figure 9.11: Hub bending results for Test 3. Left to right: hub bending mean μ_{HB}, standard deviation σ_{HB}, maximum max_{HB} and DEL_{HB}. All values are normalised by the highest value in the test set.

9.1.4 Sensitivity Test 4: Standard deviation profiles

Input flow characteristics

Figure 9.12 shows the flow properties of the two standard deviation profiles tested. While the profile shapes vary, the rotor-average σ_u is the same for both cases to ensure only the effects of the profile shape are captured.

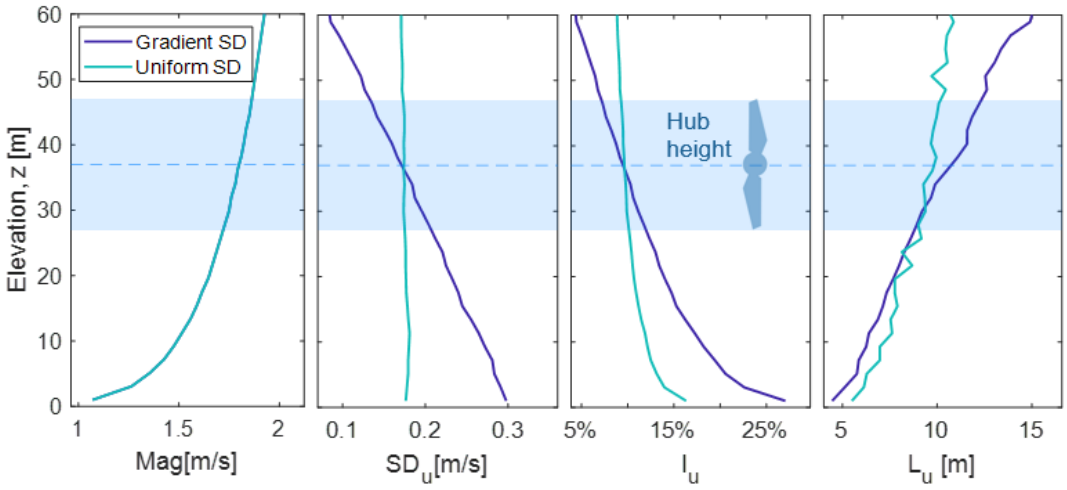

Figure 9.12: Left to right: shear, standard deviation σ_u, turbulence intensity I_u and length-scale L_u profiles of TurbSim flows for Test 4 - averaged over 30 flow iterations.

Load response

Similar to the other tests, very small changes were found in the mean load parameters. Moreover, the variations in σ_T and σ_{M_y} are also found to be small between the two profiles, with most velocity cases resulting in a less than 5% variation and no consistent trend. Hub bending also did not show any significant response (not shown). The biggest change - 13% between the profiles was found in σ_T for above-rated velocity. Figure 9.14 shows that the spectral response is very similar for both cases with a very slight variation in spectral magnitudes.

Using a realistic standard deviation profile instead of a default uniform profile had the smallest impact on loads (Figure 9.13) from all the tests. The load variations were inconsistent and mostly around 5%, suggesting that adding a realistic σ_u gradient into the model is less important than ensuring the other key parameters are correct. In this study, the rotor average σ_u was the same for the uniform and gradient cases, however when using real data a standard deviation profile is likely to result in a different rotor average σ_u. It is important that this is accurately captured as the overall standard deviation (and hence turbulence intensity) will have an impact on loads.

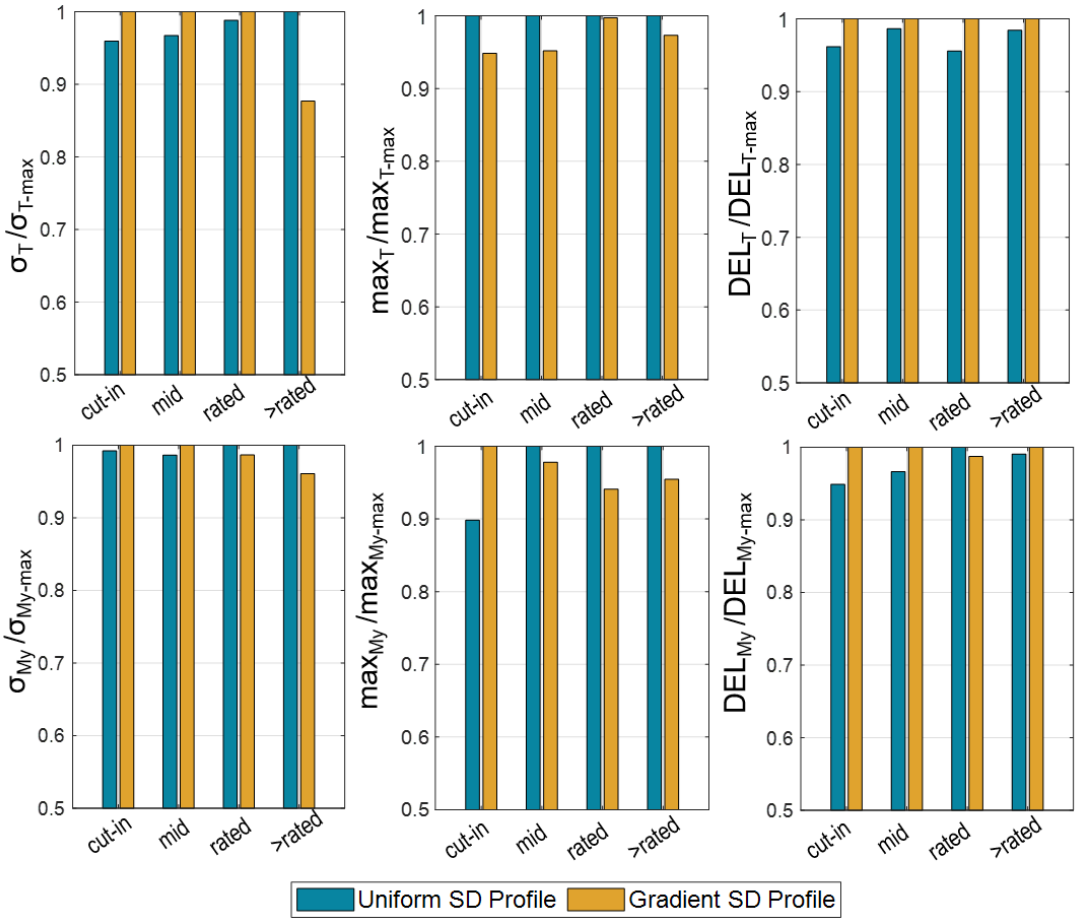

Figure 9.13: Turbine response results for Test 4. Top row (left to right): thrust standard deviation σ_T, maximum max_T and DEL. Bottom row (left to right): blade root bending moment standard deviation σ_{M_y}, maximum and DEL. All values are normalised by the highest value in the test set.

9.1.5 Sensitivity Test 5: Coherence on/off

Input flow characteristics

Two types of flow field were tested; in the coherent flow field each pair of points has predefined coherence characteristics, in the non-coherent flow, fluctuations are not correlated in space. In all velocity cases, the generated coherent flows have a slightly higher standard deviation ($2-6\%$ increase) and the length-scales vary by $1-15\%$ (see Figure 9.15), than the non coherent. This is due some parameters getting adjusted by the model to satisfy the coherence requirement. Figure 9.16 shows the non-coherent fluctuations are completely random and in the coherent case, they are spatially correlated, especially at lower frequencies (larger length-scales).

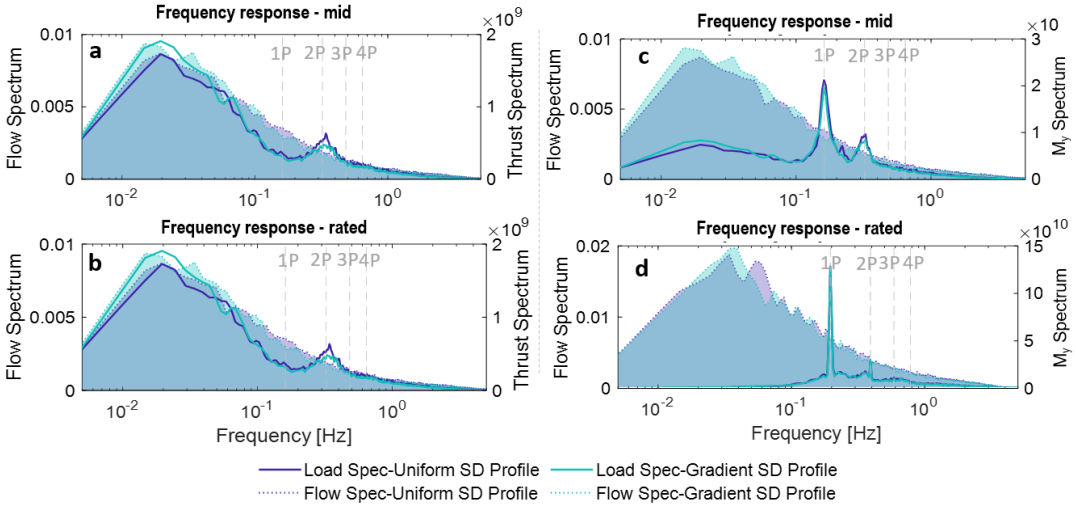

Figure 9.14: Spectral analysis of the thrust T response in panels (a) and (b) for mid and rated velocities respectively, and blade root bending moment M_y in panels (c) and (d) for Test 4. The shaded areas show the turbulence spectra (left axis), the bold lines show the corresponding load spectra (right axis).

Load response

Very small changes were found in the mean load parameters, however, significant variations were seen in σ_T between the two cases, with coherent flows resulting in 45% load increase for below-rated velocities. A smaller but opposite effect is seen for above-rated velocities - up to 17% **decrease** for coherent flows. A similar but less pronounced effect is seen for σ_{M_y} maximums and $DELs$.

The spectral analysis presented in Figures (9.18a) & (9.18b) elucidates this result. During coherent flow, the thrust spectrum reflects the turbulence spectrum at mid-velocities, whereas in the non-coherent case the load spectrum doesn't show any response to the turbulence spectrum. Moreover, in the non-coherent case, large spikes are seen at $2P$ frequency and every harmonic thereafter. In the mid-velocity case, the coherent flow results in higher load due to the coupling of load and turbulence spectra. Above rated velocity, the high-frequency spikes dominate, resulting in non-coherent loads being higher. The same is true for σ_{M_y} and DEL, although to a lesser extent. It is worth noting the increased magnitude of the spectrum for the coherent flow. This is due to the coherence function resulting in slightly higher parameters. In the non-coherent case the load spectrum is decoupled from the flow spectrum and therefore this discrepancy is unlikely to be the driver for the results.

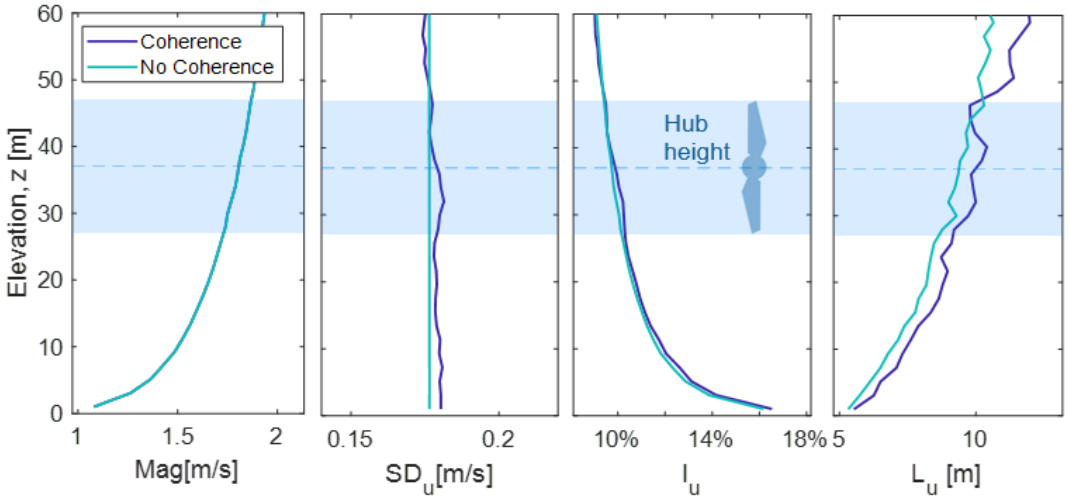

Figure 9.15: Left to right: shear, standard deviation σ_u, turbulence intensity I_u and length-scale L_u profiles of TurbSim flows for Test 5 - averaged over 30 flow iterations.

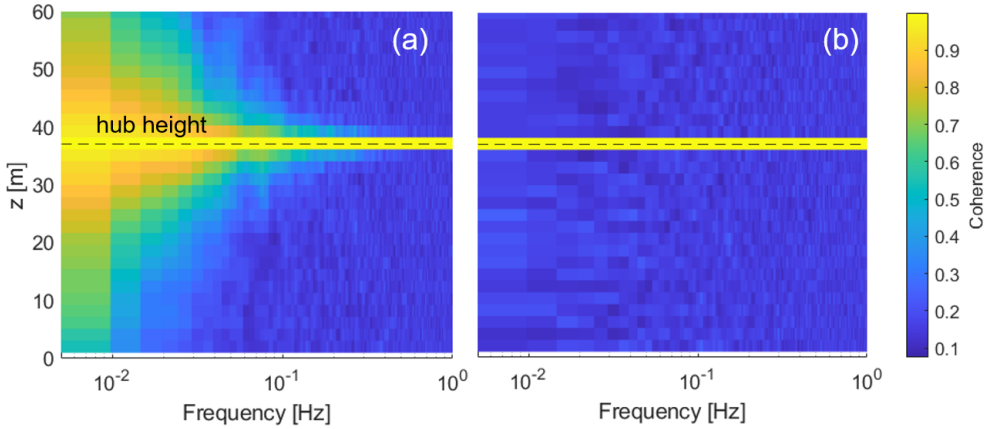

Figure 9.16: Spatial coherence for the coherent (a) and non-coherent (b) flow cases.

Specifying a spatially coherent flow field increased σ_T by up to 45% for below-rated velocities (Figure 9.17). Similar but slightly lower effects were seen for σ_{M_y} and DEL. When rated velocities are exceeded, the reverse relationship was observed and σ_T decreased. This is due to the coupling of the turbulence spectrum and load spectrum at low frequencies for up to rated velocities (Figure 9.18), and decoupling at above-rated velocities. Using a coherence model in generating turbulent flow is essential to properly model turbine load response. In Part 1, it was demonstrated that the IEC coherence model (as used in Tidal Bladed and TurbSim) was not a good representation of real flows (Figure 6.7 & 6.8), which could have an impact on modelled loads.

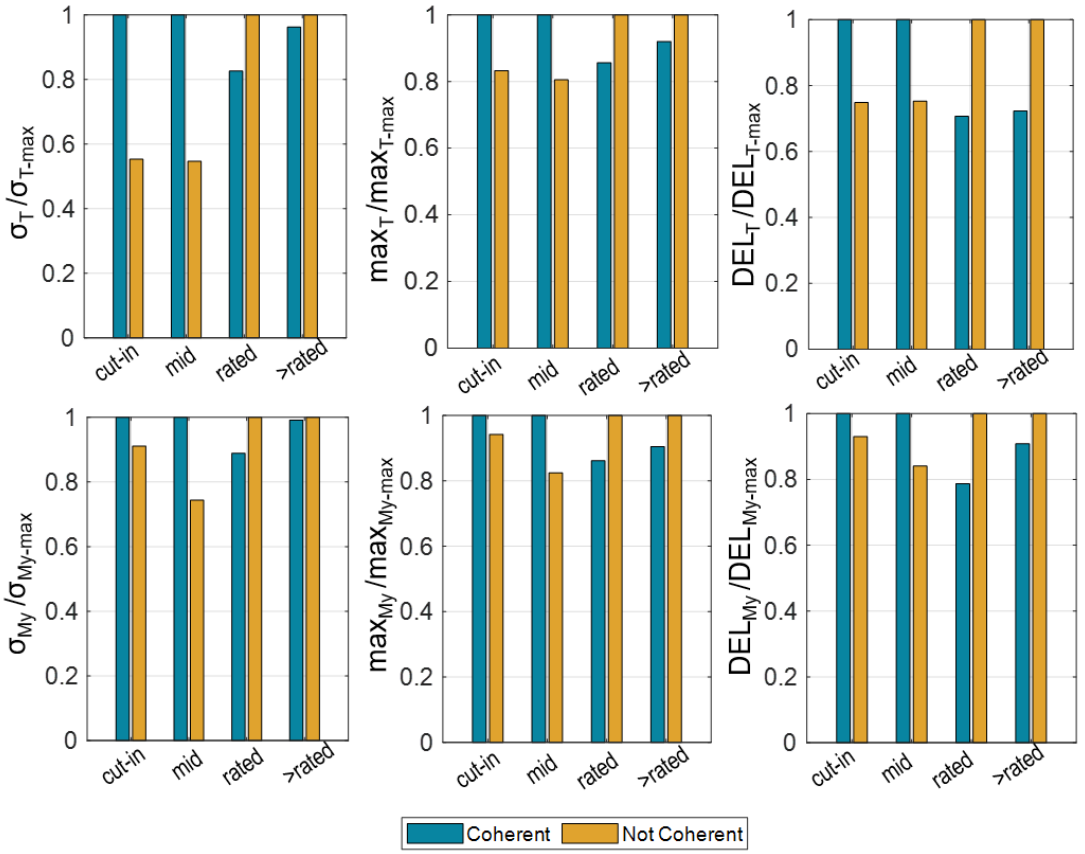

Figure 9.17: Turbine response results for Test 5. Top row (left to right): thrust standard deviation σ_T, maximum max_T and DEL. Bottom row (left to right): blade root bending moment standard deviation σ_{M_y}, maximum and DEL. All values are normalised by the highest value in the test set.

Analysis in Part 1 showed that real energetic tidal flows are non-stationary due to the presence of intermittent, energetic bursts, which can have instantaneous turbulence intensities up 80% higher than the average (Figure 6.15). It is known from wind turbine field experimentation that the greatest structural fatigue damage tends to occur during such periods of coherent, turbulent bursts (Kelley et al., 2005). While some coherence (spatial correlation) is generated in stochastic models such as the ones used here, by their nature they cannot replicate non-stationary flows. Further investigation into the effect of non-stationary coherent turbulent structures on tidal turbines would be valuable.

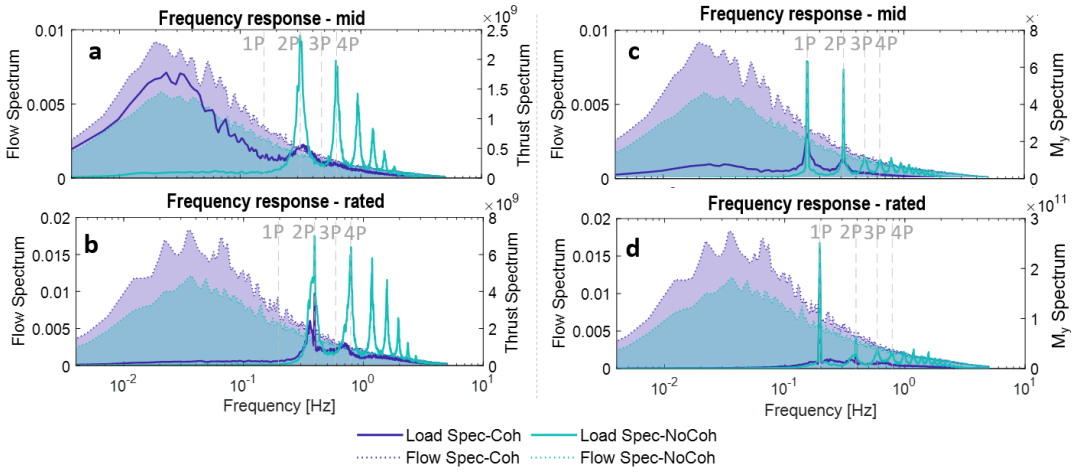

Figure 9.18: Spectral analysis of the thrust T response in panels (a) and (b) for mid and rated velocities respectively, and blade root bending moment M_y in panels (c) and (d) for Test 5. The shaded areas show the turbulence spectra (left axis), the bold lines show the corresponding load spectra (right axis).

9.2 Field Measurements

SECTION REDACTED DUE TO CONFIDENTIALITY.

Chapter 10

Conclusions

This work set out to investigate how turbulence in tidal channels affects mechanical loading on tidal energy devices. In reviewing the literature on the subject, it became apparent that the turbulence itself was not well understood. Particularly, because much of the turbulence theory, including its underlying assumptions and semi-empirical models, were developed in the context of atmospheric flows and may not be applicable to tidal flows.

For this reason, the work in Part 1 was an investigation into the suitability of models and methodologies inherited from the wind industry for tidal energy applications. This involved analysis of four ADCP datasets from two key tidal sites. Turbulence was characterised using recommended techniques and compared to a suite of parameters typically used to construct flow-fields for load modelling. Additionally, the conventional Fourier approach for analysing real, non-stationary turbulence was examined. Novel applications of wavelets were employed to compare instantaneous turbulence features to average quantities, as calculated by the Fourier method, to evaluate the suitability of the conventional method.

To understand the impact of non-representative turbulence parameters, Part 2 of this study focused on testing the sensitivities of turbulence inputs to load estimates in Tidal Bladed. Unlike previous work, the effects on simulated loads were studied by varying one turbulence parameter at a time, demonstrating the individual impacts. A total of 3720 simulations were carried out, showing the hierarchy of key input parameters in terms of their impact on load outcomes. Finally, field data from a full-scale operational TEC was analysed to investigate the most important considerations for loading in real-sea conditions.

The conclusions are summarised below in two parts, structured by the research questions which were outlined at the beginning of the thesis.

10.1 Part I

Are semi-empirical turbulence models appropriate to represent real tidal flows?

Overall, many characteristics of turbulence were found to be poorly represented by semi-empirical models.

Analysis of the turbulence spectra showed that the Kaimal model better represented the vertical spectrum, while von Kármán better represented the streamwise spectrum. In practice, only one model would be used, in which case either the vertical or streamwise turbulence components would be misrepresented. In line with other studies, it was found that, even when the spectral model shape matched the measured spectrum, the peak was often shifted to lower frequencies. In a fatigue load simulation, this would result in less frequent turbulent fluctuations (and hence fewer load cycles), and thus an underestimation of loads.

The measured length scales varied significantly between the four datasets, even within the same site. None of the length-scale measurements conformed well to open-channel flow theory nor to the default values provided in commercial models (based on atmospheric boundary layer). An incorrect length scale is likely to misrepresent the fatigue loads and the theoretical values that do not take into account the marine boundary layer should not be used. The measured coherence was found to be higher at higher frequencies and lower at lower frequencies than the IEC model predicts, although the EMEC-1 site showed slightly more agreement with the coherence model. Where the measured shear profiles followed a power law, it was not a 1/7th-power law, as is typically assumed. Shear profiles are known to be important for device loads, so it would be recommended to use a measured profile rather than an assumed one.

There is some evidence that conformity of the measured turbulence parameters to models was better for the FORCE site. The shear and length-scale profiles were found to be more canonical at the FORCE measurement locations, although there was still significant variation in measurements even at nearby locations.

The results of this study caution against using atmospheric-based turbulence models, highlighting the requirement for validating flow models used in load simulations with specific site measurements. The significant variations in measured turbulence parameters across the sites and within different locations on the same site, demonstrate that turbulence in a tidal channel will be strongly altered by bathymetry and geometry of the channel and will vary by tidal cycle and velocity. This suggests that universal models may not be appropriate for tidal flows.

Are methods of data analysis appropriate for non-stationary turbulence?

The comparison of the spectral characteristics using wavelet and Fourier methods showed that wavelet analysis is an appropriate tool for analysing turbulence in real tidal channels and when averaged, agrees favourably with the traditional Fourier approach.

The main advantage of wavelets is the time–frequency analysis, which in this study has demonstrated the presence of highly energetic, intermittent turbulent bursts at the EMEC site. Quantification of such instantaneous turbulence bursts showed that they are highly energetic, with instantaneous turbulence intensity values 80% higher than the average. This has implications for device designers as the statistical values used in load calculations, may not capture the extent of such energetic fluctuations. Comparing the instantaneous quantities to the Fourier quantities clearly demonstrates that Fourier results are insufficient to fully define transient, anisotropic, turbulent structures.

ADCP data is advantageous as it provides measurements throughout the water column. The presented spatial analysis showed that coherent structures occur throughout the water column with high energy peaks at frequencies associated with fatigue loads on turbines. Such spatial analysis could be expanded to understand the intermittency throughout the water column over time.

This work highlights the need to enhance site characterisation methodologies to include analysis on coherent and intermittent flow features, which have been found to be highly energetic and are likely to be damaging to tidal energy devices. The wavelet analysis outlined in this paper allows such events to be identified and analysed. Understanding the instantaneous turbulent fluctuations will enable to more accurately simulate loads on tidal devices and hence reduce uncertainty in design.

10.2 Part II

Which turbulence parameters are the most important for modelling device loads in BEM models.

From the five turbulence parameters investigated, turbulence intensity I_u showed the highest sensitivity with a 90% change in load fluctuations for the range of intensities tested ($I_u = 2 - 24\%$). Turbulence characterisation studies have shown that Doppler noise, waves, instrument alignment as well as calculation methods all have significant impacts on the resulting I_u value and therefore can be a significant source of inaccuracies in load modelling. For example, wave presence during turbulence data collection can overestimate the resulting DEL by 40%.

Length-scales showed the second highest variations in DELs (up to 49% for $L_u = 2 - 80m$). In Part I, it was shown that default values in Tidal Bladed (based on wind IEC standard) can be up to 4 times larger than those measured in tidal channels. Given the sensitivity these can result in significant errors in load estimates. Moreover, adding coherence into the simulated flow fields increased loads by 45% compared to non-coherent flows.

Shear profiles had a small impact on thrust estimates but did significantly affect blade-bending (16%) and hub-bending (30%), with the 1/4th power law profile generally resulting in the highest loads. While realistic shear profiles are important, realistic standard deviation profiles did not show a notable impact on loads and therefore the focus should be on specifying the other turbulence parameters correctly.

The findings of this study are relevant to developers and BEM model users, aiming to reduce the uncertainty in modelling. The results show that variations in key turbulence input parameters can have profound impacts on the modelled loads, which can lead to high uncertainty and conservatism in design. Appropriate techniques to calculate turbulence intensity is key as this is the most sensitive parameter.

What can be learned from field measurements of a full-scale TEC response to real-sea conditions?

Analysis of operational load and flow data demonstrated the various complexities with measurements of dynamic environments. The operation of the turbine will inevitably alter the flow and any turbine-mounted instruments will be affected by vibration, device movement, moorings and cables. Moreover, the control strategy of the turbine will alter the response behaviour at different incoming velocities. This means a sufficient measurement period is required to properly capture the range of responses.

The separation of periodic components of the loads demonstrated that the stochastic fluctuations (due to turbulence) contribute a larger portion to the total DELs than the periodic. This is in agreement with previous studies, and re-iterates the necessity of properly accounting for turbulence-induced loading. Load variations were seen outside the angular position at the leg, suggesting there is spatially varying shear and turbulence across the rotor area.

During the measurement period at this site, wave presence was found to have only a modest impact with DELs increasing by up to 10% due to waves. This suggests that for sheltered tidal sites such as the Fall of Warness, even for rotors located near the surface, waves are not the biggest challenge for fatigue. Despite not having a large effect on loads, the presence of waves was clearly seen in the leg-mounted (S-ADCP) flow measurements. Wave orbital motions captured by the ADCP almost doubled the I_u, compared to I_u obtained from the seabed instrument at the same berth prior to turbine deployment. The noise seen in the turbulence

spectra measured by the S-ADCP was also increased during the periods of operation due to the device vibrations, again biasing the I_u high. Given the high sensitivity of I_u to loads in modelling, measurements obtained from device-fixed instruments must be used with caution and appropriate techniques to filter out noise and waves must be applied.

Detailed wavelet analysis demonstrated that the instantaneous load spectrum is correlated to the instantaneous bursts in turbulence. However, the degree of correlation varied for different flow realisations, suggesting that not all turbulence frequencies interact with the device. At below-rated incoming velocities, there is evidence that the load frequencies correspond to turbulence with length-scales much larger than the rotor. This is contrary to the assumption that length-scales similar to rotor size are the most important. When the rated velocity is exceeded, the load response changes due to blade pitching, with some evidence of de-coupling of load and turbulence spectra. The main response here is at the blade passing frequencies, regardless of the incoming flow spectrum. These results are interesting because they show that the controller changes how different scales of turbulence interact with the rotor. This can be used to design control strategies that mitigate fatigue loading by blade pitching, as has been investigated in wind turbine design.

10.3 Further Work

Standardising approach for design conditions definition

This study has demonstrated that the assumed (wind-based) turbulence models do not always apply to tidal flows and that this can cause significant uncertainties in load modelling. Future work should focus on the development of models specific to tidal flows, utilising the increasingly available datasets across different tidal sites. Due to the variability in channel geometries and the resulting turbulence structure, universal models may not be appropriate. In this case, robust, validated methods to derive parameters such as length-scales and spectrum from measurements are required.

Wind standards such as the IEC 61400-1 offer extreme models for wind speeds, shear profiles, gusts and turbulence. No such guide exists for tidal flows, current practices are based on using a combination of extreme wave conditions and high quantiles of turbulence intensity. This study identified that energetic, short bursts of turbulent energy are present in the flow, which are not well represented in statistical measures such as turbulence intensity. Other studies have also shown that the shear profile forms vary by velocity as well as instantaneously. These findings suggest that an approach which takes into account extreme shear and coherent bursts may be required.

BEM model improvements

This study demonstrated that the inclusion of coherence in the approaching flow field has a significant impact on resulting loads. In future work, the sensitivity of various coherence curves could be investigated, especially given that IEC coherence models were shown to misrepresent tidal flows in this study. This will help to understand whether specific tidal coherence models need to be developed.

While some coherence (spatial correlation) is generated in stochastic models such as the ones used here, by their nature they cannot replicate non-stationary flows. Future work should investigate the effect of non-stationary coherent turbulent structures on tidal turbines. In stochastic wind turbulence models, coherent events (normally produced by Large Eddy Simulation (LES) models) can be superimposed in the time domain onto the more random, background turbulence to produce a more realistic flow. By separating out the coherent events in the real data, or by using LES models, a similar technique could be used to incorporate these into the stochastic tidal models.

Methods to calculate turbulence parameters from ADCPs

Although ADCPs offer a convenient way to measure turbulence at a given site, there are still challenges with computing parameters that require instantaneous velocity measurements. To obtain these from the ADCP, it must be assumed that the instantaneous flow is homogenous across the beams, an assumption which is not valid for large beam spread. In this and other studies this problem was overcome by assuming that because only the largest scales (bigger than the beam spread) are of interest, the methods are still valid. However, to be certain of such methods, validation of ADCP parameters should be carried out against those obtained through point measurements by ADVs or Converging ADPs.

10.4 Industry Recommendations for ADCP Measurements

Some of the learnings gained throughout the investigations in this work may be useful to inform industry practices and help the effort to standardise tidal site measurement and characterisation methods.

Turbulence intensity is the main parameter used in characterising turbulence. This study quantified the sensitivity of loads modelled in Tidal Bladed to the input I_u parameters, showing that each additive 1% change in I_u resulted in approximately 4% increase in fatigue load. The methods employed in measuring and calculating I_u can be a substantial source of uncertainty in design. Length-scales also showed a substantial sensitivity, and it was shown that analytical models from wind or from open channel flow theory do not apply. This means length-scales also need to be measured accurately.

To carry out a turbulence characterisation (e.g. for design), the minimum parameters that should be obtained are turbulence intensity, shear profile, integral length-scale, turbulence spectrum and coherence. It is generally understood that this will require an ADCP with at least 5 beams (see Dewey and Stringer (2007)), fixed into a frame that minimises instrument pitch and roll movement. However, additional factors must be considered when setting up the instrument, or the data could be inadequate for turbulence analysis.

ADCP alignment

The variance method (the recommended approach for calculating I_u), is based on the assumption that the beam pairs are aligned to the flow direction. This way, one beam pair resolves the streamwise and vertical components and the perpendicular beam pair resolves the transverse and vertical. If the instrument is misaligned, these quantities will be incorrect. This study has demonstrated that misalignment of the instrument to the flow can result in significant errors e.g. a 20° misalignment can result in 12-35% (proportional) decrease in I_u value, depending on flow features (Figure 5.10). The geometric rotation of Reynold's stress tensor (see Section 2.2.2) is also not possible because to carry out a full rotation, all six unique terms must be known, requiring an instrument with more than 5 beams. This is an important consideration as many instruments deployed to date, have not been aligned to the flow. It can also be an issue even if instruments are aligned because of flow asymmetry between flood and ebb tides, as found at the Fall of Warness (see Figure 5.3).

Waves

Waves are likely to be present at most sites, wave orbital motions will affect ADCP velocity readings in particular if measuring near the top of the water column. It has been shown in this and other studies (Sellar and Sutherland, 2016) that wave presence can more than double the I_u values measured with an ADCP, even in relatively sheltered sites such as Fall of Warness. Waves can also affect mean flow measurements and distort the shear profile in the upper part of the water column. Wave orbital motions generate coherent structures that appear in turbulence spectra, often occupying the same frequency bands as integral length-scales, complicating any attempt of wave-turbulence separation (Thiébaut et al., 2020b; Perez et al., 2020).

In order to improve the accuracy of turbulence measurements, wave orbital motion must be decomposed. Literature presents a number of methods for filtering the effects of waves from ADCP data (Perez et al., 2020; Togneri et al., 2021; Bian et al., 2018), however these require independent wave measurements. Unless a separate instrument is being deployed for wave measurements, ADCPs can be set up to enable altimeter readings alongside velocity measurements, which track the water surface elevation and allow calculation of wave parameters.

Sampling Regime

Sampling Rate

To capture the high frequency range of the turbulence spectrum, the sampling rate must be more than 4Hz. In this study it was shown that datasets sampled at 1Hz had insufficient resolution to analyse against spectral models. Even the data sampled at 2Hz presented some challenges with fitting a spectrum (see Figure 6.3 where FORCE-1 data was sampled at 2Hz and EMEC-1 at 4Hz).

Five beam ADCPs can generally sample up to 8Hz, the appropriate sampling frequency can be estimated using the following equation assuming Taylor's Frozen Hypothesis and isotropic turbulence in the high frequency region:

$$f_s = 2 \times \frac{\overline{U}}{\Delta z}, \tag{10.1}$$

where Δz is the vertical cell size. For a flow range of 1-3.0m/s with 1m vertical bins the limiting frequencies are 2Hz and 6Hz respectively. In this case increasing the sampling rate above 6Hz would have limited advantages due to the spatial averaging limitation of the vertical cell size. Useful discussion on filtering effects of ADCPs can be found in Guion and Young (2015) and Pearson and Hernon (2015). Increasing the sampling rate to 6Hz may be impractical due to data storage and battery life, in which case a minimum of 4Hz would be recommended.

The same relationship can be used to check the vertical bin size, there is little benefit to setting a fine vertical resolution e.g. 0.5m if using a low sampling rate. In other words, temporal and spatial averaging must both be considered when configuring instruments.

Burst Length

The best option for turbulence measurements is continuous sampling. Most ADCP set ups attempt to use burst strategies due to battery and data storage limitations. This can create a number of challenges for turbulence analysis.

Calculated turbulence parameters are highly variable and need to be ensemble averaged e.g. by velocity bin over many flow realisations. Measuring in bursts, for example, 10-mins every half an hour would mean many velocity bins would be missed out. This is illustrated in Figure 10.1, where sampling for 10 minutes every half an hour results in a 70% reduction in the number of data points compared to sampling continuously.

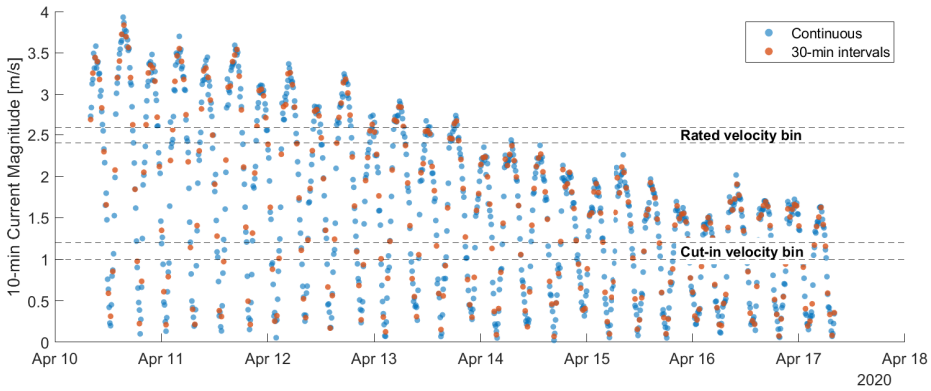

Figure 10.1: Example of velocity data from the Fall of Warness over 1 week. Blue markers show 10-min averaged velocity sampled continuously over the week, red markers show the same data re-sampled every half an hour. The dashed lines show the data points captured in a single velocity bin (0.2m/s) for two velocities of interest based on typical cut-in and rated velocities for tidal turbines.The rated velocity bin captures 11 vs 41 data points and cut-in captures 16 vs 51 points for continuous and burst sampling respectively.

Trying to overcome this problem by sampling more frequently with shorter bursts creates other issues. A long enough burst time is required to apply the time correlation methods to calculate integral length-scales. Simulations in this study found that even a 10-minute burst (as recommended by standards) may be too short to capture the biggest scales. Time intervals shorter than 10 minutes will most likely result in erroneous values of length scales.

Continuous measurement will allow the option to sensitivity test different averaging periods and provide enough data points for robust analysis. Any other sampling scheme is not recommended.

Device mounted instruments

Mounting the ADP on the device, for example on the rotor hub or support structure can offer a number of advantages and successful implementations of this have been reported in Sutherland (2015). It can give a true measurement of the approach flow, overcoming the issues of co-ordinate transform that come with seabed ADCPs. However, there are also some significant challenges with obtaining data suitable for turbulence analysis, in particular, if the ADP is mounted to a floating structure. These include waves, mooring interference, movement of the device and increased noise level due to device vibrations during operation.

Appendix A

A.0.1 Derivation of ADCP Misalignment Error

Beam velocities can be written in terms of u, v and w velocity components in channel coordinates, beam inclination angle, θ and the angle between the principle flow direction and the instrument heading, ϕ, i.e., the misalignment angle :

$$\begin{bmatrix} b_1 \\ b_2 \\ b_3 \\ b_4 \end{bmatrix} = \begin{bmatrix} sin(\theta) & 0 & cos(\theta) \\ -sin(\theta) & 0 & cos(\theta) \\ 0 & sin(\theta) & cos(\theta) \\ 0 & -sin(\theta) & cos(\theta) \end{bmatrix} \times \begin{bmatrix} cos(\phi) & -sin(\phi) & 0 \\ sin(\phi) & cos(\phi) & 0 \\ 0 & 0 & 1 \end{bmatrix} \times \begin{bmatrix} u \\ v \\ w \end{bmatrix} \tag{A.1}$$

$$b_1 = usin(\theta)cos(\phi) - vsin(\theta)sin(\phi) + wcos(\theta) \tag{A.2}$$

$$b_2 = -usin(\theta)cos(\phi) + vsin(\theta)sin(\phi) + wcos(\theta) \tag{A.3}$$

$$b_3 = usin(\theta)sin(\phi) + vsin(\theta)cos(\phi) + wcos(\theta) \tag{A.4}$$

$$b_4 = -usin(\theta)sin(\phi) - vsin(\theta)cos(\phi) + wcos(\theta) \tag{A.5}$$

$$b_5 = w \tag{A.6}$$

Assuming the Doppler noise can be removed from beam velocity variances, the beam variances can be written as follows:

$$\begin{aligned}
\overline{b_1'^2} &= \overline{w'^2}\cos^2(\theta) + \overline{u'^2}\sin^2(\theta)\cos^2(\phi) + \overline{v'^2}\sin^2(\theta)\sin^2(\phi) + \overline{u'w'}\sin(2\theta)\cos(\phi) \\
&\quad -\overline{u'v'}\sin^2(\theta)\sin(2\phi) - \overline{v'w'}\sin(2\theta)\sin(\phi) \\
\overline{b_2'^2} &= \overline{w'^2}\cos^2(\theta) + \overline{u'^2}\sin^2(\theta)\cos^2(\phi) + \overline{v'^2}\sin^2(\theta)\sin^2(\phi) + \overline{v'w'}\sin(2\theta)\sin(\phi) \\
&\quad -\overline{u'v'}\sin^2(\theta)\sin(2\phi) - \overline{u'w'}\sin(2\theta)\cos(\phi) \\
\overline{b_3'^2} &= \overline{w'^2}\cos^2(\theta) + \overline{v'^2}\sin^2(\theta)\cos^2(\phi) + \overline{u'^2}\sin^2(\theta)\sin^2(\phi) + \overline{u'v'}\sin^2(\theta)\sin(2\phi) \\
&\quad +\overline{u'w'}\sin(2\theta)\sin(\phi) + \overline{v'w'}\sin(2\theta)\cos(\phi) \\
\overline{b_4'} &= \overline{w'^2}\cos^2(\theta) + \overline{v'^2}\sin^2(\theta)\cos^2(\phi) + \overline{u'^2}\sin^2(\theta)\sin^2(\phi) + \overline{u'v'}\sin^2(\theta)\sin(2\phi) \\
&\quad -\overline{u'w'}\sin(2\theta)\sin(\phi) - \overline{v'w'}\sin(2\theta)\cos(\phi) \\
\overline{b_5'} &= \overline{w'^2}
\end{aligned}$$

We can substitute the beam variance equations above into the variance method equations below to obtain the channel co-ordinate component variances (as sampled by a misaligned beam). In this example, it is assumed beam numbers 1 and 2, and 3 and 4, are opposite; the numbering convention may change depending on the ADCP instrument.

Variance method equations:

$$\begin{aligned}
\overline{u'^2} &= \frac{\overline{b_1'} + \overline{b_2'} - 2\overline{b_5'}cos^2(\theta)}{2sin^2(\theta)} \\
\overline{v'^2} &= \frac{\overline{b_3'^2} + \overline{b_4'^2} - 2\overline{b_5'^2}cos^2(\theta)}{2sin^2(\theta)} \\
\overline{w'^2} &= \overline{b_5'^2} \\
\overline{u'w'} &= \frac{\overline{b_2'^2} - \overline{b_1'^2}}{2sin(2\theta)} \\
\overline{v'w'} &= \frac{\overline{b_4'^2} - \overline{b_3'^2}}{2sin(2\theta)}
\end{aligned}$$

From the above parameters, the total kinetic energy and anisotropy ratios can also be calculated as follows:

$$\begin{aligned}
\alpha &= \frac{\overline{w'^2}}{\overline{u'^2} + \overline{v'^2}} \\
\frac{q^2}{2} &= \frac{\overline{u'^2} + \overline{v'^2} + \overline{w'^2}}{2}
\end{aligned}$$

Approximate parameters in terms of the 'true' values and misalignment angle:

$$
\begin{aligned}
\overline{u'^2}_1 &= \overline{u'^2}\cos^2(\phi) + \overline{v'^2}\sin^2(\phi) - \overline{u'v'}\sin(2\phi) \\
\overline{v'^2}_1 &= \overline{v'^2}\cos^2(\phi) + \overline{u'^2}\sin^2(\phi) + \overline{u'v'}\sin(2\phi) \\
\overline{u'w'}_1 &= \sin^2(\theta)\csc(2\theta)\left(u^2\cos^2(\phi) + v^2\sin^2(\phi) - uv\sin(2\phi)\right) \\
\overline{v'w'}_1 &= \sin^2(\theta)\csc(2\theta)\left(v^2\cos^2(\phi) + u^2\sin^2(\phi) + vu\sin(2\phi)\right) \\
\frac{q^2}{2}_1 &= \frac{\overline{u'^2}_1 + \overline{v'}_1 + \overline{w'^2}}{2} = \frac{\overline{u'^2} + \overline{v'^2} + \overline{w'^2}}{2} \\
\alpha &= \frac{\overline{w'^2}}{\overline{u'^2}_1 + \overline{v'}_1} = \frac{\overline{w'^2}}{\overline{u'^2} + \overline{v'}}
\end{aligned}
$$

Ocean Engineering 270 (2023) 113616

Contents lists available at ScienceDirect

Ocean Engineering

journal homepage: www.elsevier.com/locate/oceaneng

Wavelet applications for turbulence characterisation of real tidal flows measured with an ADCP

Alyona Naberezhnykh [a,b,*], David Ingram [a], Ian Ashton [c]

[a] University of Edinburgh, King's Buildings Campus, University of Edinburgh, Edinburgh, EH9 3JW, United Kingdom
[b] European Marine Energy Centre, The Charles Clouston Building ORIC, Back Rd, Stromness, KW16 3AW, United Kingdom
[c] University of Exeter, College of Engineering Mathematics and Physical Sciences, Penryn, TR10 9FE, United Kingdom

ARTICLE INFO

Keywords:
Turbulence
ADCP
Wavelet analysis
Fourier analysis
Coherence
Turbulence spectrum
Intermittency
Device fatigue loads

ABSTRACT

Understanding turbulence is crucial to the design of tidal energy converters as it influences loads, fatigue life and power production. Acoustic Doppler Current Profilers (ADCPs) are normally employed in measurement campaigns to analyse turbulence at a particular location. Coherent turbulent structures are known to lead to the highest turbulence-induced stresses and are typically analysed by Fourier transform. However, this method can only yield parameters which are averaged over the signal length or the analysing window, and hence may not fully represent real flow turbulence, which is often non-stationary. This study applies wavelet time–frequency analysis to ADCP data from an active tidal test site to examine the turbulence spectrum and coherence characteristics of the flow, comparing these to Fourier methods. Results show that the average quantities from wavelet analysis agree favourably with Fourier analysis. Moreover, wavelet analysis yields instantaneous spectra and coherence, which show that at this site, high energy bursts occur at frequencies known to be significant for TEC loading and have turbulence intensities up to 80% higher than the average. We show that these intermittent, coherent bursts are obscured by the averages associated with Fourier analysis, highlighting the need for methods such as wavelets to understand interactions between fluid flow and TEC.

1. Introduction

Tidal energy could meet 10% of European electricity requirements by 2050, as well as provide a competitive solution for remote islands and areas where access to energy is difficult. However, the risks associated with the relatively new technologies are not yet fully understood and often lead to a lack of confidence from potential investors (European Commission, 2016).

To be commercially viable, tidal energy converters (TECs) must endure up to 25 years in the water without requiring major overhaul or repair (Scarlett and Viola, 2020). A number of studies including (McCann et al., 2008; Blackmore et al., 2015; Milne et al., 2015; Clark et al., 2015b; Milne et al., 2016; Scarlett and Viola, 2020), highlight that turbulence as well as other sources of unsteady loading such as waves, are major contributors to fatigue loading and power quality, affecting the device's commercial viability. In a simulation study, Scarlett and Viola (2020) found that turbulence and waves can lead to load peaks that are twice the median load. Power quality and energy yield are both affected by turbulence, the latter because a dynamic controller will sacrifice energy yield for power quality during turbulent flow (Ortega et al., 2020; McCann et al., 2008).

Acoustic Doppler Current Profilers (ADCP) are usually employed for measuring tidal flows and can be used for analysing turbulence. Typically, statistics such as turbulence intensity (TI) – defined as magnitude of fluctuations as a percentage of the mean flow velocity – are used to characterise turbulence. The turbulent energy spectrum, which describes the distribution of energy across different scales of velocity fluctuations is used to determine the integral length-scale, ADCP noise variance and check applicability of spectral models. However, even with TI and the energy spectrum, the description of turbulence is incomplete. Turbulence is not a pure random process but contains fluctuations which are correlated in space (coherent). Coherent turbulent structures are known to lead to the highest stresses in axial turbines (Kelley et al., 2005; Milne et al., 2016; Kilcher et al., 2014) so coherency must be considered, at least over the turbine rotor area, to understand interactions between fluid flow and TECs (Clark et al., 2015a).

Coherent structures can be defined as local vorticity fields, which survive for times much longer than the eddy turnover time (Farge and Schneider, 2004). In atmospheric flows, coherent motions are associated with transient bursts of coherent turbulent energy caused

* Corresponding author at: University of Edinburgh, King's Buildings Campus, University of Edinburgh, Edinburgh, EH9 3JW, United Kingdom.
E-mail address: a. (A. Naberezhnykh).

https://doi.org/10.1016/j.oceaneng.2022.113616
Received 11 March 2022; Received in revised form 24 December 2022; Accepted 31 December 2022
Available online 10 January 2023

by Kelvin–Helmholtz instabilities (Kelley et al., 2005). Analogous to these atmospheric bursts, large local features in bathymetry or channel geometry can add coherent structural content to an already turbulent inflow (Clark et al., 2015a).

2. Limitations of traditional analysis methods

Traditional theories of turbulence have mostly focused on the theoretical case of statistically stationary, homogeneous and isotropic turbulence. However, the existence of coherent structures in real flows may invalidate these assumptions (Van Den Berg, 2004).

Turbulence characterisation using ADCP data has been carried out across a number of tidal sites, e.g in France Energies Marines (2020), Milne et al. (2013), Sellar and Sutherland (2016). These typically use Fourier analysis to determine spectral and coherence characteristics. Fourier analysis is a commonly used method for identifying periodic components in oceanographic time series. However, the requirement for the data to be at least quasi-stationary (i.e. the statistical properties of the signal are not changing with time) is the main limitation when it is used in the analysis of turbulence (Emery and Thomson, 2014). Turbulent signals may contain transient, energetic bursts, which correspond to large deviations and can be seen in the wide tails of the signal's probability density function (PDF). Second-order statistics such as the energy spectrum are relatively insensitive to these rare events because their duration is small compared to the sampling period and consequently they do not dominate the integral (Farge and Schneider, 2004).

The Fourier transform decomposes a turbulent signal into a sum of infinite sine and cosine functions with different frequencies and hence generates **record-averaged** values of amplitude and phase for each frequency component. It is assumed that vortices at each scale occupy the entire timeline, so when applied to a non-stationary time series, information on the changing processes will be smeared out (Emery and Thomson, 2014; Chen et al., 2019). In other words, if a non-stationary times series is dissected, the statistical properties of the parts will not all be similar to those of the whole series, and the usual Gaussian statistics based on the whole record will be deceptive (Flinchem and Jay, 2000).

In such cases, short-time Fourier transform (STFT), a sequence of Fourier transforms performed over a sliding window across the entire time series, may be used (Akansu and Haddad, 2001). This approach attempts to address a signal's non-stationarity by analysing parts of the signal and providing the time-localised frequency information. However, the window size is predetermined and fixed, so some inaccuracy may arise from the aliasing of high and low frequency components that do not fall within the frequency range of the window (Indrusiak, 2004; Torrence and Compo, 1997).

2.1. Wavelet analysis

Wavelet analysis can be thought of as stretching and compressing the window of the short-time Fourier transform, according to the frequency to be localised. This allows the definition of scales in both time and frequency domain, helping to identify intermittent features of the flow such as the passing of coherent structures. While the Fourier transform uses trigonometric functions as the basis, the wavelet transform bases are a broad range of functions named wavelets (Chen et al., 2019).

Wavelet analysis has been widely used across different disciplines, including for processing of ADCP data in oceanography. Mihanović et al. (2009) applied a multiple cross-wavelet spectral analysis to study the relationship between the wind and tidal forcing mechanisms on the temperature variability in Lastovo, Croatia. Phanikumar et al. (2007) used multi-resolution wavelet analysis of the 2-D mean velocity fields obtained from ADCP surveys to separate the flow into regions of slow and fast moving zones and to estimate the relative sizes of the main channel and the storage zones. Petrusevich et al. (2020) analysed ADCP-measured current velocities and used wavelet transformation to derive the time-dependent behaviour of horizontal and vertical current velocities at the semi-diurnal tidal frequency band that dominates the backscatter spectrum. Wavelets have also been used in tidal applications for de-tiding (Chiao and Wang, 2004) and harmonic analysis to differentiate tidal species (Garel and Cai, 2018). In the above studies the investigation focused on longer term changes with the scales of interest in the order of hours, days and above. ADCPs in these cases have predominantly been used to obtain mean current velocities, showing long term variations. Turbulence characterisation varies in that the scales of interest are much smaller, in the region of seconds to minutes. For this, ADCPs are set up to collect continuous, high resolution (4 Hz+) measurements and the instantaneous fluctuations are the ones of interest.

Wavelets have been successfully applied for separation of turbulence and waves using the Synchrosqueezed Wavelet Transform (SWT) (Thakur et al., 2013) in studies by Bian et al. (2018), Perez et al. (2020) and Togneri et al. (2021).

Since (Farge and Schneider, 2004) introduced wavelets into turbulence, they have become pervasive in turbulent signal analysis. There are examples of wavelet methods being applied to study the turbulent boundary layer (Chen et al., 2019; Nan, 2016; Hu and Du, 2020) in experimental tanks and flume settings, and turbulence–rotor interactions for wind turbines (Kelley et al., 2000, 2005). Some studies have applied wavelet analysis to field measurements for turbulence study however only for single point measurements (Camussi et al., 2008). ADCPs profile the water column and therefore offer more potential to understand the spatial structure of turbulence, however to the authors best knowledge wavelet analysis is not generally used as a tool to characterise turbulence for tidal energy applications. Moreover, while the theoretical limitations of stationary techniques such as Fourier analysis for non-stationary phenomena such as turbulence are understood, the implications of doing so in characterising tidal turbulence have not been quantified.

In this work, we apply wavelet methods to analyse ADCP data from the European Marine Energy Centre's (EMEC) tidal test site at the Fall of Warness (FoW) in Orkney, Scotland, collected for the purpose of studying turbulence. We apply time–frequency analysis to study instantaneous, short term fluctuations and examine spectral and coherence characteristics, comparing the results to traditional Fourier methods. The ability to detect intermittency and coherency is explored and the advantages of capturing non-stationary features of the flow with regards to TEC load analysis is discussed.

3. Methods

3.1. Data

The ADCP velocity data was gathered at the FoW site over a month during the spring of 2020. Fig. 1 shows the location of the ADCP in the tidal channel as well as the bathymetry.

During the measurement campaign, the depth ranged 46–50 m and the mean current flow peaked at 3.8 m/s. Measurements were made using a Nortek Signature 500, five beam ADCP, fixed into a gimbal support on a seabed frame. The vertical bin size was set to 1 m and the instrument sampled continuously at a rate of 4 Hz. The average heading of the ADCP was such that the opposite beams 1 and 3 were oriented approximately in the stream-wise direction of the tidal current, whereas beams 2 and 4 pointed in the span-wise direction.

The raw data was processed and quality controlled (QC) using EMEC's proprietary tool IMPAQCT. This tool follows the Quality Assurance and Quality Control of Real Time Oceanographic data (QARTOD) standard (IOOS, 2019), alongside the Nortek instrument manual (Nortek, 2018), and flags any data which does not meet the QC thresholds. Half of the dataset was discarded due to instrument movement leaving approximately two weeks of data as shown in Fig. 2.

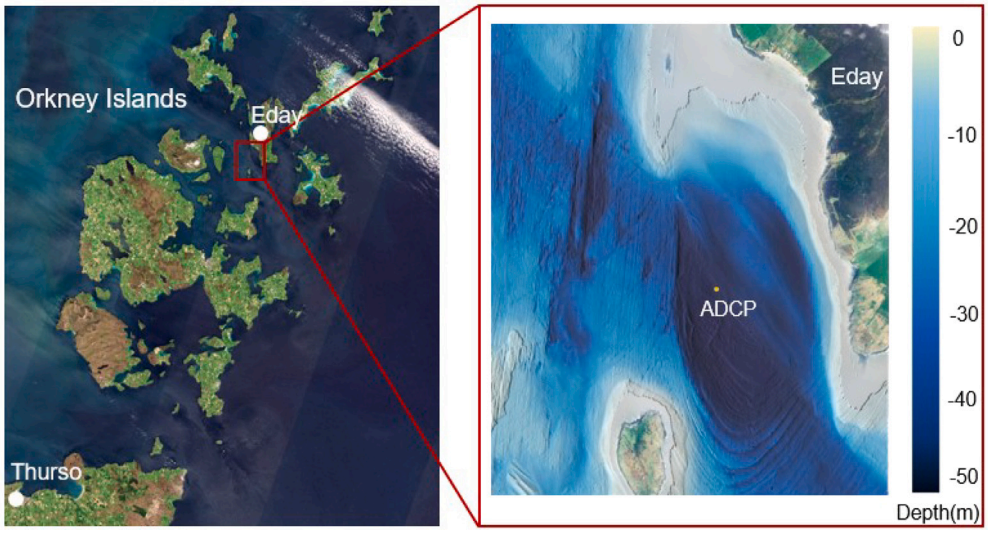

Fig. 1. Map of the Orkney Islands on the left showing the location of the Fall of Warness tidal channel - European Marine Energy Centre (EMEC) test facility. The right panel shows the bathymetry of the site, yellow dot marking the location of the ADCP for the presented data.

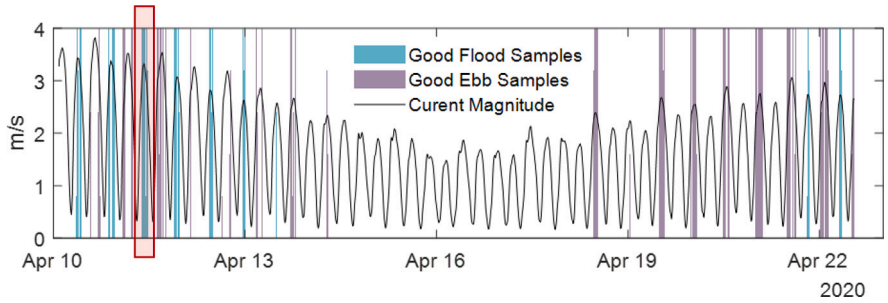

Fig. 2. Dataset with shaded areas showing suitable intervals for detailed analysis. While a number of cycles were analysed, the highlighted section relates to the results presented in this paper.

We are interested in the instantaneous, short term turbulent fluctuations, so a short time series was selected for analysis. Data was ensembled into 10 min intervals and binned by velocity, wave presence and by cycle. Fig. 2 shows the suitable data samples after filtering by cycle, no waves and velocities 2.8–3.2 m/s. A number of short samples were analysed however only one (highlighted in red) is presented in this paper for brevity. Fig. 4, top panel, shows the short time series used for analysis.

Instantaneous along-beam data was retained for turbulence analysis to avoid making the assumptions of homogeneity in resolving velocity vectors and averaging out important fluctuations. Most of the analysis was performed on the vertical beam (B5) as it gives a true measurement of the vertical velocity component. Some results are also shown for the inclined beam (B1) as it pointed into the principal flow direction and hence provides an approximation of streamwise component of the flow.

3.2. Analysis techniques

3.2.1. Stationarity test

One of the ways to assess data for stationarity is to examine how statistics converge with increasing averaging time. This was done by selecting a 20 min instantaneous velocity record and subdividing it into a range of periods from 20 s to 20 min in 20 s increments, with the mean, $\overline{u}$ and standard deviation, σ_u calculated for each period as in Sutherland et al. (2017). In stationary data, the mean is expected to converge to a value as stationarity time is approached. Typically stationarity period for tidal channel data is assumed to be 5–10 min (Clark et al., 2015a).

3.2.2. Fourier spectrum

Discrete Fourier Transform (DFT) of a detrended, statistically stationary velocity sample is defined as:

$$\hat{s}(f_k) = \sum_{n=0}^{N=1} x(n) e^{-i f_k n} \tag{1}$$

where $x(n)$ is a time series, f_k is the discrete frequency (0,1...N-1), n is the time index and $\hat{s}(f_k)$ is the spectrum. The power spectral density (PSD) defines the spectrum in terms of variance per unit frequency:

$$S(f_k) = \frac{2}{N\Delta t} |\hat{s}(f_k)|^2 \tag{2}$$

where N is the number of points in $\hat{s}(f)$ (Emery and Thomson, 2014).

MATLAB function `pwelch` was used to compute the discrete Fourier transform of time series data using a fast Fourier transform (fft) algorithm. It allows specification for window size, type and overlap. By default, x is divided into the longest possible segments to obtain as close to but not exceed 8 segments with 50% overlap, using a Hamming window. The modified periodograms are averaged to obtain the PSD estimate. The default number of discrete Fourier transform (DFT) points is the greater of 256 or the next power of 2 greater than the length of the segments.

In the PSD format, the area under the spectrum curve represents the variance, u'^2 for the data record. This can be related to turbulence intensity, TI by:

$$TI_i = \frac{\sqrt{u_i'^2}}{\overline{U}} \tag{3}$$

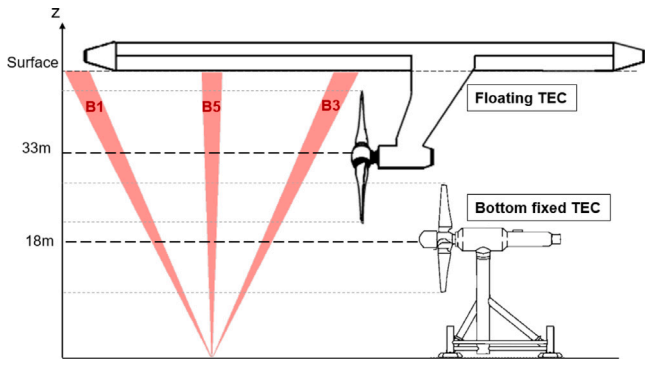

Fig. 3. Example sizes and water column locations of a floating and bottom fixed turbine concepts, overlaid over the measurement area (no TECs were present during measurement). The assumed hub heights are as shown and rotor diameters are assumed to be 20 m.

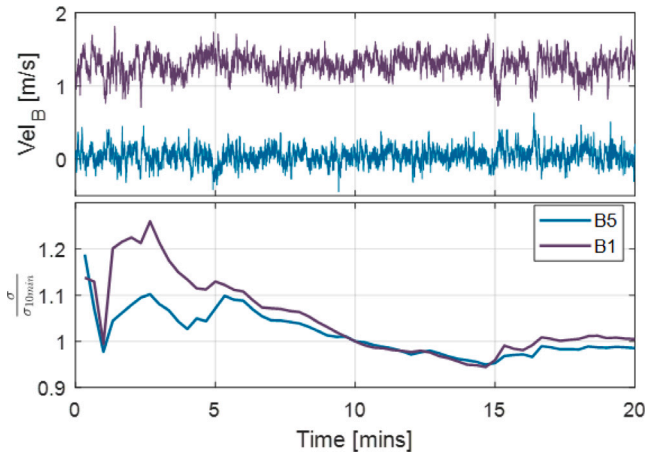

Fig. 4. Time series (top panel) and convergence (bottom) of the normalised standard deviations of along-beam velocities for the inclined (B1) and vertical (B5) beams at an elevation from seabed, $z = 18$ m. The convergence plot shows cumulative statistics for the increasing averaging time shown on the x-axis.

where i is the velocity component and $\overline{U}$ is the mean current magnitude.

3.2.3. Wavelet spectrum

The continuous wavelet transform (CWT) of a discrete sequence, $x_{n'}$ is defined as the convolution of $x_{n'}$ with the analysing wavelets ψ. The transform gives the wavelet coefficients:

$$W(s,n) = \sum_{n'=0}^{N-1} x_{n'} \psi * \left[\frac{(n'-n)\delta t}{s}\right] \tag{4}$$

where the $(*)$ indicates the complex conjugate, and by varying the wavelet scale, s and translating along the localised time index, n, a picture of amplitude versus the scale and how this amplitude varies with time can be constructed (Torrence and Compo, 1997).

The relationship between the equivalent Fourier frequency and the wavelet scale can be derived analytically for a particular wavelet function as described in Torrence and Compo (1997), to yield $W(f,t)$. The wavelet function, ψ is in general complex, so the wavelet transform is also complex. The transform can then be divided into real and imaginary parts, amplitude and phase respectively, and the wavelet power spectrum is then $|W(f,t)|^2$.

The global wavelet spectrum, $\tilde{W}(f)$ is the time-averaged wavelet spectrum over a defined period, it must be normalised according to the measured variance, u'^2 :

$$\tilde{W}(f) = \frac{1}{C}\int_0^{\infty} |W(f,t)|^2 dt \tag{5}$$

where the constant C makes:

$$\int_0^{\infty} \tilde{W}(f) df = u'^2 \tag{6}$$

Without normalisation, the scale of the wavelet spectrum would be arbitrary and not comparable to the Fourier spectrum. Once normalised, the mean wavelet spectrum, $\tilde{W}(f)$ should be a smoothed version of the Fourier energy spectrum $S(f)$.

Wavelet analysis depends both on the signal and on the analysing wavelet. The basic analysing 'mother' wavelet should exhibit a fast decay for t tending to infinity, must be oscillating and its Fourier transform $\hat{\psi}(f)$ must decay fast as wave numbers tend to infinity. For analysis of turbulent signals, Farge and Schneider (2004) recommend to use the continuous wavelet transform with complex valued wavelet such as the Morlet.

The Morlet wavelet scale is closely related to Fourier period, thus keeping the wavelet analysis close to the classical Fourier. It is common to set the frequency parameter of Morlet wavelet equal to 6. In this way, besides satisfying the necessary wavelet admissibility condition, good time–frequency localisation is achieved. This makes the Morlet wavelet especially useful for detecting localised, sporadic periodicities in time series, as well as the time evolution of these periodicities (Mihanović et al., 2009). The Morlet wavelet has been used in open channel studies and been shown to have a good balance between time and frequency localisation (Chen et al., 2019).

Some studies have found that wavelet power spectra can be biased in favour of low frequencies and large scales. For example, standard wavelet analysis of a time series composed of sinusoidal waves with the same amplitude but different frequencies cannot exactly replicate the spectral peaks, resulting in lower peaks for high frequency waves. Liu et al. (2007) and Yuan et al. (2017) present a correction for this problem using the rectified wavelet power spectra analysis (RWPSA). RWPSA divides the spectrum by the scales so that spectral peaks of the same magnitude are similar in size. Liu et al. (2007) further suggested a physically consistent definition of energy for the wavelet power spectrum, based on the square of the transformation coefficient divided by its associated scale. The adjusted wavelet power spectrum results in a substantial improvement in the spectral estimate, allowing for comparison of spectral peaks across scales (Yuan et al., 2017).

The MATLAB function `cwt`, part of the Wavelet Toolbox, has been used to compute the continuous wavelet spectrum. This function uses the sampling frequency of the signal to determine the scale-to-frequency conversions and therefore returns the spectra on a frequency scale. The `cwt` function uses L1 normalisation which overcomes the issue of the peaks at higher frequencies being reduced more than the peaks at lower frequencies. With L1 normalisation, if there are equal amplitude oscillatory components in the data at different scales, they will have equal magnitude in the CWT. Using L1 normalisation shows a more accurate representation of the signal, for a more detailed explanation see the Wavelet Toolbox documentation (The MathWorks Inc. Natick, Massachusetts, United States, 2022).

3.2.4. Coherence

Coherence measures the cross-correlation between two time series as a function of frequency, using a correlation coefficient between 0 and 1 (Torrence and Compo, 1997). In turbulence analysis, spatial coherence, Γ is usually estimated from two independent measurements of the same component of velocity, u_1, u_2 that are separated in space by a distance, $r = (\Delta x^2 + \Delta y^2 + \Delta z^2)^{1/2}$, using fast Fourier transform, $\mathcal{F}$ and $S(u) = |\mathcal{F}(u')|^2$ (Thomson et al., 2014):

$$\Gamma = \frac{|\overline{\mathcal{F}(u_1')\mathcal{F}(u_2')}|^2}{\overline{S(u_1)S(u_2)}} \tag{7}$$

The wavelet coherency method is analogous to Fourier cross-spectral analysis but with the spectra obtained using the wavelet transform. As the wavelet coherency is resolved not only in frequency but also in

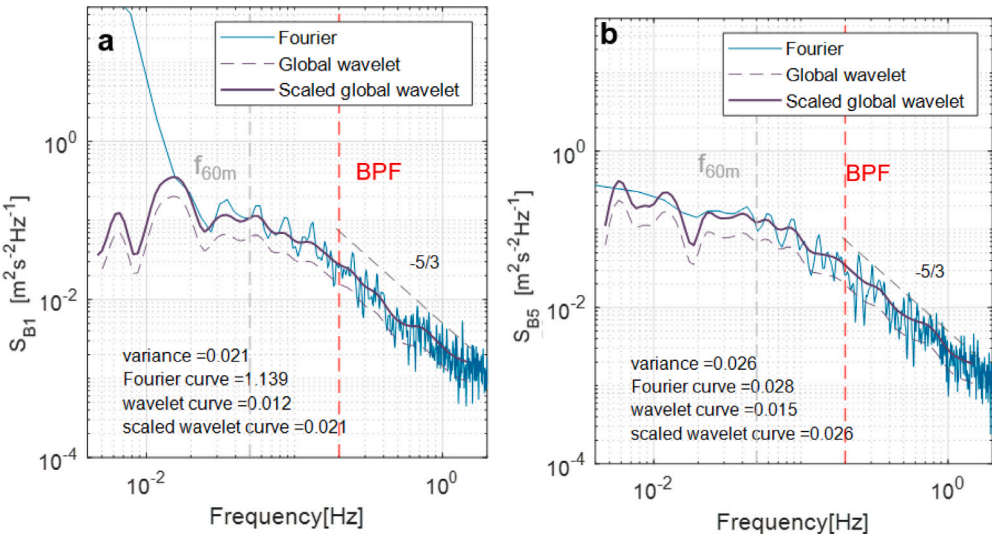

Fig. 5. Power spectral density (PSD) obtained using Fourier and wavelet methods. Panel (a) shows the slanted beam, B1 and (b) shows the vertical beam, B5 velocities at bottom-fixed TEC hub height, z =18 m. Variances were calculated from the time series and by integrating the PSD curves. BPF = Blade passing frequency, f_{60m} = frequency representing 60 m length-scale.

time, it enables the detection of short bursts of coherent energy in the flow.

The 95% confidence level of Γ measurements – above which Γ estimates can be considered valid with 95% confidence – is equal to $\sqrt{6/n_{DOF}}$, where n_{DOF} is the number of degrees of freedom in the coherence estimate (Kilcher et al., 2014).

To calculate coherence based on Fourier spectra, the MATLAB function `mscohere` is used. This function finds the magnitude-squared coherence estimate for two input signals. For the wavelet coherence the `wcoherence` function is used. This function is also part of the Wavelet Toolbox, it determines the wavelet coherence and cross-spectrum for two input signals.

3.2.5. Important scales

It is important to understand which scales of turbulent motions are important for device fatigue loading. Previous studies found that the most important turbulent scales (size of large eddies) for load considerations range from 0.5–3 times the rotor diameter, D (Ouro et al., 2017; Milne et al., 2010; Sentchev et al., 2020; Blackmore et al., 2015). According to Taylor's Frozen Eddy Hypothesis, the frequency f_L at which an eddy with a length scale L is advected by the tidal flow $\overline{U}$ past a point can be defined as (Pearson and Hernon, 2015):

$$f_L = \frac{\overline{U}}{L} \tag{8}$$

Using the mean current velocity for the data sample, we can approximate the frequency limit below which the fluctuations are no longer important for loads on a typical tidal rotor (≈20 m diameter). This is because length scales much larger than the rotor diameter are unlikely to have a significant impact on turbine fatigue (fluctuating) load as they would exert fairly uniform gusts when evaluated over a turbine disc area and will be felt as a change in the mean flow.

Another important frequency is the blade passing frequency (BPF), which depends on the rotational speed of the turbine. Flow velocity fluctuations at this frequency are known to be a significant source of fatigue loading due to blade slicing through the spatially coherent eddies. This action can give rise to significant energy contributions at multiples of the rotational frequency of the rotor, and is a primary contributor to the fatigue of rotor blades (Milne et al., 2016; McCann et al., 2008).

When considering the important frequencies in the turbulence spectrum, it must be noted that spatial averaging inside each beam is an inevitable feature of ADCPs. The accuracy of the velocity in the beam-wise direction is affected by the vertical resolution within the beam. This finite resolution acts as a filter to the vertical and horizontal velocity components. Using the beam geometry the lower bound for vertical resolution, Δz is defined by Guion and Young (2015) as :

$$\Delta z = z\theta tan(\alpha) + \Delta r cos(\alpha) \tag{9}$$

where z is the depth, θ is the beam width angle (in this case 2.9°), α is the beam inclination angle (25°) and Δr is the vertical bin size (1 m). Fluctuations at these scales would be significantly attenuated. Using this relationship the smallest length scale that can accurately be resolved for our set up is 1.3 m at the floating hub height and 1.1 m at the seabed mounted hub height. This equates to 2.5 Hz and 2.9 Hz respectively using Eq. (8). These length scales are smaller than we would expect to measure with this ADCP due to the sampling frequency used and therefore are not the main limitation.

3.2.6. Measurement area

The ADCP measurements were collected in ambient flow (i.e. no tidal energy device was present). To give context to the measurement area, Fig. 3 shows the measurement points used in analysis, as well as beam orientation in relation to hypothetical floating and bottom fixed TEC cases. Coherence was analysed along the vertical and inclined beams for half a rotor separation distance (10 m). The inclined beam coherence will include both horizontal and vertical components of velocity and the separation distance will be slightly larger due to the inclination angle.

4. Results and discussion

4.1. Stationarity

The stationarity of the data was assessed by evaluating the mean and variance of the along-beam velocities, for a range of averaging periods. Unlike data from tank experiments such as in Sutherland et al. (2017), the measured velocities do not exhibit stationarity, with the standard deviation continuing to change as the averaging time increases, see Fig. 4. It is also clear that the stationarity time of 5-10 min, frequently assumed for turbulence analysis, (Clark et al., 2015a), is not applicable in this case.

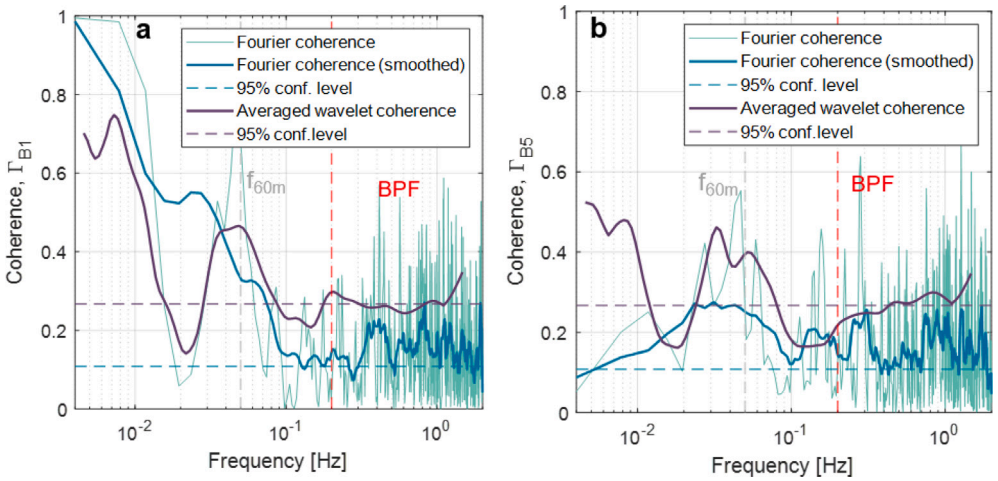

Fig. 6. Comparison of the averaged wavelet coherence and Fourier coherence calculated for a 10 min velocity sample. Panel (a) shows the slanted beam (B1) results and (b) shows the vertical beam (B5). The coherence is measured between two points at z = 18 m and z = 28 m, see Fig. 3, representing the spatial correlation across half a rotor span of a seabed mounted turbine.

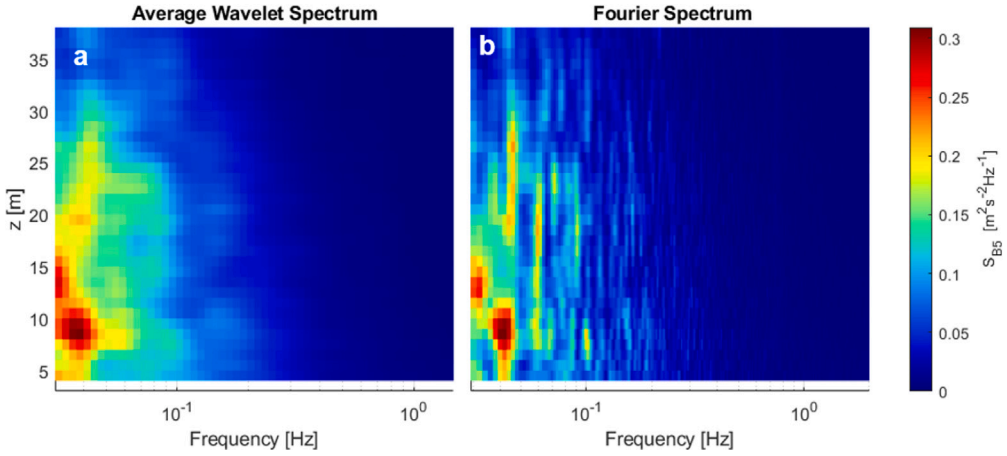

Fig. 7. Isosurface of the time-averaged wavelet PSD (a) and Fourier PSD (b).

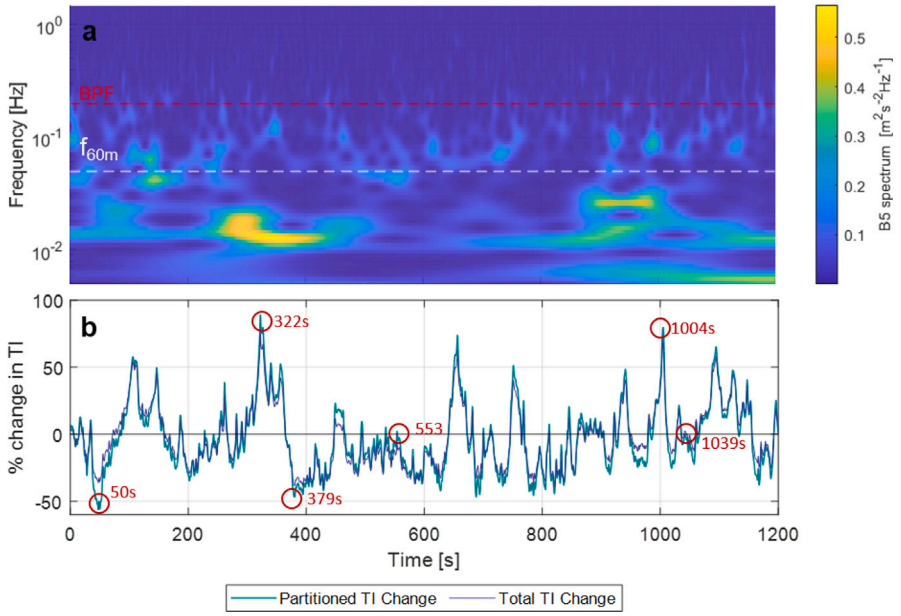

Fig. 8. Top panel (a) - instantaneous wavelet spectra calculated for the 20 min data sample for the vertical beam, B5 velocities at z =18 m. Panel (b) - instantaneous TI as a % change of the average TI. The time markers show the time instants presented in Fig. 9.

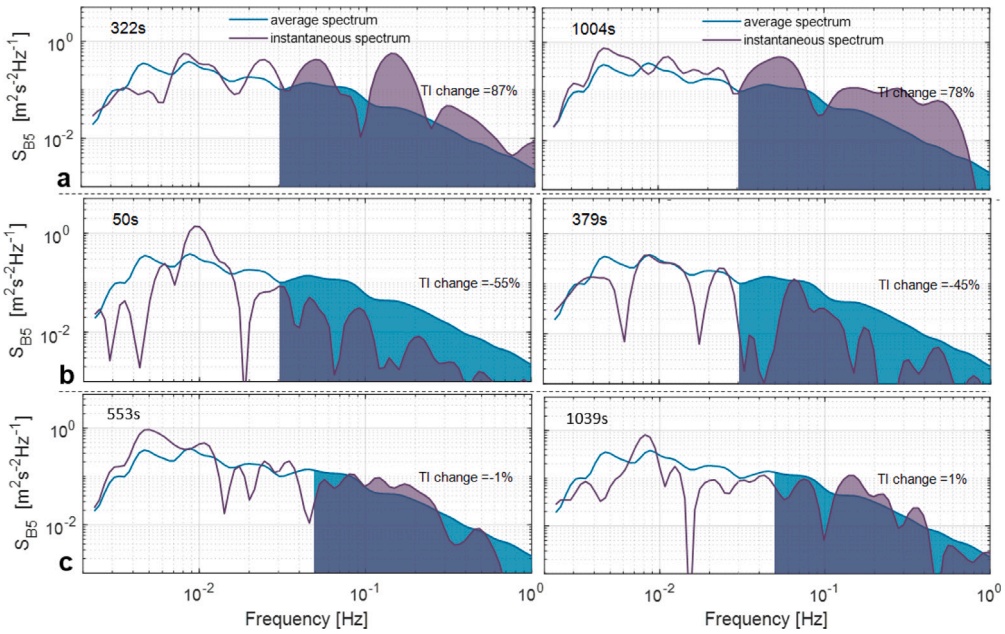

Fig. 9. Average and instantaneous spectra at time intervals shown in Fig. 8. The shaded parts show the area used in calculation of the partitioned variance and TI changes. Row (a) shows examples where instantaneous TI is significantly higher than average, (b) shows where instantaneous TI is lower than average and (c) shows where there is no significant change.

4.2. Fourier and wavelet comparison

This section presents a comparison of the Fourier and wavelet analysis results when used to derive the same quantities i.e. record averaged spectrum and coherence.

For context, turbulence frequencies which are important for device fatigue loads are marked on all the spectral analysis results. The cut-off frequency representing turbulent length-scale L, equivalent to 3 rotor diameters (60 m for the present case study) and a mean current velocity, $\overline{U}$ = 3 m/s is determined using Eq. (8), giving a frequency f_{60m} = 0.05 Hz. The BPF is based on an assumed rotational speed of 12 rpm, giving 0.2 Hz.

The average energy spectrum was calculated for a 10 min velocity sample (2400 data points) using wavelet and Fourier analysis, Eq. (1) to (6). A 10 min interval is considered suitable as it would capture the relevant turbulent scales. To compare the two methods, instantaneous wavelet spectra were time-averaged to give a global spectrum. Fig. 5 shows that the global wavelet spectrum has arbitrary scaling but once scaled using Eqs. (5) and (6), the wavelet and Fourier magnitudes are in close agreement, with the wavelet spectrum appearing as a smoothed version of the Fourier spectrum as described in Dynamique et al. (1995).

The variances calculated from the time series data and those from integrals of the PSDs are highlighted at the bottom of the plots in Fig. 5. The Fourier spectrum variances agree relatively well with the calculated variance for the vertical beam, 0.026 and 0.028, but show significant deviation for the slanted beam 0.021 and 1.139, likely due to the windowing effects. The inertial sub-range — a linear region with a -5/3 slope (Pope and Eccles, 2000) is visible for both methods, albeit obscured by the instrument noise at higher frequencies. Results for additional samples with the same flow characteristics are included in Fig. 12, and are consistent with the findings presented in Fig. 5.

Both the Fourier spectrum, Fig. 5 and Fourier coherence, Fig. 6 for beam 1 exhibit windowing effects — the aliasing of low-frequency components that do not fall within the frequency range of the window, characterised by a sharp tail at the low frequencies. This effect is not seen in the wavelet spectra and coherence.

Coherence was calculated using both Fourier and wavelet analysis for the same 10 min data extract, between two depths z = 18 m and z = 28 m, see Eq. (7). This spatial separation represents the coherence across the top half of the rotor for a seabed mounted device. To compare the two methods, instantaneous wavelet coherence was time-averaged to give a global coherence curve. Results from both methods (Fig. 6) show higher coherence at lower frequencies with the wavelet coherence appearing as a smoothed version of the Fourier coherence. The wavelet coherence tends towards a higher confidence level (due to a different number of degrees of freedom in coherence calculation) resulting in a higher discrepancy between the methods at high frequencies. Further time samples were analysed and are presented in Fig. 13. Most samples show a good agreement between the methods although, unlike the spectra, there is more variation in the measured coherence between samples.

The advantage of using ADCP data, compared to point measurements as has been done in previous studies, is that turbulence spectral characteristics can be studied throughout the water column. Fig. 7 shows the averaged spectra obtained by both methods throughout the water depth. The two methods show a similar result, with higher turbulence energy closer to the seabed. Similar to the results in Fig. 5, the wavelet spectra appear as a smoothed version of the Fourier.

Overall the averaged wavelet spectra and coherence agree well with the Fourier results, suggesting that this method is appropriate for analysing ADCP turbulence data. The main utility of wavelets however is the time–frequency analysis, which is presented in the following section.

4.3. Time–frequency analysis

Wavelet time–frequency analysis can be used to study the instantaneous spectra and coherence, allowing to detect the presence of energetic coherent bursts. A 20 min data interval was used for instantaneous analysis to observe how the turbulence spectra change in time.

4.3.1. Turbulence spectrum

The instantaneous turbulence spectrum shown in Fig. 8(a) reveals intermittent, high energy fluctuations, which can persist for up to several minutes depending on the frequency. To quantify these instantaneous bursts, we calculate the instantaneous vertical turbulence

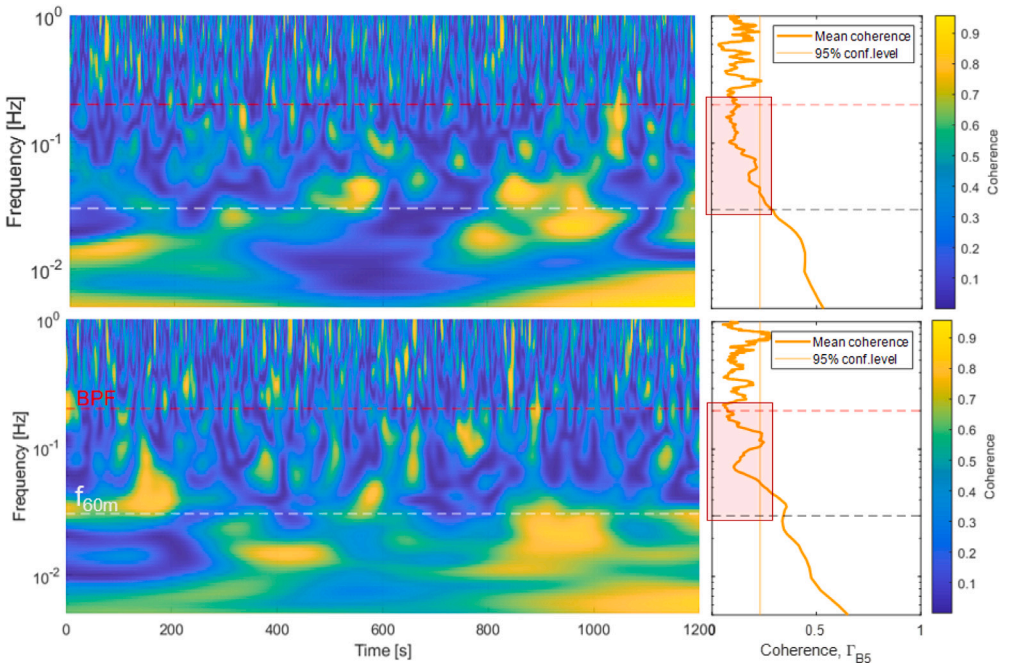

Fig. 10. Instantaneous coherence for the vertical beam (B5) compared to the average coherence obtained by Fourier analysis. Coherence was calculated for a 10 m separation distance for the bottom half of the rotor for the floating (top panel) and bottom mounted (bottom panel) cases as shown in Fig. 3.

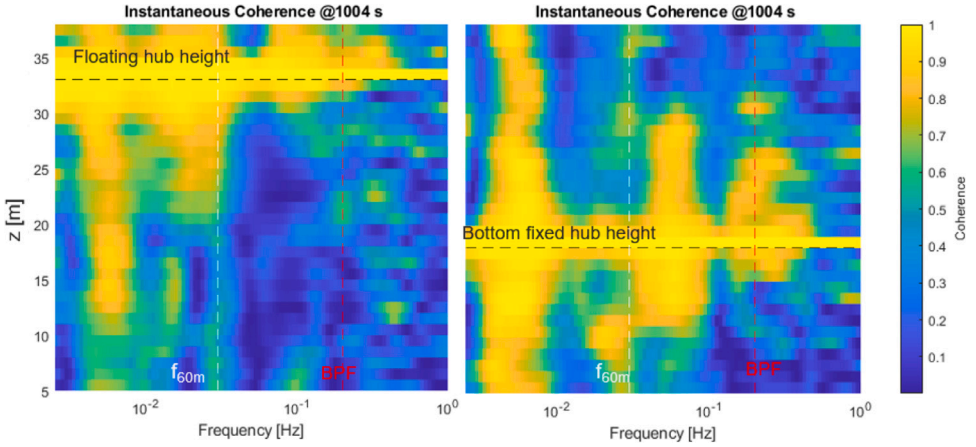

Fig. 11. Instantaneous wavelet coherence at 1004 s showing spatial correlation along the vertical beam, B5. The hub heights refer to the two case studies presented in Fig. 3.

intensity (TI) using the area under the PSD spectra using Eq. (3). Fig. 8(b) shows the instantaneous TI as a percentage of the 20 min average. The total TI is calculated using the whole spectrum and the partitioned TI is based on a band of frequencies which are the most relevant to TEC fatigue loads (0.05 Hz - 2 Hz). Fig. 8(b) shows that the TI peaks can be up to 80% higher than the average TI. This is important because typically device designers would use the average value for load calculations. These findings show that the instantaneous fluctuations can be much higher but are not represented well by averages due to their intermittency.

The results presented in Fig. 8 are for the vertical beam measurements and hence demonstrate variability in the vertical velocity components. Streamwise oriented, inclined beams (B1 and B3) were also analysed in the same way and the bursts were found to peak to similar levels 60%–85% (graphics excluded for brevity). Additionally, the partitioned TI (which is based on the most damaging TEC frequencies) deviates slightly more from the average than the one based on all frequencies, Fig. 8(b).

Fig. 9 shows how the instantaneous spectra compare to the average for the selected time instants. These demonstrate that the bursts occur across a range of frequencies, and in particular at the most damaging frequencies (f_{60m} = 0.05 Hz) which would be the most significant in terms of fatigue load impacts. In other words, when the instantaneous turbulence bursts occur, the energy is increased at frequencies known to be damaging to TECs.

4.3.2. Spatial coherence

Instantaneous wavelet coherence is compared to the Fourier coherence in Fig. 10. The very large coherent structures (f <0.01 Hz) persist for longer, occupying a large part of the timeline, whereas smaller structures tend to be more intermittent with durations ranging from several minutes to several seconds. Between the two marked frequencies, the average coherence line mostly sits below the 95% confidence level (region highlighted in red on Fig. 10), whereas the instantaneous view shows that there are frequent coherent bursts within these bands. This reflects the intermittent nature of real turbulent flows and highlights the limitations of using methods which yield average parameters, such as Fourier analysis, which tend to obscure the intermittent features.

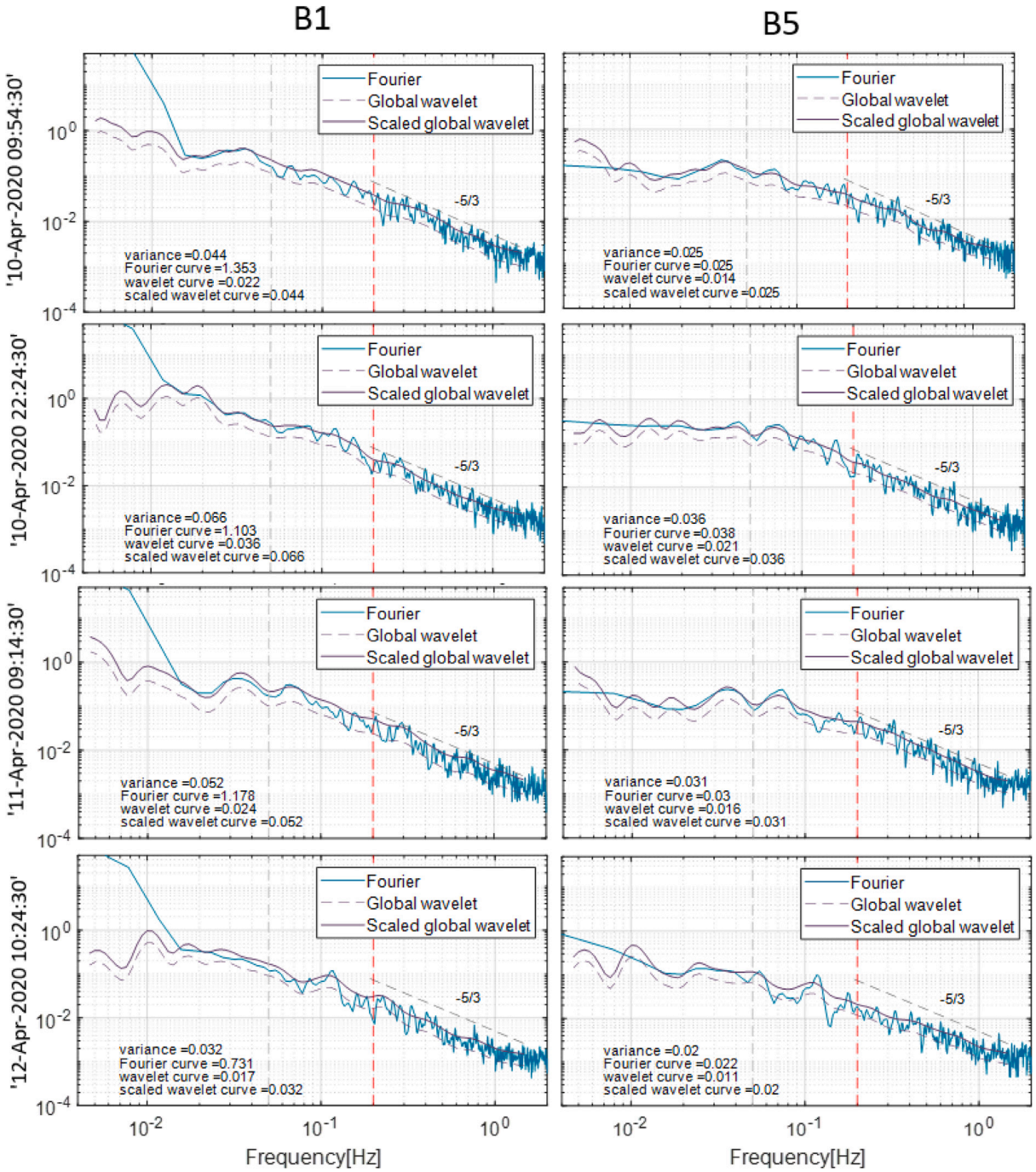

Fig. 12. Fourier and Wavelet spectra comparisons for alternative time samples. Samples are selected from flood cycles on either side of the presented cycle (as shown in Fig. 2), with the same flow characteristics.

In addition to identifying the passing of coherent structures in time, spatial analysis can be used to understand the position and extent of such structures throughout the water column. Utilising the profiling capabilities of ADCPs, the spatial variation of coherence along the vertical beam is presented in Fig. 11 for a single time instant at 1004 s (all time instants can be viewed in the supplementary video).

Fig. 11 shows that coherent structures tend to reside in fairly discrete frequency bands as described by Kelley et al. (2005). Coherency depends on the frequency analysed as well as on the separation distance. This is clearly visible in Fig. 11, where larger scale structures ($f < 0.01$ Hz) extend across most of the water column, whereas smallest scales show only a weak coherence across 2-3 m.

The large scale structures are unlikely to have a fatigue load impact on the TEC rotor as they occupy the whole water column and last for several minutes. These bursts will likely be experienced as a change of mean flow, and are unlikely to contribute to high frequency fatigue loading. However, sometimes the structures can occupy only the upper or lower half of the rotor (see supplementary video in Appendix A around 970 s), creating a coherent region that the blades will "slice" through. This means that in this case, large structure could have an

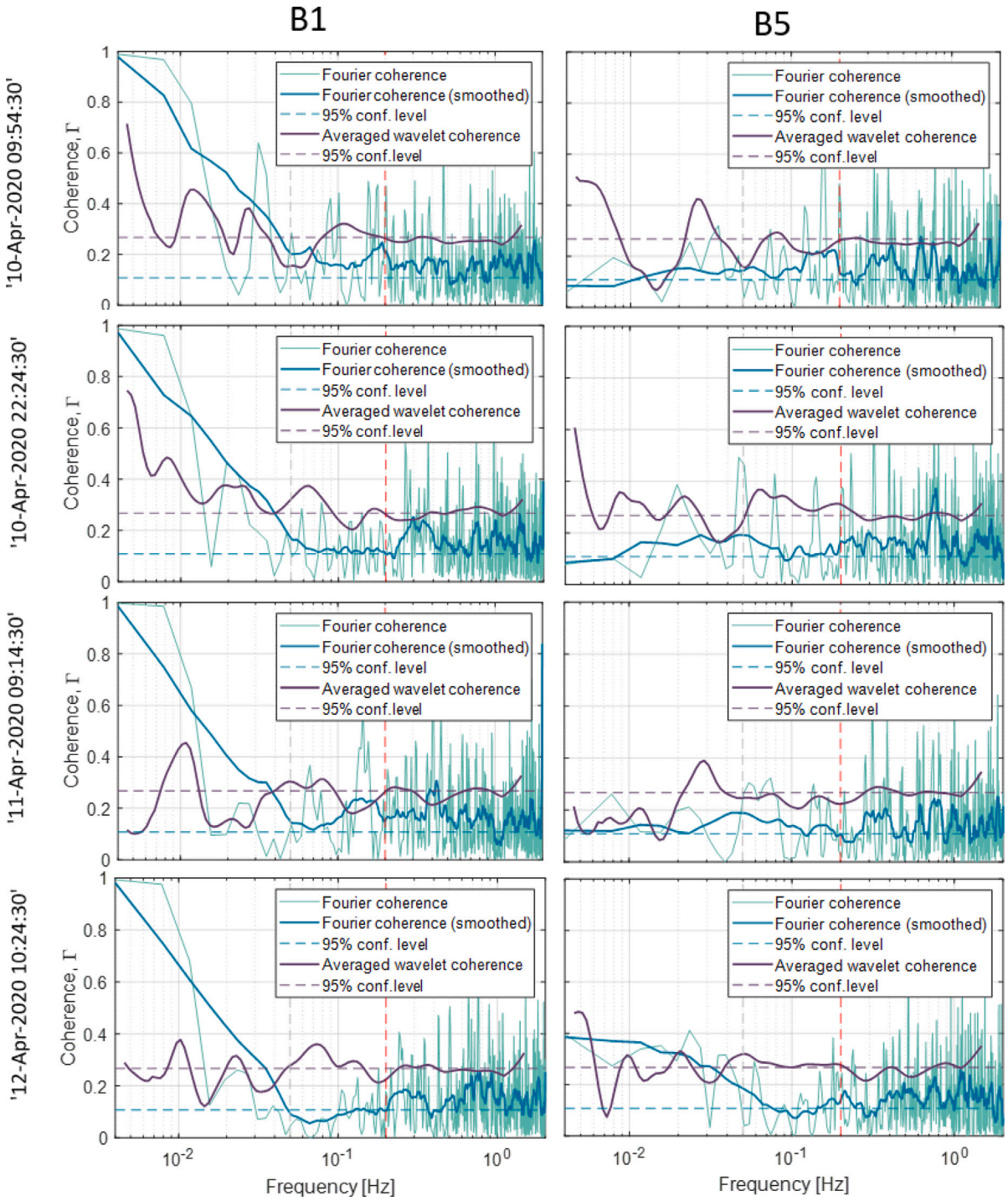

Fig. 13. Fourier and Wavelet coherence comparisons for alternative time samples. Samples are selected from flood cycles on either side of the presented cycle (as shown in Fig. 2), with the same flow characteristics.

impact on fatigue loads due to rotational sampling, which could induce eccentric bending modes on the blades and the rotor.

In the fixed TEC case (Fig. 11), the structures near the f_{60m} frequency occupy a spatial region similar to the rotor size i.e. approximately 20 m. Energetic bursts at the rotational frequency are likely to be amplified and results in significant load peaks.

By carrying out such spatial analysis over time, for example by counting the occurrence and durations of coherent structures in key positions, we can better understand the turbulence loads that will be experienced by a TEC.

It must be noted that as the turbulent flow field approaches the rotor, blockage will result in the distortion of the flow field. In a study by Milne and Graham (2019), the authors found that depending on the operating velocity and length scales, the blockage can results in an attenuation of the low-frequency spectral components or can lead to an amplification of these components. Such distortion would change the position of coherent structures and affect the intermittency of the flow. This should be taken into account when carrying out predictions of unsteady loading of turbine blades using undisturbed turbulence as the input boundary condition (Milne and Graham, 2019).

5. Conclusion

A number of previous studies have characterised the turbulence spectrum and coherence from ADCP data using Fourier analysis. In this study we have applied wavelets to perform time–frequency analysis on instantaneous ADCP data, which has allowed a detailed investigation into the coherent turbulent structures at a real tidal site.

The data was collected at the Falls of Warness tidal test site using a 5 beam ADCP, set up for turbulence measurements. The instantaneous parameters obtained from wavelet analysis were averaged to enable direct comparison with the traditional Fourier analysis. The instantaneous quantities were then further analysed to demonstrate the additional capabilities of wavelets in turbulence analysis of real flows.

The comparison of the two methods showed that wavelet analysis is an appropriate tool for analysing non-stationary turbulence in real tidal channels and when averaged, agrees favourably with the traditional Fourier analysis approach.

The main advantage of wavelets is the time–frequency analysis, which in this study has demonstrated the presence of highly energetic, intermittent turbulent bursts at this site. Quantification of such instantaneous turbulence bursts showed that they are highly energetic, with TI 80% higher than the average TI. This has implications for devices designers as the average value would normally be used in load calculations, which would not capture the extent of the energetic fluctuations. Turbulent events such as large, anisotropic eddies passing through the rotor region, are important to tidal energy converter design as they are a significant driver of loads. Comparing the instantaneous quantities to the Fourier quantities clearly demonstrates that these are insufficient to fully define transient, anisotropic, turbulent structures in the Falls of Warness tidal site.

ADCP data is advantageous as it provides measurements throughout the water column. The presented spatial analysis showed that coherent structures occur throughout the water column and are associated with high energy peaks at frequencies damaging to turbines. Such spatial analysis could be expanded to understand the intermittency throughout the water column over time.

Another potential future application of wavelet analysis could be to separate the coherent non-Gaussian components from the incoherent Gaussian components of real turbulent flows (Van Den Berg, 2004). This involves using the discrete wavelet transform and has been demonstrated in Hu and Du (2020) and Nan (2016). Such analysis could be helpful in enhancing stochastic turbulence models. These models are efficient but are only capable of producing weakly coherent flows. In stochastic wind turbulence models, coherent events (normally produced by Large Eddy Simulation (LES) models) can be superimposed in the time domain onto the more random, background turbulence to produce a more realistic flow. By separating out the coherent events in the real data, a similar technique could be used to incorporate these into the stochastic tidal models.

This work highlights the need to enhance site characterisation methodologies to include analysis on coherent and intermittent flow features, which have been found to be highly energetic and are likely to be damaging to tidal energy devices. The wavelet analysis outlined in this paper allows such events to be identified and analysed. Understanding the instantaneous turbulent fluctuations will enable to more accurately simulate loads on tidal devices and hence reduce uncertainty in design.

CRediT authorship contribution statement

Alyona Naberezhnykh: Conceptualization, Methodology, Formal analysis, Investigation, Writing – original draft. **David Ingram:** Conceptualization, Methodology, Supervision, Writing – review & editing. **Ian Ashton:** Conceptualization, Methodology, Supervision, Writing – review & editing.

Declaration of competing interest

The authors declare that they have no known competing financial interests or personal relationships that could have appeared to influence the work reported in this paper.

Data availability

The authors do not have permission to share data.

Acknowledgements

The authors wish to thank David Darbinyan from the European Marine Energy Centre and Calum Miller from Orbital Marine Energy for their support for this project.

This work was funded as part of the EPSRC, United Kingdom and NERC, United Kingdom Industrial Centre for Doctoral Training in Offshore Renewable Energy (IDCORE), Grant number EP/S023933/1.

Many thanks to Dr. Weichao Shi from the University of Strathclyde for their valuable inputs and suggestions, contributing to the redaction of this paper.

Appendix A. Supplementary data

Supplementary material related to this article can be found online at https://doi.org/10.1016/j.oceaneng.2022.113616.

References

Akansu, A.N., Haddad, R.A., 2001. Time-frequency representations. Multiresolution Signal Decompos. 331–390. http://dx.doi.org/10.1016/B978-012047141-6/50005-7.

Bian, C., Liu, Z., Huang, Y., Zhao, L., Jiang, W., 2018. On estimating turbulent Reynolds stress in wavy aquatic environment. J. Geophys. Res.: Oceans 123, 3060–3071. http://dx.doi.org/10.1002/2017JC013230.

Blackmore, T., Myers, L.E., Bahaj, A.S., Gaurier, B., Myers, L., Germain, G., 2015. The effect of freestream turbulence on tidal turbines. URL https://www.researchgate.net/publication/282807576.

Camussi, R., Robert, G., Jacob, M.C., 2008. Cross-wavelet analysis of wall pressure fluctuations beneath incompressible turbulent boundary layers. J. Fluid Mech. 617, 11–30. http://dx.doi.org/10.1017/S002211200800373X.

Chen, K., Zhang, Y., Zhong, Q., 2019. Wavelet coherency structure in open channel flow. Water (Switzerland) 11, http://dx.doi.org/10.3390/w11081664.

Chiao, L.Y., Wang, Y.H., 2004. Multiresolution interpolation and detiding of the ADCP data. J. Atmos. Ocean. Technol. 21, 122–134. http://dx.doi.org/10.1175/1520-0426(2004)021<0122:MIADOT>2.0.CO;2, not sure how relevant this is to my work....

Clark, T., Black, K., Ibrahim, J., Hernon, J., White, R., Minns, N., Fisher, S., 2015a. Part 2: Data processing, classification and characterisation of turbulent flows. Turbulence: Best Pract. Tidal Power Ind..

Clark, T., Roc, T., Fisher, S., Minns, N., 2015b. Part 3: Turbulence and turbulent effects in turbine and array engineering. Turbulence: Best Pract. Tidal Power Ind..

Dynamique, L.D.M., Cedex, P., Bascievant, C., 1995. Wavelet spectra compared to Fourier spectra. J. Math. Phys. 36, 1506–1519, URL http://link.aip.org/link/?JMAPAQ/36/1506/1.

Emery, W., Thomson, R., 2014. Data Analysis Methods in Physical Oceanography. Elsevier, URL https://books.google.co.uk/books?id=gYc4fp_ixmwC.

European Commission, 2016. Ocean energy strategic roadmap: Building ocean energy for europe. Ocean Energy Forum 74, URL https://webgate.ec.europa.eu/maritimeforum/en/frontpage/1036.

Farge, M., Schneider, K., 2004. Wavelets: Application to turbulence. Encycl. Math. Phys.: Five-Volume Set 408–420. http://dx.doi.org/10.1016/B0-12-512666-2/00274-1.

Flinchem, E.P., Jay, D.A., 2000. An introduction to wavelet transform tidal analysis methods. Estuar. Coast. Shelf Sci. 51, 177–200. http://dx.doi.org/10.1006/ecss.2000.0586.

France Energies Marines, 2020. Characterization of the vertical evolution of the three-dimensional turbulence for fatigue design of tidal turbines.

Garel, E., Cai, H., 2018. Effects of Tidal-Forcing Variations on Tidal Properties Along a Narrow Convergent Estuary. 41, Springer Stable, pp. 1924–1942, URL: https://www.jstor.org/stable/44858200 Effects of Tidal-Forcing Variations on Tidal Pro.

Guion, R.U., Young, A.M., 2015. The frequency response of acoustic Doppler current profilers: Spatiotemporal response and implications for tidal turbine site assessment. In: 2014 Oceans - St. John's, OCEANS 2014. http://dx.doi.org/10.1109/OCEANS.2014.7003057.

Hu, H., Du, X.H.P., 2020. Extracting coherent structures in near-wall turbulence based on wavelet analysis. Intech 13, URL http://dx.doi.org/10.1039/C7RA00172J%0Ahttps://www.intechopen.com/books/advanced-biometric-technologies/liveness-detection-in-biometrics%0Ahttp://dx.doi.org/10.1016/j.colsurfa.2011.12.014.

Indrusiak, M.L.S., 2004. Wavelet analysis of experimental turbulence time series. In Practice.

IOOS, 2019. Manual for real-time quality control of stream flow observations (qartod) v2.1. http://dx.doi.org/10.25923/sqe9-e310.

Kelley, N.D., Jonkman, B.J., Scott, G.N., Bialasiewicz, J.T., Redmond, L.S., 2005. The impact of coherent turbulence on wind turbine aeroelastic response and its simulation. p. 22, URL http://www.nrel.gov/docs/fy05osti/38074.pdf.

Kelley, N.D., Osgood, R.M., Bialasiewicz, J.T., Jakubowski, A., 2000. Using wavelet analysis to assess turbulence/rotor interactions. Wind Energy 3, 121–134. http://dx.doi.org/10.1002/we.33.

Kilcher, L.F., Thomson, J., Colby, J., 2014. Determining the spatial coherence of turbulence at mhk sites. In: Proceedings of the 2nd Marine Energy Technology Symposium. pp. 1–7.

Liu, Y., Liang, X.S., Weisberg, R.H., 2007. Rectification of the bias in the wavelet power spectrum. J. Atmos. Ocean. Technol. 24, 2093–2102. http://dx.doi.org/10.1175/2007JTECHO511.1.

McCann, G., Thomson, M., Hitchcock, S., Hassan, G., 2008. Implications of site-specific conditions on the prediction of loading and power performance of a tidal stream device. In: 2nd International Conference on Ocean Energy (ICOE). pp. 15–17, URL https://www.researchgate.net/profile/Graeme_Mccann/publication/228402190_Implications_of_Site-Specific_Conditions_on_the_Prediction_of_Loading_and_Power_Performance_of_a_Tidal_Stream_Device/links/5490039a0cf2d1800d8630ff/Implications-of-Site-Specific-Cond.

Mihanović, H., Orlić, M., Pasarić, Z., 2009. Diurnal thermocline oscillations driven by tidal flow around an island in the Middle Adriatic. J. Mar. Syst. 78, 157–168. http://dx.doi.org/10.1016/j.jmarsys.2009.01.021, skim read this! good explanation on coherene methods.

Milne, I.A., Day, A.H., Sharma, R.N., Flay, R.G., 2015. Blade loading on tidal turbines for uniform unsteady flow. Renew. Energy 77, 338–350. http://dx.doi.org/10.1016/j.renene.2014.12.028.

Milne, I.A., Day, A.H., Sharma, R.N., Flay, R.G., 2016. The characterisation of the hydrodynamic loads on tidal turbines due to turbulence. Renew. Sustain. Energy Rev. 56, 851–864. http://dx.doi.org/10.1016/j.rser.2015.11.095.

Milne, I.A., Graham, J.M., 2019. Turbulence velocity spectra and intensities in the inflow of a turbine rotor. J. Fluid Mech. 870, 870R31–870R311. http://dx.doi.org/10.1017/jfm.2019.339.

Milne, I.A., Sharma, R.N., Flay, R.G., Bickerton, S., 2010. The role of onset turbulence on tidal turbine blade loads. In: 17th Australasian Fluid Mechanics Conference 2010. pp. 444–447.

Milne, I.A., Sharma, R.N., Flay, R.G., Bickerton, S., 2013. Characteristics of the turbulence in the flow at a tidal stream power site. Phil. Trans. R. Soc. A 371, http://dx.doi.org/10.1098/rsta.2012.0196.

Nan, J., 2016. Wavelet analysis to detect multi-scale coherent eddy structures and intermittency in turbulent boundary layer. Intech 13.

Nortek, 2018. Signature manual; principles of operation. p. 43.

Ortega, A., Tomy, J.P., Shek, J., Paboeuf, S., Ingram, D., 2020. An inter-comparison of dynamic, fully coupled, electro-mechanical, models of tidal turbines. Energies 13, 1–19. http://dx.doi.org/10.3390/en13205389.

Ouro, P., Harrold, M., Stoesser, T., Bromley, P., 2017. Hydrodynamic loadings on a horizontal axis tidal turbine prototype. J. Fluids Struct. 71, 78–95. http://dx.doi.org/10.1016/j.jfluidstructs.2017.03.009.

Pearson, N., Hernon, J., 2015. Turbulence : Best practices for measurement of turbulent flows.

Perez, L., Cossu, R., Couzi, C., Penesis, I., 2020. Wave-turbulence decomposition methods applied to tidal energy site assessment. Energies 13, http://dx.doi.org/10.3390/en13051245.

Petrusevich, V.Y., Dmitrenko, I.A., Niemi, A., Kirillov, S.A., Kamula, C.M., Kuzyk, Z.Z.A., Barber, D.G., Ehn, J.K., 2020. Impact of tidal dynamics on diel vertical migration of zooplankton in hudson bay. Ocean Sci. 16, 337–353. http://dx.doi.org/10.5194/os-16-337-2020.

Phanikumar, M.S., Aslam, I., Shen, C., Long, D.T., Voice, T.C., 2007. Separating surface storage from hyporheic retention in natural streams using wavelet decomposition of acoustic Doppler current profiles. Water Resour. Res. 43, 1–16. http://dx.doi.org/10.1029/2006WR005104.

Pope, S., Eccles, P., 2000. Turbulent Flows. Cambridge University Press, URL https://books.google.co.uk/books?id=HZsTw9SMx-0C.

Scarlett, G.T., Viola, I.M., 2020. Unsteady hydrodynamics of tidal turbine blades. Renew. Energy 146, 843–855. http://dx.doi.org/10.1016/j.renene.2019.06.153.

Sellar, B.G., Sutherland, D.R., 2016. Tidal energy site characterisation at the fall of warness, emec, uk energy technologies institute redapt Ma1001 (Md3.8). URL http://redapt.eng.ed.ac.uk.

Sentchev, A., Thiébaut, M., Schmitt, F.G., 2020. Impact of turbulence on power production by a free-stream tidal turbine in real sea conditions. Renew. Energy 147, 1932–1940. http://dx.doi.org/10.1016/j.renene.2019.09.136.

Sutherland, D.R., Noble, D.R., Steynor, J., Davey, T., Bruce, T., 2017. Characterisation of current and turbulence in the FloWave ocean energy research facility. Ocean Eng. 139, 103–115. http://dx.doi.org/10.1016/j.oceaneng.2017.02.028.

Thakur, G., Brevdo, E., Fučkar, N.S., Wu, H.T., 2013. The synchrosqueezing algorithm for time-varying spectral analysis: Robustness properties and new paleoclimate applications. Signal Process. 93, 1079–1094. http://dx.doi.org/10.1016/j.sigpro.2012.11.029.

The MathWorks Inc. Natick, Massachusetts, United States, 2022. MATLAB and wavelet toolbox release 2022.

Thomson, J., Kilcher, L., Harding, S., 2014. Multi-scale turbulence at tidal energy sites. In: Proceedings of the 5th International Conference on Ocean Energy, Halifax, Nova Scotia. pp. 1–6.

Togneri, M., Masters, I., Williams, A., Fairley, I., 2021. A spectral-statistical filter for decoupling wave and turbulence effects at tidal sites. In: Proceedings of the European Wave and Tidal Energy Conference. 1927–1–1927–10.

Torrence, C., Compo, G.P., 1997. A practical guide to wavelet analysis. J. Mater. Sci. 32, 2623–2627. http://dx.doi.org/10.1023/A:1018662703668.

Van Den Berg, J., 2004. Wavelets in Physics. Cambridge University Press, Cambridge.

Yuan, Y., Yang, C., heng Tseng, Y., Zhu, X.H., Wang, H., Chen, H., 2017. Analysis of longer period variation of the Kuroshio Current intrusion into the Luzon Strait using rectified wavelet power spectra. Prog. Oceanogr. 156, 61–77. http://dx.doi.org/10.1016/j.pocean.2017.04.013, might need to revisit the rectified method.

energies

MDPI

Article

How Applicable Are Turbulence Assumptions Used in the Tidal Energy Industry?

Alyona Naberezhnykh [1,2,3,*], David Ingram [1], Ian Ashton [2] and Joel Culina [4]

[1] King's Buildings Campus, University of Edinburgh, Edinburgh EH8 9YL, UK
[2] College of Engineering Mathematics and Physical Sciences, University of Exeter, Exeter EX4 4QF, UK
[3] The Charles Clouston Building ORIC, European Marine Energy Centre, Back Road, Stromness KW16 3AW, UK
[4] Fundy Ocean Research Centre for Energy, 1156 W Bay Rd, Parrsboro, NS B0M 1S0, Canada
* Correspondence: a.

Abstract: As tidal current and marine hydro-kinetic energy converters start to be deployed in pre-commercial arrays, it is critical that the design conditions are properly characterised. Turbulence is known to influence fatigue loads and power production, so developers use turbulence models to generate unsteady flows in order to simulate device performance. Most such models construct a synthetic flow field using a combination of measured parameters and theoretical assumptions. The majority in use today are based on atmospheric flow conditions and may have limited applicability in tidal environments. In the present work, we compare key turbulence model assumptions (which are recommended by the tidal turbine standards and are used in design software) to turbulence measurements from two tidal test sites in Scotland and Canada. Here, we show that the two sites have different levels of conformity to theoretical models, with significant variability within nearby locations at the same site. The agreement with spectral models is shown to be depth-dependent. The vertical component spectrum is better represented by the Kaimal model, while the streamwise spectrum is better represented by the von Kármán model. With the exception of one site, the shear profiles follow a power law, although with a different exponent to that commonly assumed. Both sites show significant deviations from the theoretical length scales and isotropy ratios. Such deviations are likely to misrepresent the loads experienced by a device. These results highlight the turbulence characteristics at real deployment sites, which are not well represented by current models, and, hence, which must be determined using field measurements.

Keywords: turbulence; characterisation; model; standards; fatigue load; tidal energy; hydro-kinetic energy converter; Tidal Bladed; TurbSim

Citation: Naberezhnykh, A.; Ingram, D.; Ashton, I.; Culina, J. How Applicable Are Turbulence Assumptions Used in the Tidal Energy Industry? *Energies* **2023**, *16*, 1881. https://doi.org/10.3390/en16041881

Received: 18 January 2023
Revised: 9 February 2023
Accepted: 10 February 2023
Published: 14 February 2023

1. Introduction

Tidal energy could meet a significant portion of electricity requirements, with an estimated exploitable tidal stream resource of 11.5 GW in the UK and 35 GW in Canada alone [1,2]. Tidal energy can also provide a viable, competitive solution for remote islands and areas where access to energy is difficult. The technology development has recently received a significant boost when the UK Government announced a dedicated tidal stream allocation under its Contracts for Difference (CfD) scheme—the UK government's main mechanism for supporting low-carbon electricity generation [3]. However, the risks associated with the durability of these relatively new technologies are not yet fully understood and can lead to conservative designs, driving up costs [4].

To be commercially viable, tidal-energy converters (TECs) must endure up to 25 years in the water without requiring major overhaul or repair [5]. Several studies [5–10] highlight that turbulence, as well as other sources of unsteady loading, can significantly impact fatigue life and power output, affecting the device's commercial viability. Power quality

and energy yield are both affected by turbulence, the latter because a dynamic controller will sacrifice energy yield for power quality during turbulent flow [6,11].

There are two main sources for tidal turbine design guidelines: IEC 62600 Technical Specifications [12] and the DNVGL-ST-0.164: Tidal turbines standard [13]. Both sources provide limited information on the treatment of turbulence-induced loading. Typically, where direct measurements are not available, it is recommended to use semi-analytical models for the velocity shear profile, turbulence spectrum and spatial coherence. Such models are often based on atmospheric flow conditions and may have limited applicability in tidal environments. Recommendations from standards are also implemented in commercial software, such as Tidal Bladed and OpenFAST/TurbSim. These tools and guides were originally developed for wind energy and, hence, many of the recommendations are aligned with the wind standard (BSI Standards Publication: Wind energy generation systems IEC 61400 [14]). Tidal-flow turbulence will have different characteristics to atmospheric flows due to boundary-layer effects, tidal cycles, density and other factors. Using atmospheric-based models may present additional uncertainty in tidal turbine load simulations. In this paper, we aim to clarify the applicability of the key turbulence models typically used in the industry.

2. Review of Models

Commercial codes, such as Tidal Bladed, construct a turbulent flow field from a set of measured or assumed input parameters, as illustrated in Figure 1. The flow field is advected past the rotor area which defines the velocity vector at each calculation point at the rotor at each time instant. This is then used as input for the blade element momentum (BEM) model calculations. The key input parameters for the flow field are explained in this section.

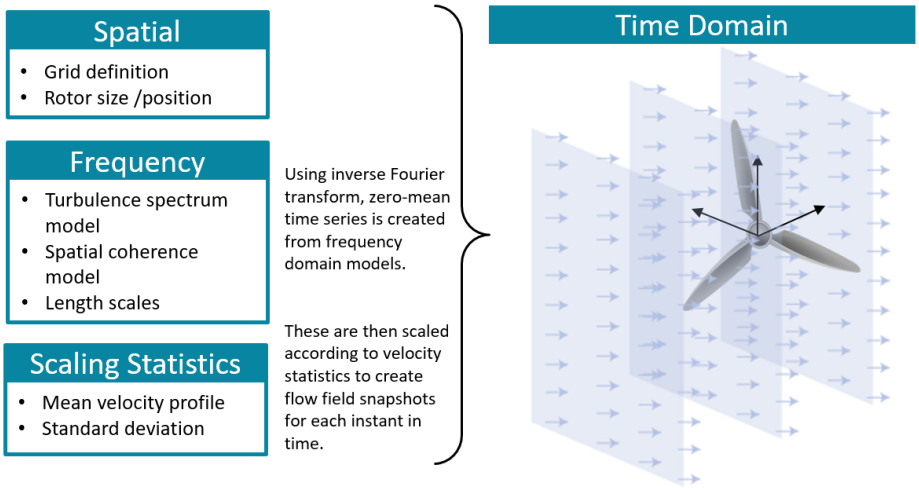

Figure 1. Simplified illustration of input parameters required to construct flow fields in Tidal Bladed and TurbSim, adapted from TurbSim user's guide [15].

2.1. Frequency

2.1.1. Turbulence Spectrum

The turbulence spectrum expresses how the turbulence energy is distributed among various frequencies. Typically, this would be represented by a model spectrum, which is a function of the current magnitude U, variance σ_u^2 and length scales, L. The Kaimal and von Kármán spectra are the most commonly used models in commercial codes and guides. These semi-empirical forms use coefficients applicable to atmospheric boundary-layer

flows. Length scales can be specified by the user or theoretical values may be applied. The models are defined in the variance-preserving format as follows:

$$\text{Kaimal: } \frac{fS_u(f)}{\sigma_u^2} = \frac{4fL_{u_K}/\overline{U}}{(1+6fL_{u_K}/\overline{U})^{5/3}}, \tag{1}$$

$$\text{von Kármán: } \frac{fS_u(f)}{\sigma_u^2} = \frac{4fL_{u_{VK}}/\overline{U}}{(1+70.8(fL_{u_{VK}}/\overline{U})^2)^{5/6}}. \tag{2}$$

The Kaimal spectrum has the same form for v and w components as in Equation (1), but with different length scales. The von Kármán form for components $i = v, w$ is:

$$\frac{fS_i(f)}{\sigma_i^2} = \frac{4fL_{i_{VK}}/\overline{U}(1+755.2(fL_{i_{VK}}/\overline{U})^2)}{(1+283.2(fL_{i_{VK}}/\overline{U})^2)^{11/6}}. \tag{3}$$

Isotropy describes the degree to which turbulence is statistically invariant under rotations. The anisotropy ratio, α is given by Equation (4) and ranges from 0 for extremely anisotropic turbulence to 0.5 for isotropic turbulence [16].

$$\alpha = \frac{\sigma_w}{\sigma_u + \sigma_v} \tag{4}$$

Isotropy is implied when using the von Kármán model [17]; the Kaimal model assumes an anisotropy ratio, $\sigma_u : \sigma_v : \sigma_w = 1 : 0.8 : 0.5$.

Tidal Bladed provides options to use either the von Kármán, Kaimal or Mann models for generating turbulent flows, while TurbSim allows the use of Kaimal or von Kármán, as well as some other case-specific, atmospheric turbulence spectra.

2.1.2. Spatial Coherence

Spatial coherence describes the correlation of the streamwise fluctuations across a separation distance, r, at each distinct frequency.

The IEC wind standard provides an empirical model of streamwise coherence [14], which can be used with the Kaimal or von Kármán model spectra. This IEC coherence model is used in codes such as Tidal Bladed and TurbSim. The model is a function of the average current magnitude, U length scales, L_u and separation distance, r and is defined as:

$$C_u(\Delta r, f) = exp\left(-8.8\Delta r\sqrt{\left(\frac{0.12}{L_u}\right)^2 + \left(\frac{f}{\overline{U}}\right)^2}\right). \tag{5}$$

2.1.3. Length Scales

The length scale, L is defined qualitatively as the size of the most energetic eddies in a turbulent flow [18]. Length scale values are required as input into the spectral and coherence models. Tidal Bladed and TurbSim give the option to use the default values or user input length scales [19]. The default values for the IEC models define the streamwise length scale, $L_u = 8.10\,\Lambda_U$, where $\Lambda_U = 0.7\times$ min (30 m, hub height), in line with the IEC 61400-1 wind standard [15,20]. The default length scale values are based on atmospheric flows and tend to ignore the upper limit on eddy size imposed by the air–water interface [21].

Another way to estimate the length scale is according to open-channel flow theory, where the measured turbulent length scales across the lower half of the water column can be approximated as $L_u \approx \sqrt{zH}$, where z is the relative elevation from the sea bottom [22].

2.1.4. Mean Velocity Profile

The shear profile of the velocity normal to the seabed in a tidal race constitutes a high Reynolds number turbulent boundary layer. The DNVGL-ST-0.164: Tidal turbines standard states that, when detailed field measurements are not available, the variation in sub-surface

current velocity with depth may be modeled as a simple power law, where the exponent α is typically taken as 1/7:

$$U_{c,sub}(z) = U_{ref}(\frac{d+z}{h_{ref}})^{\alpha} \text{ for } z \leq 0. \quad (6)$$

It does, however, caution that, in some cases, where more complex current speed shear profiles are featured, log-law or parabolic profiles could be observed [13]. Tidal Bladed recommends the use of the 1/7th-power-law profile but provides functionality to change the exponent value.

2.1.5. Turbulence Intensity

Turbulence intensity, I, is a term adopted from the wind industry and is a measure of the magnitude of fluctuations as a percentage of the mean flow velocity: [23]:

$$I_{total} = \frac{\sqrt{\frac{1}{3}\langle u'^2 + v'^2 + w'^2 \rangle}}{\overline{u}} \times 100 \quad (7)$$

$$I_u = \frac{\sqrt{u'^2}}{\overline{u}} \times 100 = \frac{\sigma_u}{\overline{u}} \times 100 \quad (8)$$

Tidal Bladed and TurbSim use the standard deviation (or turbulence intensity) for each velocity component to scale the velocity fluctuations. They typically allow input of only the hub height value, neglecting any variation across the rotor.

3. Literature Review

A number of studies have attempted to validate the models described in the preceding section against tidal-flow measurements.

Comparisons of the Kaimal and von Kármán spectrum models to measurements generally show an agreement with the shape of the curve; however, the peak of the spectrum is often not aligned. Moreover, there is no agreement on which model is more appropriate for tidal flows. Comparing the two models to ADCP data from the Grand Passage in Nova Scotia, ref. [21] found that the streamwise variance at large scales is better predicted by the Kaimal model than the von Kármán, provided that the degree of anisotropy is permitted to vary throughout the water column. Another study, from the Sound of Islay [24], found that the Kaimal model over-predicted the energy content at the lowest frequencies of the streamwise spectrum, while the von Kármán provided a better fit. Comparison of ADV measurements from a shallow tidal flow (<10 m depth) to the non-dimensionalised Kaimal spectrum, showed agreement with the general shape of the spectrum, although the variance in the measured curves was shifted towards higher frequencies [25]. Previous studies mostly focused on measurements near the seabed [24,25], so little is known about the applicability of models higher-up in the water column, which is critical for floating devices.

Due to the seabed roughness, bathymetric effects and the free surface, the real shear profiles can deviate from the analytical cases. A number of studies [26–29] found the shear profiles at EMEC's Fall of Warness tidal site had large velocity variations with complex profiles that did not follow the analytical models. Furthermore, the flood and ebb tides had two distinct profile shapes, one logarithmic and one roughly polynomial. The shear profiles were also found to vary by velocity and acceleration/deceleration. Ref. [30] found the velocity profile at Ramsey Sound (Wales, UK) during ebb tides followed a power-law distribution over the entire water column. During flood tides, the logarithmic distribution of velocities was observed over the bottom half of the water column only, with the remainder being almost uniform up to the free surface.

Although turbulence intensity is expected to vary with depth and take on different profiles for various parts of the tidal cycle, models such as Tidal Bladed make the simplification of constant standard deviation throughout the water column, normally just using

the hub height parameters [20,31]. In analysing the turbulence intensity profiles at the Ramsey Sound tidal site, in [32] showed notably asymmetric flow conditions during ebb and flood tides and variability within each tidal phase. At peak ebb flow, highest values of I_x were found near the seabed and free surface and lowest values were attained at height $z/H \approx 0.6$. Conversely, during flood tide, the lowest turbulence intensity levels were found lower down in the water column at $z/H \approx 0.2$ [32].

Models often assume isotropic turbulence or apply theoretical anisotropy ratios. Comparisons by [24] of observed tidal and atmospheric anisotropic ratios showed that the anisotropy is more pronounced in a tidal channel than in the atmospheric boundary layer. This is consistent with the notion that energy in a tidal channel is restricted by the presence of a free surface, particularly in the vertical direction. In a LES simulation, in [33] found the anisotropy ratio $\sigma_u : \sigma_v : \sigma_w$ to be 1:0.64:0.88, which was quite different to the 1:0.75:0.56 found at the Sound of Islay (Scotland) tidal site or to two-dimensional channel flows, in which the ratio is 1:0.71:0.55 [22].

Past studies suggest that some turbulence models may not be good representations of real tidal sites. The aim of this paper is to carry out a comprehensive comparison of the key parameters used in commercial codes and standards against observations from two energetic tidal test sites. This will help developers understand the applicability of models to real flows that full-scale devices will operate in, and reduce uncertainties associated with using theoretical values in modelling.

4. Methods

4.1. Measurements

The ADCP velocity data used in this study were gathered at two tidal sites, the European Marine Energy Centre (EMEC) and the Fundy Ocean Research Centre for Energy (FORCE). Data were collected from two nearby locations at each site, as shown in Figure 2, with FORCE-1 and FORCE-2 instruments located approximately 300 m apart and EMEC-1 and EMEC-2 instruments approximately 400 m apart. The instrument configurations are shown in Table 1.

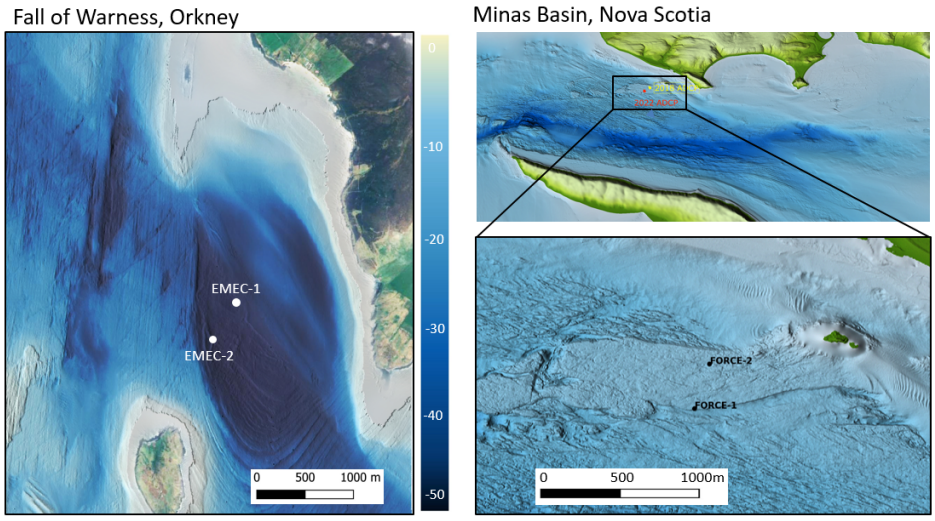

Figure 2. Channel bathymetry and the location of the ADCP instruments at FORCE and EMEC test sites.

Table 1. Instrument set up.

Reference	Instrument	Sample Rate	Bin Size	Measurement Period	Peak Flow	Depth
EMEC-1	Nortek Signature 500	4 Hz	1 m	10 Apr 2020–22 Apr 2020	3.8 m/s	48 m
EMEC-2	Sentinel V50	1 Hz	1 m	8 Nov 2019–19 Dec 2019	3.7 m/s	48 m
FORCE-1	Nortek Signature 500	2 Hz	1 m	27 Jan 2022–2 Apr 2022	4.6 m/s	38 m
FORCE-2	Sentinel V100	1 Hz	0.5 m	29 Jun 2018–29 Aug 2018	4.7 m/s	34 m

The average heading on both of the EMEC ADCP's was such that one beam pair was oriented approximately in the streamwise direction of the tidal current; however, FORCE ADCPs were not aligned with the flow (see Figure 3). This has important implications for the parameters which can be derived using the data, as explained in more detail in the following section.

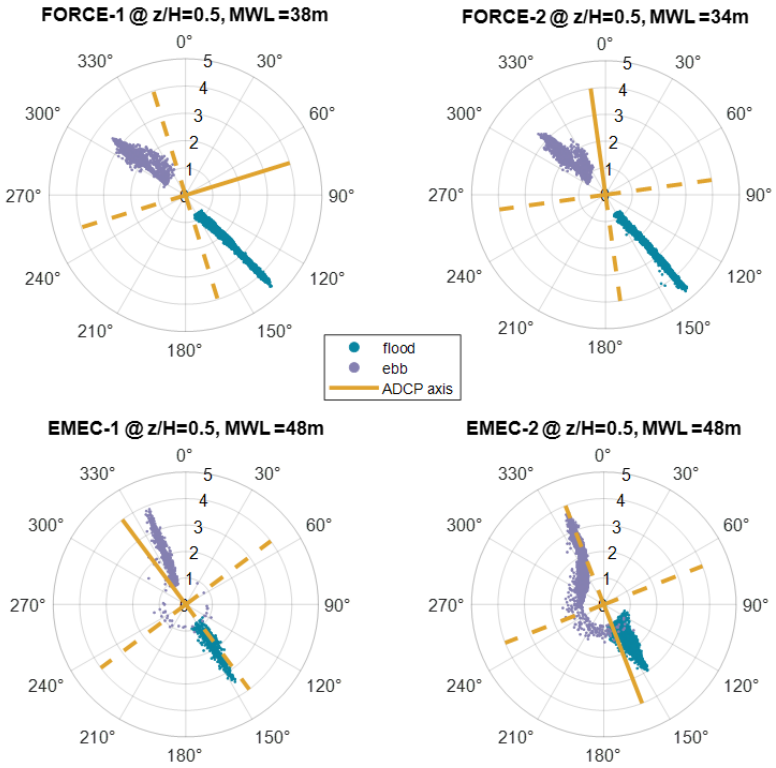

Figure 3. Tidal rose plots showing flow direction as well as ADCP orientation. Solid yellow line corresponds to the instrument heading.

4.2. Data Analysis

The raw data were processed and quality-controlled (QC) using EMEC's proprietary QC tool, IMPAQCT. This tool follows the Quality Assurance and Quality Control of Real Time Oceanographic data (QARTOD) standard [34], alongside the Nortek instrument manual [35] and flags any data which do not meet the QC thresholds.

To ensure parameters are comparable across the sites, all data have been split into 10-minute intervals and binned by tidal cycle, mean flow velocity and relative depth, z/H. Turbulence parameters were calculated for each 10-minute interval and averaged for each tidal cycle and flow velocities of 1–3 m/s for all datasets.

Due to the ADCP sampling rates, the spectral and coherence calculations were only carried out for EMEC-1 and FORCE-1 datasets.

4.2.1. Turbulence Spectrum

The MATLAB function `pwelch` was used to compute the discrete Fourier transform of each 10-minute time series using a fast Fourier transform (fft) algorithm. It allows specification for window size, type and overlap. By default, the time series is divided into the longest possible segments to obtain as close to, but not exceeding, eight segments, with 50% overlap, using a Hamming window. The modified periodograms are averaged to obtain the power spectral density (PSD) estimate. The default number of discrete Fourier transform (DFT) points is the greater of 256 or the next power of 2 greater than the length of the segments. In the PSD format, the area under the spectrum curve represents the variance for the data record.

In order to compare the measured spectra to the models, the measured spectra were de-noised and normalised by the variance so that the area under the spectrum = 1. De-noising was carried out by identifying Doppler noise variance for each beam using the spectral-fitting method [36–38] and subtracting this variance from the total beam variance. The vertical and streamwise model spectra were constructed using Equations (1) to (3), using measured values of mean velocity magnitude U and length scales L_i where $i = u, v, w$. The measured vertical spectrum was computed directly from the measured vertical beam velocities. Given that the area under the spectrum represents the variance, we apply the variance method [39,40] to calculate the streamwise spectrum from the spectra measured by individual beams:

$$S_{uu} = \frac{S_{b1b1} + S_{b2b2} - 2\cos^2\theta S_{b5b5}}{2\sin^2\theta}, \tag{9}$$

where S_{b1b1} and S_{b2b2} are the spectra of the two beams aligned to the streamwise direction, S_{b5b5} is the vertical beam spectrum, and θ is the beam inclination angle.

In the case of the FORCE-1 dataset, due to the misalignment of the instrument, streamwise metrics could not be reliably calculated. In this case, we compared the total energy spectrum, as this is unaffected by the rotation of the instrument, which is further explained in Section 4.2.6. Using the expression for obtaining the total kinetic energy [41] from the individual beam variances, the total measured spectrum was calculated as follows:

$$S_{total} = \frac{S_{b1b1} + S_{b2b2} + S_{b3b3} + S_{b4b4} - 2(2\cos^2\theta - \sin^2\theta)S_{b5b5}}{4sin^2\theta}. \tag{10}$$

The total model spectrum is constructed using equation:

$$S_{total} = \frac{S_{uu} + S_{vv} + S_{ww}}{2}, \tag{11}$$

where S_{uu}, S_{vv} and S_{ww} are calculated using Equations (1) to (3). All spectra were calculated for relative depths, $z/H = 0.2, 0.5, 0.7$.

4.2.2. Coherence

Spatial coherence, Γ was computed from two independent measurements of the same component of velocity that are separated in space by a vertical distance, r. Coherence is defined as [42]:

$$\Gamma = \frac{|\overline{F(u_1')F(u_2')|^2}}{\overline{S(u_1)S(u_2)}}, \tag{12}$$

where F is the fast Fourier transform, and $S(u) = |F(u')|^2$. We used the MATLAB function `mscohere` to calculate coherence for each beam. This function finds the magnitude-squared coherence estimate for two input signals. ADCP's do not provide a direct measurement of the streamwise velocity component, so we applied the coordinate transform to instan-

taneous beam velocities to obtain the streamwise component (making the assumption of homogeneity across the beam spread). These values were then used in the coherence calculation. Due to the uncertainty relating to the homogeneity assumption, we also calculated coherence using the raw beam velocities for comparison.

The 95% confidence level of Γ measurements—above which Γ estimates can be considered valid with 95% confidence—is equal to $\sqrt{6/n_{DOF}}$, where n_{DOF} is the number of degrees of freedom in the coherence estimate [43]. Coherence was analysed at relative depths $z/H = 0.2, 0.5, 0.7$ for a 5 m separation distance above and below the analysing depth. The model coherence was constructed using Equation (12) using measured length scales L, mean magnitude U and the separation distance, r.

4.2.3. Length Scales

Length scales were required as inputs to the spectral and coherence models, but we also compared the measured values to the default values in commercial codes.

Length scales are calculated by the auto-correlation method (Equation (13)) which measures the duration for which the largest eddies remain correlated and requires the application of Taylor's frozen field hypothesis. The hypothesis can be applied under the assumption that turbulence advects faster than it evolves (for further explanation, see [44]).

$$R(\tau) = \frac{\langle (u_t - \overline{u})(u_{t+\tau} - \overline{u}) \rangle}{\sigma_u^2}, l_u = \overline{u} \sum_{\tau=0}^{R(\tau)=0} R(\tau) d\tau \tag{13}$$

Correlation methods require instantaneous velocities, which are only reliable in beam coordinates at depths where the beam spread becomes significant. At these depths the beam spread may be interpreted as the minimum length scale of turbulence that is measured accurately by the ADCP [28]. For this reason, a check is carried out to ensure the computed length scales are greater than the beam spread.

4.2.4. Shear Profile

Shear profiles were calculated by averaging velocity magnitudes at each depth bin for the flood and ebb cycles and for the velocity range 1–3m/s. A power-law model, as described in Equation (6), was fitted to the data, calculating the exponent α.

4.2.5. Turbulence Intensity

Reynolds stresses represent the momentum flux due to turbulent fluctuations and relate to the auto- and cross-spectra terms S_{ij}. The Reynolds stress tensor is defined as [45]:

$$R_{ij} = -\rho \overline{u_i u_j} = -\rho \begin{pmatrix} \overline{u'^2} & \overline{u'v'} & \overline{u'w'} \\ \overline{u'v'} & \overline{v'^2} & \overline{v'w'} \\ \overline{u'w'} & \overline{v'w'} & \overline{w'^2} \end{pmatrix} \tag{14}$$

where ρ is the fluid density and u, v, w are the streamwise, lateral and vertical velocity components, respectively. Due to symmetry, the tensor contains six unique terms. The normal stresses, on the diagonal, are used to calculate the turbulence intensity, I, defined in Equation (7) or the turbulent kinetic energy (TKE), defined as:

$$TKE = \frac{1}{2} \langle u'^2 + v'^2 + w'^2 \rangle \tag{15}$$

The off-diagonal terms are the shear stresses, also known as Reynolds stresses.

A 5-beam ADCP allows for a true measurement of vertical velocities and the estimation of five Reynolds stress terms (all but $u'v'$), TKE, I and anisotropy directly from the along-beam velocities [46]. The orientation of the beams to the flow is vital. If the beams are not aligned with the flow direction, only the total I or TKE quantities can be reliably calculated [28], as explained in Section 4.2.6. In other words, unless the beam pairs are

aligned to the flow, the Reynolds stress components will not be resolved in the right coordinate system, and rotation of the tensor is not possible, as all six Reynolds stress terms are not known.

To calculate the Reynolds stresses, the variance method is employed. The variances are first determined in along-beam coordinates, then combined by assuming statistical characteristics (variance) are homogeneous over the beam spread (for further explanation of the method, see [41,47]). Ignoring the instrument tilt, the variance method equations for a 5-beam ADCP are as follows:

$$\overline{u'^2} = \frac{\overline{b_1'} + \overline{b_2'} - 2\overline{b_5'}cos^2(\theta)}{2sin^2(\theta)} \tag{16}$$

$$\overline{v'^2} = \frac{\overline{b_3'^2} + \overline{b_4'^2} - 2\overline{b_5'^2}cos^2(\theta)}{2sin^2(\theta)} \tag{17}$$

$$\overline{w'^2} = \overline{b_5'^2} \tag{18}$$

$$\overline{u'w'} = \frac{\overline{b_2'^2} - \overline{b_1'^2}}{2sin(2\theta)} \tag{19}$$

$$\overline{v'w'} = \frac{\overline{b_4'^2} - \overline{b_3'^2}}{2sin(2\theta)} \tag{20}$$

4.2.6. ADCP Alignment Error

Some of the instruments used in this study were not aligned with the principal flow direction. Moreover, the instruments that were aligned would still have misalignment errors due to flow asymmetry, as can be seen in Figure 3. To quantify the misalignment error, we can define the approximate variance $\overline{u'^2}_{appx}$, as calculated from the misaligned ADCP data, in terms of the actual variance $\overline{u'^2}$ and the misalignment angle ϕ. The derivations are included in Appendix A.1, and the resulting equations are:

$$\overline{u'^2}_{appx} = \overline{u'^2}\cos^2(\phi) + \overline{v'^2}\sin^2(\phi) - \overline{u'v'}\sin(2\phi) \tag{21}$$

$$\overline{v'^2}_{appx} = \overline{v'^2}\cos^2(\phi) + \overline{u'^2}\sin^2(\phi) + \overline{u'v'}\sin(2\phi) \tag{22}$$

$$\frac{q^2}{2}_{appx} = \frac{\overline{u'^2}_{appx} + \overline{v'}_{appx} + \overline{w'^2}}{2} = \frac{\overline{u'^2} + \overline{v'^2} + \overline{w'^2}}{2} \tag{23}$$

$$\alpha = \frac{\overline{w'^2}}{\overline{u'^2}_{appx} + \overline{v'}_{appx}} = \frac{\overline{w'^2}}{\overline{u'^2} + \overline{v'}} \tag{24}$$

The total quantities, such as total turbulence intensity or total TKE, and the anisotropy ratios remain unaffected by the misalignment due to the cancelling out of the covariance term $\overline{u'v'}$. However, the parameters in the streamwise and lateral directions will result in errors if the instrument is misaligned. The error will depend on the relative magnitudes of $\overline{u'^2}$, $\overline{v'^2}$ and $\overline{u'v'}$, as well as on the degree of misalignment. The curves in Figure 4 show the range of errors based on possible anisotropy ratios and relative $u'v'$ magnitudes.

Error estimates show that, in the case of the FORCE-1 and FORCE-2 datasets, with an approximate misalignment of 30°, streamwise I could have errors between 20–60% depending on the relative values of the u and v components. In the case of slight misalignment due to asymmetry, as in the EMEC-1 case (approximately 10°), the error would range from 5–15%.

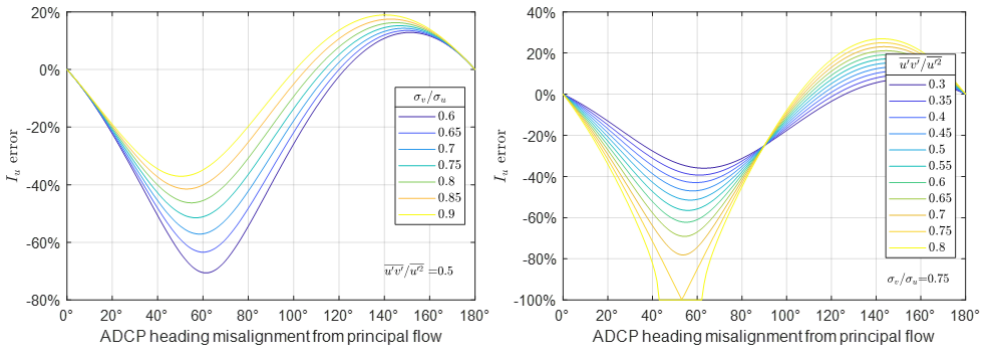

Figure 4. Error-ranges for streamwise turbulence intensity calculated from misaligned ADCP data. The ratio σ_v/σ_u was found to be 0.75 at the Sound of Islay tidal site [24]; the ratio $\overline{u'v'}/\overline{u'^2}$ ranged between 0.3–0.75 at Mahakam River, East Kalimantan, Indonesia [48].

5. Results

5.1. Length Scales

Figure 5 shows that EMEC-1 and FORCE-1 have significantly larger streamwise length scales L_u than the other datasets, which may be due to their proximity to bathymetric features. EMEC-1 has a notably larger lateral component length scale, in particular on the ebb tides, relative to the streamwise component. There is a significant variation in profile shapes on the ebb tides across all instruments.

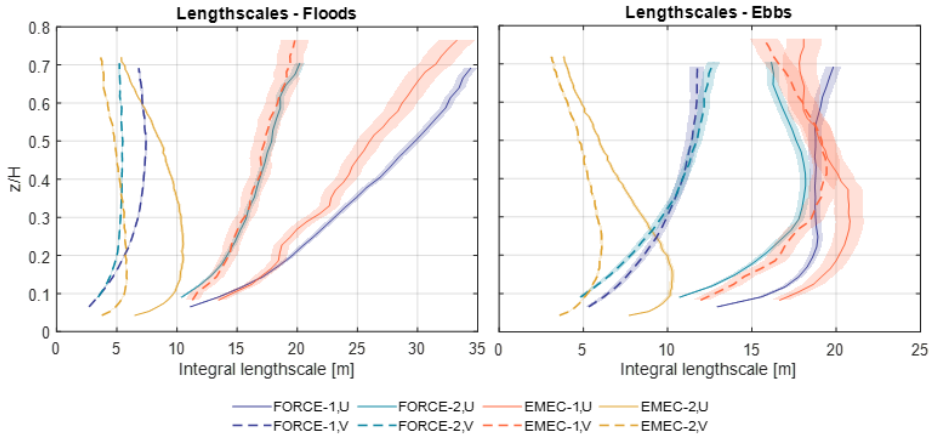

Figure 5. Length scales calculated using time-correlation method on rotated instantaneous velocity data. Shaded areas show standard error, which is larger for EMEC-1 due to a shorter dataset.

Comparing the length scale profiles to open-channel theory (Figure 6), only the FORCE-2 data show agreement with the model up to $z/H = 0.2$ on the ebb tides. The FORCE-1 length scale profile follows the theoretical shape on the floods, although skewed towards higher velocities. All other results show a significant deviation from the theoretical profile, especially on the ebb tides.

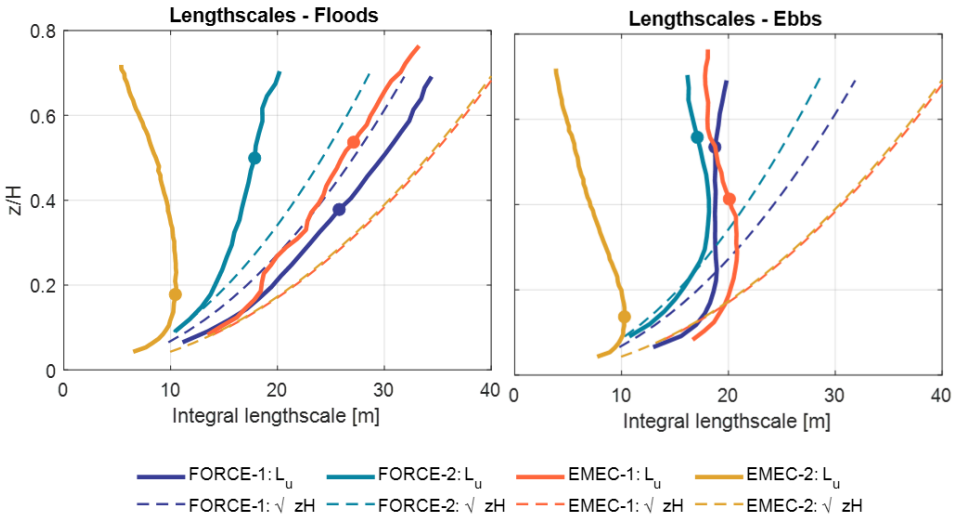

Figure 6. Streamwise length scales calculated by time-correlation method on instantaneous streamwise velocity data. The dashed lines indicate a theoretical streamwise length scale based on open-channel theory, $L_u = \sqrt{zH}$. The bold dot indicates the point above which the beam spread is larger than the length scales.

5.2. Turbulence Spectrum

The direct measurement of the vertical velocity spectrum is available from the vertical ADCP beam. The measured spectra were normalised by the variance and are compared to the Kaimal and von Kármán models, as shown in Figures 7 and 8.

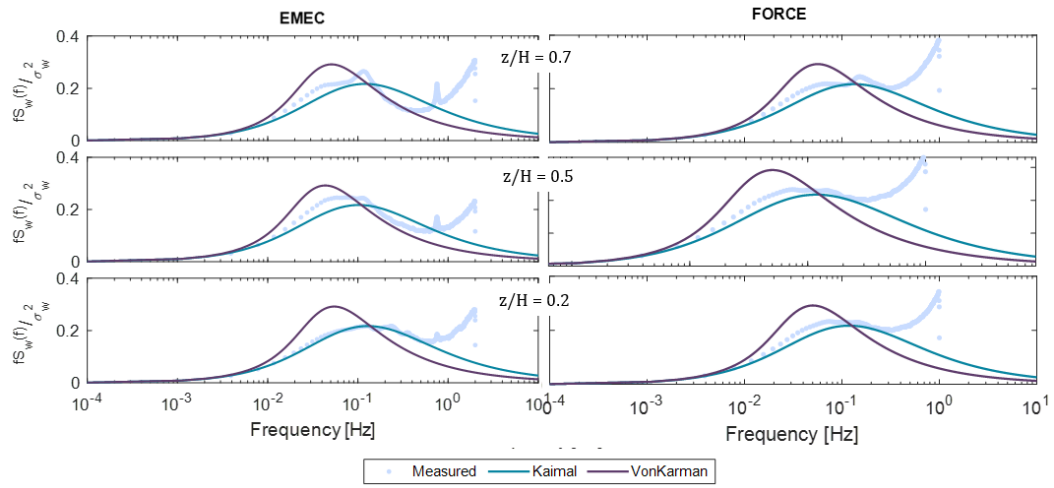

Figure 7. Comparison of vertical Kaimal and von Kármán models (based on measured length scale) to measured variance normalised spectra for flood cycles. The 10-minute spectra are averaged across all flood cycles for velocities 1–3 m/s.

For both sites, the Kaimal model provides a better fit with good agreement near the seabed. The von Kármán model peak has a higher amplitude and is shifted to lower frequencies compared to the observed spectrum. The FORCE-1 spectra show better agreement on the flood tides than the ebb, whereas EMEC-1 is similar for both.

The streamwise spectrum model is compared with the measurements for the EMEC-1 dataset only as this instrument was aligned to the flow.

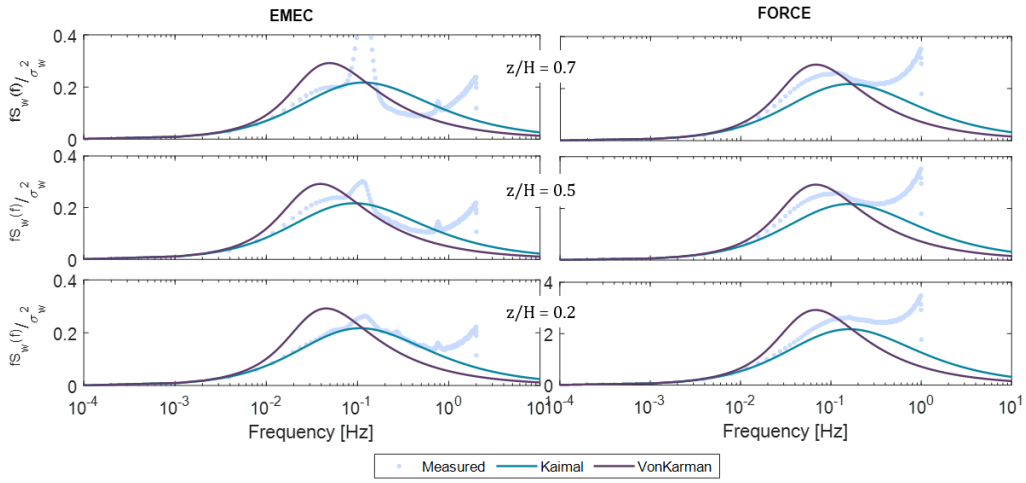

Figure 8. Comparison of vertical Kaimal and von Kárm'an models (based on measured length scale) to measured variance normalised spectra for ebb cycles. The 10-min spectra are averaged across all ebb cycles for velocities 1–3 m/s.

Figure 9 shows that, in the streamwise case, the von Kárman model better represented the measured spectra, albeit with the model peak shifted to lower frequencies. In the presented case, this means the measured energy is concentrated around a frequency almost twice as high as the model suggests. On the ebb tides, near the top of the water column, the measured spectrum deviates from the von Kármán model and aligns more to the Kaimal model. This may be due to wave interference, clearly visible as a spike at around 0.1 Hz, creating an energy deficit in the lower frequencies in the spectrum calculation.

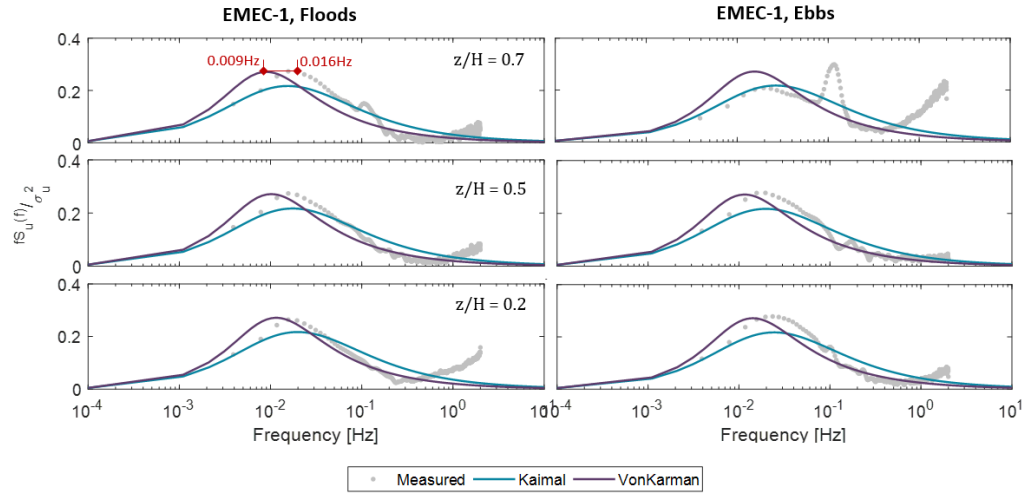

Figure 9. Comparison of the streamwise Kaimal and Von Kármán models (based on measured length scale) to variance-normalised spectra, measured at EMEC-1 location. The 10-min spectra are averaged across flood and ebb cycles with velocities 1–3 m/s.

The FORCE-1 measurements could only be analysed at a total energy level due to the instrument misalignment. Figure 10 demonstrates that, similar to the streamwise comparison of the EMEC-1 data, the von Kármán model agrees well with the total measured spectrum.

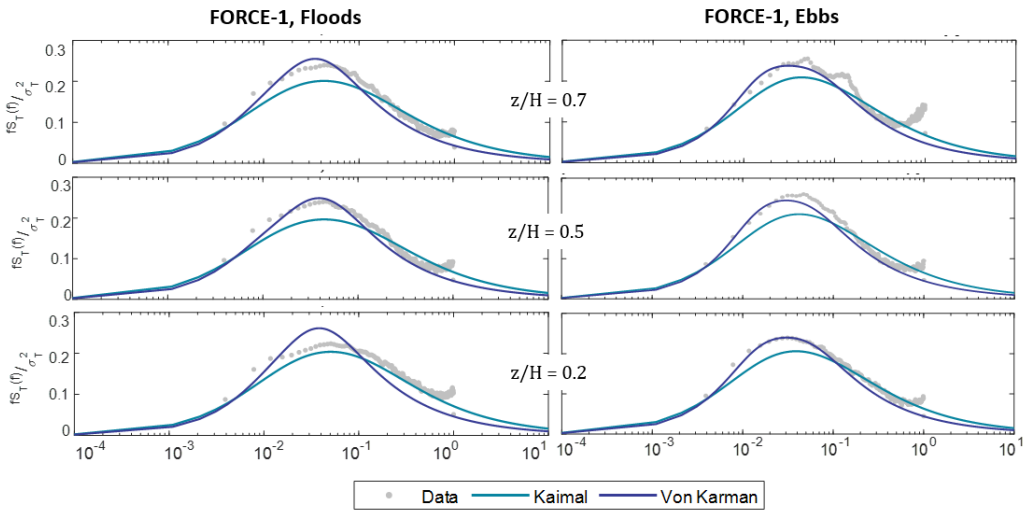

Figure 10. Comparison of the total Kaimal and von Kármán models (based on measured length scale) to variance-normalised spectra, measured at FORCE-1 location. The 10-minute spectra are averaged across flood and ebb cycles for velocities 1–3 m/s.

5.3. Coherence

As there is no definition of the general coherence model for the vertical component, we compare the horizontal model, defined by Equation (12), to the coherence calculated from the instantaneous streamwise velocity component. Due to the uncertainty of using instantaneous data in such a way, we also include the coherence from the inclined beams for comparison. The results are presented in Figures 11 and 12 and show that the EMEC-1 data agree well with the model at low frequencies in the upper water column, while the FORCE-1 data show less agreement. In both cases, the coherence curve is less steep, i.e., the measured coherence is higher in the high-frequency range. In both datasets, coherence tends to be higher in the upper water column. The measured streamwise coherence is similar to the highest beam coherence, suggesting the method used is appropriate.

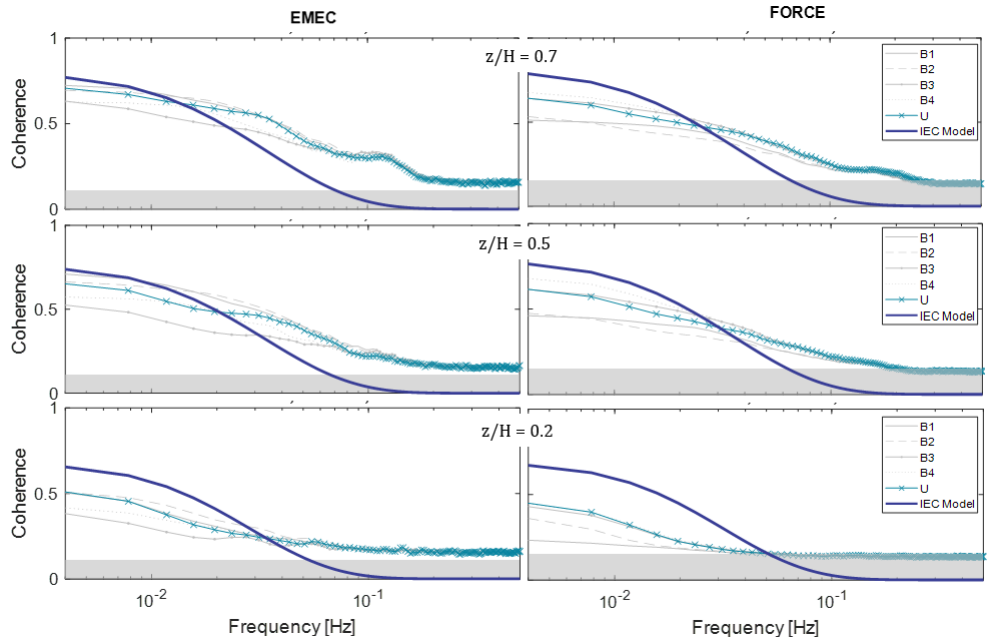

Figure 11. Measured coherence compared to the general IEC coherence model for flood cycles, velocities 1–3 m/s. The shaded area shows the 95% confidence level for measured coherence.

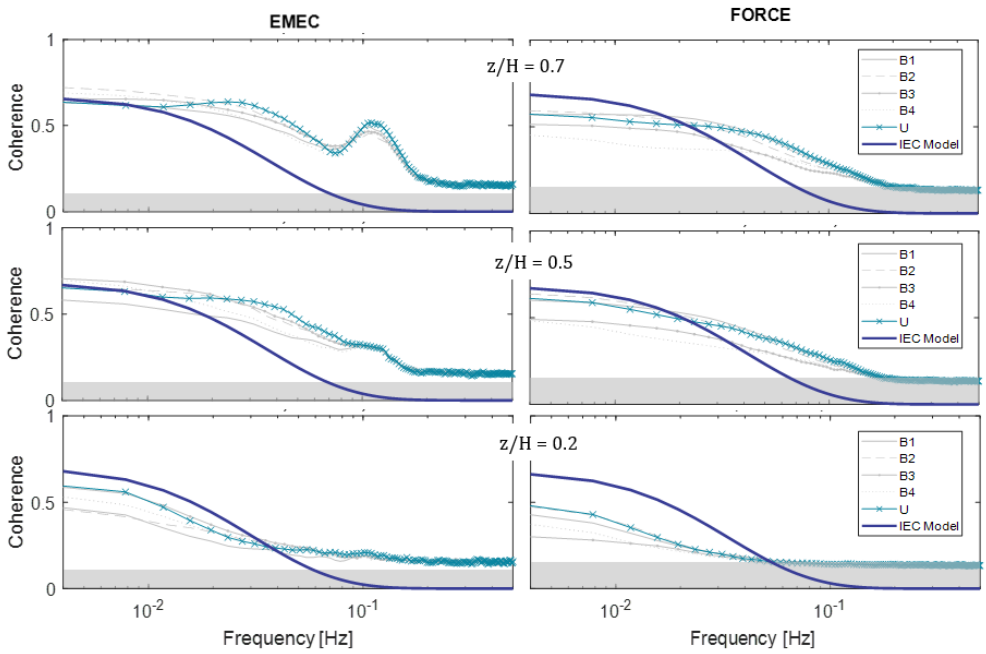

Figure 12. Measured coherence compared to the general IEC coherence model for ebb cycles, velocities 1–3 m/s. The shaded area shows the 95% confidence level for measured coherence.

5.4. Shear Profile

The shear profiles for all instruments conform to a 1/5th- or a 1/6th-power-law model relatively well on the flood cycles (Figure 13), with the FORCE-1 and FORCE-2 datasets showing the closest fit. On the ebb cycles, the EMEC-1 profiles deviate significantly from the power-law model with a three-fold increase in the sum squared error compared to the flood cycle.

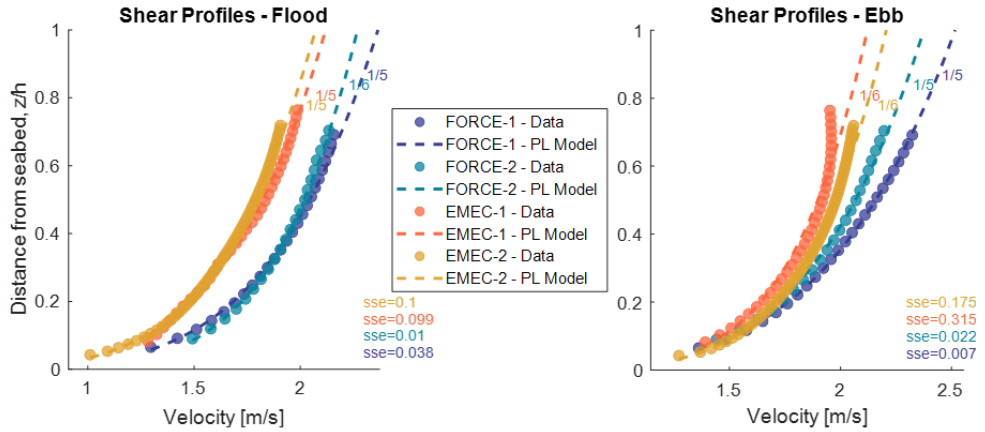

Figure 13. Shear profiles for velocities 1–3 m/s. The best-fit power-law exponents and sum squared errors (sse) are displayed for each case.

5.5. Turbulence Intensity Profiles

The turbulence intensity profiles across all locations are very similar on the flood tides, especially in the upper part of the water column (Figure 14). The EMEC-1 profile deviates from the rest below $z/H = 0.4$; this is likely due to bathymetry-driven turbulence, also seen in the TKE profiles. The EMEC-2 profiles deviate in the upper part of the water column across all parameters due to significant wave presence. The anisotropy ratios are also very

similar for all sites, especially in the lower half of the water column, with the EMEC-2 location showing the most isotropic ratio.

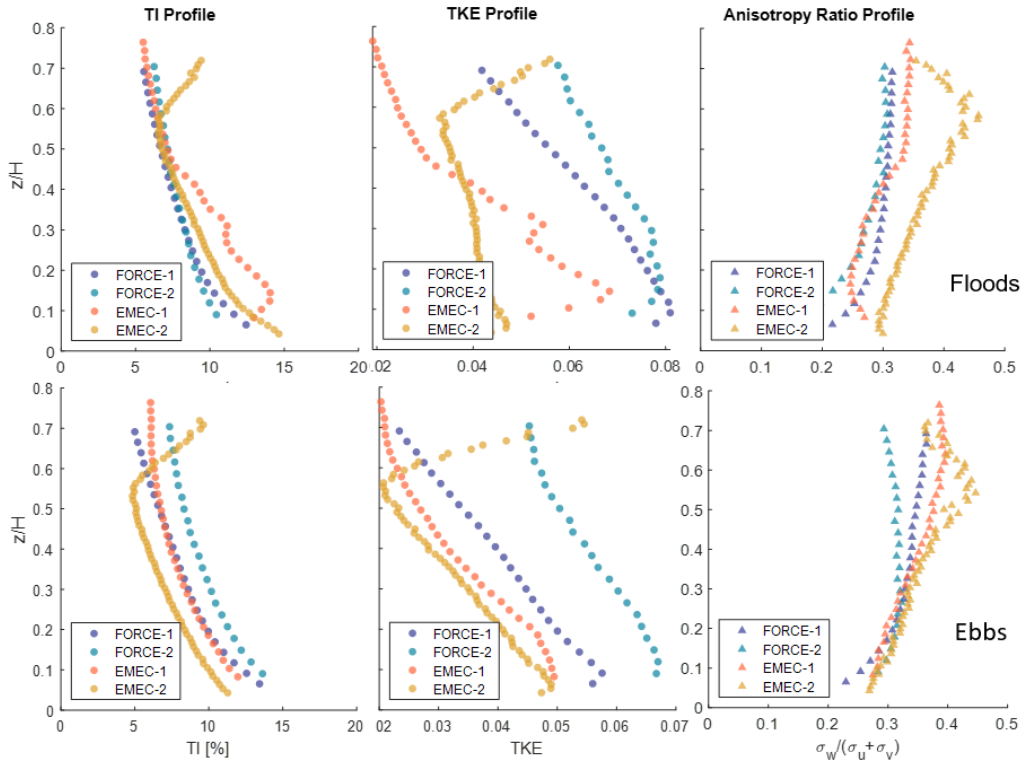

Figure 14. Total turbulence intensity, TKE and anisotropy ratios for all measurement sites for flood (**top row**) and ebb (**bottom row**) tides with flows 1–3 m/s.

6. Discussion

Commercial models, such as Tidal Bladed and TurbSim, use a combination of measured parameters and theoretical assumptions to construct turbulent flow fields using the spectral method [19], which are then used in BEM calculations. Figure 1 summarises the inputs required for such flow-field generation, which broadly consist of frequency-domain parameters and scaling parameters. The theoretical values of these parameters have been compared to measurements from two tidal sites and their applicability is discussed in this section.

6.1. Frequency Parameters (Spectrum and Coherence)

In order to define the spectrum and coherence models, length scale values must be specified. When measurements are not available, the models define the streamwise length scale, $L_u = 8.10\,\Lambda_U$, where $\Lambda_U = 0.7$ min (30 m, hub height), in line with the IEC 61400-1 wind standard. This would suggest a length scale, L_u = 113 m for the mid-water column, which is almost four times more than the highest measured length scale across all datasets (Figure 5). The theoretical values are based on atmospheric turbulence and are clearly not applicable to the tidal channels analysed here, and, therefore, should not be used. Length scales can also be approximated according to open-channel flow theory, where the measured turbulent length scales across the lower half of the water column are defined as $L_u \approx \sqrt{zH}$ [22]. At the two sites considered, such theoretical values are not representative. Only one instrument, FORCE-2 showed agreement and only up to $z/H = 0.2$, with the rest deviating significantly (Figure 6). Length scales have been found to correlate with fatigue loading [7], so, using theoretical length scale values in models is likely to significantly misrepresent loads in simulations.

The vertical velocity spectrum was well represented by the Kaimal model, although the peak was shifted towards higher frequencies in some cases; e.g., for measurements higher-up in the water column. Interestingly, for the streamwise component (and for the total spectrum), the von Kármán model showed much better agreement, again with a peak shift, but towards lower frequencies this time. This is in contrast to findings from the Grand Passage, Nova Scotia [21], where the Kaimal model was found to better predict the streamwise spectra. In previous studies [21,24,25,49], regardless of which model provided a better fit, the streamwise spectrum peak was always shifted towards low frequencies, as in this study. This shift occurs even though actual measured length scales are used as input to the spectrum model, suggesting that the issue is with the coefficients used in this semi-empirical model. In other words, even though the correct length scale is used in constructing the model, the effective length scale (determined by the position of the peak) is incorrect. The extent of this can be seen in Figure 9, where the frequency corresponding to the peak of the measured spectrum is almost double that of the model. In practice, using the 'shifted' spectrum would mean fewer load cycles at the same magnitude than the real data would suggest. This is likely to underestimate fatigue loads. So although the general shape of the spectra seem to agree with the measurements, care must be taken that the spectrum peak is not significantly shifted.

To the authors knowledge, there have been no studies on validating the IEC coherency models for tidal-energy applications. In this study, the coherence measurements did not show a good agreement with the models, in particular for the FORCE-1 location. The measured coherence curves appear less steep with high coherency continuing into higher frequencies. It is known that, without proper consideration of spatial coherency, at least over the turbine disc area, the detailed interactions between fluid flow and devices are unlikely to be accurately resolved by simulation, whether using simplified models, such as Tidal Bladed, or even higher-order computational fluid dynamics packages [45].

6.2. Scaling Parameters (Mean Velocity and Standard Deviation Profiles)

The shear profile model and standard deviation parameters are used to scale the flow field in the time domain (see Figure 1). The recommended shear profile is a 1/7th-power-law model. It is understood from previous studies ([27,29,30]) that such a power-law model may not always be applicable to real flows. In three of the four locations, the shear profiles matched the expected shape, but showed the best fit to a 1/5th- or 1/6th-power law, suggesting a 1/7th-power law is not accurate. In line with previous studies [26–29], the EMEC-1 ebb cycle profile clearly deviates from the power-law model. It is expected that shear profiles will have implications for turbine loading. The non-uniform inflow velocity gradient across a turbine's rotor will cause off-axis, bending moments on the shaft connection, which may be translated into the drive-train, causing excessive wear on internal components, such as bearings and seals [50]. It can also mean that the hub height velocity (typically taken as the reference velocity) is not representative of the average across the rotor disk.

The turbulence intensity profiles for the flood cycles are quite similar for all the measurement locations, with the exception of the EMEC-1 site in the lower half of the water column (see Figure 14). The peaks in EMEC-1 TKE and I suggest that there may be large energetic eddies present in this part of the channel. Some models, such as the Tidal Bladed model, represent the turbulent-flow field with a constant TKE profile, which clearly does not accord with our site measurements. Using a realistic TKE profile rather than a constant value is likely to result in different estimates of loads. In a similar way to the shear profile, it may create a non-uniform inflow gradient across a turbine's rotor and cause eccentric blade and hub bending.

The measured anisotropy ratio profiles are similar to those measured in other studies, where α increases from 0.2 near the seabed to 0.4 near the surface [48]. The EMEC-1 site shows the highest ratios overall, suggesting the turbulence is more isotropic. When using the von Kármán model, the flow is assumed to be isotropic, i.e., the anisotropy ratio

(Equation (4)) is equal to 0.5. This is clearly not the case for any of the site measurements in this study, in particular near the seabed.

6.3. Conclusions

Measured turbulence parameters from two energetic tidal sites were compared to turbulence models and assumptions typically used in the tidal energy industry. Measurements were collected from two nearby locations at FORCE and EMEC tidal sites, enabling comparison across different sites as well as within them. For the first time, we assess the suitability of the complete set of important turbulence parameters, which are used as inputs to commercial codes, such as Tidal Bladed and TurbSim.

The input parameters broadly fall into two categories: spectral representation, including spectrum and coherence models, and scaling parameters, which define the mean velocity profile as well as the overall standard deviation (or turbulence intensity).

Our findings show that the Kaimal model better represented the vertical spectrum, while von Kármán better represented the streamwise spectrum. In practice, only one model would be used, in which case either the vertical or streamwise fluctuations would be misrepresented. In line with other studies, we found that, even when the spectral model shape matched the measured spectrum, the peak was often shifted to lower frequencies. In a fatigue simulation, this would result in less frequent turbulent fluctuations (and, hence, fewer load cycles), potentially resulting in an underestimation of loads.

The measured length scales varied significantly between the four datasets, even within the same site. None of the measurements conformed well to open-channel flow theory. The measured length scales were also significantly smaller than those used as default values in commercial models. Such a large discrepancy is likely to result in significantly different loading behaviour, highlighting the importance of using a measured length scale value rather than a theoretical one.

Our results suggest that measured coherence is higher at higher frequencies and lower at lower frequencies than the IEC model predicts, although the EMEC-1 site showed slightly more agreement with the coherence model. The implication of such discrepancy on load simulations outcomes is unknown; however, it is understood that coherence is an important parameter when it comes to understanding turbulence-induced device loads.

In this study, where the measured shear profiles followed a power law, it was not a 1/7th-power law. Moreover, depending on the location of measurement, the profile can also deviate from a power law, as in the EMEC-1 case. Shear profiles are known to be important for device loads, so care must be taken to use a measured profile rather than an assumed one.

The results of this study highlight the requirement for validating flow models used in load simulations with specific site measurements. There is clearly a lot of variation across sites and within different locations in the same site. If unrepresentative models are used, the loads are likely to be over- or under-estimated, increasing the uncertainty in design.

Author Contributions: Conceptualization, A.N., D.I., I.A. and J.C.; methodology, A.N., D.I., I.A. and J.C.; software, A.N.; validation, A.N., D.I. and J.C.; formal analysis, A.N. and J.C.; investigation, A.N.; resources, J.C.; data curation, A.N.; writing—original draft preparation, A.N.; writing—review and editing, A.N., D.I., I.A. and J.C.; visualization, A.N.; supervision, D.I. and I.A. All authors have read and agreed to the published version of the manuscript.

Funding: This research was funded as part of the EPSRC and NERC Industrial Centre for Doctoral Training in Offshore Renewable Energy (IDCORE), grant number EP/S023933/1.

Data Availability Statement: 3rd Party Data. Restrictions apply to the availability of the data used in this study. Data was obtained from the European Marine Energy Centre and Fundy Ocean Research Center for Energy.

Acknowledgments: The authors wish to thank Caroline Lourie from the European Marine Energy Centre for their support for this project.

Conflicts of Interest: The authors declare no conflict of interest.

Appendix A

Appendix A.1. Derivation of ADCP Misalignment Error

Beam velocities can be written in terms of u, v and w velocity components in channel co-ordinates, beam inclination angle, θ and the angle between the principle flow direction and the instrument heading, ϕ, i.e., the misalignment angle :

$$\begin{bmatrix} b_1 \\ b_2 \\ b_3 \\ b_4 \end{bmatrix} = \begin{bmatrix} sin(\theta) & 0 & cos(\theta) \\ -sin(\theta) & 0 & cos(\theta) \\ 0 & sin(\theta) & cos(\theta) \\ 0 & -sin(\theta) & cos(\theta) \end{bmatrix} \times \begin{bmatrix} cos(\phi) & -sin(\phi) & 0 \\ sin(\phi) & cos(\phi) & 0 \\ 0 & 0 & 1 \end{bmatrix} \times \begin{bmatrix} u \\ v \\ w \end{bmatrix} \quad \text{(A1)}$$

$$b_1 = usin(\theta)cos(\phi) - vsin(\theta)sin(\phi) + wcos(\theta) \quad \text{(A2)}$$

$$b_2 = -usin(\theta)cos(\phi) + vsin(\theta)sin(\phi) + wcos(\theta) \quad \text{(A3)}$$

$$b_3 = usin(\theta)sin(\phi) + vsin(\theta)cos(\phi) + wcos(\theta) \quad \text{(A4)}$$

$$b_4 = -usin(\theta)sin(\phi) - vsin(\theta)cos(\phi) + wcos(\theta) \quad \text{(A5)}$$

$$b_5 = w \quad \text{(A6)}$$

Assuming the Doppler noise can be removed from beam velocity variances, the beam variances can be written as follows:

$$\begin{aligned}
\overline{b_1'^2} = {} & \overline{w'^2}\cos^2(\theta) + \overline{u'^2}\sin^2(\theta)\cos^2(\phi) + \overline{v'^2}\sin^2(\theta)\sin^2(\phi) + \overline{u'w'}\sin(2\theta)\cos(\phi) \\
& - \overline{u'v'}\sin^2(\theta)\sin(2\phi) - \overline{v'w'}\sin(2\theta)\sin(\phi) \\
\overline{b_2'^2} = {} & \overline{w'^2}\cos^2(\theta) + \overline{u'^2}\sin^2(\theta)\cos^2(\phi) + \overline{v'^2}\sin^2(\theta)\sin^2(\phi) + \overline{v'w'}\sin(2\theta)\sin(\phi) \\
& - \overline{u'v'}\sin^2(\theta)\sin(2\phi) - \overline{u'w'}\sin(2\theta)\cos(\phi) \\
\overline{b_3'^2} = {} & \overline{w'^2}\cos^2(\theta) + \overline{v'^2}\sin^2(\theta)\cos^2(\phi) + \overline{u'^2}\sin^2(\theta)\sin^2(\phi) + \overline{u'v'}\sin^2(\theta)\sin(2\phi) \\
& + \overline{u'w'}\sin(2\theta)\sin(\phi) + \overline{v'w'}\sin(2\theta)\cos(\phi) \\
\overline{b_4'} = {} & \overline{w'^2}\cos^2(\theta) + \overline{v'^2}\sin^2(\theta)\cos^2(\phi) + \overline{u'^2}\sin^2(\theta)\sin^2(\phi) + \overline{u'v'}\sin^2(\theta)\sin(2\phi) \\
& - \overline{u'w'}\sin(2\theta)\sin(\phi) - \overline{v'w'}\sin(2\theta)\cos(\phi) \\
& \overline{b_5'} = \overline{w'^2}
\end{aligned}$$

We can substitute the beam variance equations above into the variance method equations below to obtain the channel co-ordinate component variances (as sampled by a misaligned beam). In this example, it is assumed beam numbers 1 and 2, and 3 and 4, are opposite; the numbering convention may change depending on the ADCP instrument.

Variance method equations:

$$\overline{u'^2} = \frac{\overline{b_1'} + \overline{b_2'} - 2\overline{b_5'}cos^2(\theta)}{2sin^2(\theta)}$$

$$\overline{v'^2} = \frac{\overline{b_3'^2} + \overline{b_4'^2} - 2\overline{b_5'^2}cos^2(\theta)}{2sin^2(\theta)}$$

$$\overline{w'^2} = \overline{b_5'^2}$$

$$\overline{u'w'} = \frac{\overline{b_2'^2} - \overline{b_1'^2}}{2sin(2\theta)}$$

$$\overline{v'w'} = \frac{\overline{b_4'^2} - \overline{b_3'^2}}{2sin(2\theta)}$$

From the above parameters, the total kinetic energy and anisotropy ratios can also be calculated as follows:

$$\alpha = \frac{\overline{w'^2}}{\overline{u'^2} + \overline{v'^2}}$$
$$\frac{q^2}{2} = \frac{\overline{u'^2} + \overline{v'^2} + \overline{w'^2}}{2}$$

Approximate parameters in terms of the 'true' values and misalignment angle:

$$\overline{u'^2}_1 = \overline{u'^2}\cos^2(\phi) + \overline{v'^2}\sin^2(\phi) - \overline{u'v'}\sin(2\phi)$$
$$\overline{v'^2}_1 = \overline{v'^2}\cos^2(\phi) + \overline{u'^2}\sin^2(\phi) + \overline{u'v'}\sin(2\phi)$$
$$\overline{u'w'}_1 = \sin^2(\theta)\csc(2\theta)\left(u^2\cos^2(\phi) + v^2\sin^2(\phi) - uv\sin(2\phi)\right)$$
$$\overline{v'w'}_1 = \sin^2(\theta)\csc(2\theta)\left(v^2\cos^2(\phi) + u^2\sin^2(\phi) + vu\sin(2\phi)\right)$$
$$\frac{q^2}{2}_1 = \frac{\overline{u'^2}_1 + \overline{v'}_1 + \overline{w'^2}}{2} = \frac{\overline{u'^2} + \overline{v'^2} + \overline{w'^2}}{2}$$
$$\alpha = \frac{\overline{w'^2}}{\overline{u'^2}_1 + \overline{v'}_1} = \frac{\overline{w'^2}}{\overline{u'^2} + \overline{v'}}$$

References

1. Frost, C. Cost Reduction Pathway of Tidal Stream Energy in the UK and France. Available online: https://ore.catapult.org.uk/?orecatapultreports=cost-reduction-pathway-of-tidal-stream-energy-in-the-uk-and-france (accessed on 12 February 2023).
2. Marine Renewables Canada, Tidal Energy Facts. Available online: https://marinerenewables.ca/facts/tidal-energy/ (accessed on 12 February 2023).
3. West, C. Contracts for Difference Allocation Round 4 Results. The Department for Business, Energy and Industrial Strategy. Available online: https://www.gov.uk/government/publications/contracts-for-difference-cfd-allocation-round-4-results (accessed on 7 July 2022).
4. European Commission. Ocean Energy Strategic Roadmap: Building Ocean Energy for Europe. In *Ocean Energy Forum*; European Commission: Brussels, Belgium, 2016; p. 74.
5. Scarlett, G.T.; Viola, I.M. Unsteady hydrodynamics of tidal turbine blades. *Renew. Energy* **2020**, *146*, 843–855. [CrossRef]
6. McCann, G.; Thomson, M.; Hitchcock, S.; Hassan, G. Implications of Site-Specific Conditions on the Prediction of Loading and Power Performance of a Tidal Stream Device. In Proceedings of the 2nd International Conference on Ocean Energy (ICOE), Brest, France, 15–17 October 2008; pp. 15–17.
7. Blackmore, T.; Myers, L.E.; Bahaj, A.S.; Gaurier, B.; Myers, L.; Germain, G. The Effect of Freestream Turbulence on Tidal Turbines.In Proceedings of the 11th European Wave and Tidal Energy Conference, Nantes, France, 6–11 September 2015.
8. Milne, I.A.; Day, A.H.; Sharma, R.N.; Flay, R.G. Blade loading on tidal turbines for uniform unsteady flow. *Renew. Energy* **2015**, *77*, 338–350. [CrossRef]
9. Clark, T.; Roc, T.; Fisher, S.; Minns, N. Part 3: Turbulence and turbulent effects in turbine and array engineering. *Turbul. Best Pract. Tidal Power Ind.* **2015**, *21*.
10. Milne, I.A.; Day, A.H.; Sharma, R.N.; Flay, R.G. The characterisation of the hydrodynamic loads on tidal turbines due to turbulence. *Renew. Sustain. Energy Rev.* **2016**, *56*, 851–864. [CrossRef]
11. Ortega, A.; Tomy, J.P.; Shek, J.; Paboeuf, S.; Ingram, D. An inter-comparison of dynamic, fully coupled, electro-mechanical, models of tidal turbines. *Energies* **2020**, *13*, 5389. [CrossRef]
12. *PD IEC/TS 62600-2*; 2019 BSI Standards Publication Marine Energy—Wave, Tidal and Other Water Current Converters; International Electrotechnical Commission: London, UK, 2019; p. 62.
13. *DNVGL-ST-0.164*; Tidal Turbines. DNV-GL: Bærum, Norway, 2015. p. 230.
14. Gualtieri, G.; Emejeamara, F.C.; Tomlin, A.S.; Micallef, D.; Bussel, G.V.; Ishugah, T.F.; Li, Y.; Wang, R.Z.; Kiplagat, J.K.; Millward-Hopkins, J.T.; et al. BSI Standards Publication Wind Energy Generation Systems BS EN IEC 61400-1 2019. Available online: https://standards.iteh.ai/catalog/standards/clc/9027bc84-08bf-485d-b139-0869e8a96b59/en-iec-61400-1-2019 (accessed on 5 April 2019).
15. Neil Kelley National Renewable Energy Laboratory. *TurbSim User's Guide: Version 1. 50 TurbSim User's Guide*; Neil Kelley National Renewable Energy Laboratory: Golden, CO, USA, 2009.
16. Lu, Y.; Lueck, R.G. Using a Broadband ADCP in a Tidal Channel. Part II: Turbulence. *J. Atmos. Ocean. Technol.* **1999**, *16*, 1568–1579. [CrossRef]

17. Burton, T. *Wind Energy Handbook*; John Wiley & Sons, Ltd.: Hoboken, NJ, USA, 2001; p. 368.
18. Pope, S.B. *Turbulent Flows*; Cambridge University Press: Cambridge, UK, 2000. [CrossRef]
19. Jonkman, B.; Kilcher, L. *TurbSim User's Guide*; National Renewable Energy Laboratory: Golden, CO, USA, 2012; pp. 1–87.
20. Khairuzzaman, M.Q. Tidal Bladed Theory Manual. 2016.
21. McMillan, J. Turbulence Measurements in a High Reynolds Number Tidal Channel. Ph.D. Thesis, Dalhousie University, Halifax, NS, Canada, 2017.
22. Nezu, I.; Nakagawa, H. *Turbulence in Open Channel Flows*; IAHR Monograph: Madrid, Spain, 1993.
23. Sellar, B.G.; Sutherland, D.R. Tidal Energy Site Characterisation At the Fall of Warness , Emec , Uk Energy Technologies Institute Redapt Ma1001 (Md3.8). 2016. 1001. Available online: https://redapt.eng.ed.ac.uk/?p=library_redapt_reports (accessed on 1 February 2023).
24. Milne, I.A.; Sharma, R.N.; Flay, R.G. The structure of turbulence in a rapid tidal flow. *Proc. R. Soc. A Math. Phys. Eng. Sci.* **2017**, *473*. [CrossRef]
25. Walter, R.K.; Nidzieko, N.J.; Monismith, S.G. Similarity scaling of turbulence spectra and cospectra in a shallow tidal flow. *J. Geophys. Res. Ocean.* **2011**, *116*, 1–14. [CrossRef]
26. Parkinson, S.G.; Collier, W.J. Model validation of hydrodynamic loads and performance of a full-scale tidal turbine using Tidal Bladed. *Int. J. Mar. Energy* **2016**, *16*, 279–297. [CrossRef]
27. Gunn, K.; Stock-Williams, C. On validating numerical hydrodynamic models of complex tidal flow. *Int. J. Mar. Energy* **2013**, *3–4*, e82–e97. [CrossRef]
28. Greenwood, C.; Vogler, A.; Venugopal, V. On the variation of turbulence in a high-velocity tidal channel. *Energies* **2019**, *12*, 672. [CrossRef]
29. McNaughton, J.; Rolfo, S.; Apsley, D.D.; Stallard, T.; Stansby, P.K. CFD power and load prediction on a 1MW tidal stream turbine. In Proceedings of the 10th European Wave and Tidal Energy Conference, Aalborg, Denmark, 2–5 September 2013; Volume 3.
30. Togneri, M.; Masters, I. Micrositing variability and mean flow scaling for marine turbulence in Ramsey Sound. *J. Ocean Eng. Mar. Energy* **2016**, *2*, 35–46. [CrossRef]
31. Kelley, N.D.; Jonkman, B.J.J. *Overview of the TurbSim Stochastic Inflow Turbulence Simulator: Version 1.21*; (Revised 1 February 2001); U.S. Department of Energy Office of Scientific and Technical Information, Kansas City, MI, USA, 2007. pp. 1–13. [CrossRef]
32. Harrold, M.; Ouro, P. Rotor loading characteristics of a full-scale tidal turbine. *Energies* **2019**, *12*, 1035. [CrossRef]
33. Ouro, P.; Stoesser, T. Impact of Environmental Turbulence on the Performance and Loadings of a Tidal Stream Turbine. *Flow Turbul. Combust.* **2019**, *102*, 613–639. [CrossRef]
34. Integrated Ocean Observing System. *Manual for Real-Time Quality Control of Stream Flow Observations (Qartod) v2.1*; Integrated Ocean Observing System: Silver Spring, MD, USA, 2019. [CrossRef]
35. Nortek. *Signature Manual; Principles of Operation*; Nortek: Rud, Norway, 2018.
36. Thomson, J.; Polagye, B.; Durgesh, V.; Richmond, M.C. Measurements of turbulence at two tidal energy sites in puget sound, WA. *IEEE J. Ocean. Eng.* **2012**, *37*, 363–374. [CrossRef]
37. Sellar, B.G.; Wakelam, G.; Sutherland, D.R.; Ingram, D.M.; Venugopal, V. Characterisation of tidal flows at the european marine energy centre in the absence of ocean waves. *Energies* **2018**, *11*, 176. [CrossRef]
38. Durgesh, V.; Thomson, J.; Richmond, M.C.; Polagye, B.L. Noise correction of turbulent spectra obtained from acoustic doppler velocimeters. *Flow Meas. Instrum.* **2014**, *37*, 29–41. [CrossRef]
39. Lu, Y.; Lueck, R.G. Using a broadband ADCP in a tidal channel. Part I: Mean flow and shear. *J. Atmos. Ocean. Technol.* **1999**, *16*, 1556–1567. [CrossRef]
40. Milne, I.; Graham, J.; Coles, D. On the scaling of turbulence in a high Reynolds number tidal flow. *J. Fluid Mech.* **2021**, *915*, A104. [CrossRef]
41. Dewey, R.K.; Stringer, S. Reynolds Stresses and Turbulent Kinetic Energy Estimates from Various ADCP Beam Configurations : Theory. *J. Phys. Oceanogr.* **2007**, *2*, 1–35. [CrossRef]
42. Thomson, J.; Kilcher, L.; Harding, S. Multi-scale Turbulence at Tidal Energy Sites. In Proceedings of the 5th International Conference on Ocean Energy, Halifax, NS, Canada, 4–6 November 2014; pp. 1–6.
43. Kilcher, L.F.; Thomson, J.; Colby, J. Determining the spatial coherence of turbulence at mhk sites. In Proceedings of the 2nd Marine Energy Technology Symposium, Seattle, WA, USA, 15–18 April 2014; pp. 1–7.
44. Schlipf, D.; Trabucchi, D.; Bischoff, O. Testing of Frozen Turbulence Hypothesis for Wind Turbine Applications with a Scanning LIDAR System. *Univ. Stuttg.* **2010**, *12*, 5410.
45. Clark, T.; Black, K.; Ibrahim, J.; Hernon, J.; White, R.; Minns, N.; Fisher, S. Part 2: Data processing, classification and characterisation of turbulent flows. *Turbul. Best Pract. Tidal Power Ind.* **2015**.
46. Guerra, M.; Thomson, J. Turbulence measurements from five-beam acoustic doppler current profilers. *J. Atmos. Ocean. Technol.* **2017**, *34*, 1267–1284. [CrossRef]
47. Thiébaut, M.; Filipot, J.F.; Maisondieu, C.; Damblans, G.; Duarte, R.; Droniou, E.; Guillou, S. Assessing the turbulent kinetic energy budget in an energetic tidal flow from measurements of coupled ADCPs. *Phil. Trans. R. Soc* **2020**, *378*, 20190496. [CrossRef]
48. Vermeulen, B.; Hoitink, A.J.; Sassi, M.G. Coupled ADCPs can yield complete Reynolds stress tensor profiles in geophysical surface flows. *Geophys. Res. Lett.* **2011**, *38*, 2–7. [CrossRef]

49. Milne, I.A.; Sharma, R.N.; Flay, R.G.; Bickerton, S. Characteristics of the turbulence in the flow at a tidal stream power site. *Philos. Trans. R. Soc. A Math. Phys. Eng. Sci.* **2013**, *371*, 0120196. [CrossRef]
50. Nevalainen, T.M.; Johnstone, C.M.; Grant, A.D. A sensitivity analysis on tidal stream turbine loads caused by operational, geometric design and inflow parameters. *Int. J. Mar. Energy* **2016**, *16*, 51–64. [CrossRef]

Bibliography

Adcock, T. A. A., Draper, S., Willden, R. H. J., and Vogel, C. R. (2021). The fluid mechanics of tidal stream energy conversion. pages 287–310.

Ahmed, U., Afgan, I., Apsley, D. D., Stallard, T., and Stansby, P. K. (2015). Cfd simulations of a full-scale tidal turbine: Comparison of les and rans with field data. *Eur. Wave Tidal Energy Conf.*

Ahmed, U., Apsley, D. D., Afgan, I., Stallard, T., and Stansby, P. K. (2017). Fluctuating loads on a tidal turbine due to velocity shear and turbulence: Comparison of cfd with field data. *Renewable Energy*, 112:235–246.

Akansu, A. N. and Haddad, R. A. (2001). Time-frequency representations. *Multiresolution Signal Decomposition*, pages 331–390.

Bian, C., Liu, Z., Huang, Y., Zhao, L., and Jiang, W. (2018). On estimating turbulent reynolds stress in wavy aquatic environment. *Journal of Geophysical Research: Oceans*, 123:3060–3071.

Blackmore, T., Myers, L. E., and Bahaj, A. S. (2016). Effects of turbulence on tidal turbines: Implications to performance, blade loads, and condition monitoring. *International Journal of Marine Energy*, 14:1–26.

Blackmore, T., Myers, L. E., Bahaj, A. S., Gaurier, B., Myers, L., and Germain, G. (2015). The effect of freestream turbulence on tidal turbines.

Burton, T. (2001). *Wind Energy Handbook*. John Wiley and Sons, Ltd.

Camussi, R., Robert, G., and Jacob, M. C. (2008). Cross-wavelet analysis of wall pressure fluctuations beneath incompressible turbulent boundary layers. *Journal of Fluid Mechanics*, 617:11–30.

Chamorro, L. P., Hill, C., Morton, S., Ellis, C., Arndt, R. E., and Sotiropoulos, F. (2013). On the interaction between a turbulent open channel flow and an axial-flow turbine. *Journal of Fluid Mechanics*, 716:658–670.

Chen, K., Zhang, Y., and Zhong, Q. (2019). Wavelet coherency structure in open channel flow. *Water (Switzerland)*, 11.

Chiao, L. Y. and Wang, Y. H. (2004). Multiresolution interpolation and detiding of the adcp data. *Journal of Atmospheric and Oceanic Technology*, 21:122–134.

Clark, T., Black, K., Ibrahim, J., Hernon, J., White, R., Minns, N., and Fisher, S. (2015a). Part 2: Data processing, classification and characterisation of turbulent flows. *Turbulence: Best Practices for the Tidal Power Industry*.

Clark, T., Roc, T., Fisher, S., and Minns, N. (2015b). Part 3: Turbulence and turbulent effects in turbine and array engineering. *Turbulence: Best Practices for the Tidal Power Industry*.

Coles, D., Angeloudis, A., Greaves, D., Hastie, G., Lewis, M., MacKie, L., McNaughton, J., Miles, J., Neill, S., Piggott, M., Risch, D., Scott, B., Sparling, C., Stallard, T., Thies, P., Walker, S., White, D., Willden, R., and Williamson, B. (2021). A review of the uk and british channel islands practical tidal stream energy resource. *Proceedings of the Royal Society A: Mathematical, Physical and Engineering Sciences*, 477.

Davidson, P. (2015). *Turbulence. An Introduction for Scientists and Engineers*. Oxford University Press, second edition.

Dewey, R. K. and Stringer, S. (2007). Reynolds stresses and turbulent kinetic energy estimates from various adcp beam configurations : Theory. *Journal of Physical Oceanography*, pages 1–35.

DNV (2015). *DNV-ST-0164: Tidal turbines*. DNV.

DNV (2022). Tidal bladed software. dnv. `www.dnv.com/services/industry-standard-tidal-turbine-software-modelling-tool-tidalbladed-3799`.

Durgesh, V., Thomson, J., Richmond, M. C., and Polagye, B. L. (2014). Noise correction of turbulent spectra obtained from acoustic doppler velocimeters. *Flow Measurement and Instrumentation*, 37:29–41.

Dynamique, L. D. M., Cedex, P., and Bascievant, C. (1995). Wavelet spectra compared to fourier spectra. *Journal of Mathematical Physics*, 36:1506–1519.

El-Shahat, S. A., Li, G., Lai, F., and Fu, L. (2020). Investigation of parameters affecting horizontal axis tidal current turbines modeling by blade element momentum theory. *Ocean Engineering*, 202:107176.

EMEC (2023). European marine energy centre, information. `https://www.emec.org.uk/about-us/`.

Emery, R. and Thomson, W. (2001). *Data Analysis Methods in Physical Oceanography*. Elsevier, third edition.

Farge, M. and Schneider, K. (2004). Wavelets: Application to turbulence. *Encyclopedia of Mathematical Physics: Five-Volume Set*, pages 408–420.

Finnegan, W., Fagan, E., Flanagan, T., Doyle, A., and Goggins, J. (2020). Operational fatigue loading on tidal turbine blades using computational fluid dynamics. *Renewable Energy*, 152:430–440.

Flinchem, E. P. and Jay, D. A. (2000). An introduction to wavelet transform tidal analysis methods. *Estuarine, Coastal and Shelf Science*, 51:177–200.

Frost, C. (2022). Cost reduction pathway of tidal stream energy in the uk and france. *TIGER, Tidal Stream Industry Energizer*.

Galloway, P. (2013). *Performance Quantification of Tidal Turbines Subjected to Dynamic Loading*. PhD Thesis. University of Southampton.

Garel, E. and Cai, H. (2018). Effects of tidal-forcing variations on tidal properties along a narrow convergent estuary. 41:1924–1942.

Greenwood, C., Vogler, A., and Venugopal, V. (2019). On the variation of turbulence in a high-velocity tidal channel. *Energies*, 12.

Guerra, M. and Thomson, J. (2017). Turbulence measurements from five-beam acoustic doppler current profilers. *Journal of Atmospheric and Oceanic Technology*, 34:1267–1284.

Guion, R. U. and Young, A. M. (2015). The frequency response of acoustic doppler current profilers: Spatiotemporal response and implications for tidal turbine site assessment. *2014 Oceans - St. John's, OCEANS 2014*.

Gunn, K. and Stock-Williams, C. (2013). On validating numerical hydrodynamic models of complex tidal flow. *International Journal of Marine Energy*, 3-4.

Hammerum, K., Brath, P., and Poulsen, N. K. (2007). A fatigue approach to wind turbine control. *Journal of Physics: Conference Series*, 75.

Harrold, M. and Ouro, P. (2019). Rotor loading characteristics of a full-scale tidal turbine. *Energies*, 12.

Hu, H. and Du, X. H. P. (2020). Extracting coherent structures in near-wall turbulence based on wavelet analysis. *Intech*, page 13.

Hu, W., Letson, F., Barthelmie, R. J., and Pryor, S. C. (2018). Wind gust characterization at wind turbine relevant heights in moderately complex terrain. *Journal of Applied Meteorology and Climatology*, 57:1459–1476.

HydroQuest (2021). Hydroquest tidal turbine : End of tests on the edf site in raz blanchard. `https://interregtiger.com/hydroquest-tidal-turbine-end-of-tests-on-the-edf-site-in-paimpol-brehat-and-new-stages-of-development-at-the-raz-blanchard/` [accessed: 01/05/2023].

IEC (2013). *PD IEC / TS 62600-200 : 2013. BSI Standards Publication. Marine energy — Wave, tidal and other water current converters.*

IEC (2015). *PD IEC / TS 62600-201: 2015. BSI Standards Publication. Marine energy — Wave , tidal and other water current converters.* BSI Standards Limited.

IEC (2019a). *BS EN IEC 61400-1:2019. BSI Standards Publication. Wind energy generation systems. Part 1: Design Requirements*. BSI Standards Limited.

IEC (2019b). *PD IEC / TS 62600-2 : 2019. BSI Standards Publication. Marine energy - Wave, tidal and other water current converters.* BSI Standards Limited.

IEC (2020). *PD IEC / TS 62600-3 : 2020. BSI Standards Publication Marine energy - Wave , tidal and other water current converters*. BSI Standards Limited.

Indrusiak, M. L. S. (2004). Wavelet analysis of experimental turbulence time series. *In Practice*.

IOOS (2019). *Manual for Real-Time Quality Control of Stream Flow Observations v2.1*. Quality Assurance of Real-Time Oceanographic Data (QARTOD).

Jeffcoate, P., Starzmann, R., Elsaesser, B., Scholl, S., and Bischoff, S. (2015). Field measurements of a full scale tidal turbine. *International Journal of Marine Energy*, 12:3–20.

Jonkman, B. and Kilcher, L. (2012). Turbsim user's guide. *National Renewable Energy Laboratory*, pages 1–87.

Kelley, N., Jonkman, B., Scott, G., Bialasiewicz, J., and Redmond, L. (2005). The impact of coherent turbulence on wind turbine aeroelastic response and its simulation. *National Renewable Energy Laboratory*, page 22.

Kelley, N. D. and Jonkman, B. (2009). Turbsim user ' s guide : Version 1 . 50. *National Renewable Energy Laboratory*.

Kelley, N. D., Osgood, R. M., Bialasiewicz, J. T., and Jakubowski, A. (2000). Using wavelet analysis to assess turbulence/rotor interactions. *Wind Energy*, 3:121–134.

Khairuzzaman, M. Q. (2016). Tidal bladed theory manual, v4.8. *DNV*, 4:64–75.

Kilcher, L. F., Thomson, J., and Colby, J. (2014). Determining the spatial coherence of turbulence at mhk sites. *Proceedings of the 2nd Marine Energy Technology Symposium*, pages 1–7.

Kolmogorov, A. N. (1961). A refinement of previous hypotheses concerning the local structure of turbulence in a viscous incompressible fluid at high reynolds number. *Steklov Mathematical Institute, Academy of Sciences of the U.S.S.R., Moscow*.

Lake, T., Hughes, J., Togneri, M., Williams, A. J., Jeffcoate, P., Starzmann, R., Kaufmann, N., and Masters, I. (2021). Strain gauge measurements on a full scale tidal turbine blade. *Renewable Energy*, 170:985–996.

Lu, Y. and Lueck, R. G. (1999). Using a broadband adcp in a tidal channel. part ii: Turbulence. *Journal of Atmospheric and Oceanic Technology*, 16:1568–1579.

MacEnri, J., Reed, M., and Thiringer, T. (2013). Influence of tidal parameters on seagen flicker performance. *Philosophical Transactions of the Royal Society A: Mathematical, Physical and Engineering Sciences*, 371.

Magallanes (2021). Magallanes renovables. `https://www.emec.org.uk/about-us/our-tidal-clients/magallanes-renovables/` [accessed: 23/06/2023].

MathWorks (2022a). Matlab documentation - magnitude-squared coherence function. `https://uk.mathworks.com/help/signal/ref/mscohere.html` [accessed: 23/07/2023].

MathWorks (2022b). Matlab documentation - rainflow function. `https://uk.mathworks.com/help/signal/ref/rainflow.html` [accessed: 12/04/2023].

MathWorks (2022c). Matlab documentation, welch's power spectral density estimate. `https://uk.mathworks.com/help/signal/ref/pwelch.html` [accessed:12/04/2023].

MathWorks (2023). Matlab wavelet toolbox. `https://uk.mathworks.com/help/wavelet/` [accessed: 06/03/2023].

McCaffrey, K., Fox-Kemper, B., Hamlington, P. E., and Thomson, J. (2015). Characterization of turbulence anisotropy, coherence, and intermittency at a prospective tidal energy site: Observational data analysis. *Renewable Energy*, 76:441–453.

McCann, G., Thomson, M., Hitchcock, S., and Hassan, G. (2008). Implications of site-specific conditions on the prediction of loading and power performance of a tidal stream device. *2nd International Conference on Ocean Energy (ICOE)*, pages 15–17.

McMillan, J. (2017). *Turbulence Measurements in a High Reynolds Number Tidal Channel*. PhD Thesis, Dalhousie University.

McMillan, J. M. and Hay, A. E. (2017). Spectral and structure function estimates of turbulence dissipation rates in a high-flow tidal channel using broadband adcps. *Journal of Atmospheric and Oceanic Technology*, 34:5–20.

McNae, D. M. (2013). *Unsteady Hydrodynamics of Tidal Stream Turbines*. PhD Thesis, Imperial College London.

McNaughton, J., Rolfo, S., Apsley, D. D., Stallard, T., and Stansby, P. K. (2013). Cfd power and load prediction on a 1mw tidal stream turbine. *Proceedings of the 10th European Wave and Tidal Energy Conference*.

Mihanović, H., Orlić, M., and Pasarić, Z. (2009). Diurnal thermocline oscillations driven by tidal flow around an island in the middle adriatic. *Journal of Marine Systems*, 78:157–168.

Milne, I., Graham, J., and Coles, D. (2021). On the scaling of turbulence in a high reynolds number tidal flow. *Journal of Fluid Mechanics*, 915:A104.

Milne, I. A., Day, A. H., Sharma, R. N., and Flay, R. G. (2015). Blade loading on tidal turbines for uniform unsteady flow. *Renewable Energy*, 77:338–350.

Milne, I. A., Day, A. H., Sharma, R. N., and Flay, R. G. (2016). The characterisation of the hydrodynamic loads on tidal turbines due to turbulence. *Renewable and Sustainable Energy Reviews*, 56:851–864.

Milne, I. A. and Graham, J. M. (2019). Turbulence velocity spectra and intensities in the inflow of a turbine rotor. *Journal of Fluid Mechanics*, 870:870R31–870R311.

Milne, I. A., Sharma, R. N., and Flay, R. G. (2017). The structure of turbulence in a rapid tidal flow. *Proceedings of the Royal Society A: Mathematical, Physical and Engineering Sciences*, 473.

Milne, I. A., Sharma, R. N., Flay, R. G., and Bickerton, S. (2010). The role of onset turbulence on tidal turbine blade loads. *17th Australasian Fluid Mechanics Conference 2010*, pages 444–447.

Milne, I. A., Sharma, R. N., Flay, R. G., and Bickerton, S. (2013). Characteristics of the turbulence in the flow at a tidal stream power site. *Philosophical Transactions of the Royal Society A: Mathematical, Physical and Engineering Sciences*, 371.

Minesto (2021). Minesto dg100 in the faroe islands. `https://www.offshore-energy.biz/minesto-up-and-running-again-in-the-faroe-islands/` [accessed: 01/05/2023].

Mullings, H. and Stallard, T. (2019). Unsteady loading in a tidal array due to simulated turbulent onset flow. *Advances in Renewable Energies Offshore - Proceedings of the 3rd International Conference on Renewable Energies Offshore, RENEW 2018*, pages 227–235.

Mullings, H. and Stallard, T. (2021). Assessment of dependency of unsteady onset flow and resultant tidal turbine fatigue loads on measurement position at a tidal site. *Energies*, 14.

Murray, R. E., Thresher, R., and Jonkman, J. (2018). Added-mass effects on a horizontal-axis tidal turbine using fast v8. *Renewable Energy*, 126:987–1002.

Mycek, P., Gaurier, B., Germain, G., Pinon, G., and Rivoalen, E. (2014). Experimental study of the turbulence intensity effects on marine current turbines behaviour. part i: One single turbine. *Renewable Energy*, 66:729–746.

Nan, J. (2016). Wavelet analysis to detect multi-scale coherent eddy structures and intermittency in turbulent boundary layer. *Intech*, page 13.

Nevalainen, T. M., Johnstone, C. M., and Grant, A. D. (2016). A sensitivity analysis on tidal stream turbine loads caused by operational, geometric design and inflow parameters. *International Journal of Marine Energy*, 16:51–64.

Nezu, I. and Nakagawa, H. (1993). *Turbulence in Open Channel Flows.* IAHR Monograph.

Nortek (2018). Signature manual; principles of operation.

Nova (2020). Nova innovation - shetland tidal array. `https://marine.gov.scot/sma/assessment/case-study-nova-innovation-shetland-tidal-array`[accessed: 12/05/2023].

Noyes, C., Qin, C., and Loth, E. (2020). Tower shadow induced blade loads for an extreme-scale downwind turbine. *Wind Energy*, 23:458–470.

NREL (2021). Turbsim. `https://www.nrel.gov/wind/nwtc/turbsim.html`[accessed: 16/03/2023].

Old, C., Dorward, M., Sellar, B., Nicolas, E., Marcille, J., and Hassen, J. E. (2018a). Advanced monitoring, simulation and control of tidal devices in unsteady, highly turbulent realistic tide environments: Deliverable 3.1 generalised tide to wire model.

Old, C., Ortega, A., Ingram, D., Marcille, J., and Battaglia, B. (2018b). The inter-comparison of bemt, blade-resolved cfd, and bemt-cfd models of scale turbines. d3.4 wp3.

Orbital (2022a). Orbital marine power information. `https://www.orbitalmarine.com/` [accessed: 14/06/2023].

Orbital (2022b). Orbital marine power, o2 deployment. `https://www.emec.org.uk/about-us/our-tidal-clients/orbital-marine-power/` [accessed: 01/05/2023].

Ortega, A., Tomy, J. P., Shek, J., Paboeuf, S., and Ingram, D. (2020). An inter-comparison of dynamic, fully coupled, electro-mechanical, models of tidal turbines. *Energies*, 13.

Osalusi, E. (2010). Analysis of wave and current data in a tidal energy test site. page 280.

Ouro, P., Harrold, M., Stoesser, T., and Bromley, P. (2017). Hydrodynamic loadings on a horizontal axis tidal turbine prototype. *Journal of Fluids and Structures*, 71:78–95.

Ouro, P. and Stoesser, T. (2019). Impact of environmental turbulence on the performance and loadings of a tidal stream turbine. *Flow, Turbulence and Combustion*, 102:613–639.

Parkinson, S. G. and Collier, W. J. (2016). Model validation of hydrodynamic loads and performance of a full-scale tidal turbine using tidal bladed. *International Journal of Marine Energy*, 16:279–297.

Payne, G. S., Stallard, T., Martinez, R., and Bruce, T. (2018). Variation of loads on a three-bladed horizontal axis tidal turbine with frequency and blade position. *Journal of Fluids and Structures*, 83:156–170.

Pearson, N. and Hernon, J. (2015). Turbulence : Best practices for measurement of turbulent flows .

Perez, L., Cossu, R., Couzi, C., and Penesis, I. (2020). Wave-turbulence decomposition methods applied to tidal energy site assessment. *Energies*, 13.

Perez, L., Cossu, R., Grinham, A., and Penesis, I. (2022a). An investigation of tidal turbine performance and loads under various turbulence conditions using blade element momentum theory and high-frequency field data acquired in two prospective tidal energy sites in australia. *Renewable Energy*, 201:928–937.

Perez, L., Cossu, R., Grinham, A., and Penesis, I. (2022b). Tidal turbine performance and loads for various hub heights and wave conditions using high-frequency field measurements and blade element momentum theory. *Renewable Energy*, 200:1548–1560.

Petrusevich, V. Y., Dmitrenko, I. A., Niemi, A., Kirillov, S. A., Kamula, C. M., Kuzyk, Z. Z. A., Barber, D. G., and Ehn, J. K. (2020). Impact of tidal dynamics on diel vertical migration of zooplankton in hudson bay. *Ocean Science*, 16:337–353.

Phanikumar, M. S., Aslam, I., Shen, C., Long, D. T., and Voice, T. C. (2007). Separating surface storage from hyporheic retention in natural streams using wavelet decomposition of acoustic doppler current profiles. *Water Resources Research*, 43:1–16.

Pope, S. B. (2000). *Turbulent Flows*. Cambridge University Press.

Richmond, M. C. and Durgesh, V. (2011). Inflow characterization for marine and hydrokinetic energy devices . fy-2011 : Annual progress report. *Renewable Energy*.

Robertson, A., Sethuraman, L., Jonkman, J., and Quick, J. (2018). Assessment of wind parameter sensitivity on ultimate and fatigue wind turbine loads. NREL.

Sabella (2022). Sabella d10 test campaign. `https://www.offshore-energy.biz/sabella-reinstalls-d10-tidal-turbine-for-third-test-campaign-offshore-france/` [accessed: 23/07/2023].

Scarlett, G. T. and Viola, I. M. (2020). Unsteady hydrodynamics of tidal turbine blades. *Renewable Energy*, 146:843–855.

Schlipf, D., Trabucchi, D., and Bischoff, O. (2010). Testing of frozen turbulence hypothesis for wind turbine applications with a scanning lidar system. *Geophysical Research Abstracts*, 12:5410.

Sellar, B., Harding, S., and Richmond, M. (2015). High-resolution velocimetry in energetic tidal currents using a convergent-beam acoustic doppler profiler. *Measurement Science and Technology*, 26.

Sellar, B. G. and Sutherland, D. R. (2016). Tidal energy site characterisation at the fall of warness ma1001 (md3.8). 1001.

Sellar, B. G., Wakelam, G., Sutherland, D. R., Ingram, D. M., and Venugopal, V. (2018). Characterisation of tidal flows at the european marine energy centre in the absence of ocean waves. *Energies*, 11.

Sentchev, A., Thiébaut, M., and Schmitt, F. G. (2020). Impact of turbulence on power production by a free-stream tidal turbine in real sea conditions. *Renewable Energy*, 147:1932–1940.

SimecAtlantis (2022). Simec atlantis - meygen deployment. `https://www.offshore-energy.biz/simec-atlantis-redeploys-another-meygen-tidal-energy-turbine/`[accessed: 01/05/2023].

SME (2022). Sustainable marine ready to launch in nova scotia. `https://www.oceanenergy-europe.eu/industry-news/sustainable-marine-ready-to-launch-tidal-energy-onto-nova-scotias-grid/` [accessed: 15/04/2023].

Smyth, M. (2019). Three-dimensional unsteady hydrodynamics of tidal turbines.

Sutherland, D. R., Noble, D. R., Steynor, J., Davey, T., and Bruce, T. (2017). Characterisation of current and turbulence in the flowave ocean energy research facility. *Ocean Engineering*, 139:103–115.

Thiébaut, M., Filipot, J. F., Maisondieu, C., Damblans, G., Duarte, R., Droniou, E., Chaplain, N., and Guillou, S. (2020a). A comprehensive assessment of turbulence at a tidal-stream energy site influenced by wind-generated ocean waves. *Energy*, 191.

Thiébaut, M., Filipot, J.-F., Maisondieu, C., Damblans, G., Duarte, R., Droniou, E., and Guillou, S. (2020b). Assessing the turbulent kinetic energy budget in an energetic tidal flow from measurements of coupled adcps. *Phil. Trans. R. Soc*.

Thiébaut, M., Filipot, J. F., Maisondieu, C., Damblans, G., Jochum, C., Kilcher, L., and Guillou, S. (2020c). Characterization of the vertical evolution of the three-dimensional turbulence for fatigue design of tidal turbines. *Philosophical Transactions of the Royal Society A*, 378.

Thomson, J., Kilcher, L., and Harding, S. (2014). Multi-scale turbulence at tidal energy sites. *Proceedings of the 5th International Conference on Ocean Energy, Halifax, Nova Scotia*, pages 1–6.

Thomson, J., Polagye, B., Durgesh, V., and Richmond, M. C. (2012). Measurements of turbulence at two tidal energy sites in puget sound, wa. *IEEE Journal of Oceanic Engineering*, 37:363–374.

Togneri, M. and Masters, I. (2016). Micrositing variability and mean flow scaling for marine turbulence in ramsey sound. *Journal of Ocean Engineering and Marine Energy*, 2:35–46.

Togneri, M., Masters, I., Williams, A., and Fairley, I. (2021). A spectral-statistical filter for decoupling wave and turbulence effects at tidal sites. *Proceedings of the European Wave and Tidal Energy Conference*, pages 1927–1–1927–10.

Torrence, C. and Compo, G. P. (1997). A practical guide to wavelet analysis. *Journal of Materials Science*, 32:2623–2627.

Veers, P. S. (1988). Three-dimensional wind simulation.

Vermeulen, B., Hoitink, A. J., and Sassi, M. G. (2011). Coupled adcps can yield complete reynolds stress tensor profiles in geophysical surface flows. *Geophysical Research Letters*, 38:2–7.

Walter, R. K., Nidzieko, N. J., and Monismith, S. G. (2011). Similarity scaling of turbulence spectra and cospectra in a shallow tidal flow. *Journal of Geophysical Research: Oceans*, 116:1–14.

Welch, P. (1967). The use of fast fourier transform for the estimation of power spectra: a method based on time averaging over short, modified periodograms. *IEEE Transactions on audio and electroacoustics*, 15(2):70–73.

Winter, A. I. (2011). Differences in fundamental design drivers for wind and tidal turbines. *OCEANS 2011 IEEE - Spain*.

Zhu, Q., van Prooijen, B. C., Wang, Z. B., Ma, Y. X., and Yang, S. L. (2016). Bed shear stress estimation on an open intertidal flat using in situ measurements. *Estuarine, Coastal and Shelf Science*, 182:190–201.